UNIVERSITÉ DE STRASBOURG

ÉCOLE DOCTORALE DES SCIENCES CHIMIQUES

UMR 7006 Institut de Science et d'Ingénierie Supramoléculaires

THÈSE

présentée par :

Cosimo ANICHINI

soutenue le : **14 décembre 2020**

pour obtenir le grade de : **Docteur de l'université de Strasbourg**

Discipline/ Spécialité : Chimie / Chimie

Matériaux fonctionnels hybrides à base de graphène

THÈSE dirigée par :

M. SAMORÌ Paolo	Professeur, Université de Strasbourg

RAPPORTEURS :

M. CAVALLINI Massimiliano	Directeur de recherche, CNR-ISMN Sez. Bologna, Bologna (Italie)
M. BONCEL Slawomir	Professeur, Silesian University of Technology, Gliwice (Pologne)

AUTRES MEMBRES DU JURY :

M. STADLER Adrian-Mihail	Chargé de recherche, Université de Strasbourg

Resumé

Le monde dans lequel nous vivons évolue rapidement et pendant les dernières années nous avons eu à notre disposition des appareils électroniques de plus en plus intelligents, portables et connectés. Les technologies actuelles peinent à répondre aux demandes des utilisateurs, qui veulent des appareils de plus en plus performants, avec des batteries à charge rapide et longue durée, des écrans flexibles, avec une interactivité en croissant et donc de plus en plus capables d'échanger des données avec l'environnement. Il existe donc un besoin urgent de nouveaux matériaux et technologies capables de répondre aux demandes des utilisateurs. Presque simultanément aux progrès des appareils électroniques et de leurs caractéristiques, dans la communauté scientifique nous avons observé la découverte d'un matériau qui a promis d'apporter une application révolutionnaire dans presque tous les domaines de recherche, de la médecine à la photonique. Ce matériau est le graphène, dont les propriétés physiques et chimiques exceptionnelles ont été révélées en 2004 par Novoselov et Geim, qui ont ensuite reçu le prix Nobel de physique pour leurs études révolutionnaires.[1] Le graphène est une couche d'épaisseur monoatomique, composée d'atomes de carbone hybrides sp^2, structurellement analogue au graphite. Le matériau présentait des propriétés exceptionnelles, soit une conductivité électrique élevée avec transport de charge balistique et sans bande interdite, conductivité thermique, transparence, imperméabilité et résistance mécanique remarquable. Malgré le grand potentiel, l'introduction du graphène de haute qualité dans les produits finis du marché a été entravée, principalement en raison de son coût élevé et de sa production à petite échelle. Cependant, l'oxyde de graphène (GO) et l'oxyde de graphène réduit (rGO) sont apparus comme des analogues « imparfaits » et peu coûteux du graphène, avec lequel ils partagent certaines propriétés, tout en différant des autres. Au cours des 15 dernières années les méthodes permettant la production à grande échelle de graphène se sont multipliées, bien que les produits qui en résultent ne répondent pas toujours aux attentes du marché. Les chercheurs ont réagi de la manière la plus évidente et la plus directe, en appliquant l'approche hybride au graphène, c'est-à-dire en combinant le graphène avec d'autres matériaux pour obtenir de nouveaux matériaux hybrides. L'approche hybride a permis de fabriquer de nouveaux matériaux aux propriétés inédites, qui sont bien plus que la simple somme des propriétés des constituants.

Cette thèse est centrée sur le développement des structures hybrides à base de graphène, qui a été associé à des molécules et à des nanostructures métalliques 1D à l'aide d'interactions non covalentes et covalentes. Les propriétés de matériaux hybrides obtenues les rendent intéressants pour des applications en tant que systèmes conducteurs, en optoélectronique et en détection.

D'une part, l'oxyde de graphène réduit a été combiné via des interactions non covalentes avec des nanofils métalliques, pour obtenir un nouveau composite possédant une

conductivité électrique élevée et une transparence élevée ; ces caractéristiques rendent le composite intéressant comme électrode conductrice transparente, avec une application prometteuse dans les écrans électrochromes. D'autre part, l'oxyde de graphène réduit a été fonctionnalisé de manière covalente avec des molécules conçues pour cibler les capacités de détection de l'hybride ; ces matériaux ont été utilisés comme capteurs d'humidité extrêmement sensibles et fiables.

Dans le chapitre 2 de la thèse, un aperçu complet des structures hybrides à base de graphène a été présenté. Une stratégie la plus puissante et la plus viable pour augmenter les performances du graphène consiste en sa fonctionnalisation avec d'autres nanostructures ou molécules dans le but de preparer de nouveaux matériaux hybrides. A cet égard, les 10 dernières années ont vu une explosion de publications sur des structures hybrides à base de graphène avec des applications dans les domaines les plus disparates. Au sein de l'hybride, le graphène peut être lié aux molécules ou nanostructures soit via des interactions non covalentes soit par des liaisons covalentes. En règle générale, la fonctionnalisation covalente du graphène vierge compromet la structure sp^2, et ça conduit à la dégradation de ses propriétés électroniques ; cependant lorsque rGO et GO sont fonctionnalisés de manière covalente, une dégradation des propriétés électroniques n'est généralement pas observée en raison de la présence abondante de défauts dans ces matériaux avant la fonctionnalisation.[2] En plus, le graphène vierge est plutôt inerte et sa fonctionnalisation covalente nécessite des conditions difficiles. Pour ces raisons, sur le graphène vierge la fonctionnalisation non covalente est généralement privilégiée. Le premier chapitre donne une brève introduction au graphène, en mettant l'accent sur ses propriétés et ses méthodes de production. Ensuite les assemblages hybrides à base de graphène sont présentés, comme les hybrides de graphène avec d'autres nanomatériaux, à leur fois classés en fonction la dimensionnalité (i.e. nanomatériaux 0D, 1D, 2D), et les hybrides de graphène avec des molécules, avec un accent sur la fonctionnalisation covalente et les interactions non covalentes. Par la suite, l'application de ces matériaux hybrides est présentée et classée pour les matériaux actifs, avec applications dans la détection, la purification de l'eau, la (photo)catalyse et le photovoltaïque, et pour les matériaux électroniques, avec applications comme électrodes conductrices transparentes et électrodes pour le stockage d'énergie.

Dans le chapitre 3, nous avons discuté les méthodes expérimentales et les techniques de caractérisation utilisées pour le travail de recherche de cette thèse, y compris les procédures de synthèse des nanofils de cuivre et de l'oxyde de graphène, et les méthodes de dépôt. L'accent a été mis sur le développement de méthodes de synthèse efficaces (flux de processus simple, rendement élevé, faible coût des matières premières, évolutivité) et durables (faible toxicité, respect de l'environnement, faibles déchets), qui sont une condition préalable à la production de masse dans de futures applications réelles. Finalement, une introduction complète des diverses méthodes de caractérisation utilisées, en tant qu'outils pour acquérir une compréhension approfondie de la structure, des propriétés et de la composition

chimique des matériaux et des dispositifs, a été fournie. Ces techniques comprennent les mesures électriques, les caractérisations spectroscopiques (c'est-à-dire la spectroscopie Raman et IR, la spectroscopie UV-Vis, la spectrométrie photoélectronique X, la diffraction des rayons X) et les caractérisations de surface (c'est-à-dire l'angle de contact avec l'eau, la microscopie à force atomique, la microscopie électronique à balayage et la microscopie optique).

Dans le chapitre 4, un nouveau matériel hybride à base de graphène chimiquement modifié a été développé et utilisé comme capteur d'humidité très performant. Les capteurs capables de mesurer l'humidité relative (HR) avec une haute précision sont des dispositifs clés pour la surveillance de l'environnement et jouent un rôle important dans les domaines de la vie quotidienne, de l'industrie, de l'agriculture, de la biomédecine et de l'environnement. Les capteurs d'humidité de type résistif, qui mesurent la variation d'humidité relative en tant que variation de la résistance électrique, sont particulièrement intéressants en raison de leur simplicité. Dans le cadre de la recherche de nouveaux matériaux aux performances supérieures et à moindre coût, les capteurs d'humidité basés sur GO ont émergé en raison de leurs propriétés prometteuses telles qu'un coût faible et une sensibilité élevée. Cependant, les capteurs actuels basés sur GO souffrent de certains inconvénients importants, notamment une réponse et une récupération lente, et une faible stabilité. D'autre part, rGO présente une stabilité plus élevée, mais s'accompagne d'une sensibilité plus faible à l'humidité en raison de sa nature hydrophobe.[3] Dans le but d'améliorer les performances de détection de l'humidité de rGO, nous avons présenté un nouveau type de capteur d'humidité basé sur une simple modification chimique de rGO, avec des molécules hydrophiles conçues ad-hoc qui interagissent spécifiquement et de manière réversible au niveau supramoléculaire avec les molécules d'eau (rCMGO-1). Nous avons concentré notre attention sur le tri(éthylène glycol) qui peut interagir avec les molécules d'eau formant des liaisons hydrogène faibles (donc réversibles) par rapport aux carbonyles, acides carboxyliques et hydroxyles.[4] En parallèle, un rGO chimiquement modifié et hydrophobe (rCMGO-2), présentant des chaînes aliphatiques pendantes, a été produit pour comparaison avec rCMGO-1. Ces deux matériaux et le rGO ont été entièrement caractérisés pour obtenir un aperçu de leur composition chimique et de leurs propriétés structurelles, puis ils ont été déposés en couches minces et transparentes pour former des capteurs d'humidité de type résistif et exposés à l'humidité (**Figure 1.1-1 a**). Le but étant celui d'améliorer les performances de détection de l'humidité par le rGO, nous avons prouvé que le dispositif comprenant le rCMGO-1 hydrophile effectivement présente les meilleures performances de détection de l'humidité. Cet appareil présente une réponse positive intéressante à l'humidité avec une sensibilité remarquable (jusqu'à 31% lorsque l'HR est décalée de 2 à 97%, **Figure 1.1-1 b**), une grande stabilité du signal après 100 impulsions d'air humide, une réversibilité complète, une réponse et un temps de récupération rapides (respectivement 25 ms et 127 ms), et une stabilité à long terme surpassant ainsi de nombreux dispositifs commerciaux et autres dispositifs de type résistif à base de rGO. En outre, le

capteur rCMGO-1 affiche également une sélectivité élevée à l'humidité par rapport aux petites molécules organiques polaires représentatives. Inversement, rCMGO-2 décoré de chaînes alkyles, et le rGO non fonctionnalisé présentent une sensibilité plus mauvaise, des temps de réponse et de récupération plus longs et un comportement instable. Enfin l'utilisation de mesures de diffraction des rayons X dépendant de l'humidité (en collaboration avec le Dr V. Morandi et le Dr F. Liscio, IMM-CNR de Bologne) et de simulations de dynamique moléculaire (MD) (en collaboration avec le groupe du Prof. D Boljonne, Université de Mons) a permis d'éclairer l'origine physique des meilleures performances des appareils à base de rCMGO-1. Alors que les groupes fonctionnels présents sur la surface rGO ont un faible impact sur les changements structurels des matériaux lorsqu'ils sont exposés à un environnement humide, leurs différentes interactions avec les molécules d'eau, élucidées par des simulations MD, conduisent à différents comportements électroniques, et différentes performances de réponse à l'humidité.

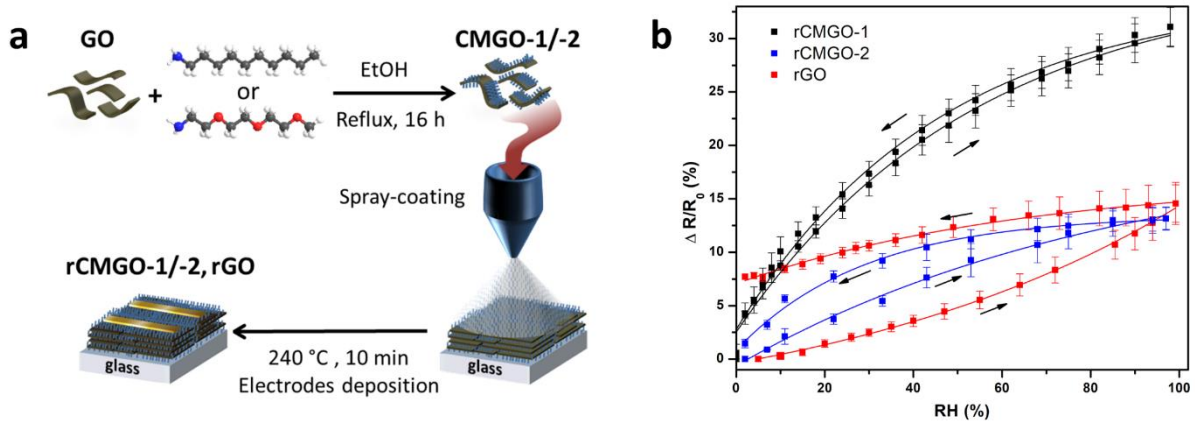

Figure 1.1-1 : (a) Représentation schématique de la fabrication des capteurs d'humidité, rCMGO-1, rCMGO-2 et rGO. (b) Réponse des capteurs d'humidité rCMGO-1, rCMGO-2 et rGO, en fonction de l'humidité relative.

Dans le chapitre 5, la fabrication d'une électrode flexible, transparente et hautement conductrice basée sur l'assemblage hybride d'oxyde de graphène réduit et de nanofils de cuivre (Cu NW) est présentée. Les électrodes transparentes sont des composants clés de nombreux appareils électroniques tels que les écrans tactiles, les écrans, les cellules solaires et les diodes électroluminescentes organiques. De nos jours, le marché des conducteurs transparents est dominé par l'oxyde d'indium-étain (ITO) en raison de sa stabilité, de sa transparence dans le domaine visible et de sa conductivité élevée. Cependant, les principales préoccupations concernant les films ITO sont leur coût élevé et leur faible eco-durabilité en raison de la rareté de l'indium dans la croûte terrestre.[5] En outre, la fragilité des films ITO les rend impropres à une utilisation dans des dispositifs flexibles. Par conséquent, le développement de nouvelles électrodes transparentes à faible coût, stables, flexibles et hautement transparents est l'un des défis majeurs des sciences des matériaux. Les nanofils métalliques et les nanofils de cuivre en particulier émergent comme des alternatives

possibles à l'ITO pour leur faible coût, leur conductivité élevée et leur transparence lorsqu'ils sont déposés pour former des maillages interconnectés.[6] Malheureusement, les films de nanofils de cuivre souffrent d'une mauvaise stabilité car le cuivre est très sujet à l'oxydation. Pour améliorer leur stabilité chimique, différentes stratégies ont été proposées, y compris leur revêtement avec du rGO, qui est bon marché, suffisamment transparent et conducteur.[7] Nous avons développé une méthode de préparation de films Cu NWs/rGO qui repose sur la formation bottom up des Cu NWs au moyen de la réaction de Maillard et sur l'utilisation de GO commercial.[8] Ces deux composants sont traités en couches minces sur tout substrat arbitraire par spray-coating d'une suspension de Cu NWs, suivi d'une suspension de GO. Ensuite, les films ont été placés dans une solution aqueuse de NaBH4 où les deux composants ont été simultanément réduits chimiquement (**Figure 1.1-2 a**). Après le traitement, les films ont présenté une résistance (Rs) de 30 ohm/sq et une transmittance de 71% (à 550 nm). Ces films ont montré une stabilité à l'air pendant des mois, une lavabilité dans les détergents ménagers les plus courants et une résistance à la flexion élevée, pouvant supporter jusqu'à 10000 cycles de cintrage à 1 cm de rayon sans aucune baisse des performances (**Figure 1.1-2 b**). Ces films ont également été mis en œuvre comme électrodes dans des dispositifs électrochromiques (en collaboration avec le Prof. C. Laia, Unversitade Nova de Lisboa), montrant de bonnes performances en termes de contraste optique, de temps de commutation et de cyclabilité (**Figure 1.1-2 c**).

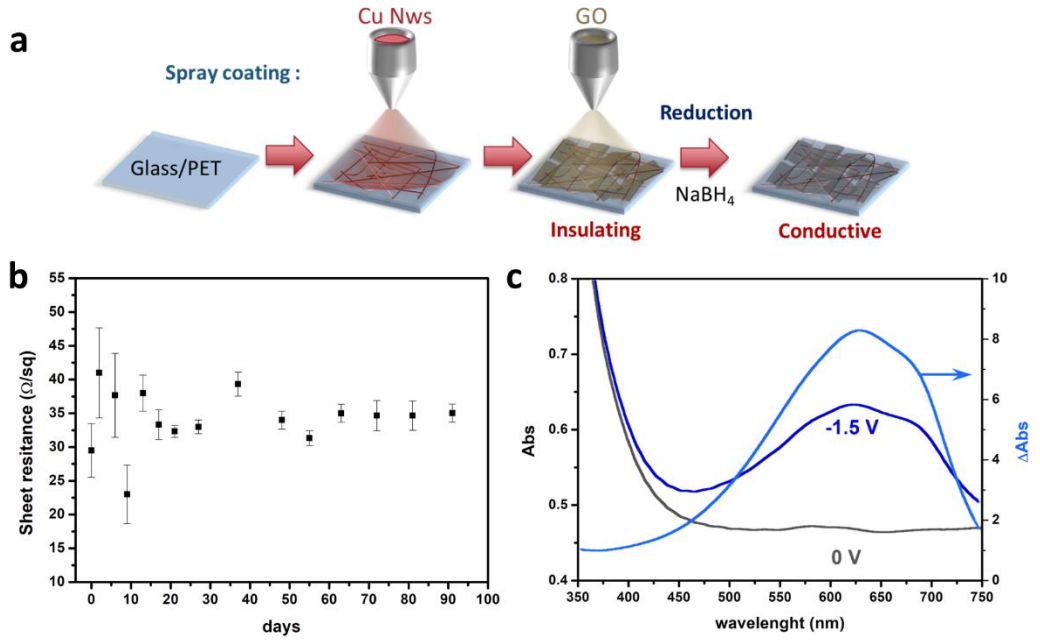

Figure 1.1-2 : (a) Représentation schématique de la fabrication de l'électrode transparente basée sur la structure hybride Cu NWs/rGO. (b) Stabilité de l'électrode exposée à l'air. (c) Absorbance aux états colorés et blanchis d'un dispositif électrochromique assemblé avec l'électrode Cu NWs/rGO.

En conclusion, nous avons exploité l'approche hybride pour construire de nouveaux matériaux à base d'oxyde de graphène réduit, dont les propriétés émergent de la

combinaison synergique des propriétés de chaque composant. Dans le premier projet, rGO a été fonctionnalisé de manière covalente avec des molécules hydrophiles, pour une application de détection d'humidité. Dans ce cas, rGO a été choisi pour sa bonne conductivité, son faible coût et sa grande stabilité, et sa faible affinité pour l'eau a été corrigée en le fonctionnalisant avec des molécules hydrophiles capables de former des liaisons hydrogène faibles et réversibles. Le matériau hybride résultant présentait une conductivité élevée et une stabilité élevée, ainsi qu'une sensibilité et une sélectivité élevées à l'humidité associées à des temps de réponse et de récupération rapides, surpassant de nombreux capteurs d'humidité commerciaux et basés sur rGO. Dans le deuxième projet, un assemblage hybride non covalent de rGO et de nanofils de cuivre a été utilisé comme film conducteur transparent. Dans ce cas, les nanofils de cuivre ont été choisis pour leur faible coût, leur synthèse simple et verte, leur conductivité électrique et leur grande transparence du film. Leur tendance à l'oxydation a été traitée en les recouvrant de rGO, qui est à son tour transparent, assez conducteur et imperméable. L'hybride résultant a présenté une transparence et une conductivité élevées ainsi qu'une résistance améliorée à l'oxydation par rapport aux seuls nanofils de cuivre. Le faible coût, les matières premières largement disponibles, les procédures de synthèse et les méthodes d'assemblage simples et évolutives, et les excellentes performances des dispositifs hybrides présentés ici en font des candidats attractifs pour la mise en œuvre dans des dispositifs commerciaux.

Abstract

The world in which we are living is evolving fast and in the last few years, we have at our disposal electronic devices which are increasingly smarter, portable and connected. Current technologies struggle to keep up with users' requests, who want devices more and more performing, with fast-charging and long-lasting batteries, flexible screens, with crescent interactivity and thus increasingly capable to exchange data from the environment. Therefore there is an urgent need for new materials and technologies that can meet user demand. Almost contemporary to the progress of electronic devices and their features in the scientific community we observed the discovery of a material which has promised to bring revolutionary application in almost any research field from medicine to photonic. This material is graphene, whose outstanding physical and chemical properties were revealed in 2004 by Novoselov and Geim, later awarded the Nobel Prize in physics for their ground-breaking studies.[1] Graphene is an atomic-thick layer of Carbon atoms hybridized sp^2, structurally analogue to graphite. The material exhibited outstanding properties, such as high electrical conductivity with ballistic charge transport and zero bandgap, thermal conductivity, transparency, impermeability and remarkable mechanical strength. Despite the great potential, pristine graphene struggled to enter in end-products of the market mainly due to high cost and low-scale production. On the other hand, graphene oxide (GO) and reduced graphene oxide (rGO) have emerged as low cost, yet imperfect, graphene analogues, with which they share some of the properties, while differing from others. During the last 15 years methods that afford the large-scale production of graphene have multiplied, though the resulting products do not always meet the market expectations. Researchers reacted in the most obvious and straightforward way, by applying the hybrid approach to graphene, i.e. by combining graphene with other materials to obtain new hybrid materials. The hybrid approach made it possible to manufacture new materials with novel properties, which are much more than just the sum of the properties of the constituents.

This thesis is focussed on the use of non-covalent and covalent interactions in order to develop hybrid structures based on graphene combined with molecules and 1D metallic nanostructures for applications as conductive systems, in opto-electronics and sensing.

On the one hand, reduced graphene oxide was combined *via* non-covalent interactions with metallic nanowires, to create a new composite possessing high electrical conductivity and high transparency. These characteristics make the composite of interest as transparent conductive electrode, with promising application in electrochromic displays.

On the other hand, reduced graphene oxide was covalently functionalized with designed molecules to target the sensing capabilities of the hybrid. These materials were used as highly sensitive and reliable humidity sensors.

In the Chapter 2 of the Thesis a comprehensive overview on the hybrid structures based on graphene has been presented. A most powerful and viable strategy to increase the performances of graphene consists in its functionalization with other nanostructures or molecules to yield new hybrid materials. In this respect, the last 10 years has witnessed an explosion of publications on hybrid structures based on graphene with applications in a broadest variety of fields. Within the hybrid the graphene may be bonded to the molecules or nanostructures either *via* non-covalent interactions or through covalent bonds. Generally, covalent functionalization of pristine graphene compromises its sp^2 structure, which leads to a degradation of electronic properties, however when rGO and GO are covalently functionalized a decrease in the electronic properties is usually not observed due to the abundant presence of defects in these materials before functionalization.[2] Furthermore pristine graphene is rather inert and its covalent functionalization requires harsh conditions. For these reasons, on pristine graphene, noncovalent functionalization is usually favoured.

The first Chapter gives a brief introductive background and motivations of this thesis. Then, Chapter 2 begins with an informative introduction to graphene with a focus on its properties and production methods. Next, the hybrid assemblies based on graphene are presented as hybrids of graphene with other nanomaterials, in turn classified for dimensionality (i.e. 0D, 1D, 2D nanomaterials), and hybrids of graphene with molecules, with an accent on the covalent functionalization, and non-covalent interactions. Subsequently the application of these hybrids materials are presented and classified for active materials, with applications in sensing, water purification, (photo)catalysis and photovoltaic, and for electronic materials, with applications as transparent conductive electrodes, and electrodes for energy storage.

In Chapter 3, we have discussed the experimental methods and characterization techniques, including the synthetic procedures of copper nanowires. An emphasis has been devoted to developing efficient (straightforward process flow, high yield, low cost of starting materials, scalability) and sustainable (low toxicity, environmentally friendly, low waste) synthetic methods, which are precondition for mass production in the upcoming real application. Eventually a comprehensive introduction of various characterization methods used as tools to acquire a deep insight into structure, properties and chemical composition of the materials and devices has been provided. These techniques include electrical measurements, spectroscopic characterizations (*i.e.* Raman and IR Spectroscopy, UV-Vis spectroscopy, X-ray Photon Spectroscopy, X-ray diffraction), and surface characterizations

(*i.e.* Water contact angle, Atomic Force Microscopy, Scanning Electron Microscopy and Optical microscopy).

Sensors capable of measuring the relative humidity (RH) with a high precision are key devices for monitoring the environment and are playing an important role in our daily life, industry, agriculture, bio-medical and environmental fields. Resistive-type humidity sensors, which measure the variation in relative humidity as a variation of the electrical resistance, are particularly appealing because of their simplicity. Within the search for new materials with superior performances and lower cost, GO-based humidity sensors have emerged because of their promising properties such as low-cost and high sensitivity. However, current GO-based sensors suffer from some important drawbacks including slow response and recovery, and poor stability. On the other hand, rGO exhibits higher stability, yet accompanied by a lower sensitivity to humidity due to its hydrophobic nature.[3] With the aim of improving the sensing performance towards humidity of rGO, in Chapter 4 we presented a novel kind of high-performing humidity sensor based on a simple chemical modification of rGO, with designed hydrophilic molecules that interact specifically and reversibly at the supramolecular level with water molecules (rCMGO-1). We have focused our attention on triethylene glycol that can interact with water molecules forming weak, thus reversible, hydrogen bonding when compared to carbonyls, carboxylic acids and hydroxyls.[4] In parallel a hydrophobic chemically modified rGO (rCMGO-2), exhibiting dangling aliphatic chains was produced for comparison with rCMGO-1 (**Figure 1.1-3 a**). These two materials and rGO were fully characterized to obtain an insight into their chemical composition and structural properties, and then they were processed in thin and transparent resistive-type humidity sensors and exposed to humidity. We proved that the device comprising the hydrophilic rCMGO-1, possesses the better sensing performances towards humidity. This device shows an interesting positive response to humidity with a remarkable sensitivity (up to 31 % when the RH is shifted from 2 to 97 %, **Figure 1.1-3 b**), high stability of the signal after 100 humid pulses, complete reversibility, fast response and recovery time (respectively 25 ms and 127 ms), and long-term stability thereby outperforming many of the commercial devices and other rGO based resistive type devices. Furthermore, the rCMGO-1 sensor displays also high selectivity to humidity when compared to representative small polar organic molecules. Conversely, the alkyl decorated rCMGO-2 and the non-functionalized rGO exhibit worse sensitivity, longer response and recovery times and instable behaviour. Finally the use of humidity dependent X-ray diffraction measurements (in collaboration with Dr V. Morandi and Dr F. Liscio, IMM-CNR of Bologna) and Molecular dynamic (MD) simulations (in collaboration with the group of Prof. D. Boljonne) made it possible to cast light on the physical origin of the better performances of rCMGO-1 based devices. While the functional groups present on the rGO surface have low impact on the structural changes of the materials when they are exposed to a humid environment, their different interaction with the water molecules, elucidated by MD simulations, lead to diverse electronic behaviours and diverse humidity sensing performances.

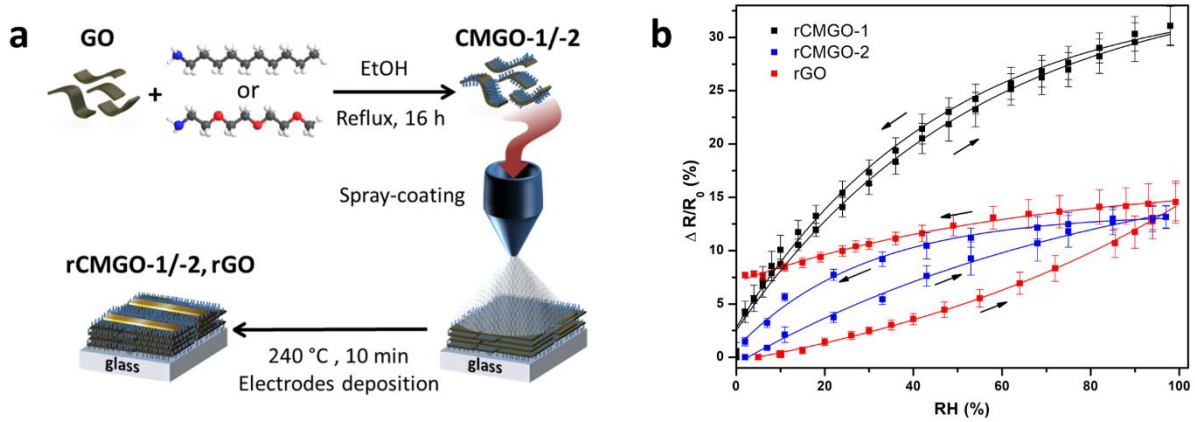

Figure 1.1-3 : (a) Schematic of the synthesis of rCMGO-1 and rCMGO-2 and fabrication of the humidity sensors based on rCMGO-1, rCMGO-2 and rGO. (b) Response of the sensors rCMGO-1, rCMGO-2 and rGO, as a function of the relative humidity.

In Chapter 5 the fabrication of a flexible, transparent and highly conductive electrode based on the hybrid assembly of reduced graphene oxide and copper nanowires (Cu NWs) is presented. Transparent electrodes are key components in numerous electronic devices such as touch screens, displays, solar cells, and organic light-emitting diodes. Nowadays the market of transparent conductors is dominated by Indium-tin oxide (ITO) because of its stability, transparency in the visible range and high conductivity. However, major concerns about ITO films are their high cost and low sustainability due to the scarcity of indium in the earth's crust.[5] Furthermore the fragility of ITO films makes them poorly suitable for flexible electronics. Therefore, the development of new, low-cost, stable, and large-area transparent electrodes is one of the major challenges in material sciences. Metallic nanowires and copper nanowires in particular are emerging as possible alternatives to ITO for their low cost, high conductivity and transparency when deposited to form interconnected networks. Unfortunately, copper nanowires films suffer from poor stability because copper is highly prone to oxidation. To enhance their chemical stability different strategies have been proposed, including their coating with rGO, which is cheap, sufficiently transparent and conductive.[6] We developed a method for the preparation of Cu NWs/rGO films which relies on the bottom-up formation of Cu NWs suspensions by means of the Maillard reaction and on the use of commercial GO.[8] These two components were processed in thin films onto any arbitrary substrate through spray deposition of Cu NWs suspension followed by GO suspension (**Figure 1.1-4 a**). Then the films were placed in a water solution of $NaBH_4$ where the two components were simultaneously chemically reduced. After the treatment, the films displayed sheet resistance of 30 ohm/sq and transmittance of 71 %. These films were stable in air for months, were washable in the most common household detergents and could stand up to 10000 cycles of bending at 1 cm radius without any drop in the performances (**Figure 1.1-4 b**). These films were also implemented as electrodes into electrochromic devices (in collaboration with Prof. C. Laia, Unversitade Nova de Lisboa), showing good performances in terms of optical contrast, switching times and cyclability (**Figure 1.1-4 c**).

~ X ~

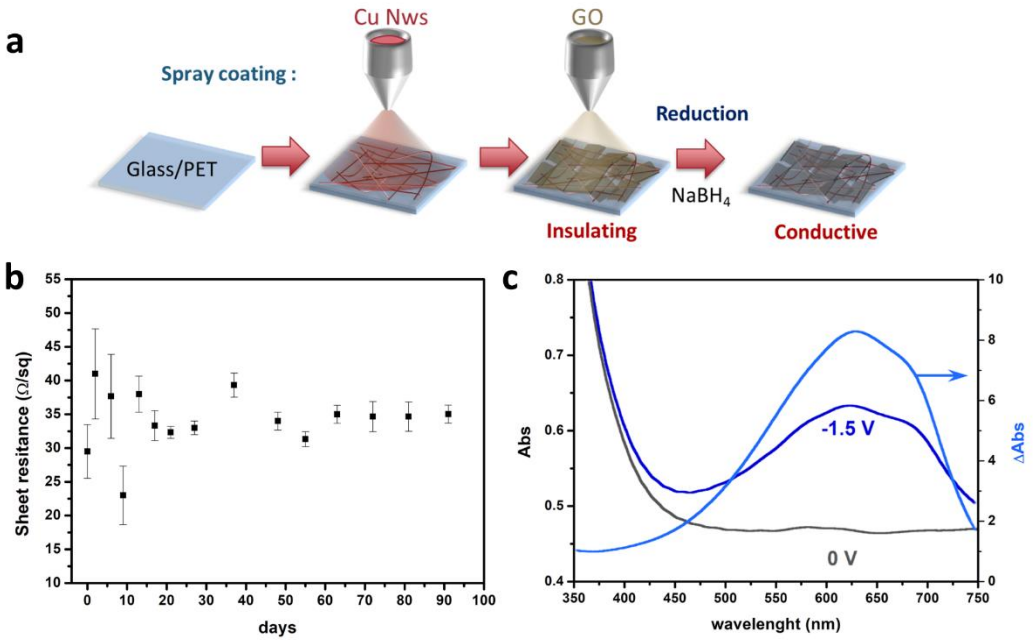

Figure 1.1-4 : (a) Schematic of the fabrication of the Cu NWs/rGO hybrid transparent electrode. (b) Stability of the electrode exposed to air for 100 days. (c) Absorbance of the electrochromic device based on the Cu NWs/rGO electrode in the coloured (-1.5 V) and bleached state (0 V).

In conclusion we have exploited the hybrid approach to build new materials based on reduced graphene oxide, whose properties emerge from the synergic combination of the properties of each component. In the first project rGO was covalently functionalized with designed hydrophilic molecules for humidity sensing application. In this case rGO was chosen for the good conductivity, low cost and high stability, and its low affinity for water was addressed by functionalizing it with hydrophilic molecules able to form weak and reversible hydrogen bonds. The resulting hybrid material exhibited high conductivity and high stability, as well as high sensitivity and selectivity to humidity combined with fast response and recovery times, outperforming many commercial and rGO based humidity sensors. In the second project a non-covalent hybrid assembly of rGO and copper nanowires was employed as transparent conductive film. In this case copper nanowires were chosen for their low cost, straightforward and green synthesis, electrical conductivity, and high transparency of the film. Their tendency to the oxidation was addressed by covering them with rGO, which is in turn transparent, fairly conductive and impermeable. The resulting hybrid presented high transparency and conductivity as well as improved resistance to the oxidation in comparison to the sole copper nanowires. The low cost, the largely available raw materials, the simple and scalable synthetic procedure and assembly methods, and the excellent performances of the hybrid devices here presented make them appealing candidates for the implementation in commercial devices.

Table of Contents

Abbreviations

ABF	Adiabatic Biasing Force
AFM	Atomic force microscopy
ALD	Atomic layer deposition
APTES	(3-aminopropyl) triethoxysilane
ATR	Attenuated total reflectance
ATRP	Atom transfer radical polymerization
BSA	Bovine serum albumin
BSE(s)	Back-scattered electron(s)
CBB	Coomassie Brilliant Blue
CCD	Charge-coupled device
CE	Colouration efficiency
CMGO(s)	Chemically modified graphene oxide(s)
CNF(s)	Carbon nanofiber(s)
CNT(s)	Carbon nanotube(s)
CTAB	Cetyltriamoninum bromide
CVD	Chemical vapour deposition
DC	Direct current
DMMP	Dimethyl methylphosphonate
DOF	Depth of field
EASA	Electrochemically active surface area
DMMP	Dimethyl methylphosphonate
DNA	Deoxyribonucleic acid
DSSC(s)	Dye-sensitized solar cell(s)
ECD(s)	Electrochromic device(s)
ECL	Electrochemiluminescence
EDA	Ethylenediamine
EDAC	Ethyl(dimethylaminopropyl) carbodiimide
EDLC	Electrostatic double-layer capacitance
EDTA	Ethylenediamine triacetic acid
EDX/EDS	Energy-dispersive X-ray spectroscopy
EEG	Electrochemically exfoliated graphene

EIS	Electrochemical impedance spectroscopy
ESCA	Electron Spectroscopy for Chemical Analysis
ETD	Everhart-Thornley Detector
EtOH	Ethanol
FEG	Field-effect gun
FET(s)	Field-effect transistor(s)
FRET	Förster resonance energy transfer
FT-IR	Fourier transform IR spectrometer
GAFF	General AMBER force field
GCE	Glassy carbon electrode
GNR(s)	Graphene nanoribbon(s)
GO	Graphene oxide
HDA	Hexadecylamine
HER	hydrogen evolution reaction
HOPG	Highly oriented pyrolytic graphite
HOR	Hydrogen oxidation reaction
IGG	Indocyanine green
IoT	Internet of things
IR	Infrared
ITO	Indium tin oxide
LB	Langmuir Blodgett
LbL	Layer-by-Layer
LCD	Liquid crystal display
LIB	Lithium-ion batteries
LPE	Liquid-phase exfoliation
LPG	Liquid petroleum gas
LSPR	Localized surface plasmon resonance
MB	Molecular beacon
MC	Merocyanine
MD	Molecular Dynamic
MIR	Mid-infrared
MPc	Metallo-phthalocyanines
MWCNT(s)	Multiwalled carbon nanotube(s)
NCA	Nonacosylamine
NHS	*N*-hydroxysuccinimide

NP(s)	Nanoparticle(s)
NT(s)	Nanotube(s)
NTEG	2-[2-(2-methoxyethoxy)ethoxy]ethylamine
NW(s)	Nanowire(s)
OA	Oleylamine
ODA	Octadecylamine
OER	Oxygen evolution reaction
OLED(s)	Organic light-emitting diode(s)
OPV(s)	Organic photovoltaic(s)
ORR	Oxygen reduction reaction
OSC	Organic solar cells
P3HT	Poly(3-hexylthiophene)
PAA	Poly(amic acid
PAM	Poly(acrylamide)
PANI	Polyaniline
PCBM	Phenyl-C61-butyric acid methyl ester
PCE(s)	Power conversion efficiency(ies)
PDDA	Poly(diallyldimethylammonium chloride
PDI	Perylenediimide
PDT	Photodynamic therapy
PE-CVD	Plasma-enhanced CVD techniques
PEDOT	Poly(3,4-ethylenedioxythiophene
PEDOT:PSS	Poly(3,4-ethylenedioxythiophene): poly(styrene sulfonic acid)
PEG	Poly(ethylene glycol)
PEI	Poly(ethyleneimine)
PESA	Photoelectron spectroscopy in air
PI	Pair Interaction
PMA	Particle mesh Ewald
PMF	Potential of Mean Force
PMMA	Poly(methyl methacrylate)
PPy	Polypyrrole
PS	Polystyrene
PTCDI	Perylene-3,4,9,10-tetracarboxylic-3,4,9,10-diimide
PTT	Photothermal therapy
PVA	Poly(vinyl alcohol)

QD(s)	quantum dot(s)
RH	Relative humidity
ROS	Reactive oxygen species
RT	Room temperature
S-rGO	Sulfonated Rgo
SAXS	Small-angle X-ray scattering
SAM	Self-assembled monolayers
SE	Secondary electron(s)
SEM	Scanning electron microscopy
SERS	Surface-enhanced Raman scattering
SLG	Single-layer graphene
SMU	Source measure unit
SP	Spiropyran
SPANI	Sulfonated polyaniline
ssDNA	Single-stranded DNA
SPM	Scanning probe microscopy
STM	Scanning tunnelling microscopy
SWCNT(s)	Single-walled carbon nanotube(s)
SY	Sunset Yellow
TCE(s)	Transparent conductive electrode(s)
TCF(s)	Transparent conductive film(s)
TCNQ	Tetracyanoquinodimethan
TEG	Triethylene glycol monomethyl ether
TEM	Transmission electron microscopy
TGA	Thermogravimetric analysis
TGS	Triglycine sulfate
TMC	1,3,5-benzenetricarbonyl trichloride
TMD(s)	Transition metal dichalcogenide(s)
TNT	Trinitrotoluene
UHR-TEM	Ultra-high resolution transmission electron microscopy
UILPE	Ultrasound-induced liquid-phase exfoliation
UV	Ultraviolet
Vis	Visible
VOC(s)	volatile organic compounds(s)
VDWE	Van der Waals epitaxy

XPS	X-ray photoelectron spectroscopy	
XRD	X-Ray	diffraction

Chapter 1.

Introduction

1.1. Context and motivation

During the last few years, smart electronic devices have become ubiquitous. Smart phones, smart bands, smart watches, smart refrigerator, smart cars, smart speakers are now vital tools in our everyday life. The main common features of such electronic devices are the universal presence of sensors, which impart to the device the capacity to interact with the external environment by collecting information, and the presence of connectivity to interact, by exchanging information, with other smart devices and/or other mechanisms to interact and share information with the human users, by means of displays and speakers mainly. The importance of sensors is misjudged: without sensors, the capabilities of a device such as a smartphone will be mostly nullified. Common smartphones integrate a multitude of sensors including microphones, photo cameras, gyroscope, accelerometer, proximity sensor, light sensor, touch sensors, magnetometer, barometer and thermometer. The functionalities of smart devices such as smartwatches and smart bands would be even more limited without sensors. On the other hand, the information collected by such sensors is often shared by wireless connectivity (e.g. Bluetooth, Wi-Fi, NFC, etc.) with other classes of smart devices, constituting the so-called *Internet of things* (*IoT*). Nonetheless, the final users of such smart devices are always humans, and since we are not able to interact directly with the low energy electromagnetic radiations that are exploited by the wireless connectivity and decrypt the therein contained information, we need electronic tools to collect such information and provide an output which can be perceived by means of one of our five senses, generally *via* sight and hearing. For this reason, the presence of display screens and/or speakers become a mandatory characteristic for such smart devices to interact with the human final user.

The incredibly fast spreading of these smart devices has raised two important concerns that the engineers and researchers behind the development of such devices need to face. On the one hand, there is the need and demand of the users who claim devices that are each time more performing and feature larger and flexible screens, better cameras, faster processors, longer lasting batteries, more accurate sensors, etc. On the other hand, there is increasing attention about the environmental and energetic impact represented by the exponentially growing number of electronic devices. In particular, many components of these smart electronic devices comprise rare elements and critical materials, such as rare

earth and noble metals, which are susceptible of supply shortage in the near future and have great environmental implication.[9] Furthermore, the challenge of cutting and gradually reducing to zero the greenhouse gas emissions to mitigate their impact on the climate change requires, on the one hand, the escalation in the use of renewable energy sources and on the other hand the optimization of the production cycles and of the same electronic devices to increase their energy efficiency.

Within this complex frame, scientists and researchers are called to find new materials and design new devices presenting, at the same time, better performances and higher energetic and environmental sustainability. Among these new materials, graphene ignited the interest of the academic world and beyond it by virtue of its astonishing properties. Graphene, a monatomic-thick layer of hexagonally arranged carbon atoms, was firstly isolated in 2004 by Geim and Novoselov (who later were awarded the Nobel Prize in chemistry for this discovery) and rapidly became the most investigated and employed material in science.[10] The unique properties of such material, which is a zero-bandgap ambipolar semiconductor, include extremely high electrical and thermal conductivity, great mechanical strength together with high flexibility, transparency, and impermeability.[11] Thanks to these remarkable properties and to its relatively easy and low-cost production, graphene has found potential application in any corner of science and technology, from ultrafast optoelectronics to water filtration and medicine. In particular, graphene oxide (GO) and reduced graphene oxide (rGO) are structurally closely related to pristine graphene and share many of its unique properties, though they can not only be produced in a much larger scale and at a lower cost but they also possess higher processability and versatility compared to pristine graphene.[12]

The potential of graphene, GO and rGO can be greatly increased by combining them into hybrids with other nanostructures and/or molecules bearing additional functionalities. Such hybrid materials possess not only the properties of the individual components but exhibit new properties and enhanced characteristics arising from the synergic interaction of the components.[2] In order to manifest this synergic interaction, the hybrid components must be intimately connected, and interact together through non-covalent or covalent interactions at the nanoscopic scale. This common characteristic of hybrid materials differentiates them from composite materials, which are characterized by the physical mixing of the components on a micro/macro scale.[13] The combination of graphene with functional nanomaterials or molecules can confer to the graphene hybrid new properties (such as bio-compatibility, luminescence, dispersibility into different solvents, enhanced conductivity, catalytic activity and specific binding to target analytes) that makes it possible to exploit such hybrid systems for applications such as drug-delivery, bio-imaging, (bio)chemical sensing, (electro)catalysis, photovoltaic, batteries, supercapacitors, photodetection and in transparent electrodes for optoelectronic devices.[2, 14-16]

Thus, graphene-based hybrid materials may be the right answer to the aforementioned challenges in the development of smart electronic devices. This thesis is focussed on the preparation of low-cost, straightforward and sustainable graphene-based hybrids to respond to the request of low-cost, low-consumption reliable humidity sensors and environmentally sustainable transparent flexible electrodes. In order to reduce the costs, increase the environmental sustainability and the industrial scalability, we have focussed on the use of reduced graphene oxide, which is at the present time the cheapest and most abundant form of graphene. On the one hand, we have exploited the covalent functionalization of rGO with simple functional molecules to form a rGO-molecules hybrid with remarkable humidity sensing performances. This hybrid combines the conductivity and stability of the hydrophobic rGO with the hydrophilic nature of triethylene glycol molecules to obtain a hydrophilic rGO-molecules hybrid with high stability, good conductivity, and high selective sensitivity to water. On the other hand, we have exploited the non-covalent assembly of rGO with metallic 1D nanostructures (copper nanowires)[17] to obtain hybrid flexible and transparent electrodes for optoelectronic devices. In this case, the high conductivity, transparency and flexibility of films of copper nanowires (Cu NWs) are combined with the transparency, conductivity, flexibility, inertness and impermeable properties of rGO films to obtain a hybrid transparent, conductive and flexible film with enhanced robustness.

1.2. Structure of the thesis

This thesis is organised as follows:

Chapter 2. Graphene is briefly introduced, and its properties and production methods are discussed. Then, the hybrid assemblies based on graphene are presented as hybrids of graphene with other nanomaterials, which are in turn classified for dimensionality (i.e. 0D, 1D, 2D nanomaterials), and hybrids of graphene with molecules, with an accent on the covalent functionalization and non-covalent interactions. Subsequently, the applications of these hybrid materials are detailed and classified in two groups: hybrids as active materials, with different kinds of applications presented, and hybrids as transparent conductive electrodes for optoelectronic devices.

Chapter 3. The working principles of different characterization methods employed in this thesis, including spectroscopic techniques, microscopies, etc., are discussed to have an accurate and comprehensive understanding of the rGO based hybrid functional materials developed in this thesis. The different strategies of synthesis of copper nanowires, which are at the base of the hybrid transparent electrode developed in chapter 5, are also discussed.

Chapter 4. A novel humidity sensor based on a rGO-molecules hybrid is presented. We functionalized rGO with amine-terminated triethylene glycol molecules, by exploiting the ring-opening reaction obtained when an amine terminal group attacks an epoxide group of

GO. Such a molecule was chosen because it can interact with water molecules by forming weak, thus reversible hydrogen bonding. In parallel, rGO was functionalized with a hydrophobic alkyl amine to compare its humidity sensing performances to those of the rGO-thriethylene glycol hybrid. The two hybrid materials developed were processed in thin films *via* spray-coating and comprehensively characterized. Their humidity sensing performances, as well as their cross-sensitivity to other vapours and robustness were investigated. In particular, the rGO-thriethylene glycol hybrid exhibited impressively superior humidity sensing performances compared to both pristine rGO and alkylated rGO hybrid. Finally, the sensing mechanism and the different performances of the two hybrids and rGO were elucidated by means of humidity-dependent X-ray diffraction and molecular dynamic simulations.

Chapter 5. The development of "green" and low-cost transparent electrodes based on a Cu NWs/rGO hybrid is reported. Dispersions of copper nanowires were obtained following a wet-chemistry green and scalable procedure,[8] and processed in thin films by spray-coating onto different substrates. Then, a thin layer of GO was deposited on top of the Cu NWs film as a barrier against the oxidation. The conductivity of the hybrid film was enabled through a mild reduction treatment that reduced both components simultaneously. The obtained Cu NWs/rGO hybrid film, as well as films of the single components, were fully characterized. In particular, the resulting hybrid transparent conductive film outperformed the films of the single components, as it exhibited higher and more uniform conductivities, lower roughness, high flexibility, and improved resistance to the oxidation. Finally, the hybrid film was employed as a transparent electrode in flexible electrochromic devices (ECD) and the photoelectrochemical properties and long-term stability of such devices were investigated. The ECD assembled with such a hybrid transparent electrode displayed high performances, being comparable to those obtained by ECD assembled with the commercially standard, yet scarcely sustainable indium tin oxide (ITO) electrodes.

Chapter 6. A summary of the presented work is provided, together with the outlooks for its future development.

Chapter 2.

Hybrid assemblies based on graphene

2.1. Introduction

Hybrid materials are formed by combining two or more materials exhibiting different properties on the nanoscale to produce new bi- or multi-component systems displaying unique characteristics. In fact, the strong interactions existing between the components in the hybrid yields a synergistic effect, which leads to the emergence of new properties. Graphene is an extraordinary material which was first isolated in 2004. Since then, it has become a most investigated material which has been the subject of more than 120000* papers by 2020. This atomically thin material exhibits unique properties including huge surface area, excellent electron mobility and conductivity, great mechanical strength and flexibility, high transparency and stability. Soon after the graphene discovery, while many of its properties were still unknown, some scientists sought the answer to the question: "what happens if we combine this wonder material with other materials or molecules to form a hybrid?". The implementation of the hybrid approach to graphene paved the way to its use in a broadest variety of applications and devices, including (bio)chemical sensors, photovoltaic cells, photodetectors, memories, photocatalysis, water purification, supercapacitors, batteries, drug-delivery, bioimaging, etc.. Graphene-based hybrids can be obtained by combining such 2D material with molecules and macromolecules, either *via* covalent or non-covalent functionalization. Properly chosen molecules can confer to the hybrid various new properties, such as selective interaction with target (bio)molecules or ions, biocompatibility, semiconductive behaviour, luminescence, catalytic activity, etc.. In addition, graphene can be combined with other organic and inorganic nanostructures, to form hybrids exhibiting properties such as transparency, electrical conductivity, increased surface area and porosity, mechanical resistance, flexibility, chemical stability, etc. The combination of graphene with multiple organic or inorganic components makes it possible to develop multifunctional materials. [18-21]

This chapter describes the most enlightening approaches of hybrid materials based on graphene and their primary fields of application. In section 1.2 graphene is described in more detail, by highlighting its principal properties and the main methods of production.

* Source: Web of Science (Titles containing: "graphene")

Graphene oxide and reduced graphene oxide are also introduced in the section, as materials strictly related to graphene. In section 1.3 graphene based hybrid assemblies are classified in view the type of the second component including nanomaterials (whose 0D, 1D, 2D dimensionality is exploited as categorizing criteria) and (macro)molecules, with an accent on both covalent and non-covalent functionalization. Subsequently, in section 2.3 some relevant applications of these hybrids materials are presented and classified for active materials, with a special focus on sensing, water purification, (photo)catalysis, biomedical, energy storage and hybrids as transparent electrodes for optoelectronics, providing some proofs of concepts when integrated into solar cells, display technologies and photodetection.

2.1.1. Graphene: properties and preparation methods

Graphene is an allotrope of carbon characterized by a two-dimensional, honey-comb lattice of sp^2-hybridized carbon atoms. It can be seen either as a single monolayer of graphite or as an indefinitely large polycyclic aromatic hydrocarbon. Graphene is the basic building block of other carbon allotropes: it can be stacked to form 3D graphite, rolled to form 1D nanotubes, and wrapped to form 0D fullerenes. Graphene was hypothesised in the second half of the XXI century, and in this period many of its properties were already predicted, however, it was believed that it would have not been stable in the free state.[22] Finally, in 2004 Andre Geim and Konstantin Novoselov succeeded in isolating graphene monolayer on thermally oxidized silicon wafers (Si/SiO_2) by mechanical cleavage of graphite with common adhesive tape. For this discovery, and the successive investigation on graphene properties, Geim and Novoselov were awarded the Nobel Prize in Physics in 2010.[10]

Graphene exhibits many outstanding thermal, mechanical, and electrical properties, arising from its structure which is characterized by a long-range π-conjugation. Each carbon atom is sp^2-hybridized, with three planar σ bonds connecting its three neighbouring carbons. The overlapping of the p_z orbitals on each carbon give rise to two band levels, π and π*, with bonding and antibonding characters, which are filled and unfilled, and named valence band and conduction band, respectively. These two bands take the shape of two inverted cones, whose vertices meet in the Dirac point. For this reason, graphene behaves as a zero band-gap ambipolar semiconductor or semimetal. Another effect of the graphene band structure is that holes and electrons in graphene behave as massless relativistic particles, or the Dirac fermions, that present an unimpeded ballistic motion.[10] The mobility of charge carrier in graphene is weakly dependent on the temperature and can be exceptionally high and even overtake the theoretical limit of 2×10^5 $cm^2 \cdot V^{-1} \cdot s^{-1}$ at room temperature for high-quality graphene flakes insulated between two hexagonal boron nitride (h-BN) layers.[23] Graphene is incredibly strong and flexible, with an elastic modulus of 1 TPa and intrinsic strength of 130 GPa,[24] over 100 times stronger than steel, and possesses also a record thermal conductivity. Moreover, a single graphene layer is nearly transparent, although being unexpectedly highly opaque for an atomic monolayer, adsorbing approximately 2.3% of

light, and is perfectly impermeable to even the smallest gas molecule.[25, 26] Nevertheless, it is important to notice that many of these values have been obtained for samples of the highest quality of small lateral size, under special conditions. For example, the previously reported charge mobility is true only for mechanically exfoliated graphene flakes on substrates free of dangling bonds and charge traps such as h-BN; the same flake on a common Si/SiO_2 substrate exhibits maximum mobility which is decreased down to 10000 $cm^2 \cdot V^{-1} \cdot s^{-1}$ because of the strong interactions with the substrate.[27] Bigger mechanically exfoliated graphene flakes and graphene obtained by other routes display lower mobilities because of the appearance of grain boundaries, inhomogeneities and defects.[28] Likewise, the mechanical properties exhibit less exciting characteristics as a result of the appearance of defects and wrinkles.[29]

All these qualities have made graphene the most researched materials, with potential application in endless technologies, from medicine to water filtration and ultrafast optoelectronics. Soon after the first studies on graphene that unveiled all its enormous potential, science has witnessed a tremendous race on discovering, isolating, and characterizing other 2D materials. Despite its potentials, high-quality graphene struggles to be integrated into end products because of the persisting difficulties in obtaining high-quality and easy processable graphene, with low cost, and in high quantity.

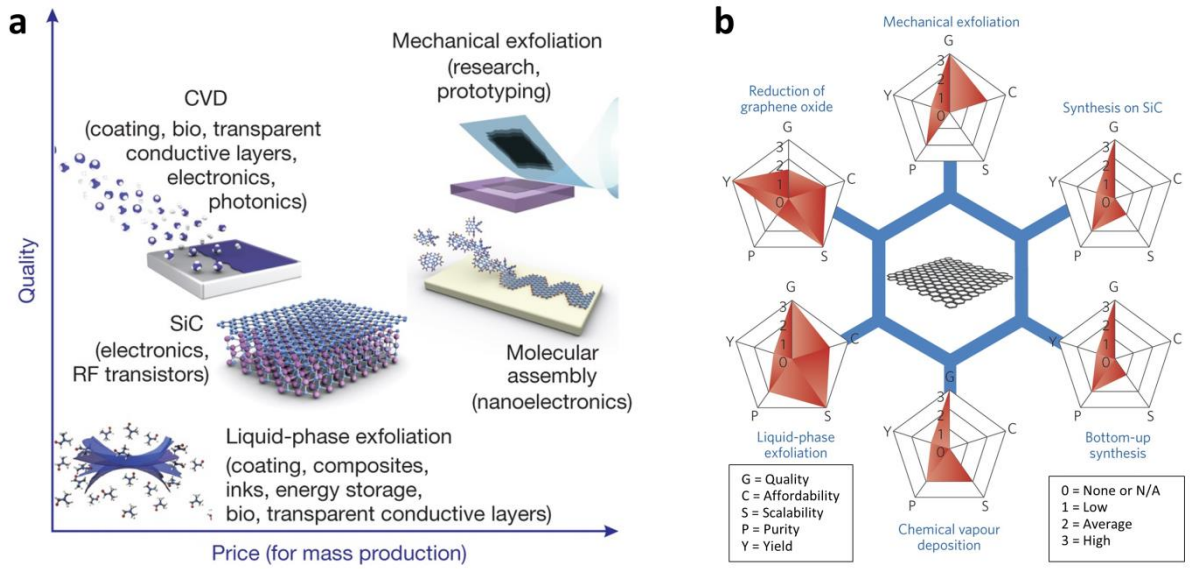

Figure 2.1-1: (a) Schematic graph of different production methods of graphene as a function of the quality and price of the obtained graphene. Adapted from Ref. [11] (b) Schematic of the most common graphene production method evaluated as a function of quality, affordability, scalability, purity and yield. Adapted from Ref. [30]

Several methods are nowadays well established for producing graphene: each one has pros and cons and suitability for a certain application. These methods can be categorized into top-down and bottom-up approaches: the former includes mechanical exfoliation and liquid-phase exfoliation, while the letter comprises total organic synthesis, chemical vapour deposition and thermal evaporation of SiC (

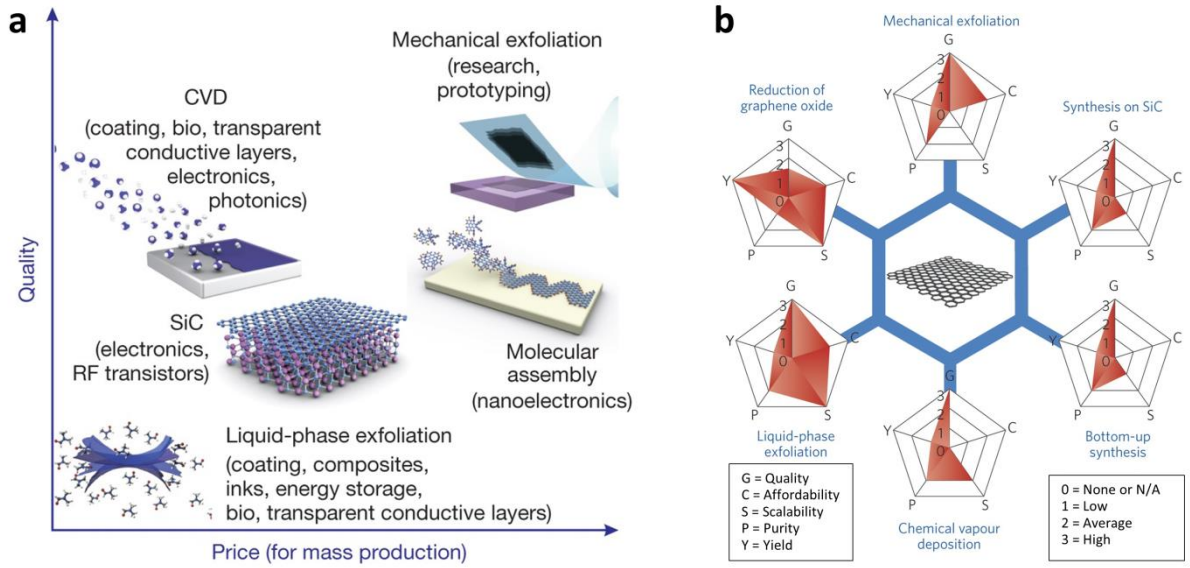

Figure 2.1-1).

The first method developed is the mechanical exfoliation which consists of pulling apart monolayers of graphene from a bulk layered crystal of graphite using adhesive tape. This method has produced so far the highest quality samples, which possess the above mentioned outstanding characteristics. However, the method is neither high throughput nor high yield, making the flakes produced in this fashion the most expensive and the method unlikely to be industrially scalable. Other types of mechanical exfoliation have been implemented, yet they all suffer from the same limitations. The bottom-up approach relies on the use of organic synthesis, to create larger and larger polycyclic aromatic hydrocarbons which can be seen as 2D macromolecules.[31, 32] They can be grown with a preferential axis of growth or backbone leading to highly versatile graphene nanoribbons. These can be substituted with a range of aliphatic chains, modifying their solubility, yet the latter becomes an insurmountable problem with the increasing molecular weight. Also, this is accompanied by an increased occurrence of side reactions. Another method to produce bottom-up graphene is the thermal decomposition of SiC. Heating silicon carbide at 1100 °C in high vacuum leads to the sublimation of Si atoms from the SiC surface, giving an epitaxial monolayer of graphene on the surface. The method produces high-quality large graphene layers, but has been scarcely developed for the high cost of the SiC wafers, the high temperatures employed and the impossibility to move the graphene layer to a different substrate.[33, 34]

The second substrate-based growth method is chemical vapour deposition (CVD) of graphene on transition metal substrate. Typically the metal film is heated up to 900 – 1000 °C in an atmosphere of hydrogen and hydrocarbons such as methane and then cooled down, producing a good quality layer of graphene on the metal surface.[35] Initially expensive metals as ruthenium and iridium were used, later substituted with cheaper copper and nickel.[36] This technique has been largely improved, by reducing the temperature and the costs, and by

increasing the quality of graphene produced and the throughput up to the roll-to-roll synthesis of CVD graphene on copper.[37] For instance, the development of plasma-enhanced CVD techniques (PE-CVD) has allowed greatly reducing the substrate temperature and the reaction times.[38] CVD makes it possible to produce high quality, metre sized, continuous single or few layers of graphene, which can be transferred from the metal to any substrate; nevertheless, the highest quality of mechanically exfoliated graphene has not be reached yet. The major drawback of the method, in addition to the large energy consumption of the synthesis, is the transfer process of graphene from the nucleation metal, which becomes more critical with the increasing of the size of the graphene layer. In fact, during the transfer process impurities are often introduced into the graphene layer and the transfer represents the lowest throughput process, because of the many steps required.[35] Several methods of transfers have been developed, including "wet" and "dry" methods, each one with its pros and cons.[39] However, most of these methods include some sacrificial substrates, including the metal substrate, which is usually dissolved by an etchant, largely contributing to increase the overall cost of the process.[39] Lately, some promising methods that allow recycling the copper substrate have been developed.[40, 41]

The methods that allow producing large quantities of graphene belong to the category of liquid-phase exfoliation (LPE). All these methods rely on a top-down approach: bulk graphite is exposed to a solvent which is capable of overcoming the van der Waals forces that keep the layers together. To help the solvent intercalate into graphite layers and overcome the strong van der Waals forces between the layers, eventually leading to the complete detachment of one graphene layer, an external force must be applied. This external force may come from ultrasonication, high-shear mixing, and microfluidization.[42, 43] Prolonged treatments yield a significant fraction of monolayer thick flakes in the suspension, which can be further selected by centrifugation. Each one of these techniques has advantages and limitations; nevertheless, the increase of treatment time and decrease of the thickness of the obtained graphene flakes are always accompanied by a reduction in the lateral size of the flakes.[43] The exfoliation can be assisted by some molecules, such as surfactants, that intercalate between graphene layers and stabilize the exfoliated flakes in the solvent.[42, 44] Related methods are electrochemical exfoliation, in which graphene is exfoliated by applying an electrical potential to an electrochemical cell in which graphite is used as anode or cathode in presence of an electrolyte-containing medium[45], and the graphite intercalation with salts, followed by thermal expansion and sonication to separate the exfoliated flakes.[46] With liquid-phase exfoliation methods is possible to obtain graphene in good quantity, making them industrially scalable. Nevertheless, the yield of monolayers is usually low, and the so obtained graphene flakes have small lateral dimensions and exhibit some defects. Among the various LPE methods, electrochemically exfoliation enables the production of graphene with the higher yield and the higher lateral dimension of the flakes.[45]

2.1.2. Graphene Oxide and Reduced Graphene Oxide

The production of graphene oxide (GO) and its subsequent reduction to form reduced graphene oxide (rGO) can be considered as an alternative method to generate another graphene related material in large quantity and lowest cost, with a production procedure that can be considered being closely correlated to the liquid exfoliation method previously reported. Graphene oxide can be obtained from the exfoliation in water under moderate sonication of graphite oxide, which is a strongly oxidized form of graphite. Graphite oxide was firstly produced in late 1859 by Brodie.[47] Nowadays, graphite oxide is prepared mostly by using the protocol devised by Hummers and Hoffman in 1958,[48] where the oxidation of graphite to graphite oxide is achieved by treating graphite with an anhydrous mixture of concentrated sulfuric acid, sodium nitrate and potassium permanganate. Some modifications to the method have been proposed, which are usually named modified Hummers methods, but the main strategy is unchanged. Graphite oxide has a layered structure similar to graphite, but each carbon layer in graphite oxide is heavily decorated by oxygen-containing groups, which not only expand the interlayer distance but also make the atomic-thick layers hydrophilic: this enables water molecules to readily intercalate in-between graphite oxide layers. As a result, these oxidized layers of graphite oxide can be exfoliated in water when subjected to moderate sonication, leading to a stable water dispersion of monolayers called graphene oxide (**Figure 2.1-2**). The yield of GO is a result of various factors, among the others the sonication time, and can be up to 95 %.[49]

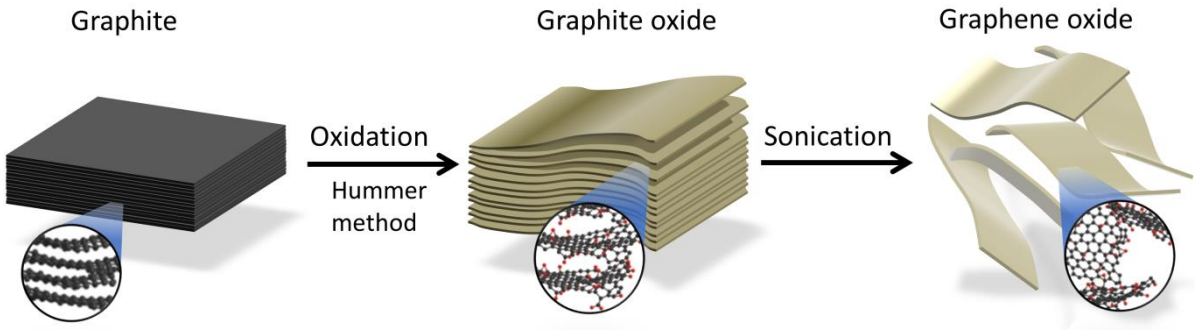

Figure 2.1-2: Schematic of the synthesis of Graphene Oxide (GO).

Although it has been developed for over 60 years, the precise chemical structure of GO is still not fully unravelled. GO is a semi-amorphous complex material, whose exact composition greatly depends on the preparation method, making its full characterization a complicated task. Many different structures have been proposed over time, including models of GO displaying a regular lattice of discrete repeated units. The most accepted GO model was proposed by Lerf and Klinowski, portrayed in **Figure 2.1-3**:[50] it is a nonstoichiometric model, in which the basal plane is decorated with hydroxyl, epoxy and some carbonyl groups, while carboxyl groups are present along the sheet edge The oxygen content and the

proportion between the various oxygen functional groups are dependent on the synthetic route, yet the first one may be as high as 50 %.[49]

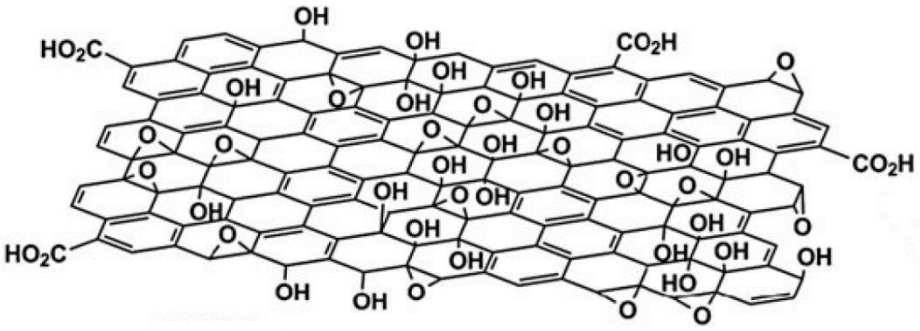

Figure 2.1-3: Lerf-Klinowski model of GO. Adapted from Ref. [49]

Recently, thanks to new investigations carried out with the aid of techniques offering a highest spatial resolution such as ultra-high resolution transmission electron microscopy (UHR-TEM) and scanning tunnelling microscopy (STM), the fine structure of GO has been revealed.[51] It consists of a random distribution of oxidized region with sp^3 carbons and oxygen-containing functional groups, combined with non-oxidized regions where most of the carbon atoms preserve their sp^2 hybridization and graphitic structure, whose size is between 1 and 6 nm^2.[49] Some holes, caused by the CO_2 evolution during the graphite oxidation, are also present on the basal plane. The conductivity of graphene mainly relies on the long-range conjugated network of the graphitic lattice. Although there are conjugated areas in GO, long-range conductivity is blocked by the absence of percolating pathways between sp^2 carbon clusters to allow classical carrier transport to occur. For this reason GO sheets are typically insulating, exhibiting a conductivity often below 1×10^{-4} S/m.[52] The conjugation and thus the conductivity can be partially restored by reducing GO to obtain reduced graphene oxide (rGO). When compared to GO, the rGO possesses a much lower oxygen content (from 20 % to less than 1 % depending on the reduction method) and a much higher electrical conductivity, up to 10^5 S/m.[53]

Several methods can be used to produce rGO, ranging from reduction of GO with a wide range of reducing agents to thermal annealing at high temperature in air, inert atmosphere or reducing atmosphere. The ability to restore the structure of the graphite, and therefore its conductivity, depends on the method used, but it is typically higher for annealing at high temperatures. In any case, even when all the oxygens are eliminated via reduction, rGO still contains many defects, such as holes, point defects, and presence of 5 and 7-membered rings.[49] For this reason, its electrical conductivity remains orders of magnitude lower than that of mechanically exfoliated or CVD graphene, making rGO less suitable for application in fast electronics. However, the low-cost of the starting material, the high yield and scalability of the method have rendered GO and rGO the graphene derivatives most widely produced

and employed. Furthermore, for many applications where a record conductivity is not required, GO and rGO are preferred also for their easier processing in comparison to the pristine graphene.

2.2. Classes of hybrid assemblies based on graphene

2.2.1. Assemblies of graphene with other nanomaterials

Nanomaterials are materials which have at least one of their physical dimensions below 100 nm. The great interest towards nanomaterials comes from the fact that usually, nanomaterials possess properties (e.g. optical, electrical, chemical…) that are highly different from their bulk counterpart. Graphene has been combined with other nanomaterials with the aim of creating a new hybrid material possessing new properties. The incorporation of graphene into bulk materials such as polymers, ceramic and other inorganic materials is usually classified under the name of composites. These are characterized by weak interactions between graphene and the bulk material and by properties which remain substantially that of the bulk material, albeit being enhanced. In other words, the properties of composites are the sum of the properties of the various components. On the contrary, when graphene is combined with other materials on the same size scale, i.e. with other nanomaterials, the interactions between the two materials are usually much stronger, at the (sub)nanometre level. The "strong coupling" between graphene and the other nanomaterial leads to a new hybrid material exhibiting novel properties which are not necessarily just the sum of the properties of the constituents. Graphene can be bonded to the other nanostructures *via* covalent or non-covalent interactions; however, the non-covalent interactions usually prevail. In the following section, some examples of hybrid assemblies of graphene and other nanomaterials, classified in view of their dimensionality (i.e. 0D, 1D, and 2D) are presented.

2.2.1.1. *Assemblies of graphene and 0D nanostructures*

Hybrid composites made by combining graphene with functional 0D nanomaterials such as nanoparticles (NPs), quantum dots (QDs), and nanocrystals are probably among the most explored because of their facile production and increased functionalities and properties that the 0D materials confer to the assembly. Nanoparticles are materials that are confined to the nanoscale in all three dimensions. They can be widely found in nature and are the first nanomaterials known and employed. In fact, they were already used in the prehistory. Quantum dots are semiconducting nanoparticles. Nanoparticles and QDs can be prepared by bottom-up or top-down approaches, although the bottom-up growth from chemical precursors is more widespread. Graphene and 0D nanomaterials assemblies are especially investigated for sensing applications by virtue of their increased porosity compared to films

of pristine graphene, which results in increased accessible surface area and enhanced sensing capabilities due to the combination of the graphene functionalities with the functionality conferred by the nanomaterials in addition to their synergistic effects. For example, metallic and metal oxides nanoparticles can enhance the sensitivity and selectivity due to specific catalytic effects. Other important applications of hybrids based on graphene and nanoparticles regard the water purification from organic and metallic pollutants, photo and electrocatalysis, hydrogen generation and photodetectors.

Synthetic routes for the production of graphene/0D nanomaterials assembly include *in-situ* growth of the nanomaterials on graphene or *ex-situ* nanomaterial synthesis and subsequent combination with graphene. The assembly can take place in solution, by mixing the graphene flakes with the nanoparticles or, more often, by growing them directly on the graphene starting from a metal salt as a precursor and a reductant. The interaction is usually driven by electrostatic and Van der Waals forces, in particular in GO the oxygen atoms favour the nucleation of the NPs. Then the assembly may be deposited onto a substrate by different techniques. Alternatively, the 0D nanostructures can be deposited or grown on graphene already laying on a substrate, for example, by employing a *layer by layer* approach.

Graphene/NPs assemblies have been often used for gas sensing. Pd and Pt NPs/graphene nanocomposites have been extensively explored to sense H_2 gas by virtue of the well-known catalytic activity of these two metals towards the adsorption of hydrogen.[54] For instance, Kaniyoor et al.[55] produced a hydrogen sensor based on GO decorated with Pt NPs: in this case, the Pt NPs were grown in situ directly onto the GO surface and then the so decorated GO was drop-casted on an alumina substrate with pre-patterned electrodes. The response of the device to hydrogen was analysed by reading its changes in resistance: this showed an increase of 16% when the device was exposed to 4% H_2. However, the response was slow. The use of CVD graphene rather than GO allowed Chung *et al.*[56] to reach a higher sensitivity. The group realized a flexible hydrogen sensor composed of CVD graphene decorated with Pd NPs which exhibited an impressive sensitivity of 30% to 1% H_2. Li et al.[57] employed rGO decorated with Pd NPs to sense NO gas for medical applications. The Pd NPs were first synthesized and physically adsorbed onto the rGO surface in solution by exploiting the electrostatic interaction between the two; then the hybrid assembly was deposited on CVD graphene-coated Ni electrodes. This device exhibited high sensitivity (up to 28 % increase in conductivity when the device was exposed to 1 ppm of NO), with an impressive limit of detection of 2 ppb. The sensitivity of this device was notably higher than the one of reference devices assembled without decorated rGO or CVD graphene-coated electrodes. Pd NPs may have a dual role in increasing the sensitivity. On the one hand, Pd NPs may act as absorption sites for NO molecules, facilitating the donation of electrons from NO to rGO. On the other hand, the interaction of the hybrid with NO can lower the Schottky barriers between rGO and Pd NPs, leading to a further increase in the conductance.

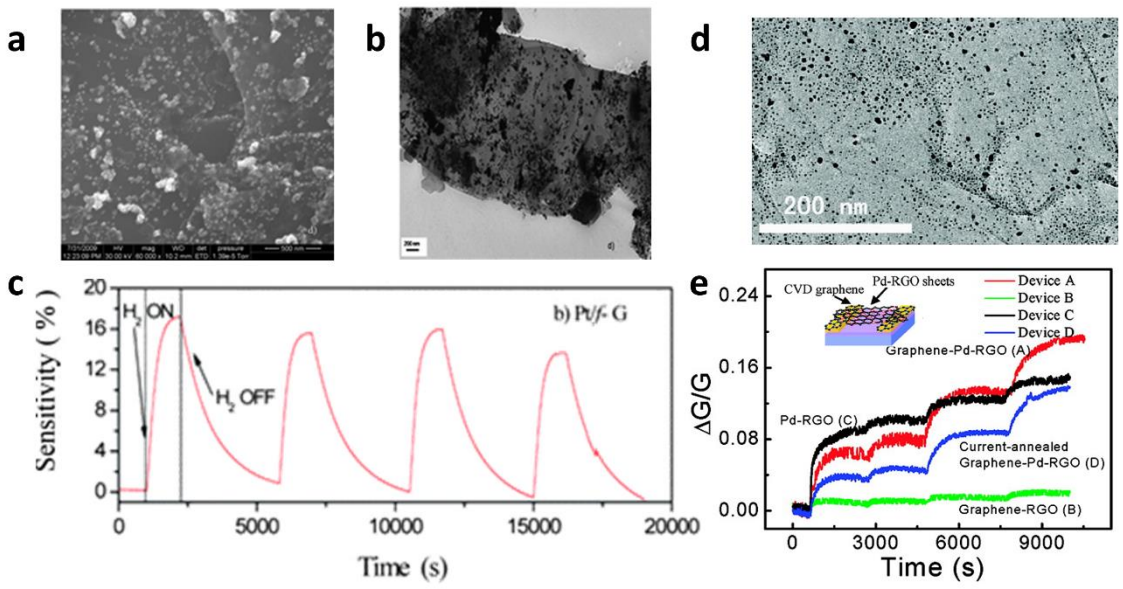

Figure 2.2-1: (a) Scanning electron microscopy (SEM) and (b) Transmission electron microscopy (TEM) images of the hybrid rGO/Pt NPs. (c) Sensitivity of the rGO/Pt NPs gas sensor exposed to hydrogen (4 % volume). Adapted from Ref. [55] (d) TEM image of rGO7Pd NPs sheet. (b) Relative changes in the conductance of the various devices versus time when exposed to 1, 10, 60, and 120 s pulses of NO gas. Inset: Scheme of the device. Adapted from Ref. [57]

Interestingly, the functionalization of rGO with p-dopant molecules can be combined with the catalytic activity of metal NPs. For example, Huang et al.[58] assembled a flexible, all-printed NO_2 sensor based on a hybrid sulfonated rGO/Ag NPs. The rGO was firstly sulfonated and then Ag NPs were grown in situ on the rGO surface *via* hydrazine reduction of $AgNO_3$. The rGO/Ag NPs based ink was printed onto a plastic substrate with pre-printed Ag electrodes. This sensor displayed a 74.6% fast response to 50 ppm of NO_2 and robustness with good stability over time and tolerance to humidity. The sensor could also detect NH_3, with a similar, yet negative response. Hybrid materials composed of graphene and metal oxide nanoparticles, nanocrystals or quantum dots[59-64] have also proved to enhance the sensing performances of graphene to NO_2, ethanol, H_2S and other gases. Semiconducting metal oxides such as ZnO, SnO_2, In_2O_3, and Cu_2O have been already employed alone in gas sensing, yet the high operating temperature and low intrinsic conductivity represented a severe limit towards their application. For example, Zhou et al.[60] developed a H_2S sensor based on a GO/Cu_2O nanocrystal hybrid. The Cu_2O nanocrystals were hydrothermally grown *in situ* on the GO surface by exploiting the electrostatic interaction between the negatively charged groups on GO surface and the positively charged Cu^{2+} ions. The suspension of the hybrid material was then drop-casted onto a Si/SiO_2 substrate exposing pre-patterned gold electrodes. The GO/Cu_2O assembly exhibited better performances compared to the isolated components, with a high 11% sensitivity to 5 ppb of H_2S at room temperature and response and recovery times in the few minutes time scale. Lee *et al.*[64] developed a hydrogen and liquid petroleum gas (LPG) sensor based on rGO decorated with SnO_2 quantum dots. The SnO_2 QDs were grown *in situ* on the rGO surface and then the

hybrid was dried and pressed into pellets that were connected to two electrodes. The sensor showed an impressive response of 89% to 500 ppm of H_2 and 92% to 500 ppm of LPG, high selectivity towards the sensed gases and long-term stability, yet the operating temperature was high (200°C). A rGO hybrid decorated with SnO_2 nanocrystals was used by Mao *et al.*[59] to sense NO_2 and NH_3 gases. In this case, the SnO_2 nanocrystals were firstly prepared, and then deposited on the rGO sheets. The sensed NO_2 and NH_3 molecules were absorbed onto the hybrid surface and induced electron transfer with rGO, thus changing its conductivity. The fabricated sensors showed high sensitivity to the target gases at room temperature (sensitivity of 300 % to 100 ppm of NO_2 and detection limit of 1 ppm) (**Figure 2.2-2** a-b). Curiously, the hybrid rGO/SnO_2 nanocrystals exhibited enhanced sensitivity to NO_2 and lower sensitivity to NH_3 compared to the bare rGO sensor. Huang *et al.*[63] developed a formaldehyde sensor based on synthetic graphene sheets decorated with zinc oxide quantum dots. The ZnO QDs are nucleated and grown on the surface of the graphene. The hybrid material exhibited 4 times enhanced sensitivity to formaldehyde compared to pure graphene at room temperature. Moreover, the hybrid sensor exhibited a fast response (ca. 30 seconds) and recovery (ca. 40 seconds), good selectivity and stability (**Figure 2.2-2** c-e).

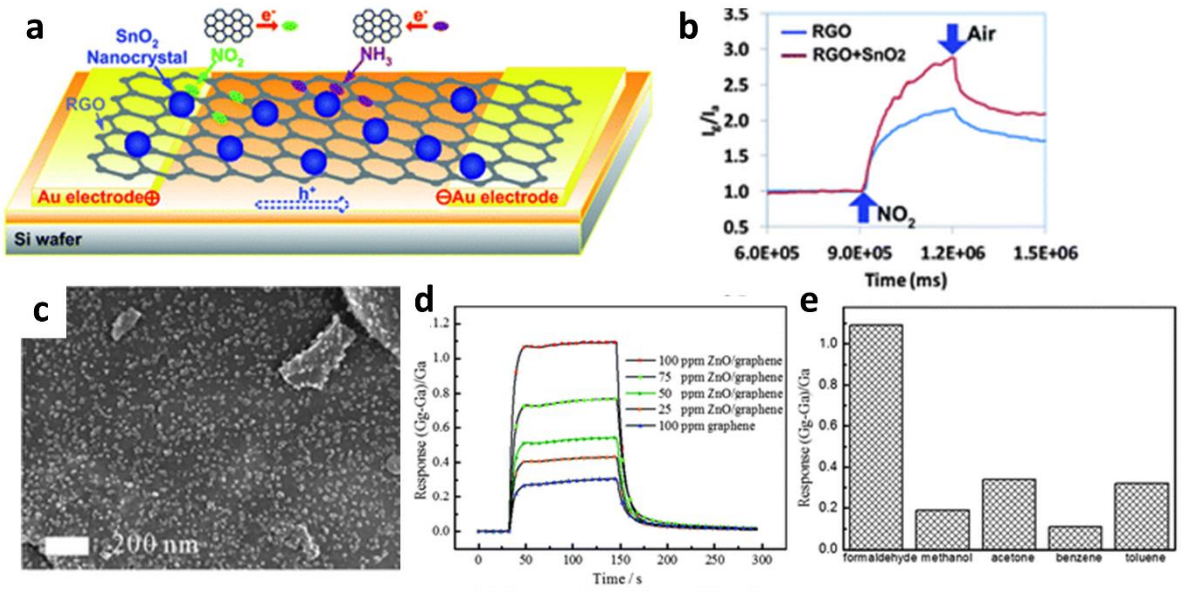

Figure 2.2-2: (a) Schematic of the sensing process of the rGO/SnO_2 NCs sensor exposed to NO_2 and NH_3. (b) Response of the rGO and rGO/SnO_2 NCs devices when exposed to 100 ppm of NO_2. Adapted from Ref. [59] (c) SEM image of the Graphene/ZnO QDs hybrid. (d) Response of the Graphene/ZnO QDs device to different concentrations of formaldehyde, compared to the response of bare graphene. (e) Cross sensitivity of the device to other vapours.

An effective way to purify water is by absorption of its contaminants on the surface of a material named absorber, which then can be easily removed. Graphene-based materials are being considered as the most promising adsorbents for capturing various heavy metal ions by virtue of their extremely large surface area.[65] In particular, among the graphene forms, GO is especially promising due to the presence of numerous oxygen-rich functional groups

on its surface that can both interact via dipole-dipole or strong electrostatic interactions with metal ions and act as reactive sites for further covalent functionalization. On the other hand, also nanoparticles are excellent pollutant adsorbents due to their large surface to volume ratio, high catalytic activity and multiple active sites. However, bare nanoparticles may easily agglomerate due to a high surface free energy which results in a reduction of the active adsorption sites. Graphene emerges as perfect supporting material for nanoparticles because prevents their aggregation and offers itself excellent absorbing properties that combine with the absorbing properties of nanoparticles; furthermore, if magnetic NPs are used these bring the great advantage of easy separation of the absorbent from water by means of a magnetic field.[66] One of the earliest works on the use of nanoparticles functionalized graphene as water polluting adsorbent was reported by Chandra *et al.*[67] In this study a water-dispersible hybrid rGO/magnetite (Fe_3O_4) NPs was used for the removal of arsenic pollutant from water. The assembly was synthesized *in situ* by the simultaneous reduction of GO, $FeCl_2$ and $FeCl_3$ that led to the formation of 10 nm magnetite nanoparticles on the rGO sheets. The composite material showed a high binding capacity for As(III) and As(V) (99.9% arsenic removal). Furthermore, due to its superparamagnetic behaviour at room temperature, the material could be easily magnetically separated from water. This work was followed by several other papers on the removal of arsenic from water using hybrids graphene/Fe based nanoparticle which exhibits magnetic properties.[66] Zhu *et al.*[68] employed graphene decorated with core@double-shell magnetic nanoparticles ($Fe@Fe_2O_3$@Si-S-O), for the removal of Cr(VI) from water. The hybrid material was synthesized *in situ* starting from graphene sheets and $Fe(CO)_5$ dispersed in DMF. The core-shell structure of the NPs was formed by thermally annealing the hybrid material at 500 °C for 2 h in H_2/Ar atmosphere. The material exhibited almost complete removal of Cr(VI) from water within 5 min and could be separated from the solution using an external magnetic field. Hybrid materials based on graphene and nanoparticles assemblies have been successfully applied for the adsorption of organic pollutants, such as dyes, hydrocarbons, gasoline, and polycyclic aromatic. In particular, rGO, thanks to its low cost, the processability from solution, and hydrophobic structure, has been employed to fabricate superhydrophobic and super-oleophilic hybrid materials addressed to the removal of organic pollutants and oils from water. Cong *et al.*[69] produced a macroscopic 3D rGO/ Fe_3O_4 NPs hydrogel for the efficient removal of spilt gasoline from water. The hydrogel was formed under synergistic effects of the self-assembly of GO sheets in water and *in situ* simultaneous deposition of magnetic Fe_3O_4 NPs on graphene sheets and reduction of GO induced by ferrous ions (**Figure 2.2-3** a-d). In another work Yang *et al.*[70] synthesized hybrids GO/iron oxide NPs and rGO/iron oxide NPs via *in situ* NPs growth and used them to remove organic and inorganic pollutants from water. In particular, the hybrid based on GO could be used to successfully remove Pb(II) from water, but not 1-naphthol and 1-naphthylamine thanks to its oxygen-containing group; on the contrary, the rGO hybrid was a good absorber for the two organic molecules (**Figure 2.2-3** e).

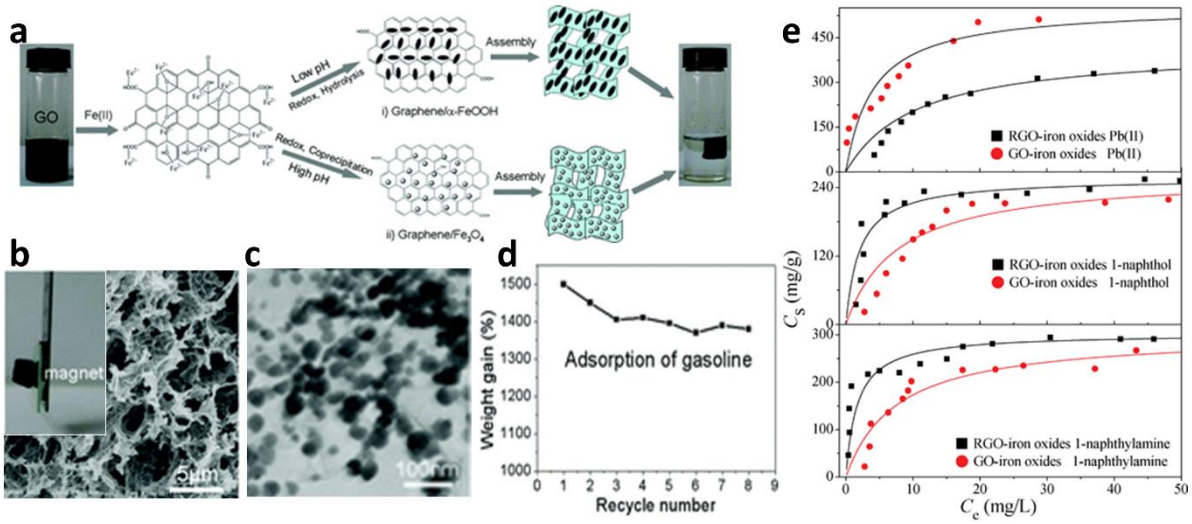

Figure 2.2-3: (a) Schematic of the formation mechanism of the graphene/iron oxide NPs magnetic hydrogels. (b) SEM and (c) TEM of the rGO/ Fe_3O_4 NPs hydrogel (inset: photo of the magnetic hydrogel). (d) Adsorption in weight of gasoline by the rGO/ Fe_3O_4 NPs hydrogel as a function of the number of cycles. Adapted from Ref. [69] (e) Adsorption isotherms of Pb(II), 1-naphthol and 1-naphthylamine on (r)GO/iron oxides NPs. Adapted from Ref. [70]

Graphene/nanoparticle and in particular graphene/quantum dots hybrids have been used also for fluorescence-based sensors for various analytes in solutions, from metals to (bio)organic molecules.[71] The use of fluorescence as the readout in the detection of chemical species and biomolecules holds potentials for cheap, effective, and highly sensitive device applications. A fluorescence sensor requires the use of a fluorophore capable of emitting light and a receptor that binds to the analyte. In particular, quantum dots may be used as fluorophores and graphene and GO can be used to quench the fluorescence. One of the approaches is based on Förster resonance energy transfer (FRET) and it is useful for the quantitative determination of target molecules. Graphene or GO usually work as an acceptor, quenching the fluorescence of a donor, such as the QD. When the analyte is added, this interacts with the receptor and restores the fluorescence of the QDs. For example, a fluorescent quantum dot (QD)–aptamer–GO sensor was designed by Qian *et al.* to detect Pb^{2+} ions.[72] The graphene QDs are covalently attached to the aptamer and absorbed onto the GO surface, which quenches their fluorescence. In the presence of Pb^{2+} ions, the aptamers get bound to them, releasing the QDs from the GO, and restoring their fluorescence. The authors demonstrated high selectivity towards Pb(II). A similar mechanism based on GO/QDs hybrids has been used by Dong *et al.*[73] to sense specific fragments of DNA. The CdTe QDs were firstly covalently functionalized with a molecular beacon (MB) specifically designed to recognise the DNA segment. These functionalized QDs were absorbed onto the GO surface in solution, which quenched their fluorescence. In presence of the DNA segments, the MB conformation is changed, which distances the QDs from the GO surface, inhibiting the FRET and restoring the QDs fluorescence. Kaur *et al.* prepared a hybrid rGO/CdS NPs for the fluorescence determination of Ag^{+} and the dye Sunset Yellow (SY).[74] In this case, the hybrid material is strongly fluorescent in solution because the light emitted by the CdS

nanoparticles is not quenched from rGO. In presence of Ag^+ and SY the fluorescence is quenched respectively because of the binding of Ag^+ with the sulphur atoms of CdS NPs and because of FRET to SY. This sensor exhibited also good selectivity towards the two analytes.

Hybrids of GO, rGO with NPs and QDs have also been used for electrochemical sensing. For example, Gong *et al.* reported an ultrasensitive Hg(II) electrochemical sensor using rGO decorated with monodispersed Au nanoparticles.[75] The sensor exhibited a detection limit as low as 6 ppt and excellent selectivity for Hg^{2+} among many metal ions. In another work of Li *et al.*[76] rGO decorated with Au NPs was used for the electrochemical selective determination of dopamine. The rGO/Au NPs hybrid was deposited onto a glassy carbon electrode and allowed a good selective determination of dopamine with a lower detection limit of 1.86 μM.

Materials based on the assembly of graphene with nanoparticles and quantum dots have also been employed for photodetection, (photo)catalysis, solar cells, water splitting and hydrogen generation.[2] In particular, in these applications the graphene has two main roles: on the one hand, it enhances the catalytic activity of NPs by uniformly distributing them onto its surface, on the other hand, its conductivity and electron-accepting ability allow for efficient charge separation and collection. For example, Zeng *et al.* fabricated a hierarchical hybrid architecture in which a magnetic ferrite microparticle was covered with polydopamine and rGO decorated with AuNPs and used it for the efficient catalysis of the reduction of *o*-nitroaniline to benzenediamine by $NaBH_4$.[77] The material was synthesized by firstly coating the ferrite particles with GO in solution and then depositing *in situ* the AuNPs on the rGO surface. Dopamine was used both as a binding agent between the ferrite particles ad GO and between rGO and the AuNPs and as a reducing agent for the *in situ* reduction of GO to rGO and for the synthesis of AuNPs. In another work, Yang *et al.* synthesized core-shell Ag@Co and Ag@Ni NPs supported on rGO and used them for the hydrogen generation from the hydrolysis of ammonia borane.[78] The material was synthesized via an *in situ* one-step procedure, using methylamine borane for the simultaneous reduction of GO and the core-shell metallic NPs and showed improved catalytic performances compared to the same NPs supported on different materials. Lv *et al.* fabricated a noble metal-free hybrid of graphene decorated with CdS and TiO_2 NPs for the photocatalytic hydrogen evolution from methanol.[79] The material was prepared via one-pot solution method and exhibited enhanced photocatalytic activity compared to the bare nanoparticles (with a hydrogen production rate 4 times higher) and to Pt co-catalyst. The graphene not only allowed a better distribution of the NPs, but acted as an electron acceptor, contributing to the suppression of charge-recombination. A similar photo-catalyst for hydrogen production based on a hybrid rGO decorated with CdS NPs was produced by Li *et al.*[80] and exhibited an H_2-production rate of 1.12 mmol h^{-1}, which was 5 times higher than that of pure CdS NPs. Xiao *et al.*[81] prepared a multi-layer structure of modified rGO flakes and CdS QDs for photoelectrochemical and photocatalytic applications. The multi-layer structure was absorbed on an FTO electrode exploiting the Layer-by-Layer (LbL) technique: the electrode was alternatively soaked in a

solution of the negatively charged CdS QDs and in the suspension of the positively charged modified rGO flakes. This multi-layer hybrid stacking demonstrated promising photoelectrochemical performances and good photocatalytic activity under visible light irradiation towards the reduction of aromatic nitro compounds. The enhanced performances compared to CdS QDs alone were attributed to the electron-accepting behaviour of rGO, which allowed an efficient separation of the photo-generated holes and electrons.

S

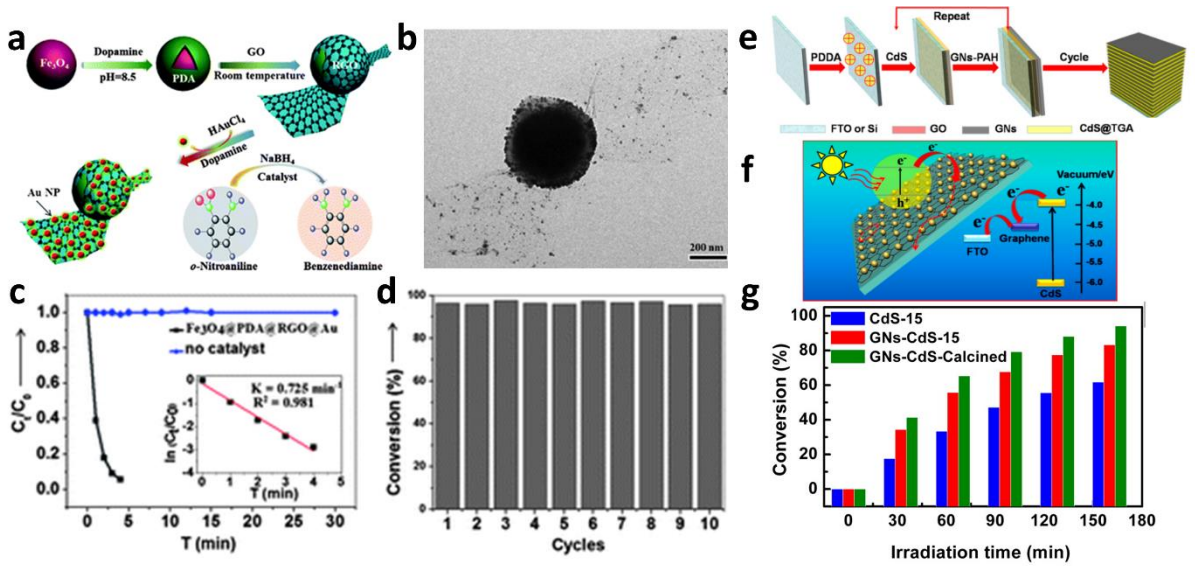

Figure 2.2-4: (a) Schematic of the preparation of the Fe_3O_4@PDA@rGO@Au nanocatalyst and (b) TEM image of the same. (c) Concentration of o-nitroaniline versus reaction time with Fe_3O_4@PDA@RGO@Au catalyst and without. (d) Conversion efficiency in ten cycles with the catalyst. Adapted from Ref. [77] (e) Schematic of the LbL assembly rGO/CdS QDs and (f) Schematic of the photocatalytic process. (g) Conversion efficiency vs. light irradiation time (λ > 420 nm) of LbL CdS, rGO/CDs and calcinated rGO/CDs. Adapted from Ref. [81]

2.2.1.2. *Assemblies of graphene and 1D nanostructures*

One dimensional (1D) nanomaterials are those materials characterized by at least two dimensions in the nanoscale (below 100 nm) and by a large aspect ratio. Most representative components of this class of nanostructures include nanotubes (NTs), nanowires (NWs), and nanorods. These materials can exhibit conductive, semiconductive, or insulating properties. Carbon nanotubes are one of the allotropes of carbon; discovered before graphene in 1993, they are hollow cylinders made of carbon atoms with sp^2 hybridization forming a honeycomb lattice. The walls of the cylinders may be composed by either one single atomic thick layer of C atoms or by two or more layers. Conversely, nanowires are thin wires with diameter usually below 100 nm and can be made of several materials. Hybrid materials based on graphene assembled with 1D nanomaterials have been extensively studied in the last 10 years as testified by the continuous increase of the number of works related to these materials which can be found in the literature. In particular, hybrid materials based on graphene and conductive 1D materials such as metallic nanowires and carbon nanotubes

(CNTs) have been extensively investigated as transparent conductive electrodes for optoelectronics[7, 82-87] and supercapacitors.[88-91] Assemblies of graphene with semiconductive nanowires have found many applications as materials for batteries[20, 92, 93] and sensing devices.[82, 94-97]

Assemblies of graphene and carbon nanotubes or metal nanowires have been the subject of intense research endeavour to generate transparent and opaque conductive electrodes. The network of metal NWs or CNTs is electrically conductive and its discontinuous morphology enables light transmission through the voids between NWs/CNTs. On the other hand, graphene is also conductive and possesses high transmittance in the visible light, thus contributing to the conductivity of the electrode, while maintaining good transparency. However, in most of the cases, graphene holds an additional function: its inertness and low reactivity, together with its layered structure make it almost impermeable to most molecules.[98] By exploiting such characteristics it was used to protect the CNTs and metal NWs from the oxidation. Kumar *et al.* produced a CNTs/CVD graphene transparent electrode for organic light-emitting diodes (OLEDs), by depositing first the CNTs network on a Cu foil and then the CVD graphene directly on top.[99] The resulting highly interconnected film was then transferred to arbitrary substrates by using a PMMA sacrificial layer. When assembled into the OLED device this electrode exhibited performances comparable to indium tin oxide (ITO) electrodes (**Figure 2.2-5** a-c). In another work of He et al.,[100] transparent electrodes based on rGO and CNTs were produced and showed good performances with a sheet resistance of ~80 Ω/sq and 86% transparency. In this case, GO was used to stabilise the dispersion of CNTs in water. Then, the homogenous dispersion was deposited on PET substrates and the GO was reduced to the conductive rGO by microwave irradiation. Metal nanowires, especially copper and silver nanowires (Cu NWs and Ag NWs), have emerged in recent years as components for low cost and environmentally friendly transparent electrodes. However, these nanowires and especially Cu NWs are quite prone to oxidation; for this reason, several works on hybrid electrodes based on Ag/Cu NWs and an oxidation protective layer of rGO or CVD graphene have been published. For example, Ricciardulli *et al.* assembled a transparent conductive electrode based on Ag NWs and electrochemically exfoliated graphene (EEG) that exhibited a sheet resistance of 13.7 Ω/sq and high optical transmittance.[101] The electrodes were produced by spray-coating sequentially Ag NWs and EEG on flexible transparent substrates. EEG had the triple role of increasing the long-term stability of the electrode, decreasing the surface roughness and the electrical resistivity. Liang *et al.* reported the preparation of a hybrid Ag NWs/rGO transparent electrode.[102] The Ag NWs were firstly deposited onto PET followed by the soaking of the substrate in a GO solution. The GO flakes helped to solder the nanowires together, lowering the sheet resistance down to 14 Ω/sq (at 88% Transmittance), and increasing the oxidation resistance of the electrode. In 2013 Ruoff *et al.* [7] produced a transparent electrode based on Cu NWs and rGO on a glass substrate. The electrode was produced by depositing the Cu NWs, then a rGO layer was transferred on top of the Cu

NWs through a complicated dry transfer process involving a sacrificial PDMS layer. In order to obtain conductivity reduction of GO with hydrazine and three thermal annealing steps in H_2/Ar up to 400 °C were used (**Figure 2.2-5** d-f). Dou *et al.* reported a solution-based approach to coat the Cu NWs with a self-assembled layer of GO nanosheets.[103] Then the wrapped Cu NWs@GO were deposited onto a substrate, followed by a mild thermal annealing to reduce GO, yielding a conducting network. The conducting film exhibited a sheet resistance of 14.8 Ω/sq at transmittance of 86.5%.

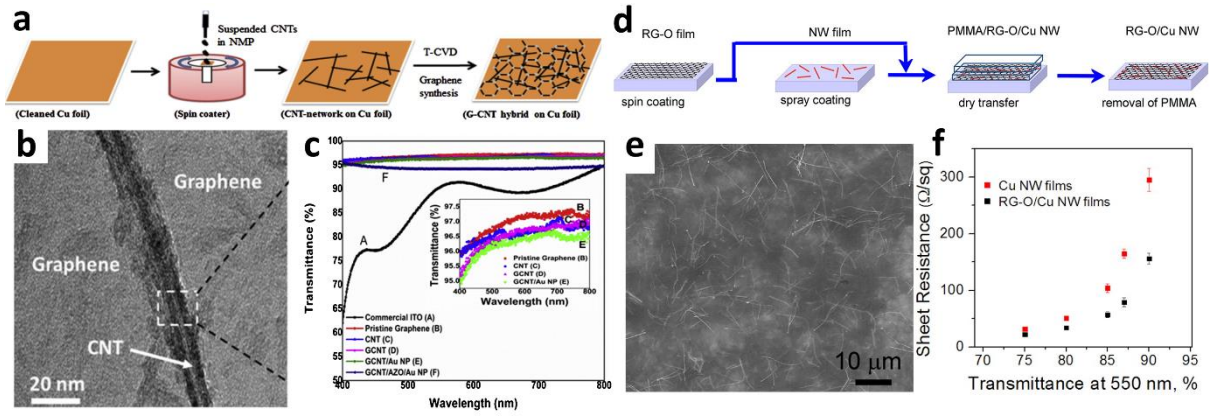

Figure 2.2-5: (a) Schematic of the preparation of the hybrid CNTs/CVD graphene transparent film and (b) TEM image of the hybrid. (c) Transmittance spectra of the hybrid vs CVD graphene and CNTs alone and commercial ITO. Adapted from Ref. [99] (d) Schematic of the preparation of Cu NWs/rGO hybrid and (e) SEM image of the hybrid. (f) Sheet resistance as a function of Transmittance of Cu NWs film and Cu NWs/rGO film. Adapted from Ref. [7]

Supercapacitors are among the first and foremost important applications of graphene.[104] The electrodes constituting a supercapacitor should store charges at the liquid-electrode interface, thus conductive materials exhibiting a large surface area are required for such application. Hybrids of graphene with 1D materials, and in particular CNTs, may benefit from the increased surface area and conductivity. One of the first reports of a supercapacitor based on a hybrid of graphene and CNTs was published in 2009 by Yu and Dai.[89] They produced a multi-layer self-assembled GO/CNTs hybrid by LbL deposition of positive rGO-poly(ethyleneimine) (PEI) and negatively charged acid-oxidized multiwalled carbon nanotubes. The hybrid showed a specific capacitance of 120 F/g. Later Jung et al. fabricated another supercapacitor based on a composite of stacked graphene and CNTs in which the graphene and CNTs were covalently tethered.[88] The two components were bonded together by amide bond obtained by reacting a NHS (*N*-hydroxysuccinimide) functionalized GO with amine-functionalized CNTs. Subsequently, the aqueous solution of GO-CNTs hybrid was reduced to rGO-CNT by a microwave hydrothermal (MWHT) method in presence of hydrazine and ammonia and then filtered to obtain the stacked structure, which exhibited a very high volumetric capacitance of 165 F/cm^3. Li et al fabricated *via* an extended filtration assisted method a flexible asymmetric supercapacitor based on a 3D architecture in which the negative electrode was composed of stacked graphene sheets spaced by CNTs.[91] CNTs

had a dual role, acting as a hard spacer to prevent restacking of graphene sheets but also as a conductive and robust network to facilitate the electrons collection and transport in order to fulfil the demand of high-rate performance of the asymmetric supercapacitor. Graphene hybrids with 1D materials have also been employed as electrodes for lithium batteries. For instance, Wang *et al.* fabricated a hierarchical architecture employed as anode of a Li-ion battery in which Si NWs encapsulated with CVD graphene were sandwiched between rGO sheets.[93] The Si NWs were firstly synthesized *via* a CVD vapour–liquid-solid (VLS) method and then CVD graphene was growth on their surface (Si NWs@G), finally the Si NWs@G and GO were filtered together and thermally reduced to obtain the stacked Si NWs@G @rGO structure (**Figure 2.2-6**). In the structure, the CVD graphene coating prevented the direct exposure of encapsulated silicon to the electrolyte and enabled the structural and interfacial stabilization of silicon nanowires, while the conductive rGO sheets accommodated the volume change of embedded Si NW@G and maintained the structural and electrical integrity of the assembly. Li *et al.* fabricated a free-standing electrode for Lithium sulphur batteries based on a 3D assembly of rGO and titanium nitride nanowires (TiN NWs).[92] The electrode was assembled by firstly dispersing $H_2Ti_3O_7$ nanowires and GO in water, to which sodium ascorbate was added to reduce GO and form a hydrogel. Then the 3D gel was annealed at 800 °C in NH_3 atmosphere to obtain the composite rGO/TiN NWs. In 2018 Xue *et al.* reported the assembly of a 3D hierarchical structure based on rGO and Ag NWs employed as anode for Li-metal batteries.[20] The porous 3D structure was formed by freeze-drying an ice-templated hydrogel of GO and Ag NWs and then reducing with hydrazine vapours the resulting aerogel.

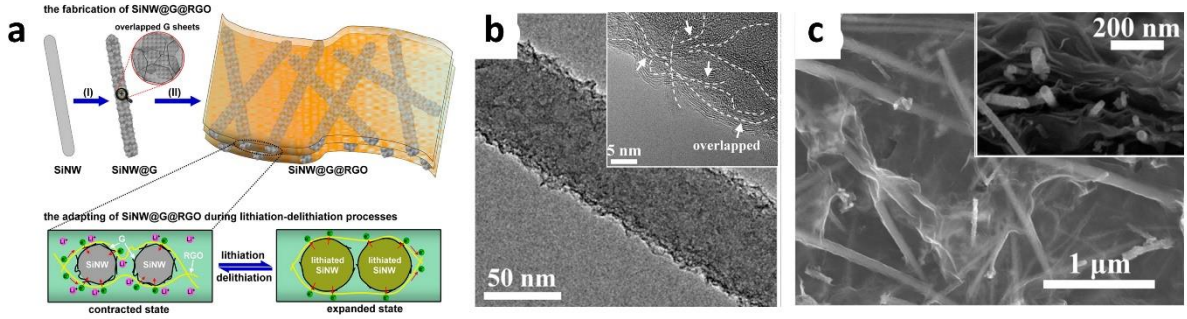

Figure 2.2-6 : (a) Schematic of the fabrication (upper panel) and adapting (lower panel) of Si NWs@CVD graphene/rGO hybrid. (b) TEM images of the Si NWs@CVD graphene and (c) SEM images of the hybrid Si NWs@CVD graphene/rGO. Adapted from Ref. [93]

Assemblies of graphene and 1D materials have been also largely employed in sensing devices, by taking advantage of the increased surface area, which is essential for sensing, and the additional functionality that the 1D material may confer to the hybrid. In 2010 Jeong *et al.* produced a flexible NO_2 sensor using a CNTs/rGO hybrid film.[105] A rGO film was deposited onto a plastic substrate with pre-patterned electrodes, on which vertically aligned CNTs were deposited on top by CVD. The so-fabricated sensor exhibited a sensitivity of 20% after exposure to 10 ppm of NO_2 at room temperature. Yi *et al.*[106] assembled an ethanol sensor by

hydrothermally growing semiconductive vertically aligned ZnO nanorods on a metal bottom electrode and depositing CVD few-layer graphene on top as the top contact. The sensor displayed a geometry similar to those of metal-insulator-metal devices and showed a 900% sensitivity to 10 ppm of ethanol. However, a high operating temperature of 300 °C was required. A hybrid based on vertically aligned ZnO nanorods, hydrothermally grown on a rGO film was employed by Cuong *et al.* to sense H_2S.[107] The sensor exhibited a good sensitivity in oxygen, yet long response and recovery times. Hybrid assemblies have also been used to sense (bio)molecules in liquid media. Woo *et al.* prepared a hybrid rGO/CNTs electrochemical sensor for the determination of H_2O_2.[94] The material was prepared by the simultaneous reduction of GO dispersed in water with hydrazine in presence of dispersed CNTs. Then, the hybrid was deposited on a glassy carbon electrode. The hybrid displayed a large electrochemical surface area and fast electron transfer properties which allowed the determination of H_2O_2 concentration with a detection limit of 9.4×10^{-6} M. He *et al.* fabricated a dopamine electrochemical sensor based on a hybrid rGO/MnO_2 NWs electrode.[95] The material was prepared by mixing GO and MnO_2 NWs in solution and then drop-casting the self-assembled composite onto a glassy carbon electrode. The hybrid was then electrochemically reduced to rGO/MnO_2 NWs and used to sense dopamine, with a detection limit of 1 nM and good selectivity even in the presence of high concentrations of ascorbic acid and uric acid.

2.2.1.3. *Assemblies of graphene and other 2D materials*

Despite the outstanding electronic properties of graphene, the difficulty in producing high-quality graphene in large quantities at low cost and the lack of a bandgap in its electronic structure have prevented the efficient use of graphene for several electronic and optoelectronic applications. To overcome this limitation, in recent years the research activity has been broadened to other 2D layered materials, and in particular to transition metal dichalcogenides (TMDs), hexagonal boron nitride (h-BN) and phosphorene. Hexagonal boron nitride (h-BN) is a remarkable layered insulator with a structure similar to that of graphene. TMDs are compounds of the type MX_2, with M a transition metal atom (Mo, W, etc.) and X a chalcogen atom (S, Se, or Te), which can be made atomically thick. Phosphorene is a single or few-layer thick version of the thermodynamically stable black phosphorus. Both TMDs and phosphorene are semiconductors with bandgaps between 1 and 2 eV.[108] Interestingly, hybrid structures can be made by combining graphene with one or more of these 2D materials, by stacking them together in a vertical alignment or by stitching them in a lateral alignment (**Figure 2.2-7**); these hybrids structures are often referred as 2D heterostructures or van der Waals heterostructures since the different components are held together by van der Waals forces which are the same forces that keep together the different layers in the bulk material.[108-110] These heterostructures allow not only overcoming the inherent limitations of every single component, but also the combination of multiple 2D materials may bring novel peculiar properties foreign to the single components.

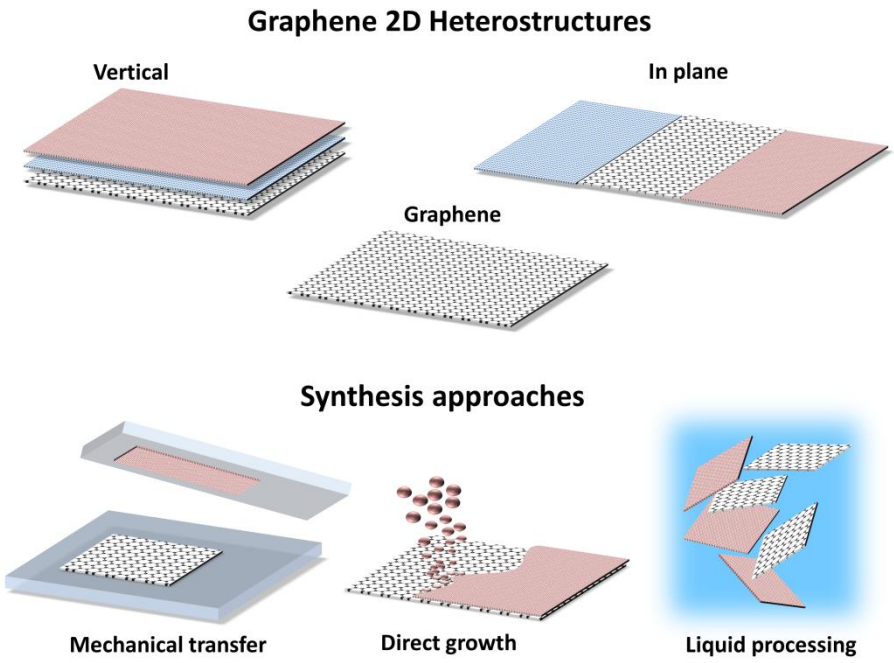

Figure 2.2-7: Schematic overview of the different kinds of graphene 2D heterostructures introduced in this paragraph, and methods usually employed to fabricate them.

The first example of a graphene-based heterostructure was reported in 2010 by Dean and co-workers.[111] The group fabricated a transistor on a vertical heterostructure in which an exfoliated single and bi-layer graphene was placed on top of thin hBN crystal by using a mechanical transfer process. The two layers were closely attached together by van der Waals forces. The use of a 2D layer of h-BN for supporting the graphene flake brought new interesting characteristics: for example, the graphene had carrier mobility almost an order of magnitude higher than devices on SiO_2 and presented reduced roughness, different reactivity and intrinsic doping. Since the publication of this work, several hundred of papers and dozens of reviews have been published about lateral and vertical heterostructures based on h-BN and graphene which can be produced by mechanical transfer methods, assembling in liquid phase of the liquid exfoliated graphene and h-BN and direct growth by vapour deposition methods.[108, 110, 112-115] One interesting characteristic of h-BN is its atomically smooth surface that is almost completely free of dangling bonds and charge traps, which is the reason of the superior carrier mobility that Dean *et al.* had observed for graphene flakes stacked onto h-BN. In plane h-BN/graphene heterostructures may present semiconductive behaviour and tunable band-gap, antiferromagnetism and low thermal conductance.[113] On the contrary, vertical stacks of graphene and h-BN exhibited unique physical properties. For example, since graphene and h-BN share an almost-but not perfectly identical crystal lattice, when they are superimposed they generate a periodic moiré pattern which is at the origin of some quantic effect experientially observed in these sample for the first time, such as the Hofstadter's butterfly effect[116] and the superlattice Dirac cone (**Figure 2.2-8** b-c).[117] Furthermore, when the angle between the lattice of h-BN and graphene is small a bandgap

appears in the last. The graphene can also be fully encapsulated between two h-BN layers, which protect it from the environment. H-BN has been reported also as ultrathin dielectric gate, for field-effect transistor based on vertical h-BN/graphene heterostructures.[118]

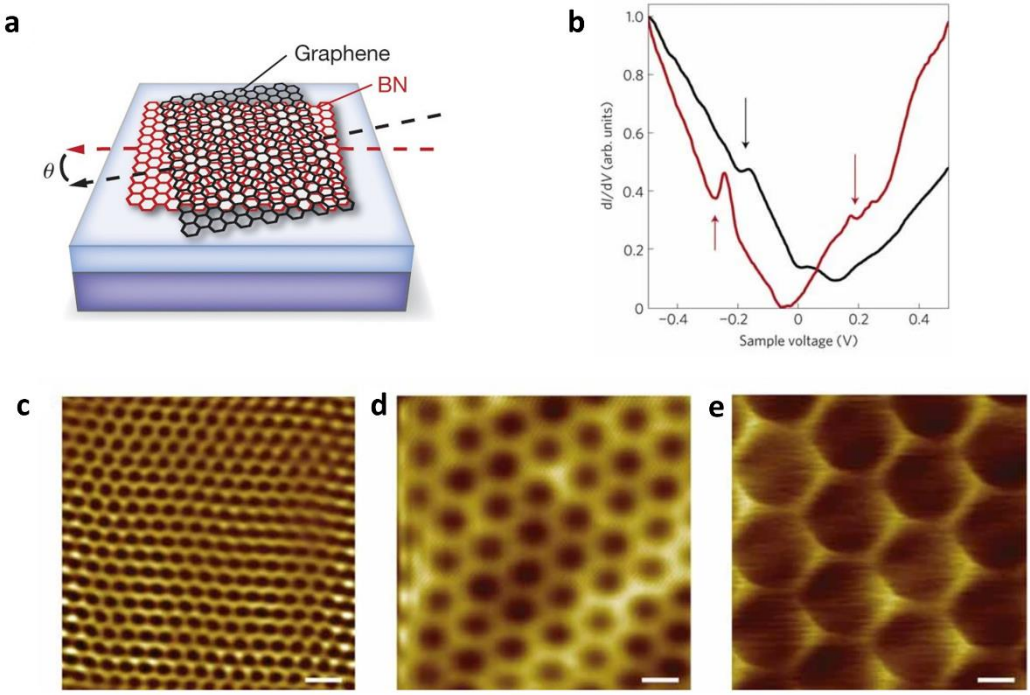

Figure 2.2-8 : (a) Sketch of graphene on h-BN showing the emergence of a moiré pattern. The moiré wavelength varies with the mismatch angle, θ. Adapted from Ref. [116] (b) Experimental dI/dV curves of the vertical heterostructure h-BN/Graphene for two different moiré wavelengths, 9.0 nm (black) and 13.4 nm (red). The dips in the dI/dV curves are marked by arrows. (c-e) STM topography images showing 2.4 nm (c), 6.0 nm (d) and 11.5 nm (e) moiré patterns. The scale bar is 5 nm. Adapted from Ref. [117]

Vertical heterostructures can be fabricated by using different techniques that include mechanical transfer methods, chemical growth, and liquid phase assembly. As aforementioned, mechanical "wet" transfer was firstly demonstrated by Dean *et al.* for the production of graphene transistor devices supported by h-BN.[111] The first step was the mechanical exfoliation of a thin flake of h-BN on a substrate, along with the exfoliation of graphene on a PMMA thin membrane supported on a Si/SiO2 substrate. The second step was the transfer of the PMMA membrane with the exfoliated graphene flake, on top of a transparent glass slide. Finally, under an optical microscope, the glass slide was placed hanging on the top of the h-BN, with the graphene flake facing down. With the aid of a micromanipulator, the glass slide was moved to perfectly align the graphene flake over the h-BN, then both were brought into contact and the two flakes were attached closely by van der Waals forces (**Figure 2.2-9**a). This method has been extensively used also to produce vertical heterostructures of mechanically exfoliated graphene with TMDs and phosphorene.[109] Furthermore, by repeating this procedure it is possible to stack multiple layers of different materials, with increasing complexity and functionality (**Figure 2.2-9**b).[108,

[119] However, since the many steps involved in the transfer method, contaminants are often present at the interface between the two 2D materials. These contaminants may be removed after annealing, though not all the materials can tolerate annealing without degrading.[108] For this reason, dry transfer techniques have been developed in which the contact of the interfaces with solvents or polymers is avoided (**Figure 2.2-9**d).[120, 121] Liquid phase exfoliations of graphene and other 2D materials can be used to obtain vertical randomly stacked heterostructures. [122-124] Typically the bulk materials are exfoliated in liquid phase and, after centrifugation steps, stable suspension of single and few layers 2D materials are obtained, then the suspensions are mixed together in different ratios. The electrostatic and van der Waals interaction between the graphene flakes and the other 2D materials flakes drive their self-assembly forming stacked heterostructures, which are finally separated from the liquid.

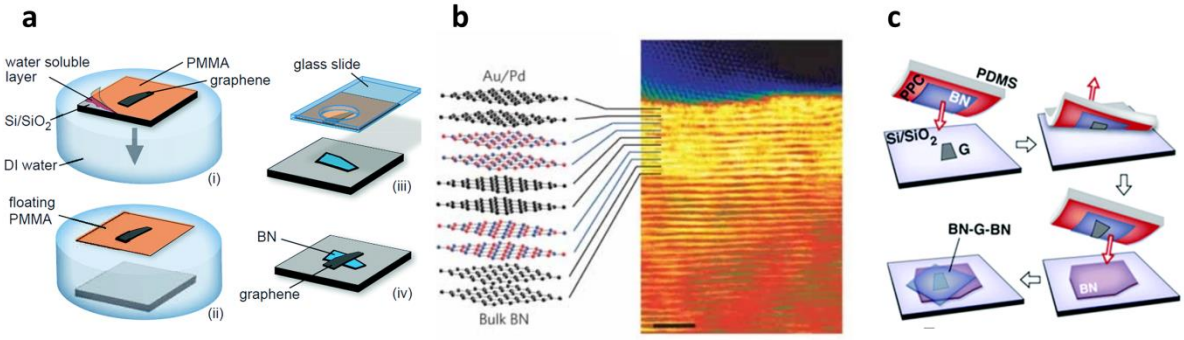

Figure 2.2-9 : (a) Schematic illustration of the "wet" transfer process used to fabricate graphene-on-BN devices. Adapted from Ref. [111] (b) Sectional STEM image and schematic of a heterostructure fabricated by the sequential stacking of graphene and h-BN layers. Adapted from Ref. [70] (c) Schematics for the polymer-free stacking technique of h-BN/G/h-BN aided by van der Waals interactions. Adapted from Ref. [120]

Chemical synthesis is another method used to produce vertical 2D heterostructures. Mechanical transfer methods produce high-quality heterostructures, suitable for fundamental research purposes. However, the small size of the obtained heterostructures, the laborious procedures and low output volume hinder their applications outside the research area. On the other hand, liquid-phase methods are easily scalable and produce high-volume of materials. However, heterostructures fabricated by these methods are usually randomly stacked and thus not suitable for certain purposes. Chemical vapour deposition is a technique to grow high-quality pristine 2D materials in large areas and can be employed to fabricate large-area vertical heterostructures. Individual layers of 2D materials can be grown separately and then stacked together with various transfer methods to produce large heterostructures that found application in optoelectronics.[109] Also in this case, the transfer methods, although simpler than the transfer of mechanically exfoliated flakes that necessitate sub-micrometric precision and electron-beam lithography technique, involve the use of solvents and polymers which brings contamination of the surfaces. Furthermore, the transfer of large-area CVD films often results in cracks and wrinkles.[109] It is possible to overcome this

problem by directly growing one kind of 2D material onto another 2D material used as substrate. The first example of direct growth was reported by Liu *et al.* and consisted in the CVD growth of h-BN on CVD graphene.[125] As aforementioned, graphene and h-BN are very similar, they are isoelectronic and have a very similar crystal lattice; furthermore, both can be easily grown by CVD on copper. First, graphene was grown on Cu foil at 950 °C using hexane as a precursor. Then h-BN was grown on the graphene through the decomposition of ammonia borane at 1000 °C. However, Raman spectroscopy revealed the damage of the graphene during the second CVD. The growth of graphene on h-BN has been more widely studied than the opposite, as h-BN represents an excellent dielectric substrate for graphene, making these structures more useful for electronic applications, and h-BN resists better to the second CVD growth compared to graphene. Various methods have been developed; in an early example, CVD graphene has been grown by CVD using benzene as a precursor at 800 °C onto an epitaxial h-BN thin film on Ni.[126] Yan et al. developed a smart method to deposit bilayer graphene film directly onto insulating substrates including h-BN.[127] The h-BN was coated with a thin polymeric film, followed by the evaporation of 500 nm of Nickel on top of the polymer. Then the substrate was annealed in reducing atmosphere of H_2/Ar at 1000 °C for a few minutes. The polymeric film was converted into graphene, which can be exposed after the etching of Ni. One of the main challenges regarding the growth of graphene onto h-BN it is the modest catalytic activity of the latter, which renders necessary the presence of some exposed metal.[113] However, recently the number of methods to grow graphene layers onto h-BN, with and without metal catalysts, has increased; these methods rely on techniques such plasma enhanced CVD (PE-CVD) and low pressure CVD (LPCVD) and make use of different carbon feedstocks, included liquids.[108, 109, 115] It is worth noting the work of Song *et al.* who recently developed a procedure for the growth of patterned graphene on 2D h-BN.[128] The group firstly deposited PMMA seeds in copper, then by using LPCVD and ammonia borane as precursor they grew the h-BN layer and finally, using benzoic acid as a precursor, they grew graphene whose domains nucleated exactly over the underlying PMMA seeds.

In addition to h-BN vertical heterostructures of graphene and TMDs have also been extensively studied. Although they possess quite different properties, vertical stacks of Graphene/TMD/Graphene have found different applications, such as in FET with high I_{on}/I_{off} ratios, in optoelectronics and photovoltaics. In addition to the numerous transfer methods that have been reviewed previously, these heterostructures have been synthesized *via* various direct growth procedures. For instance, Ling *et al.* showed that MoS_2 monolayers could be grown onto graphene from sources of MoO_3 and S, using fluorinated phthalocyanine as nucleation seeds.[129] Other common Graphene/TMD heterostructures have been prepared also by van der Waals epitaxy (VDWE) method, which is the growth of layered materials onto clean and smooth surfaces with no dangling bond, even in presence of a large lattice mismatch between the two layers. The result is a heterostructure with a high-quality interface due to the absence of surface defects and dangling bonds, in which the two

layers are held together only by van der Waals forces. Vertical heterostructures of graphene and TMDs have found many applications as ultrafast and ultrasensitive photodetectors[130] and light harvesting,[131] memory devices,[132] light-emitting diodes,[133] and highly efficient FET.[108, 109] In most of the cases, graphene act as source, drain and gate electrodes, and as electron collector, while the TMD layers as the proper semiconductor. Flexible and transparent devices based on vertical heterostructures supported on PET have also been produced.[108] On the contrary, stacking of graphene (including GO and rGO) and other 2D materials (such as TMDs, phosphorene and h-BN) obtained by liquid-phase processing have found interesting applications in the field of energy storage, with applications in supercapacitors, lithium-ion batteries and sodium-ion batteries.[16, 108, 134] For example, Bissett *et al.* fabricated a graphene/MoS_2 composite supercapacitor from liquid phase exfoliated material.[135] Dispersions of graphene and MoS_2 were mixed together and filtered to create thin flexible electrodes in a symmetrical supercapacitor based on aqueous electrolyte. The performances of the supercapacitor based on the graphene/ MoS_2 composite with ratio 1:3 were greatly enhanced over either individual component. This was attributed to a combination of effects. On the one hand, MoS_2 flakes could intercalate and prevent restacking of the larger graphene sheets. On the other hand, MoS_2 enhanced conductivity and pseudocapacitance of the hybrid by increasing the ion adsorption sites. For lithium-ion batteries anodes, aerogels papers based on rGO and MoS_2 have also been employed.[136, 137] Firstly, hydrogel of rGO and MoS_2 were formed with hydrothermal methods that involve the *in situ* simultaneous reduction of GO and formation of the hybrid structure, then the samples were freeze-dried to form the aerogel. In these examples, MoS_2 mostly acted as a spacer facilitating the Li-ion intercalation in the electrode. Composites of phosphorene and graphene have been successfully employed in sodium-ion batteries; in fact, phosphorene can react with sodium and lithium to form Na_3P and Li_3P, increasing ion storing potential of the electrode and thus the specific capacity of the battery that can reach the 2596 mAh/g.[123] In these composites with phosphorene graphene plays a role as an elastic buffer, accommodating the big changes in the volume of the electrode that deforms reversibly without breaking.

Lateral, in-plane heterostructures in which unidimensional junctions are created between the different materials have also attracted much interest.[108, 109, 113] The combination of more 2D materials on the same plane allows achieving ultra-thin devices. However, the development of these structures has been slower than for vertical heterostructures for two main reasons. The first reason is the challenging connection of the two materials on the same plane since thin unidimensional interfaces need to be perfectly in contact. This implies the lack of a straightforward method, such as the mechanical stacking for vertical heterostructures, to produce lateral heterostructures. To ensure the intimate connection between the 2D materials, all the methods rely on the bottom-up synthesis of at least one of the materials. The second reason is that these interfaces can only be realized by *in situ* techniques, in which one of the materials starts to grow directly from the edge of the other. Since the conditions for the direct growth of the second material from the edge of the first

material may damage the latter, compatible techniques had to be developed. Nevertheless, in the last years, the advances in the techniques allowed the growth of these in-plane heterostructures that possess interesting properties. The first lateral heterostructures realized, and also the most studied, are based on h-BN and graphene because the two materials share many characteristics, and these are the structures with the most interesting properties. As it was previously stated, graphene and h-BN have the same structure and a lattice mismatch of just 1.7 %, furthermore, they both grow well on Cu and Ni substrates. The first structures realized was a random heterostructure formed by h-BN and graphene domains growth simultaneously by CVD from CH_4 and ammonia borane.[138] This method suffered from poor control over the size and shape of the domains of each material, as well as over the quality of the interfaces. More recently, numerous methods which allow controlling the size, shape and position of each material have been developed. In general, these are all two-steps growth processes and involve the use of some kind of mask and/or lithographic process to pattern the first material before the deposition of the second (**Figure 2.2-10**).[108, 109, 114, 139, 140] It is worth to note that in some conditions the second material grows with epitaxial orientation respect to the first material, and it has been shown that the two materials are strongly connected by covalent bonds.[114] Few examples of in-plane heterostructures of graphene and TMDs also exist in the literature, however, the number of studies is still small compared to the structures with h-BN.[141-143] In general, all these structures have been fabricated by CVD growth of the first material, followed by patterning and by the CVD growth of the second material. Differently from the case of h-BN, graphene and TMDs have different structure and crystal lattice. These differences lead to the overlapping of the two materials at the interfaces, where the two materials interact by van der Waals forces. Perfect unidimensional interfaces between the two layers are more challenging and have not been realized yet. Lateral heterostructures of graphene and TMDs have been used to fabricate atomically thin FETs that possess good Ohmic contact between the TMD and the two source and drain electrodes made of monolayer graphene.[142, 143]

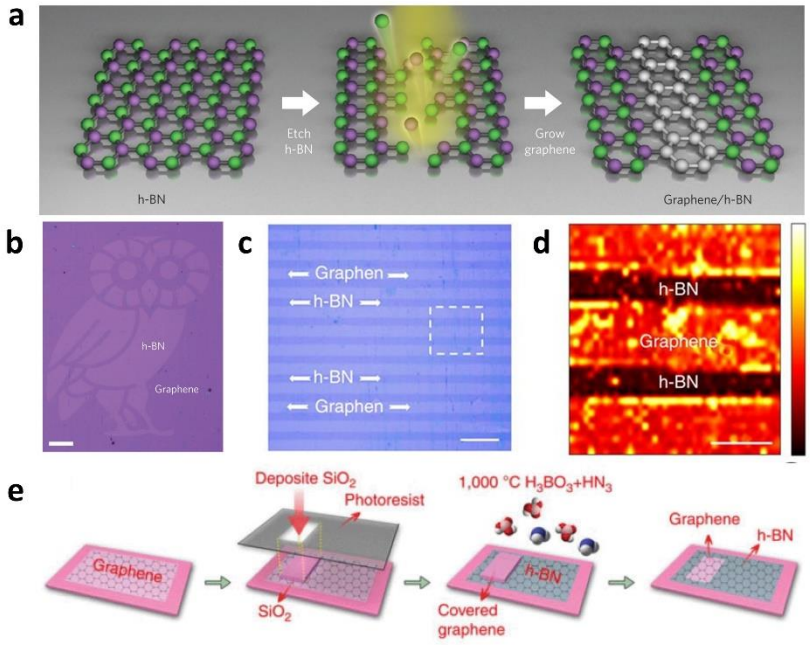

Figure 2.2-10 : (a) Schematic of the fabrication process of a patterned in-plane graphene/h-BN heterostructure. (b) Optical microscope image of the so obtained heterostructure on a Si/SiO_2 substrate. Adapted from Ref. [139] (c) Optical microscope image of graphene/h-BN alternative strips on Si/SiO_2 substrate. (d) Raman mapping of the marked area in (c) at 2D peak (2,700 cm^{-1}) of graphene. (e) Schematic of the fabrication of the graphene/h-BN patterned in-plane heterostructure involving the CVD growth of graphene, a photolithographic process to pattern the graphene and conversion of the unprotected graphene to h-BN. Adapted from Ref. [140]

2.2.2. Graphene modified with molecules

The chemical modification of graphene opens the possibility to tailor its properties, such as the electrical properties, to add new functionalities and to enhance its processability, solubility, and compatibility with other materials. For instance, graphene can become a semiconductor with an adjustable bandgap *via* the functionalization of its basal plane.[144] The functionalization of graphene can be carried out at the covalent or non-covalent level. A difference should be made between pristine graphene, graphene oxide and reduced graphene oxide, because the presence of some oxygen-containing groups in the last two increases the number of available reactions and kind of non-covalent interactions with other molecules in comparison with pristine graphene. In fact, a limited number of methods have been reported for the covalent functionalization of pristine graphene; these methods usually involve very reactive species generated *in situ* such as nitrenes and free radicals.[145] If the purpose is to keep unaltered the electronic properties of pristine graphene and just increase its processability and solubility non-covalent functionalization is preferred. Molecules can physisorb on pristine graphene exploiting van der Waals and π-π interactions, among which π-π stacking interactions are the strongest, thus most used. On the other hand, GO, and in a lesser extent rGO, possess residual oxygen groups in form of epoxides, hydroxyls, carboxylic acids and ketones on their surfaces that make available a wide series of reactions.

Furthermore, because of the oxygen groups and carboxyls, in GO also the possible non-covalent interactions with molecules are more numerous, including ionic bonds, electrostatic interactions, and hydrogen bonds.

2.2.2.1. *Chemical covalent functionalization of graphene*

The functionalization of pristine graphene sheets with organic molecules has been developed for several purposes. In the first instance, there is a need to improve the dispersibility of pristine graphene in common organic solvents. The dispersion of graphene in organic solvents is the first and crucial step towards the formation of graphene-based hybrid materials. Furthermore, chemical modification with functional molecules is a viable approach to confer new properties to graphene such as photoluminescence, semiconductivity or specific interactions with certain analytes that can combine with typical properties of graphene such as the high stability, conductivity and transparency. In most cases, when molecules are covalently attached on the graphene surface, a modification of the aromatic structure of graphene takes place, thereby perturbing its electrical properties. Among the various possible perturbations, the possibility of opening a tunable bandgap is the most explored for its implications in the fields of electronics and photonics. Pristine graphene is a material composed exclusively of carbon atoms with sp^2 hybridization, likewise its structurally related allotropes graphite, carbon nanotubes and fullerenes. For this reason, graphene has benefited from the numerous reactions previously developed for fullerenes and carbon nanotubes. However, the curved structure and misaligned π-orbitals of fullerenes and carbon nanotubes make them more reactive than graphene which, as a result of its fully delocalized π system, is rather inert.

In the case of pristine graphene, free radicals or dienophiles are used to covalently attach the C=C bonds of its basal plane. The use of diazonium salts has been one of the first methods to functionalize pristine graphene. These salts usually are freshly prepared before the reaction, because of their instability. The functionalization reaction takes place through the decomposition of diazonium cation that releases N_2 and the formation of an aryl radical that attacks an sp^2 carbon of graphene.[2] Tour *et al.* made use of this reaction to decorate graphene nanoribbons with nitrophenyls (**Figure 2.2-11** a).[146] The groups showed that, during chemical functionalization, the conductivity of graphene decreased due to the re-hybridization of carbon atoms from sp^2 to sp^3 and consequent disruption of the aromatic system. Similarly, Niyogi and co-workers covalently attached nitrophenyls to graphene *via* diazonium chemistry.[147] The reaction created a controllable band gap in graphene, opening its application as a semiconducting nanomaterial. Benzoyl peroxide is another route to generate free aryl radicals reactive with graphene. Liu *et al.* employed benzoyl peroxide to functionalize mechanically exfoliated graphene.[148] The reaction was conducted in toluene solution and initiated photochemically by focussing a laser onto the graphene surface and

the success was monitored by following the appearance of the D band in the Raman spectrum of graphene (**Figure 2.2-11** b-d).

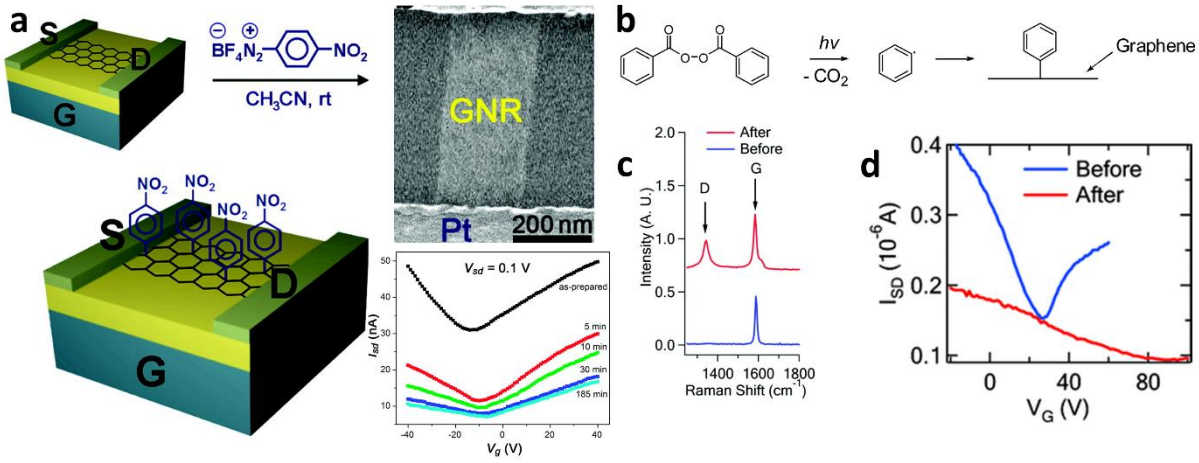

Figure 2.2-11: (a) Schematic representation of the covalent functionalization of a graphene nanoribbon (GNR) with nitrophenyls. Insets: SEM image of the GNR device and transfer curves of the device recorded at V_{sd} = 0.1 V for the same electronic device in panel (a) after several consecutive grafting experiments. Adapted from Ref. [146] (b) Schematic reaction of graphene with benzoyl peroxide photochemically activated. (c) Raman spectra and (d) transfer curves of graphene before and after the functionalization. Adapted from Ref. [148]

Cycloadditions are the second class of possible reactions with pristine graphene. Azomethine ylides are one of the most common dienophiles that have been successfully applied in the functionalization of graphene through 1,3 dipolar cycloaddition.[149, 150] This reaction has been extensively used by Prato and his group to functionalize CNTs with a variety of derivatives that conferred applications in the fields of biotechnology, drug delivery and optoelectronic devices.[2] The azomethine ylide can be formed *in situ* by condensation of an aldehyde with an amine. This constitutes a great advantage because of the possibility to choose among several aldehydes or α-amino acids as precursors that yields a variety of functional groups that can be grafted on graphene. For instance, Zang *et al.* decorated liquid-phase exfoliated graphene with palladium porphyrins by employing the porphyrin aldehyde and sarcosine as precursors.[150] Another technique for the functionalization of pristine graphene that can afford a large variety of substituents relies on the use of organic azides. Their reactivity with the C=C bonds in graphene is triggered by light or heat and goes through the formation of a reactive nitrine intermediate. For example, Liu *et al.*[145] functionalized solvent-exfoliated graphene flakes with different para-substituted perfluorophenylazide, using either heat or light irradiation (**Figure 2.2-12** a-b). They also functionalized with the same procedure graphene immobilized in FET. They found out that in this case, the carrier mobility of functionalized graphene was doubled in comparison to pristine graphene and they did not observe a defective D peak in the Raman spectrum, suggesting that this reaction did not perturb the aromatic structure of graphene. This reaction was used also to functionalize graphene with a variety of alkyl azides which greatly

increased the dispersibility of graphene in organic solvents,[151] and to functionalize graphene with azidophenylalanine amino acids (**Figure 2.2-12** c).[152] Cycloadditions to graphene can be realized *via* benzynes reactive intermediates that can be generated by removal of two ortho-substituents of benzene. For example, Zhong *et al.* covalently attached aryl rings to graphene using 2-(trimethylsilyl)aryl triate as benzyne precursor, greatly increasing the dispersibility of modified graphene in various solvents.[153]

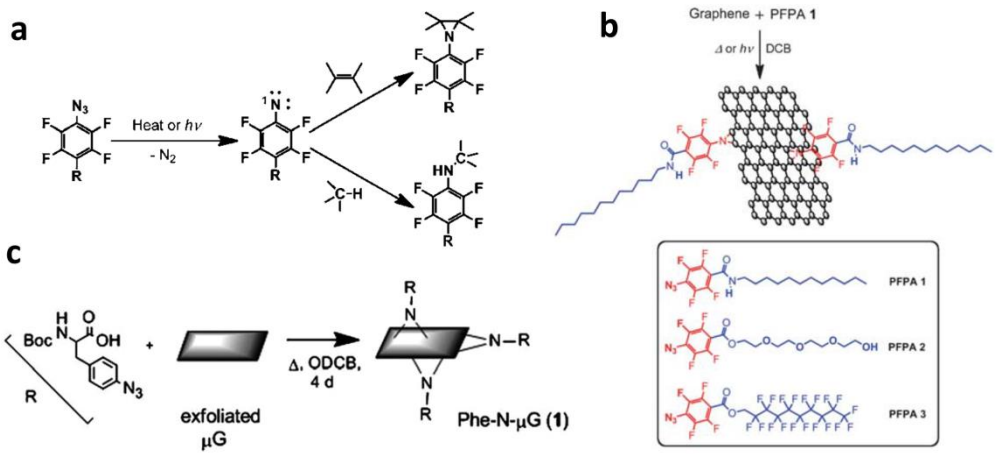

Figure 2.2-12: a) Insertion and addition reactions of singlet nitrene generated from photolysis or thermolysis of azides. b) Solution-phase functionalization of pristine graphene with perfluorophenylazides. Adapted from Ref.[145] c) Nitrene addition to graphene flakes using Boc-protected azidophenylalanine. Adapted from Ref. [152]

Graphene oxide is a mono or few-layers graphitic material characterized by a random distribution of ordered sp_2 carbon regions and disordered oxygen-rich regions with sp_3 carbons. After the reduction of GO by chemical, thermal and microwave treatments most of the oxygens are eliminated and the aromatic conjugation is restored. This causes the increase in electrical conductivity that ranges from around $1 \cdot 10^{-4}$ S/m of GO up to 10^2 S/m of rGO.[52, 154] However, many defects remain in rGO, which are confirmed by its lower charge carrier mobility and electrical conductivity compared to pristine graphene and by the persistence of a strong D band in the Raman spectrum of rGO. Because of this reason, when graphene is derived by the reduction of GO is usually referred to as reduced graphene oxide. The presence of hydroxyl, carboxyl and epoxy groups on GO allows a wide series of reactions and makes it the material of election for introducing functionalities on graphene through the covalent attachment of organic functional groups.

The carboxylic acids existing at the edges of GO flakes can be used for amide and esters formation with amines and alcohols. For example, Liu et al. prepared an oligothiophene functionalized GO exploiting the amide bond formation between an amine-terminated oligothiophene and the carboxylic groups at the edges of GO flakes (**Figure 2.2-13** a).[155] The hybrid material exhibited an improved absorption of light with optical limiting

characteristics and efficient quenching of the photoluminescence of oligothiophene. Yu *et al.*[156] functionalized GO flakes with regioregular poly(3-hexylthiophene) (P3HT) terminated with methanol groups through the formation of ester bonds with the carboxyl groups of GO. This material, which exhibited increased solubility in organic solvents, was used as active material in an organic solar cell where it showed an increase of 200% in power conversion efficiency compared to the P3HT alone. Xu *et al.* reported the covalent functionalization of GO *via* amide bond formation with porphyrins (**Figure 2.2-13** b).[157] The energy transfer efficiency from the porphyrin to GO was greatly enhanced by the covalent bond between them and the hybrid material exhibited better optical limiting properties compared to fullerene C_{60} and to the physical mixture of GO and the porphyrin. The reaction of carboxylic acids with amines and alcohols to form respectively amides and esters are rather slow reversible reactions and necessitate harsh reaction conditions such as high temperature and presence of dehydrating agents to accelerate the reaction and shift the equilibrium toward the products. For this reason, often the carboxylic acid is activated to a more reactive intermediate before the reaction with the mild nucleophile amine or alcohol. Such activation of the carboxylic acid becomes mandatory when GO needs to be functionalized with molecules sensitive to harsh conditions such as proteins. For instance, Shen *et al.* functionalized GO flakes with the protein bovine serum albumin *via* diimide activation of the carboxyl groups before amidation.[158] The reaction consisted in two steps: firstly, the carboxyl groups on GO are activated by ethyl(dimethylaminopropyl) carbodiimide (EDAC), which in presence of N-hydroxysuccinimide (NHS) form a stable ester. Secondly, the active ester, which is a good leaving group, reacts at room temperature with the amines of BSA forming an amide bond (**Figure 2.2-13** c). The group verified that in this way the protein was not denatured. The same diimide chemistry has been used to functionalized GO with DNA strands used as specific receptors for DNA fragments.[159, 160]

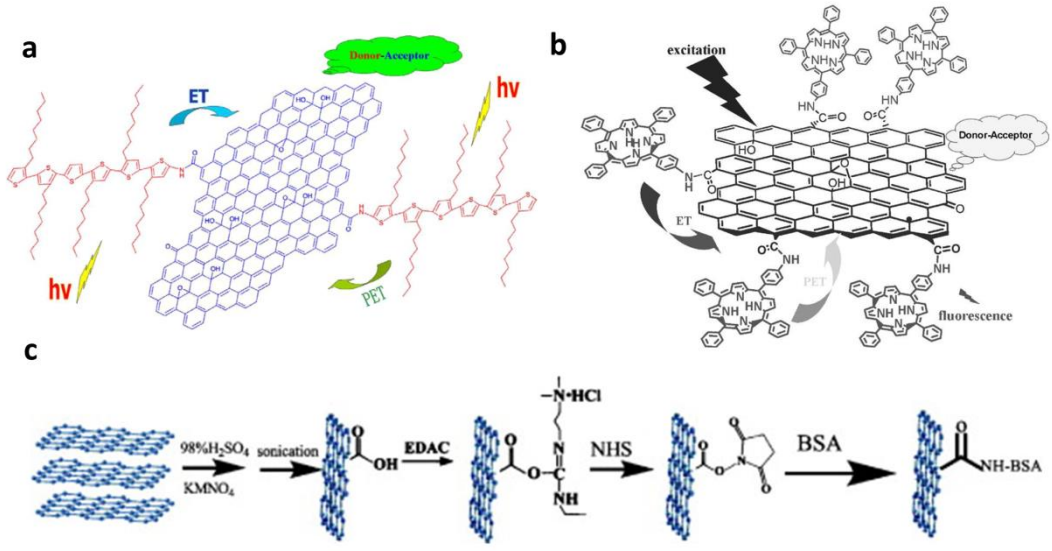

Figure 2.2-13: a) Structure of oligothiophene functionalized GO and energy transfer mechanism. Adapted from Ref. [155] b) Schematic structure of the porphyrin functionalized GO and

quenching mechanism. Adapted from Ref. [157] c) Mechanism of the reaction between GO and BSA protein involving the use of a diimide intermediate. [158]

GO can be grafted via amide and ester bond formation to polymers that bear hydroxyl and amine functional groups such as poly(vinyl alcohol) (PVA), poly(ethylene glycol) (PEG), and polyallylamine. The properties of these hybrid materials are a combination of the properties of graphene such as mechanical strength and electrical conductivity with the properties of the polymeric part like dispersibility in certain solvents. For instance, GO can be made better dispersible in water by covalently modifying it with PEG chains. Liu *et al.*[161] functionalized GO with PEG molecules terminating with amine groups by amide bond formation and used it as a deliverer for the water-insoluble cancer drug camptothecin. Camptothecin, which has an aromatic structure, attaches non-covalently via π-π stacking to the GO flakes, which in turn is solubilized in water by the PEG chains. Salvagione *et al.* covalently grafted PVA with GO via ester bond formation. The ester could be formed either by Steglich esterification between the carboxylic acids of GO and PVA using dicyclohexylcarbodiimide as a coupling reagent or by firstly converting the carboxyl groups to the more reactive acyl chloride.

Another class of reaction that involves GO are the epoxide ring-opening reactions. The epoxide ring can be opened by nucleophiles such as amines and thiols in presence of basic or acid catalysis. Since GO is acidic for the presence of carboxyl groups and some sulphate groups, the reaction can take place by self-catalysis, without need for the addition of acids.[162] The reaction between GO and amines or thiols can take place in mild conditions and have been exploited to attach a great range of amines and thiols to GO.[163-167] Furthermore, it has been shown by Vacchi *et al.* that the reaction between GO and amines occurs *via* ring-opening of the epoxides preferentially to the amidation, since the first happens in milder conditions and epoxides are more abundant than carboxyl groups in GO.[168] The authors suggested that in the papers that describe the functionalization of GO by amide formations the functionalization of the epoxides would have occurred more easily. Shan *et al.*[169] described the functionalization of rGO with the biocompatible poly(l-lysine) via epoxide ring-opening. This modified rGO was soluble in biological media. After functionalization, the modified GO was used as an H_2O_2 efficient biosensor by firstly covalently attaching it to a gold electrode, then by immobilizing a peroxidase on the poly(l-lysine) chains (**Figure 2.2-14** a). Compton *et al*. firstly functionalized the epoxide groups of GO flakes with hexylamine and then reduced the modified GO to modified rGO with hydrazine.[163] This modified rGO had better solubility and processability compared to GO, while exhibited good electrical conductivity. Thomas *et al*. functionalized GO with potassium thioacetate via ring-opening of epoxide groups to form thiol-functionalized GO. [164] This material showed high affinity for Au NPs that selectively deposited on its surface. The chemical modification of GO with specific functional groups is greatly exploited in the field of sensing. In fact, designed receptors can be grafted to GO, providing it with specific sensitivity to target gases, molecules or biomolecules. In 2012 Yuan *et al.*[170] fabricated a NO_2 resistive-type gas sensor

based on sulfonated rGO (S-rGO) and rGO functionalized with ethylenediamine (EDA–rGO). The sulfonated rGO was produced by reacting a sulfonated aryl diazonium salt with partially reduced GO, while EDA-rGO was synthesized by ring-opening of epoxide groups. The sensors were prepared by depositing the materials onto interdigitated electrodes; in particular, S-rGO displayed a response to NO_2 10 times greater than rGO and 3 times larger than EDA–rGO. In the same year, Hu *et al.*[171] developed a dimethyl methylphosphonate (DMMP) sensor based on rGO functionalized with *p*-phenylenediamine, which was deposited from solution on an interdigitated electrode. The device exhibited a response to DMMP vapours that was 7 times higher than the response of hydrazine reduced GO. It is possible to build sensor arrays of GO functionalized with different molecules that can be used to recognize different analytes. In a recent study, Teradal *et al.*[172] assembled a capacitive-type porous graphene oxide (pGO) vapours sensor in which the GO was deposited on a pre-patterned electrode through a freeze-drying technique in order to maximize the area exposed to the gas. In parallel, the GO was also chemically functionalized with aniline (phenyl-GO), dodecylamine (dodecyl-GO) and ethanolamine (ethanol-GO) by amide bond formation: firstly the carboxylic acids of GO where converted to the acyl chloride with $SOCl_2$ and then these were reacted with the amines (**Figure 2.2-14** b). These three differently functionalized GOs were deposited and combined with pGO in a sensors array that makes it possible to selectively detect the presence of water, NH_3, toluene, EtOH, phenol and cyclohexane (**Figure 2.2-14** c). Furthermore, the sensors array presented high sensitivity towards the target gases, high reproducibility and fast response and recovery times. Chemically modified GO has been used also for metal ions sensing and removal. For instance, Seenivasan *et al.*[173] used a cysteine functionalized GO/polypyrrole nanocomposite for Pb^{2+} ions detection and removal from water. The cysteine functionalized GO (sGO) was synthesized in a two-steps process *via* amide and carbamate bond formation using carbonyldiimidazole as a sacrificial linker. Then the nanocomposite of sGO with polypyrrole was formed on a working electrode by electrochemical deposition. The concentration of Pb^{2+} ions was measured by anodic stripping of the modified electrode, and the sensor presented a limit of detection of 0.07 ppb.

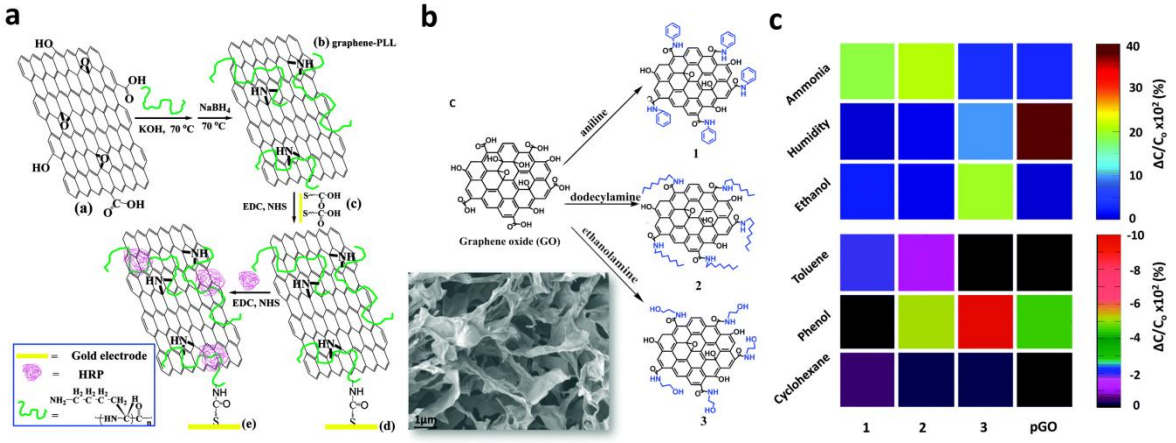

Figure 2.2-14: a) Schematic Diagram of GO-poly(l-lysine) synthesis and assembly process of modified GO at a gold electrode and following assembly with a peroxidase (HRP). Adapted from Ref. [169] b) Schematic structure of the synthesis of phenyl-GO (1); dodecyl-GO (2); and ethanol-GO (3) and SEM image of the p-GO. c) Sensitivity to different vapours (180 ppm) using the functionalized pGO capacitive sensor: phenyl-GO (1); dodecyl-GO (2); and ethanol-GO (3). The colours indicated in the diagram correspond to the sensitivity, according to the colour keys shown on the right. Adapted from Ref. [172]

Madadrang *et al.*[174] synthesized an ethylenediamine triacetic acid (EDTA) functionalized GO for the removal of Pb(II) from water. The EDTA-GO was synthesized via silanization reaction between N-(trimethoxysilylpropyl) EDTA and the hydroxyl and epoxide groups on the GO surface. The functionalized GO had enhanced absorption capacity because of the chelating ability of EDTA and revealed an adsorption capacity for Pb(II) removal of 479 ± 46 mg/g.

Graphene oxide has also been covalently functionalized with polymers such as polystyrene (PS), poly(acrylamide) (PAM), poly(methyl methacrylate) (PMMA) using the atom transfer radical polymerization (ATRP) approach. [2, 175] The technique involves the covalent attachment of the initiator to GO, followed by the ATRP in presence of the monomers. Following this approach, Lee *et al.*[175] synthesized GO sheets functionalized with PS, PMMA and poly(butyl acrylate). Firstly, GO was functionalized with the polymerization initiator *a*-bromoisobutyryl bromide which reacted with the hydroxyl groups of GO by ester formation. Then the polymers were grown by suspending the functionalized GO in DMF in presence of the monomers and copper as a catalyst. The obtained nanocomposites exhibited enhanced mechanical and thermal properties compared with the pure polymers. Similar mechanisms have been proposed to produce GO covalently grafted with PMMA and PS.[176-180] In all the cases the composites were produced in two steps, by firstly covalently attaching the ATRP initiator to the functional groups of GO or directly on its basal plane and then by growing the polymer on the functionalized GO. The resulting nanocomposites possessed higher dispersibility in organic solvents and improved mechanical properties such as an increase in the elastic modulus, hardness and strength. Free radical polymerization has been used also by Yang *et al.*[181] to functionalize rGO with water-soluble poly(acrylamide) (PAM)

and use it to adsorb Pb(II) and methylene blue from water (**Figure 2.2-15** a). The rGO/PAM hybrid showed an adsorption capacity of 1000 and 1530 mg/g for Pb(II) and methylene blue respectively. GO and rGO have been also functionalized with conductive polymers such as polypyrrole, polythiophene and polyaniline. These hybrid materials found mostly application as supercapacitors[182-185] and solar cells.[156] For instance, in 2019 Li *et al.* synthesized an aerogel based on rGO grafted with polyaniline and tested it as a supercapacitor.[183] Firstly amino groups were introduced on GO by conversions of the carboxylic groups to amides and attachment of benzamide molecules on the basal plane of GO *via* diazonium salt chemistry (**Figure 2.2-15** b). Then polyaniline was polymerized from the amino groups. The final hybrid material exhibited a maximum capacitance of 553 F/g in 1 M H_2SO_4. Yadav *et al.*[184] fabricated a supercapacitor by covalently grafting polypyrrole on the carboxylic groups of GO. During the polymerization reaction GO was reduced to rGO by pyrrole. The assembled supercapacitor showed a capacitance of 230 F/g that was retained after 5000 cycles.

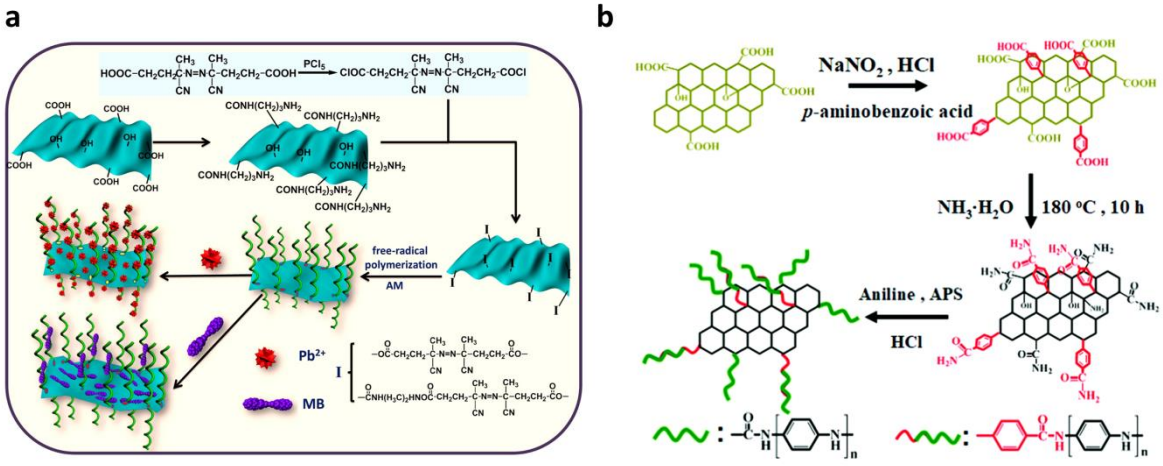

Figure 2.2-15: a) Schematic of the synthesis of polyacrylamide functionalized rGO by free radical polymerization and adsorption of Pb(II) and Methylene Blue. Adapted from Ref. [181] b) Schematic illustration showing the covalent functionalization of GO with polyaniline. Adapted from Ref.[183]

2.2.2.2. *Hybrid based on non-covalent interactions*

The majority of hybrid structures based on graphene with other molecules or nanostructures relies on non-covalent interaction rather than on covalent bonds. Non-covalent interactions rule the world around us; for instance, the presence of liquids is due to non-covalent interaction. Non-covalent interactions between molecules are the basis of supramolecular chemistry and determine the existence of biological systems, such as the DNA structure, the cell membrane and the 3D structure of proteins. Supramolecular/non-covalent bonds are usually reversible and kinetically labile, thus allowing for important mechanisms such as molecular recognition and self-correction.[186] Among these forces we have ionic bonds, which are the strongest, with energies that range from 100-350 kJ/mol,

followed by ion-dipole and coordinate (dative) bonds with energies between 50 and 200 kJ/mol, hydrogen bonds (8-39 kJ/mol), π-π and π-CH interactions (5-30 kJ/ml) and lastly van der Waals interactions (0.5-5 kJ/mol) (**Figure 2.2-16**).[15] Pristine graphene may interact non-covalently with other molecules *via* π-π stacking and van der Waals forces, while GO and rGO, in addition to these, may also interact forming hydrogen, ligand-metal and ionic bonds through their oxygen functional groups.

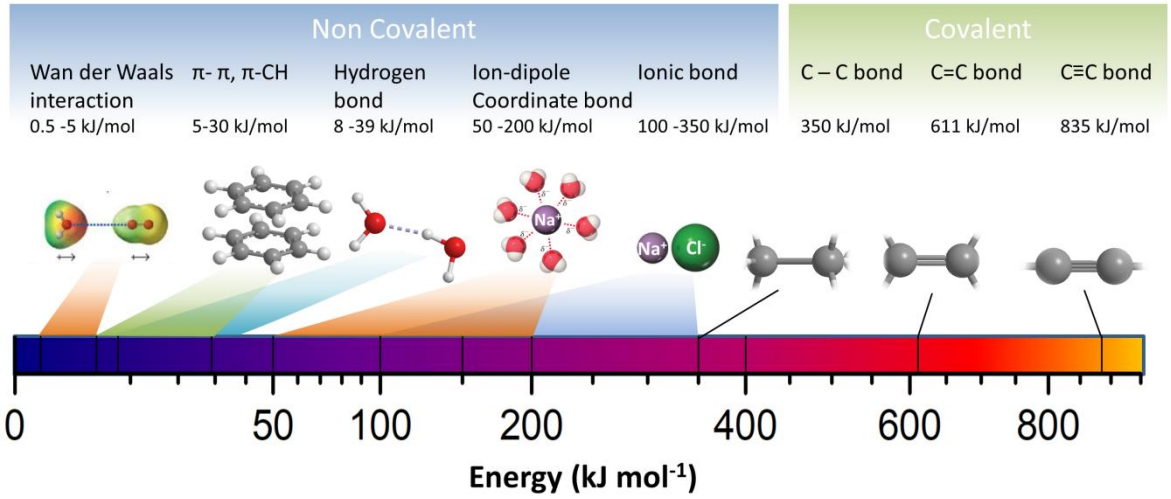

Figure 2.2-16: Schematic of the different covalent and non-covalent interactions with the corresponding energy ranges expressed in kJ/mol.

All forms of graphene, including its derivatives GO and rGO, can be functionalized with aromatic molecules exploiting the π-π interaction with its extended aromatic structure. The more extended are the two aromatic structures, the strongest is the resulting supramolecular bond. Besides, another requirement for the formation of π-π interaction is the overlapping of the two π systems, which is favoured by the planarity of the aromatic system.[15] Experiments have shown that affinity and the binding constants between graphene materials and aromatic structures such as pyrenes follows the order GO<rGO<pristine graphene, because of the increased aromaticity and planarity of the structure passing from GO to pristine graphene.[187, 188] The formation of π-π stacking between aromatic molecules and graphene has been used to facilitate its exfoliation from graphite, increase its dispersibility in organic solvents and water, form hybrid structures and nanocomposites with new advanced properties and functionalities and employed as a platform for drug delivery.[2, 14, 15] Molecules containing pyrene and perylenediimide (PDI) units are often used because of their strong interaction with graphene. In 2009 Su *et al.*[189] functionalized rGO sheets with pyrene and PDI sulfonic acid derivatives. The resulting hybrids exhibited strong interaction between rGO and the two aromatic molecules and were highly dispersible in water due to the presence of sulfonic groups attached to the pyrene and PDI, which induced repulsive forces between the hybrid nanostructures. Furthermore, they observed from the shift of the G band in Raman spectra the existence of a remarkable charge-transfer effect between the electron donor

pyrene and rGO or between the electron acceptor PDI and rGO. The presence of the absorbed molecule was confirmed also by AFM imaging of the hybrid, which revealed an increased thickness of the rGO monolayer compatible with the height of the molecule. Pyrenes and other mall aromatic molecules decorated by lipophilic or hydrophilic have extensively been used to facilitate the ultrasound-induced liquid-phase exfoliation (UILPE) of graphene.[15, 44] The small and flat aromatic molecules act as wedges: they penetrate between the layers of graphite with the aid of sonication and weaken the interactions that hold together the graphitic sheets by forming new competitive π-π interaction with those. Eventually, the graphenic layers are completely dissociated and separated from each other; at this point the hydrophilic or lipophilic lateral chains that decorate the organic molecules aid to keep the graphene sheets dispersed in water or organic solvents respectively and to avoid the restacking between them. Palermo *et al*.[190] studied the effects of the different functional groups decorating the aromatic molecule on the exfoliation and stabilization of graphene by UILPE. They employed four different pyrene molecules functionalized with one to four sulfonic groups, which are electron acceptors, while two of these molecules were also functionalized asymmetrically with one and two hydroxyl groups, which are electron donors (**Figure 2.2-17** a). They find out that the more sulfonic groups were attached to the pyrene the less these molecules were adsorbed on graphite, while the exfoliation and stabilization in water were favoured by the molecule with the highest dipole moment, namely the one with two sulphonic and two hydroxyl groups. Pyranine modified rGO was used by Chen *et al*.[191] to assemble a fast and highly sensitive humidity sensor. The hybrid was produced in a one-pot procedure by contemporarily reducing GO with hydrazine and forming the non-covalent assembly with pyranine which assisted in stabilizing rGO in water (**Figure 2.2-17** b). Qu et al. [192] assembled a supramolecular hybrid of rGO and pyrene functionalized fullerene and employed it as electron-accepting layer in an organic solar cell. The pyrene was used as an anchoring bridge to link rGO and the C_{60} fullerene. The performances of the cell with the hybrid material were greatly improved compared to the cell assembled with the single components.

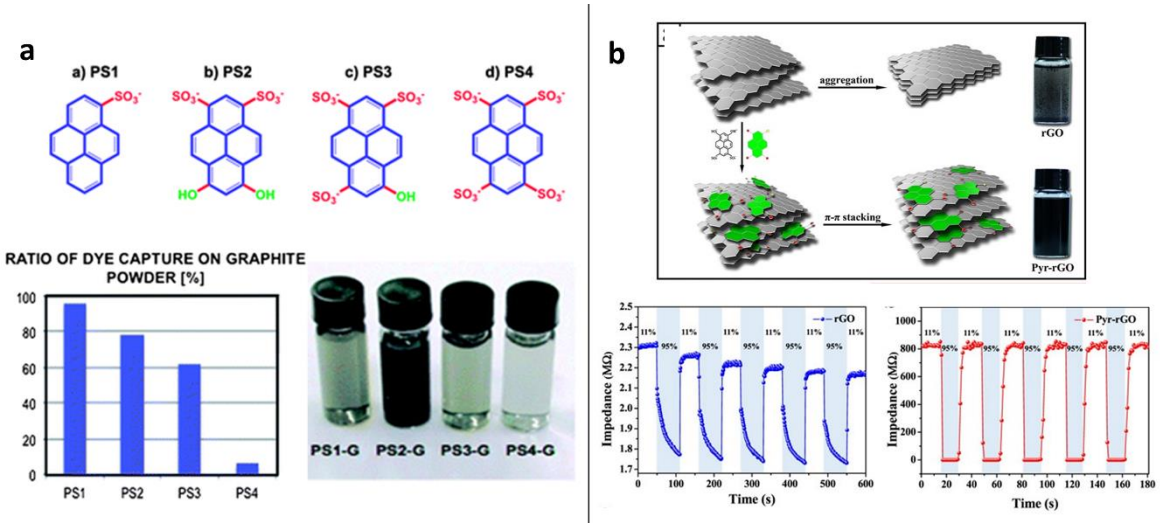

Figure 2.2-17: (a) Molecular structure of the 4 pyrene units modified with hydroxyl and sulfonic groups. Bottom left: the ratio of the molecules absorbed on graphite. Bottom right: Suspensions of UILP exfoliated graphene with the 4 dyes. Adapted from Ref. [190](b) Stabilization of rGO by pyranine. Bottom: Impedance at 100 Hz of rGO (blue) and pyranine-rGO (right) sensors under exposure to humidity between 11% and 95%. Adapted from Ref. [191]

Aromatic electron-rich or electron-poor molecules adsorbed onto graphene can also modify its electrical properties, for instance, various theoretical papers have shown that molecules such as perylene-3,4,9,10-tetracarboxylic-3,4,9,10-diimide (PTCDI) can open a bandgap in pristine graphene.[193, 194] The advantage of using supramolecular assemblies of graphene with doping molecules is that this method allows tailoring the electrical properties of graphene without introducing in it any structural defect or irreversibly change its form. In 2011 Zhang *et al.*[195] showed that the I_{on}/I_{off} ratio of a FET based on mechanically exfoliated bi-layer graphene could be increased of 6 times upon physisorbing triazine molecules on the graphene surface. The molecules were thermally evaporated and AFM characterization showed the formation of a uniform layer of molecules on the basal plane of graphene. An electrical bandgap up to ~111 meV at room temperature was estimated.[195] Chen et al.[196] studied the p-doping effect of the electron acceptor, tetrafluoro-tetracyanoquinodimethane (F4-TCNQ) on epitaxial graphene grown on SiC(0001). Using synchrotron-based high-resolution photoemission spectroscopy they revealed that the p-type doping of graphene is caused by the electron transfer from graphene to F4-TCNQ. Metallo-phthalocyanines (MPc) and porphyrins are other aromatic compounds that have been used to functionalize non-covalently graphene. In 2009 Gao *et al.*[197] investigated the self-assembly of various magnetic phthalocyanines on epitaxial graphene monolayer by means of STM. They observed that the Pc self-assembled on the top of graphene by forming highly ordered supramolecular structures with a Kagome geometry that follow the lattice of epitaxial graphene yielding a Moiré pattern (**Figure 2.2-18** a-b). Sainio and co-workers showed by STM that cobalt phthalocyanine self-assembled on epitaxial graphene grown on Ir(111) forming large and ordered domains with a square unit cell.[198] The interaction between the delocalized π system of graphene and the π system of the adsorbed molecule can be so strong that can modify the

structure of the latter. Xu *et al.*[199] demonstrated this rational using a porphyrin substituted with methylpyridinium groups at the extremities (TMPyP). Normally the steric hindrance causes these groups to be aligned almost perpendicularly to the porphyrin plane. However, when they were absorbed on rGO the pyridinium groups were forced to align with the plane of the porphyrin to maximize the interaction with rGO. This was observed by a significant red-shift in the maximum of absorbance of the porphyrin (**Figure 2.2-18** c-d). Furthermore, in the TMPyP/rGO assembly they observed a 100% quenching of the fluorescence of porphyrin by rGO and a huge acceleration of the coordination reaction between Cd^{2+} ions and porphyrin that the group exploited to build a new optical probe for sensing Cd^{2+} ions. Jiang *et al.*[200] created a water-dispersible self-assembled structure between a hydrophilic copper phthalocyanine (TSCuPc) and graphene sheets, by simply sonicating them together in water. The presence of the hybrid was pointed out by the UV-Vis absorbance spectra that showed the disappearance of the band typical of the Pc dimer and the appearance of the band of the monomer, which was red-shifted for the interaction with graphene. This hybrid was tested for photothermal and photodynamic therapy; after irradiating the hybrid dispersed in water at 650 nm for 10 min they observed a significant raise in the temperature of the suspension (**Figure 2.2-18** e). Guo *et al.*[201] used hemin, which is a Fe(III) porphyrin, to synthetize a hybrid with graphene sheets *via* π-π interaction. The hybrid material exhibited interesting properties: it possessed intrinsic peroxidase-like activity and it was able to differentiate between single-strand and double-strand DNA owing to the different affinity of the hybrid towards the two DNA forms.

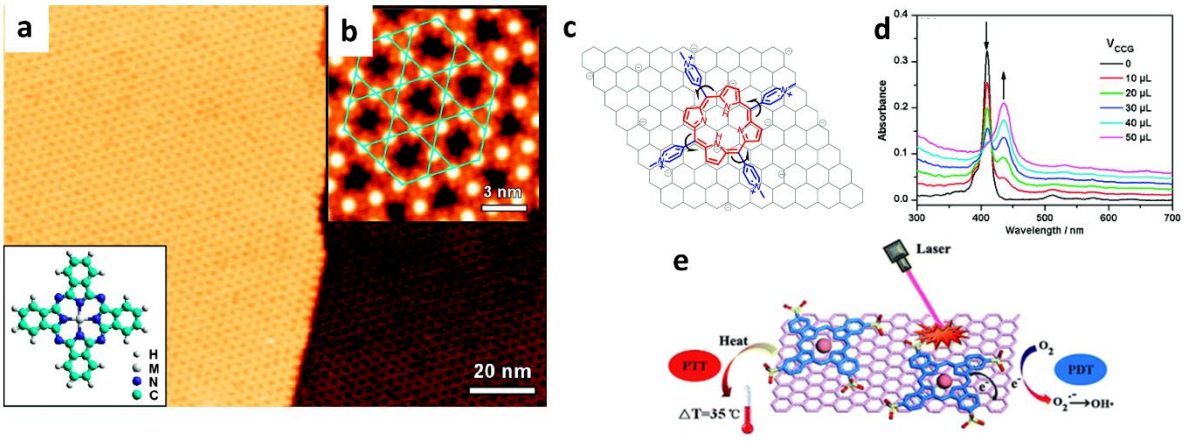

Figure 2.2-18: (a) STM images obtained of FePc adsorbed at RT on epitaxial graphene monolayer. The structural model of Pc is shown in the inset. (b) Magnified STM image showing details of the Kagome lattice of FePc. Adapted from Ref. [197] (c) Schematic of the TMPyP adsorbed on graphene. (d) Absorption spectra recorded during the process of titration of an aqueous solution of TMPyP with rGO dispersion showing the red-shift in the absorbance peak of TMPyP. Adapted from Ref. [199] (e) Schematic showing the TsCuPc adsorbed on graphene and its use for photothermal (PTT) and photodynamic (PDT) therapy. Adapted from Ref. [200]

In addition to π-π stacking, non-aromatic molecules can adsorb onto graphene *via* van der Waals interactions; this is particularly true for alkyl chains and polymers whose collective

interaction with graphene might be even stronger than the discussed π-π interaction.[44] By exploiting van der Waals interactions, many composites comprising graphene and several plastic polymers have been produced, in which graphene act as a filler that confers to the composite enhanced electrical and thermal conductivities and increased mechanical properties such as elastic modulus, strength and toughness.[202, 203] Small molecules exposing alkyl lateral chains can form ordered self-assembled structure onto pristine graphene, and can also modify its electrical properties.[44] De Feyter et al.[204] reported the formation of self-assembled monolayers (SAMs) of oleylamine (OLA) on highly oriented pyrolytic graphite (HOPG) and epitaxial graphene on SiC. The detail of the supramolecular ordered structure was highlighted from AFM and STM images which revealed the formation of a lamellar structure in which the oleylamine molecules lie parallel one another forming a lamellar adlayer onto the basal plane of graphene. When the electrical characteristics of such hybrid structure was tested in back-gated FET, it was observed that oleylamine induced a tunable n-doping effect in graphene and at the same time did not cause any change in the electron and hole mobility. The same group studied also SAM of octadecylamine (ODA) and nonacosylamine (NCA) on HOPG and CVD graphene showing the formation of similarly ordered structure and a different n-doping level for the two molecules.[205] In fact, the doping unit is the amine group, while the alkyl chains are responsible for the ordered self-assembly of the molecules. Since NCA has a longer alkyl chain than ODA, when NCA is assembled onto graphene it causes a lower density of amines on the surface, which ultimately leads to a lower doping effect, as it was confirmed by Raman spectroscopy and electrical measurements on FETs. Molecules composed by a photochromic or photoreactive head and a long aliphatic chain can form ordered molecular SAM on graphene and exhibit light-triggered dynamic doping effect, as it was recently demonstrated by our group.[206-208] In 2017, Gobbi *et al.*[206] demonstrated the formation of self-assembled 2D supramolecular lattices on graphene using 3-trifluoromethyl-3-(3-octadecyloxyphenyl)diazirine (MBB-1) (**Figure 2.2-19** a). This molecule exhibited a photoreactive diazirine head group substituted with an electron-withdrawing CF_3 moiety. Upon UV light irradiation of MBB-1 in chloroform, the photolysis of the diazirine unit produced a new molecule (MBB-2) exposing the CF_3 group perpendicular to the molecular plane (**Figure 2.2-19** b). Both molecules spin-coated on CVD graphene monolayers produced ordered SAM with lamellar structure. However, while MBB-1 did not produce a noticeable shift in the Dirac point of graphene, MBB-2 produced a strong p-doping, with a positive shift in the Dirac point of more than 25 V. The reason was attributed to a strong gating effect caused by the vertical orientation of the CF_3 group in respect to the graphene plane in MBB-2, and thus by the high vertical dipole moment. In another work, Gobbi *et al.* studied the ordered SAM on graphene of a photochromic molecule consisting of a spiropyran head and a long aliphatic chain both on solid[207] and at the solid-liquid interface.[208] Spiropyran (SP) is a molecule that can reversibly isomerize to a metastable zwitterionic form with high dipole moment called merocyanine (MC) (structures in **Figure 2.2-19** c). Both molecular forms were deposited on a graphene FET, on which they

formed highly ordered lamellar structures. However, while the SP form had no doping effect on graphene, the MC form produced a high n-doping effect. By irradiating the supramolecular assembly with UV and visible light, it was possible to trigger the reversible isomerization of the molecules between the SP and MC forms, thereby yielding a reversible switching of n-doping on and off. The self-assembly of the same molecule on graphene was also studied at the solid-liquid interface. In this case only the MC form of the molecule was able to adsorb from solution on graphene forming an ordered lamellar SAM (**Figure 2.2-19** c). By following the shift in the Dirac point of a graphene FET coated with a drop of the SP solution it was possible to monitor in real time the dynamic of the SAM formation caused by the isomerization of SP to MC upon irradiation with UV light (**Figure 2.2-19** d-f).

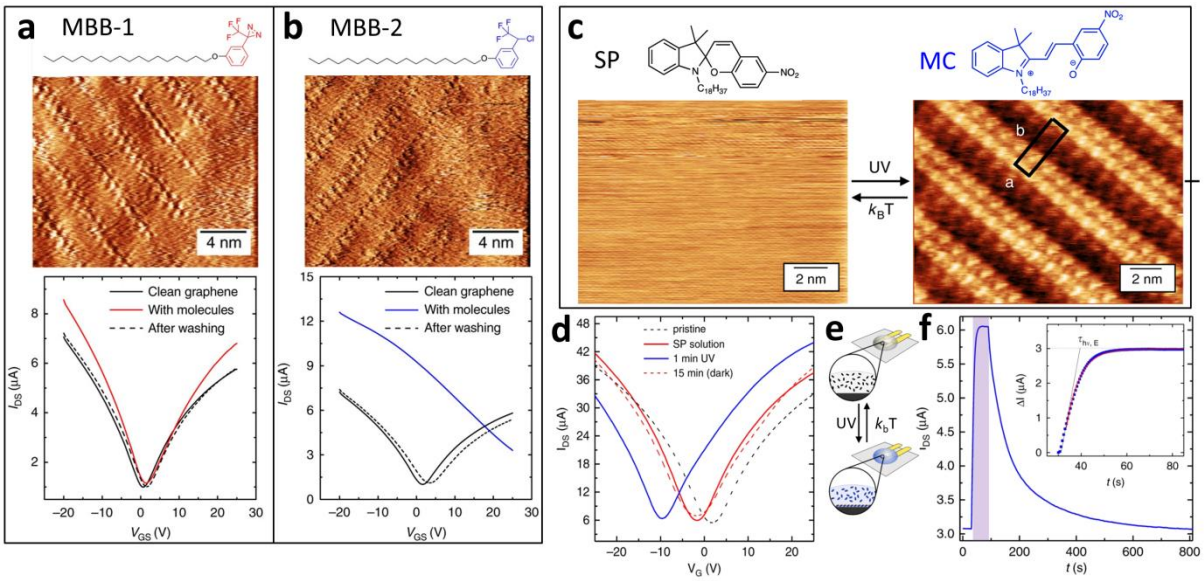

Figure 2.2-19: (a-b) Top panel: molecular structure of MBB-1 (a) and MBB-2 (b). Centre: STM image (current channel) of the SAM of (a) MBB-1 and (b) MBB-2 on CVD graphene. Lower panel: transfer curves of a graphene FET device before and after the deposition of (a) MBB-1 and (b) MBB-2. Adapted from Ref. [206] (c) Molecular structure of SP and MC isomers and STM of SP (left) and MC (right) isomers assemblies at the solid-liquid interface between HOPG and a SP/MC solution. (d) Transfer curves of a graphene FET with a drop of SP solution on top as deposited, after UV irradiation (MC form), and after thermal relaxation (SP form). (e) Schematic of the isomerization between the two forms SP (black) and MC (blue) and self-assembly process on the graphene FET. (f) Dynamic monitoring of I_{DS} (at $V_{GS} = 0$ V) before, during (in purple) and after UV irradiation. Adapted from Ref. [208]

Various other larger macromolecules such as polymers, including conductive ones like polyaniline, and biomolecules such as DNA have been combined with graphene by tailoring their interactions primarily *via* van der Waals forces, albeit other kinds of interactions could also be present. Assemblies of these macromolecules with graphene have been extensively studied by targeting at diverse applications in many different fields.[2, 15, 209] For instance, Choi *et al.*[210] reported a free-standing flexible conductive rGO/Nafion hybrid which was employed for the electrochemical sensing of organophosphate. The hybrid was formed by self-assembly of Nafion and rGO in solution, which was driven by the van der Waals

interaction and hydrophobic effect between the fluorinated alkyl chain of Nafion and rGO. The hydrophilic sulfonated part of Nafion guaranteed to the hybrid a high dispersibility in water. After filtering the resulting conductive hybrid paper was used as biosensing platform for organophosphate with high sensitivity and detection limit of 1.37×10^{-7} M. Bai *et al.*[211] produced a hybrid of rGO and sulfonated polyaniline (SPANI), by reducing GO in presence of SPANI. The hybrid was stably dispersed in water and, after deposition on a glassy carbon electrode, showed improved electrochemical stability and enhanced electrocatalytic activity. Wang *et al.*[212] fabricated a graphene/PANI hybrid paper *via in-situ* electropolymerization of PANI. The flexible and mechanically resistant hybrid paper was tested as a supercapacitor and exhibited a capacitance of 233 F g^{-1} and 135 F cm^{-3}. DNA has been used extensively to decorate graphene non-covalently.[209] DNA can interact with graphene and GO *via* van der Waals, π-π interactions and hydrogen bond formations. In 2009 Mann *et al.*[213] presented one of the first examples of hybrid DNA-rGO. They showed that the reduction of GO in presence of single strand DNA produced a hybrid structure which is highly dispersible in water, that self-assembled forming layered structures after solvent evaporation (**Figure 2.2-20** a). Liu *et al.*[214] reported a rGO/DNA/AuNPs hybrid structure. DNA strands terminated with a thiol group were self-assembled onto GO flakes, which were then reduced with hydrazine. The resulting hybrid rGO/DNA dispersions were highly stable in water and were used to selectively adsorb AuNPs thanks to the thiol groups, forming the hybrid rGO/DNA/AuNPs (**Figure 2.2-20** b-c). In 2010 Xu *et al.*[215] discovered that GO and DNA could self-assemble forming a stable hydrogel with high mechanical strength and environmental stability, high dye-adsorption capacity, and self-healing function. The hydrogel structure was formed by heating a water suspension of GO and double strand DNA: upon heating the DNA unwounded into a single strand form, cross-linking together the GO flakes *via* strong non-covalent interactions (**Figure 2.2-20** d-f).

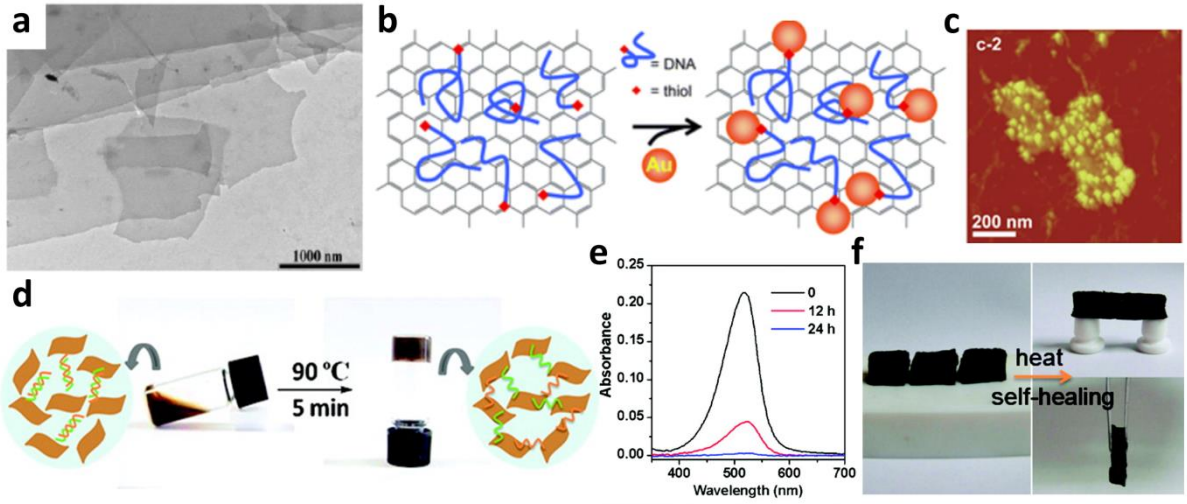

Figure 2.2-20: (a) TEM image of layered structure rGO-DNA. Adapted from Ref. [213] (b) Schematic of the self-assembled hybrid rGO/DNA-SH and selective adsorption of Au NPs. (c) AFM image of rGO/DNA-SH/Au NPs hybrid. Adapted from Ref. [214] (d) Schematic procedure of preparing GO/DNA self-assembled hydrogel and the proposed gelation mechanism. Absoprtion spectra of

a aqueous solution of safranine O after adsorption by GO/DNA hydrogel and (f) self-healing capability of the hydrogel. Adapted from Ref. [215]

As previously discussed, GO contains several oxygen-bearing functional groups, including carboxylic groups which donate to GO a negative charge, in fact, GO can be considered an anionic polyelectrolyte. For this reason, GO can form self-assembled structures *via* hydrogen bonds, yet more importantly via electrostatic and ionic interactions. These considerations are partially true also for rGO, which conserves part of the oxygen functionalities and thus part of the negative charge. Müllen and co-worker firstly exploited this effect in 2009 to assemble non-covalently functionalized GO and rGO dispersible in organic solvents such as chloroform[216]. They mixed a GO water suspension with positively charged quaternary ammonium salts with long alkyl chains. The amphiphilic molecules were self-assembled on the GO and rGO surface with the hydrophobic part oriented towards the water phase. Upon mixing the suspension with chloroform the hybrid was transferred to the organic phase (**Figure 2.2-21** a). The electrostatic interactions between GO/rGO and positively charged molecules have been extensively used to build self-assembled layer-by-layer (LbL) structures for disparate applications. Zhao *et al.*[217] reported a self-assembled LbL structure of alternating GO and PVA, obtained by soaking cyclically a substrate in a PVA and GO solution. The assembly in a layered structure was driven by the formation of hydrogen bonds between GO and PVA (**Figure 2.2-21** b). The composite exhibited a 98.7% improvement of elastic modulus and a 240.4% increase of hardness compared to PVA. Hu and Mi presented a membrane for forward osmosis composed by a LbL assembly *via* electrostatic interactions between GO and the positively charged poly(allylamine hydrochloride).[218] The membrane showed high permeability to water and ions, while it was impermeable to sucrose. In 2014 Zou and Kim[219] showed that the positively charged branched polyethyleneimine (PEI) dripped into a water suspension of GO induced the self-assembly of the latter in porous layered structures. The LbL assembly was driven by diffusion of PEI through the porous structure and by the electrostatic interaction between the two components and therefore could progress without additional external forces or stimuli. By adjusting the concentration of GO the researchers were able to obtain hollow spheres composed by the LbL assembly with diameters of several mm, that once analysed at SEM revealed a porous layered structure (**Figure 2.2-21** c-d). These beads showed efficacy in absorbing oil and exhibited electrical conductivity once reduced. LbL structures have also been employed for sensing. For example, Zhang *et al.*[220] fabricated a humidity sensor based on the LbL assembly of GO and the cationic polyelectrolyte poly(diallyldimethylammonium chloride) (PDDA). The nanostructured film was fabricated by immersing alternatively a substrate into PDDA and GO suspensions for five repetitive cycles, after which it was chemically reduced. The assembled device exhibited a 37% response passing from 0% RH to 97% RH and long-term stability over time.

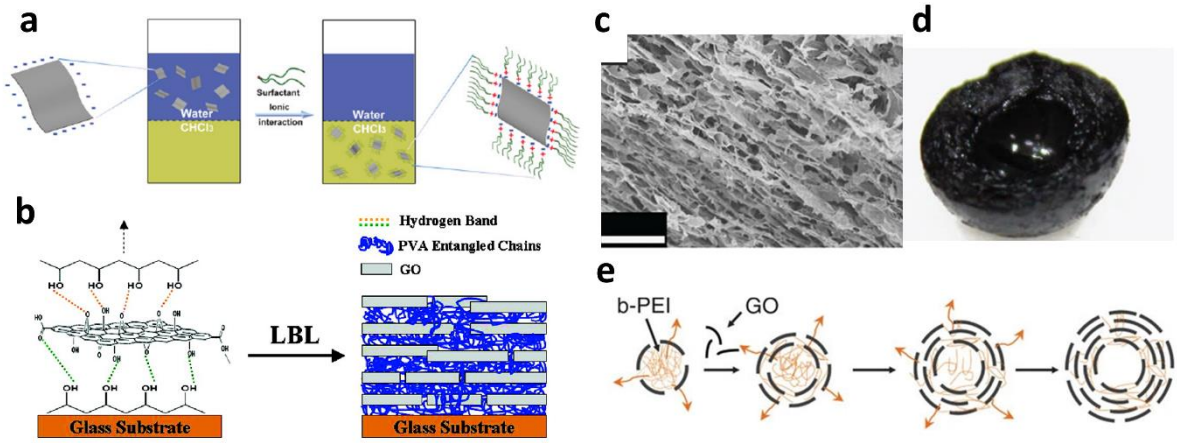

Figure 2.2-21: (a) Schematic of the self-assembly between negatively charged GO and positively charged quaternary ammonium salts, that make it soluble in chloroform. Adapted from Ref. [216] (b) Schematic of the LbL assembly between GO and PVA. Adapted from Ref. [217] (c) SEM image and (d) photograph of the self-assembled LbL GO/PEI porous layered structure and (e) schematic of the spontaneous formation of the structure. Adapted from Ref. [219]

2.3. Application of hybrid assembly based on graphene

2.3.1. Active materials

Graphene possesses some outstanding characteristics such as the enormous surface to volume ratio, electrical and thermal conductivity, and mechanical strength. Its combination with organic molecules or inorganic nanostructures is a powerful strategy to impart it additional functionalities, yielding functional hybrids which can be efficiently applied as the active material for numerous applications, including sensing of molecules and biosensing,[71] water purification and removal of contaminants,[71, 221] (photo)catalysis and water splitting[222] and biomedical applications.[223, 224]

For example, the use of the hydrophilic GO, or rGO functionalized with hydrophilic molecules to increase its dispersibility in water is of primary importance for applications in water purification and in biomedical applications since graphene need to be stable in biological fluids.[2, 15, 223] On the other hand, the aromatic core of rGO may be important in drug delivery systems, to adsorb non-covalently hydrophobic drugs *via* π-π stacking and van der Waals interactions.[225] Systems for the adsorption of water pollutant benefit also from the coupling with magnetic nanoparticles, such as Fe_2O_3, which facilitate the hybrid adsorbent separation from water.[65, 66] Furthermore, the same nanoparticle can also increase the adsorbing capacity of rGO/GO by increasing the surface area. Hybrids of graphene and quantum dots have been used in bioimaging and in photodynamic therapy exploiting the high photoluminescence of QDs.[226, 227] QDs and graphene hybrids have been also employed to build highly efficient photodetectors[228] and solar cells,[229] in which the QDs absorb the incident light and generate an exciton, and graphene contributes by efficiently separating

and collecting the photogenerated charges. Hybrids of graphene and NPs with catalytic activity, such as Pd, Pt, TiO_2 and MoS_2 have been successfully employed in (photo)catalysis and hydrogen generation. Also in this case, graphene contributes mainly by supporting and increasing the stability of the NPs and by separating and collecting the electrons. Specific molecular receptors attached to the graphene can enhance the sensitivity and selectivity of graphene-based chemical sensors.

In the following section, some of the most relevant applications of hybrid materials based on graphene in the fields of sensing, water purification, (photo)catalysis and water splitting, and biomedical applications are presented and discussed.

2.3.1.1. *Sensing materials*

One important field of application of graphene-based hybrid materials is chemical sensing, which is the sensing of (bio)molecules and metal ions. Other from chemical sensing, graphene-based hybrid materials have also been studied as sensors of the electromagnetic radiation (i.e. photodetectors) and sensors of physical properties (e.g. temperature and pressure sensors). Most of the sensing devices are electrical sensors, in which the quantity that is measured is commuted to a change in a measurable electrical quantity. The performances of a sensor are characterized by different figures of merit, among which the most important are the sensitivity, selectivity, limit of detection, hysteresis, and response time. The main advantages of using graphene as an electrical sensor are its high conductivity, its low intrinsic electrical noise,[230] that allows detecting minimal changes in the charge carrier density or electrical resistance, and its vast surface area, that allows maximizing the exposure to the sensed quantity.[71] Graphene, GO and rGO can be combined with molecules or nanostructures that act as specific receptors able to interact with the sensed analyte or physical quantity (e.g. absorbing a defined wavelength), thus increasing its sensitivity and selectivity toward the measured quantity. Besides, the hybrids based on graphene typically exhibit significantly increased porosity compared to films of pristine graphene, which results in an enhanced accessible surface area.

Chemical sensing

Gas sensors play an important role in many industrial sectors, in environmental monitoring and personal safety. In an effort to improve the sensitivity and selectivity of gas sensors and reduce their consumption and cost, graphene-based hybrid materials are emerging as alternatives to current technological applications based mainly on metal oxides and inorganic semiconductors.[231] For example, metallic nanoparticles (NPs) can enhance the sensitivity and selectivity to the sensed analytes due to specific catalytic effects. [71] Li *et al.*[57] fabricated a NO sensor based on reduced GO decorated with Pd NPs. This device exhibited high sensitivity with an impressive limit of detection of 2 ppb, which is notably higher than

that of the reference device assembled without decorated rGO. GO decorated with Pt NPs[55] and CVD graphene decorated with Pd NPs[56] have been used to sense hydrogen gas, by taking advantage of the high affinity of hydrogen towards these noble metals. An assembly of sulfonated rGO and Ag NPs was used to Huang et al to sense NO_2. [58] The Ag NPs were reduced *in situ* on the rGO surface (**Figure 2.3-1** a-b). This sensor displayed a 74.6% fast response to 50 ppm of NO_2 (**Figure 2.3-1** c). GO and rGO decorated with metal oxides such as ZnO, SnO_2, In_2O_3, and Cu_2O nanoparticles, nanorods and nanocrystals have also been used in the sensing of gases such as NO_2, [18, 21, 232] NH_3, [61] H_2S, [60, 107] CO[61]. For example, Liu *et al.*[18] fabricated a hybrid of rGO and flower-like In_2O_3 nanocrystals *via* a facile one-step hydrothermal method and used it to sense NO_2 (**Figure 2.3-1** d). This rGO-In_2O_3 composite showed enhanced sensing performance towards in comparison with the pure In_2O_3 sample, with a detection limit of 10 ppb (**Figure 2.3-1** e).

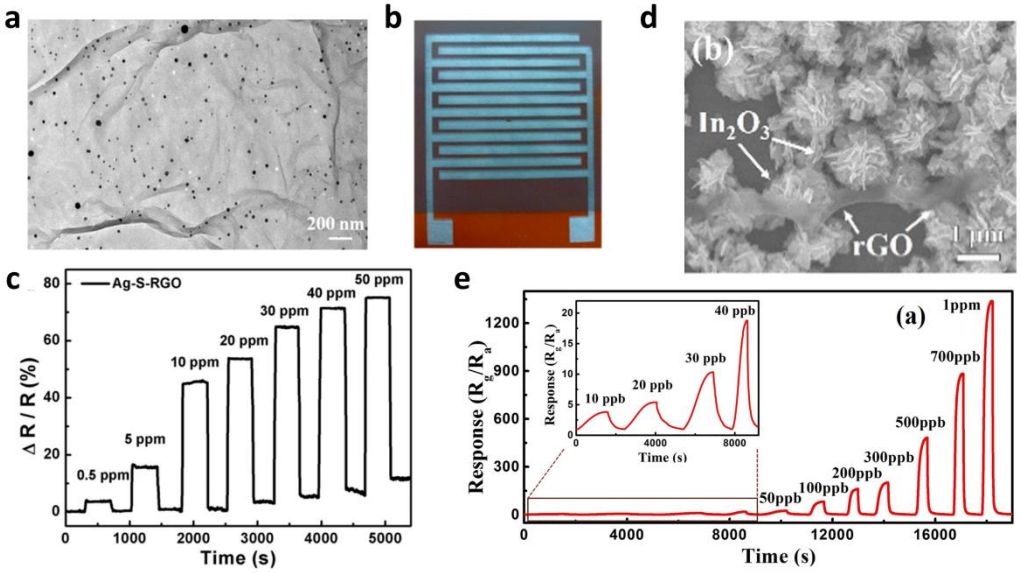

Figure 2.3-1: (a) Transmission electron microscopy (TEM) image of sulfonated rGO/Ag NPs and (b) photograph of the sensing device. (c) Response of the s-rGO/Ag NPs sensor as a function of time in various concentrations of NO2 gas. Adapted from ref. [58] (d) SEM of rGO-In_2O_3 hybrid. e) Response of the rGO-In_2O_3 hybrid to various concentrations of NO_2 . Adapted from Ref. [18]

In order to target specifically the sensed gases, GO and rGO have also been functionalized covalently or non-covalently with polymers and molecules exhibiting specific functional groups. Assemblies with polymers may also contribute to increased porosity. For example, Al-Mashat and collaborators [233] reported a hydrogen sensor based on an assembly of polyaniline (PANI) adsorbed on the rGO surface, synthesized by *in-situ* polymerization of aniline selectively on rGO surface. The hybrid rGO/PANI displayed a 16.6 % response to 1 % H_2 gas, which was better compared to pure rGO and PANI (**Figure 2.3-2** a-b). An assembly of rGO and PANI has been used also to sense NH_3.[234] Conductive polymers have also been used to assemble with GO gas-sensitive conductive hydrogels by Shi and co-workers. [235] In particular, hydrogels of GO/polypyrrole (PPy), GO/PEDOT, and GO/PANI were fabricated

by *in-situ* chemical polymerization of the corresponding monomers in aqueous dispersions of GO. The GO/PPy gel in particular, once lyophilized, exhibited a good sensitivity to NH_3 gas. LbL assembly of GO with charged polyelectrolytes have also been used for gas sensing; for example, Zhang and co-workers [220] developed a flexible, resistive-type humidity sensor based on the LbL assembly of GO and poly(diallyldimethylammonium chloride) (PDDA). After the alternate deposition of GO and PDDA for 5 consecutive cycles on interdigitated electrodes, the assembly was chemically reduced by HBr and used to sense moisture. The device exhibited a 37 % response (from 0 % RH to 97 % RH), excellent linearity and a long stability over time (**Figure 2.3-2** c-e). Chemically modified GO/rGO decorated with small functional molecules has also been used for gas sensing. In particular, the choice of functional units allows adjusting the sensitivity to specific gases, as Jelinek *et al.*[172] showed recently in their work, in which they combined in a given sensors array three different porous GO functionalized with different dangling units (phenyl-GO, ethanol-GO and dodecyl-GO). The different response to different vapours of the 3 materials allowed the sensor to discern between water, NH_3, toluene, EtOH, phenol and cyclohexane.

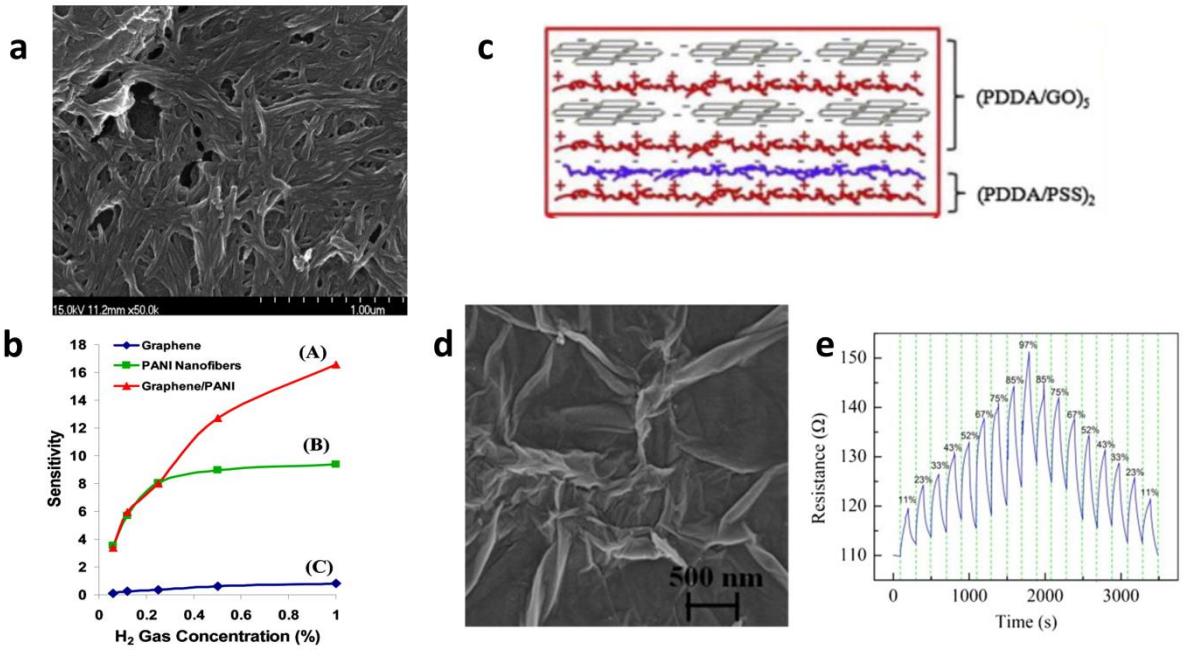

Figure 2.3-2: (a) SEM of rGO-PANI hybrid. b) Sensitivity of the rGO, rGO-PANI, and PANI sensors to different H_2 concentrations. Adapted from Ref. [233]Schematic (c) and SEM (d) of the PDDA/GO LbL assembly. (e) Resistance of the PDDA/GO sensor as a function of time at different RH %. Adapted from Ref. [220]

Graphene-based hybrid materials have also been used for the sensing of metal ions. These sensors rely on different mechanisms of detections: electrical sensors such as resistive sensors, field-effect transistor (FET) based sensors and electrochemical sensors are the most diffused, however, fluorescence-based sensors have also been developed. In FET based sensors usually, the metal ions are adsorbed by the functional molecules or nanostructures that compose the hybrid and provoke a change in the Dirac point or carrier mobility of

graphene metal, which is detected as a change in one of the FET characteristics such as the field-effect mobility, threshold voltage and I_{on}/I_{off} ratio. In a typical example, Zhang *et al.*[236] reported the sensing of Hg^{2+} with a FET based on mechanically exfoliated graphene functionalized with SAM of 1-octadecanethiol. The sensing of Hg^{2+} was detected as a shift in the Dirac point, and the detection limit was 10 ppm of Hg^{2+}. Furthermore, they observed from AFM images of the sensor an increase in the height of 1.6 nm after the adsorption of Hg^{2+} by the thiol groups (**Figure 2.3-3** a-b). For the detection of heavy metal ions, hybrids of graphene with biomolecules are commonly used thanks to the high binding affinity of the last to inorganic contaminants. Sudibya *et al.*[237] presented a FET sensor based on a micro-patterned film of rGO functionalized *via* pyrene linkers with metal binding metallothionein type II protein for the selective recognition of Hg^{2+} and Cd^{2+}. The high affinity of the protein for these two metals allowed the sensor to detect concentrations of Hg^{2+} and Cd^{2+} as low as 1nM. An *et al.* [238] reported a flexible device based on CVD graphene functionalized non-covalently with an aptamer for detection of Hg^{2+}. In particular, the aptamer was covalently bonded to a linker comprising a naphthalene unit attached *via* π-π stacking to graphene. The graphene/aptamer hybrid was contacted with gold electrodes and used as liquid-ion gated FET sensor that was able to detect selectively Hg^{2+} ions with an extremely low detection limit of 10 pM (**Figure 2.3-3** c-e). Graphene-aptamer complexes have also been used as fluorescent probes for the detection of metal ions, in which graphene acts by quenching the emission of a fluorophore. In other cases, GO itself may act as a fluorophore whose emission is quenched by the presence of the metal. For example, Li *et al.*[239] fabricated a fluorescence probe Hg^{2+} ions based on a supramolecular assembly between GO and single-stranded DNA (ssDNA) aptamer. The GO/ssDNA assembly is dispersed in solution and exhibits strong fluorescence emission of GO at 600 nm; in presence of Hg^{2+} ions, the ssDNA folds to form double-stranded DNA complexed with the metal ions, which quenches the emission of GO. An assembly of GO and a short ssDNA fragment has been used by Wen *et al.* [240] to sense Ag^{+} ions. In this case, a ssDNA with high affinity for Ag^{+} ions was used. The DNA bears attached a fluorescein molecule and is non-covalently adsorbed on GO, which quenches the fluorescence of fluorescein. In presence of Ag^{+} the DNA folds to complex the metal ions and is released from the GO surface, in this way the fluorescence of fluorescein is restored. This sensor showed very high selectivity to Ag^{+} versus 12 different interfering metal ions.

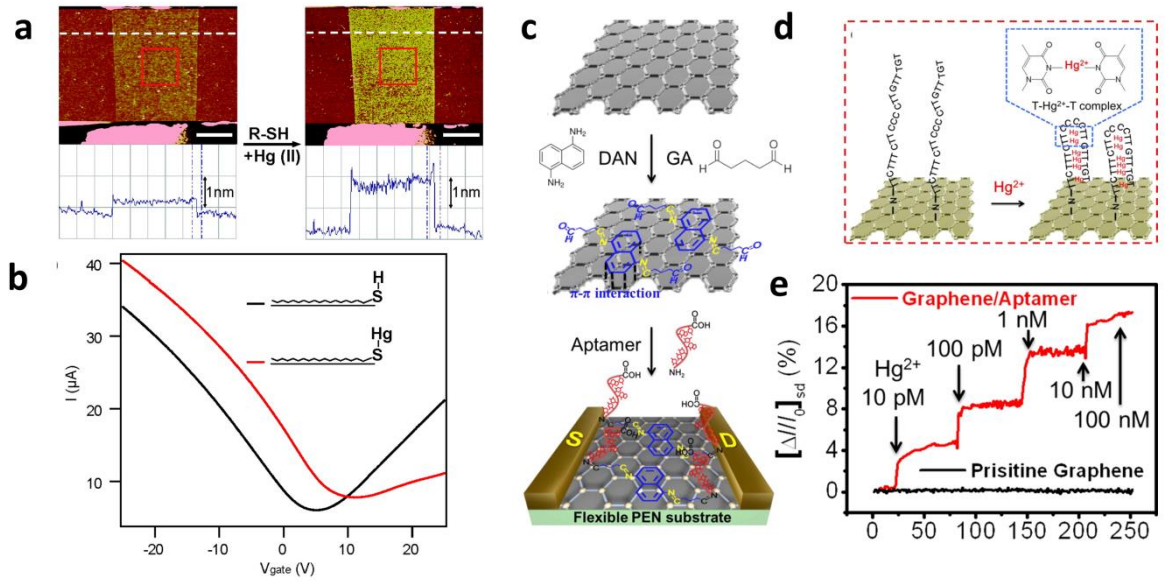

Figure 2.3-3: (a) AFM and height profiles of the mechanically exfoliated graphene functionalized with SAM of 1-octadecanethiol before (left) and after (right) the adsorption of Hg^{2+}. (b) Transfer characteristic of the assembled FET device before (red) and after (black) Hg^{2+}adsorption. Adapted from Ref. [236] (c) Schematic of the assembly steps of the CVD graphene/DNA aptamer device. (d) Schematic of the selective binding of the aptamer to Hg^{2+}. (e) Real-time responses (%) of the CVD graphene/aptamer device (red) and CVD graphene only (black) to various Hg^{2+} concentrations. Adapted from Ref. [238]

Fluorescence sensors have also been used to sense biomolecules, such as DNA. Dong and co-workers [73] realized a quantum dots (QDs)/GO hybrid capable to detect specific DNA fragments. The QDs are functionalized with a molecular beacon (MB) complementary to the target DNA. In absence of the analyte, the QDs are adsorbed on the GO surface by van der Waals interactions between the MB and GO and their fluorescence is quenched. In presence of the target DNA, the MB links it and straightens, bringing the QD far from the surface of GO and restoring its fluorescence. In addition to fluorescence sensors, biomolecules and organic molecules have been detected by FET sensors and electrochemical sensors. For example, a FET sensor for target DNA fragments was produced by the non-covalent functionalization of rGO with a peptide nucleic acid. The highly specific interaction of the peptide nucleic acid with the complementary DNA strand caused a shift in the transfer characteristic curve of the FET; the sensor had a detection limit of 0.1 pM.

Electrochemical sensors are powerful tools for the selective determinations of molecules and ions in solution. In fact, the different molecules can be selectively detected by their different reduction and oxidation potentials. Graphene hybrid materials are used as free-standing electrodes or deposited on another electrode. The advantage of using graphene is its high surface area, that allows for efficient adsorption of the analyte, its low charge transfer resistance and relatively wide potential window.[71] The sensitivity and selectivity of graphene can be enhanced by combining it with functional molecules or nanostructures. For instance, Guo et al.[241] reported a one-step, microwave-assisted fabrication of Pt NPs

functionalized rGO for sensing H_2O_2 and the explosive trinitrotoluene (TNT). The hybrid material was deposited on a glassy carbon electrode (GCE) and used to sense various analytes by cyclic voltammetry. In particular, the modified electrode showed much higher current densities and sensitivities compared to the bare GCE and exhibited particular catalytic activity towards H_2O_2 and TNT which were detected in concentrations as low as 80 nM and 1.3 μm respectively. Luo et al.[242] reported a rGO/Cu NPs modified GCE for the determination of glucose. The increased catalytic activity of this modified electrode allowed detecting glucose in a concentration of 0.5 μM.

2.3.1.2. *Water purification*

The availability of potable water for the entire world population, which is constantly growing, has become a major concern in recent years. The scientific community is called to the challenge of developing new, more efficient technologies for the desalination of seawater and the removal of metallic and organic pollutants from freshwater. Graphene, and in particular GO and rGO, have found promising applications as membranes for the desalination of water and as adsorbents for pollutants. One of the most employed technologies for water desalination is reverse osmosis and graphene may contribute to the construction of more efficient semipermeable membranes. Graphene has the unique property of being extremely thin, yet being impermeable to the passage of even the smallest molecule,[26] nonetheless the creation of nanopores in the graphene structure may allow the selective permeability to water.[243, 244] While several methods to achieve the formation of nanopores of controlled size in graphene layers have already been developed, large continuous layers of graphene are still too expensive to be implemented into commercial products.[245] A more affordable and achievable alternative is the use of multilayer stacks of GO/rGO flakes, which can form mechanically strong membranes semipermeable to water.[221, 246, 247] In these, water molecules can pass through the narrow hydrophobic channels formed by the unoxidized regions of GO.[200] The rejection of ions or bigger molecules takes place mainly for size exclusion since these cannot pass between the stacked GO flakes, yet anions can also be rejected by electrostatic interactions.[248] However, over time GO membranes tend to lose the semipermeability because the interlayer spacing between flakes increases.[249] On the other hand, rGO membranes have higher stability but the narrower channels decrease also the permeability to water. The selective permeability to water and the stability of GO/rGO membrane can be enhanced by combining GO with molecules or nanostructures that can increase the strength of the membrane by connecting together the different flakes and tune the size of the channels, thus permitting a higher flux of water and rejection of other molecules and ions. For example, Hu and Mi presented a membrane of stacked GO flakes, assembled by LbL procedure in which the flakes were cross-linked by 1,3,5-benzenetricarbonyl trichloride (TMC) (**Figure 2.3-4** a).[250] The cross-linking of GO flakes not only increased the stability of the membrane against dissolution in water but also tuned the spacing between the flakes. The membrane exhibited a water flux up to 10 times higher

than that of common commercial nanofiltration membranes, and 95 % rejection of Rhodamine-WT, however, the rejection of salt was low (**Figure 2.3-4** b-c). Endo *et al.* [250]presented a selective water permeable membrane produced by spray-coating water dispersions of GO, few-layer graphene flakes and deoxycholate onto a porous polysulfone support. The assembly was then cross-linked by Ca^{2+} ions. They showed that the insertion of deoxycholate in the structure allowed increasing the interlayer distances, the filtration performances and the rejection of NaCl. This membrane was robust enough to withstand 120 h of cross-flow shear and exhibited a NaCl rejection of 85% and 96% for an anionic dye. The interlayer distance in the membrane can be engineered by introducing nanostructures such as CNTs or nanosheets. Recently Hiu *et al.*[251] fabricated a hybrid GO/laponite flakes layered membrane for the selective permeation. The strength of the membrane was assured by the strong electrostatic interaction between the negative GO and the positive laponite nanosheet. The membrane showed an efficient rejection of basic fuchsin and brilliant yellow dyes. Gao *et al.*[252] produced a 40 nm thick membrane composed by GO intercalated by single-walled carbon nanotubes (SWCNTs) that exhibited a water permeation of 660–720 L m^{-2} h^{-1} bar^{-1} and a rejection > 97 % for molecules bigger than 1.8 nm (**Figure 2.3-4** d-f). Similarly, Han et al.[253] prepared a hybrid multilayer assembly of rGO and multiwalled carbon nanotubes (MWCNTs), in which MWCNTs act as spacers between the rGO flakes. The hybrid membrane showed a water flux up to 11.3 L m^{-2} h^{-1} bar^{-1}, almost double of that of rGO alone, high dye rejection (>99% for Direct Yellow and >96% Methyl Orange) and moderate salt rejection (51.4% for NaCl). Sun *et al.*[254] fabricated a layer stacked membrane of GO and ZnO NPs whose interlayer spacing could be finely adjusted by partial reduction of GO *via* UV-irradiation. The addition of ZnO NPs to GO allowed increasing 5 times the permeability to water, while maintaining unaltered the rejection of organic dyes (98.4 %) and enhancing the antibacterial properties.

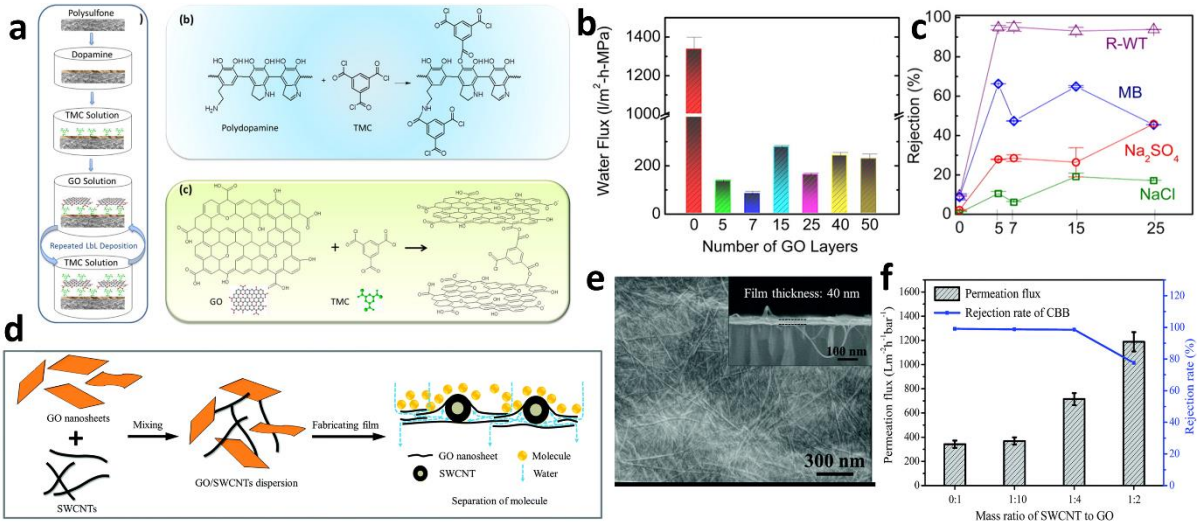

Figure 2.3-4: (a) Schematic representation of the LbL assembly between GO and TMC anchored at the polysulfone substrate by polydopamine. (b) Water permeation of the GO/TMC LbL structure and (c) Rejection in % of the reported salts and dyes as a function of the number of layers.

Adapted from Ref. [250] (d) Schematic representation of the fabrication of the hybrid GO/SWCNTs and (b) SEM image of the hybrid (cross-section in the inset). (f) Permeability to water and rejection rate of Coomassie Brilliant Blue (CBB) as a function of the mass ration between SWCNTs and GO. Adapted from Ref. [252]

In addition to the insufficient availability of freshwater, water pollution by heavy metals and organic pollutants represent two other major problems brought into play by the population growth and the increasing use of land by humans. Water purification through removal of the pollutant can be accomplished by using adsorbents that sequestrate the pollutant *via* non-covalent interactions. Adsorption depends on several parameters, such as pH, temperature and concentration of the pollutant, and on the nature of the adsorbent. Graphene and graphene oxide have promising application as adsorbent mainly thanks to their large surface area and porosity.[66] In particular, the lipophilicity of graphene (and rGO) and its conjugated structures make them good adsorbents for aromatic and hydrophobic molecules, while the hydrophilicity and the numerous oxygen functional groups make GO a good adsorbent for ionic species. The functionalization of these materials with molecules or nanomaterials increases the surface area for adsorption, prevents the aggregation of the graphene/GO flakes that would result in a decrease of the adsorbing surface, and makes the adsorption more selective.[66, 71] Nanomaterials, and nanoparticles, in particular, have been used for adsorbing pollutant for their small size, large surface area and catalytic activity. However, their tendency to aggregate reduces the active adsorption sites. The formation of hybrid assembly with graphene hinders the aggregation of both nanoparticles and graphene and contributes to a large increase in the adsorbing capabilities. Moreover, if magnetic NPs are used, they facilitate the separation of the adsorbent from water by means of a magnetic field. In 2010 Chandra *et al.*[67] fabricated a hybrid rGO/Fe_3O_4 magnetic NPs for the efficient removal of As(II) and As (V) (99% removal). The hybrid was synthesized by *in situ* simultaneous reduction of GO and Fe(II/III) precursors and exhibited uniformly distributed magnetite NPs on the rGO surface. The magnetic behaviour of the hybrid allowed for a simple separation from water (**Figure 2.3-5** a-b). Following this work other papers based on assemblies of GO and rGO with iron-based magnetic nanoparticles have been presented, for increasing the adsorption efficiency of As(III/V) (e.g. by increasing the pH range of adsorption)[255, 256] and for adsorbing other heavy metals such as Pb(II)[70, 257], Cr(VI)[68, 257, 258], Hg(II)[257]. In some cases, the magnetic nanoparticles have shown also efficient catalytic activity towards the reduction or oxidation of the metal ions to less toxic forms, for instance from Cr(VI) to Cr(III).[258] As aforementioned, GO is a better adsorbent for heavy metal cations than rGO, because of its negative charge and the presence of oxygen atoms that can coordinate the metals. Yang et *al.*[70] decorated both GO and rGO with magnetic iron oxide NPs and demonstrated that the GO hybrid was a good adsorbent for Pb(II), but not for 1-naphthol and 1-naphthylamine, while the rGO based hybrid behaved oppositely. In addition to nanoparticles, GO and rGO functionalized with organic molecules and polymers have also found applications as adsorbents for metal ions and organic pollutants with

increased adsorption capabilities and selectivity. Polymers with heterocyclic units such as polypyrrole (PPy) and polythiophene have heteroatoms that can coordinate cations, which make them good adsorbent for metal ions. Chandra and Kim[259] prepared a highly porous structure of rGO functionalized with PPy *via* non-covalent interactions. This hybrid showed highly selective Hg(II) removal from water (**Figure 2.3-5** c-d). A hybrid of rGO and PPy was used by Li *et al.*[260] for the removal of Cr(VI). In this case, the porosity was increased by templating the polymer over a MnO_2 scaffold. Chitosan is another polymer with many coordinating groups that can form supramolecular assemblies with GO. Li *et al.*[261] prepared an assembly of GO, chitosan and magnetic cyclodextrin containing a Fe_3O_4 core and used it for the adsorption of Pb(II). Zhang *et al.*[262] synthesized a biodegradable, highly porous hydrogel of chitosan and GO for the adsorption of heavy metal from aqueous solutions. Shahzad *et al.*[263] synthesized a hybrid assembly of GO and EDTA-functionalized magnetic chitosan that exhibited maximum adsorption capacity 206.5 mg/g for Pb^{2+} and 207.2 for Cu^{2}.

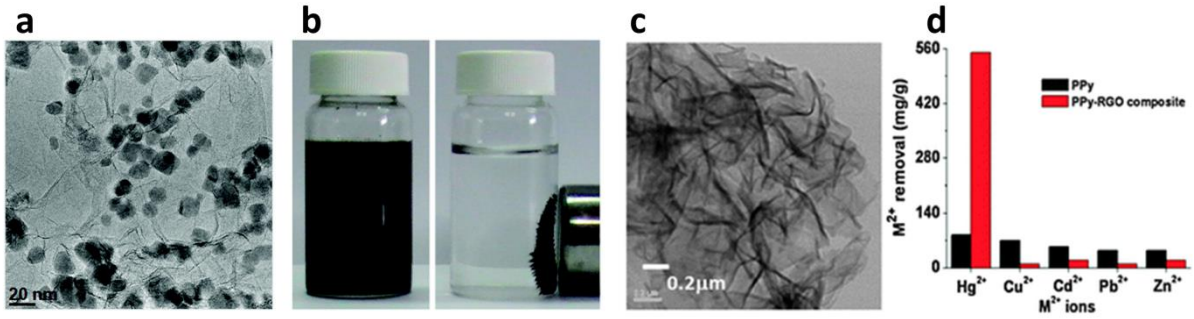

Figure 2.3-5: (a) TEM image of the Fe_3O_4 NPs/rGO hybrid and (b) magnetic separation of the adsorbent from solution. Adapted from Ref. [67] (c) TEM image of the PPy/rGO hybrid. (d) Maximum adsorption capacity of various metal ions from aqueous solution using the PPy/rGO hybrid showing the high selectivity towards Hg(II). Adapted from Ref. [259]

Hybrid of GO and rGO have also been successfully employed as adsorbents for organic pollutants, e.g. dyes, polycyclic aromatic and halogenated organic compounds, oils, and gasoline. Also in this case, magnetic hybrids have been largely investigated for the easier separation from water of the exhausted adsorbent. Different groups have synthesized hybrids of rGO and magnetic nanoparticles of Fe_3O_4, Fe or Ni *via in-situ* deposition methods and have used them to absorb various aromatic dyes and gasoline.[66] Fan *et al.*[264] fabricated a magnetic chitosan GO hybrid and used it for the adsorption of methyl blue. The hybrid was synthesised by first coating Fe_3O_4 NPs with chitosan, cross-linked by glutaraldehyde, and then grafted by covalent and non-covalent interactions to GO flakes. In this case, the adsorbing performances were greatly enhanced by the presence of chitosan, which can form ionic interactions between its amino groups and the negatively charged methyl blue. Instead of using dispersions of the hybrid adsorbent, which then need to be separated from water, another strategy consists in the use of monolithic sponge-like hybrids in form of foams or aerogels with high porosity that can be easily removed from water after the adsorption. These sponge-like hybrids are particularly useful to remove large quantities of spilt oils since

when the oil is charged in the pores of the foam is retained there by hydrophobic effect. For instance, Dong *et al.*[265] fabricated a hybrid foam of CVD graphene/CNTs in which the CNTs grown over the graphene surface have the function of enhancing the hydrophobicity of the hybrid forming a nanostructured rough surface (**Figure 2.3-6** a-c). The hybrid was formed by CVD deposition of graphene over a Ni foam template, followed by the CVD deposition of CNTs and dissolution of the Ni scaffold. The ultralight resulting foam exhibited a high adsorption capacity of different oils and organic solvents between the 80 and 130 times the weight of the dry foam, and good recyclability (**Figure 2.3-6** d). Shi and co-workers[266] prepared a rGO/TiO_2 nano-needles hybrid by a hydrothermal method starting from GO and commercial TiO_2 NPs. The hybrid resulted in a highly porous structure with a good adsorption capacity of methylene blue (83 mg/g). Li *et al.*[267] prepared a mesoporous hybrid of rGO coated by $Mg(OH)_2$ *via* hydrothermal method and demonstrated its adsorption capabilities towards methylene blue.

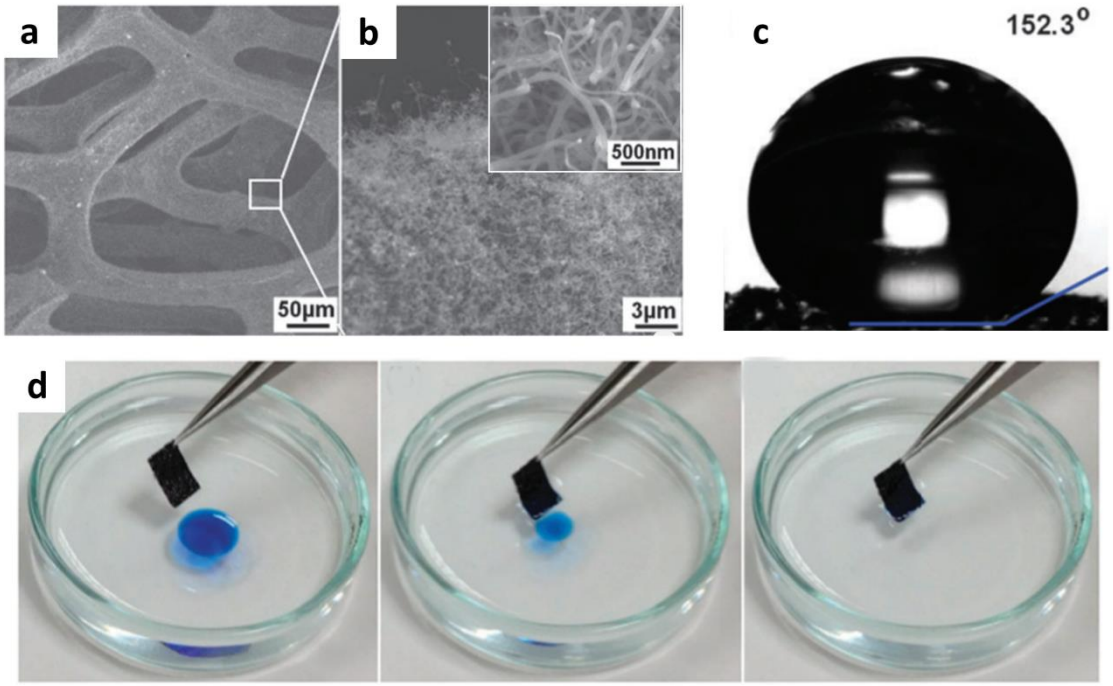

Figure 2.3-6: (a-b) SEM images of CVD graphene/CNT hybrid foam with different magnifications. (c) Water contact angle of the CVD graphene/CNT hybrid foam (the water contact Angle of the graphene foam without CNTs is 108.5 °). (d) Photographs of the removal of a toluene droplet from water using the graphene/CNT hybrid foam. Adapted from Ref. [265]

2.3.1.3. *Catalysis, Photocatalysis and water splitting*

Hybrid assemblies based on graphene can be used as catalysts, to increase the rate of several reactions, and as photocatalysts. In particular, in photocatalysis the catalyst is usually a semiconductor which absorbs light, producing an exciton, in which one electron is excited from the valence band to the conduction band, that can then reduce or oxidize another molecule by donating to it one electron or hole (**Figure 2.3-7** a). The term photocatalysis can

also include the use of a molecule, called photosensitizer, which adsorbs light forming an excited state that can either transfer the energy to another molecule, which is, in turn, excited or can react by oxidizing or reducing another molecule. Photocatalysis can be used to split water and produce oxygen and hydrogen in the processes that are referred to as oxygen evolution reaction (OER) and hydrogen evolution reaction (HER). Furthermore, photocatalysis can also be used to degrade pollutant in water by the formation of highly reactive radicals (such as •OH and O_2^-•). An electrocatalyst instead is a catalyst used to increase the rate and reduce the overpotential of electrochemical reactions, in galvanic cells and electrolytic cells. Electrocatalysts are used in fuel cells, for the oxygen reduction reaction (ORR) and hydrogen oxidation reaction (HOR). Pristine graphene is inert and has low catalytic activity. However, the chemical modification of graphene and the combination with nanostructures can greatly enhance its catalytic activity.[268] Graphene can be combined with NPs or other nanostructures of materials that are commonly used for their catalytic activity, such as noble metals, transition metal oxides (TiO_2, Co_3O_4, MnO_2, Mn_3O_4, etc..), transition metals chalcogenides (CdS, ZnS_2, Co_3S_4, MoS_2, etc.) and nitrides, and greatly enhance their catalytic performances.[268, 269] Graphene can offer a large area where the catalytic nanostructures can uniformly distribute, preventing their aggregation. Moreover, the electrical and mechanical properties of graphene confer to the hybrid electrical conductivity, with enhanced charge separation, increased mechanical strength, thermal and chemical stability. Graphene itself can become a good catalyst after the substitutional doping with nitrogen atoms, especially as electrocatalyst for ORR.[270]

The most investigated hybrid of graphene for catalytic applications comprises TiO_2 NPs. TiO_2 in fact is one of the prototypical materials used in photocatalysis for its superior photocatalytic properties, low cost, high availability, stability, and nontoxicity. Several synthetic techniques have been employed to prepare TiO_2/graphene hybrids, which include UV-assisted photoreduction, sol−gel, hydro/solvothermal, and self-assembling methods. Most frequently, GO is used because of its low cost, easy processability and dispersibility in water. The same TiO_2 nanoparticles can catalyse its photoreduction to rGO.[271] For instance, Zhang *et al.*[272] prepared a rGO/TiO_2 nanocomposite for photocatalytic HER. The hybrid, containing just 5% of rGO, exhibited an evolution of H_2 almost two times higher than commercial standard TiO_2 P25. The enhancement was primarily due to the conductivity of the rGO substrate, which collects the electrons and lowers the charge-recombination rate. Xiang *et al.*[273] prepared a rGO/TiO_2 nanosheets hybrid *via* a microwave-assisted hydrothermal method for the photocatalytic HER using methanol as sacrificial reagent (**Figure 2.3-7** a-b). The hybrid with 1 % of rGO showed a H_2 production rate of 736 $\mu mol/h^{-1}g^{-1}$, 41 times superior to the pure TiO_2 nanosheets. Hybrids of rGO and TiO_2 have also been extensively investigated for the photocatalytic degradation of organic pollutants.[274-277] The potential of rGO/TiO_2 hybrids for the degradation of organic pollutants was shown in 2009 by Zhang et al.[274], who presented a hybrid of rGO and commercial TiO_2 P25 NPs synthesized *via* hydrothermal method that could efficiently adsorb methylene blue from

water and then photo-degrading it under visible light irradiation. The efficiency of photocatalysis was 4.3 times higher than P25 alone. These performances were overtaken 3 years later by Lee et al. [275] who prepared crystalline TiO_2 NPs wrapped into rGO sheets. The material was prepared by one-step hydrothermal reduction of GO and phase change from amorphous TiO_2 to crystalline (**Figure 2.3-7** c). The band-gap of TiO_2 in the hybrid was significantly reduced to 2.8 eV and the efficiency of photocatalysis of the hybrid towards the degradation of methylene blue was 13 times higher than P25 NPs (**Figure 2.3-7**).

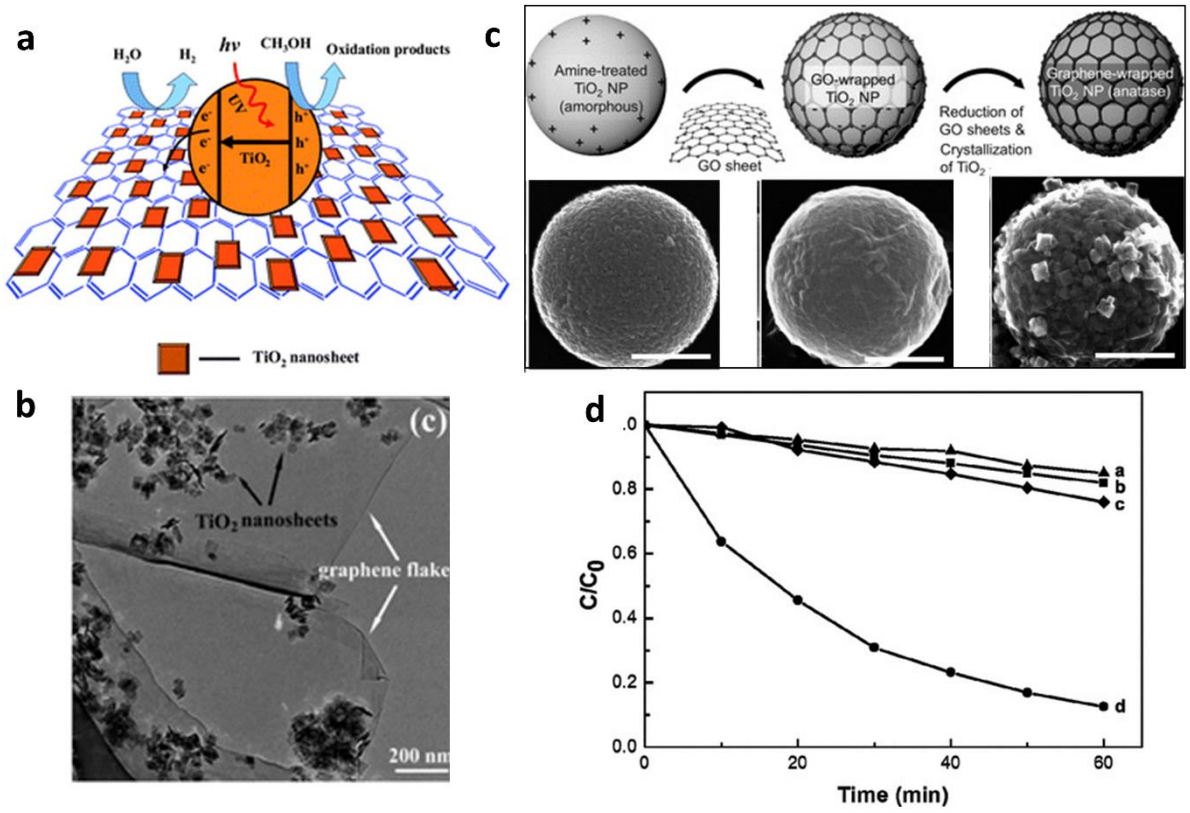

Figure 2.3-7: (a) Schematic illustration for the charge transfer and separation in the rGO/ TiO_2nanosheets hybrid under UV light irradiation; (b) TEM image of the hybrid. Adapted from Ref. [273] (c) Schematic illustration of synthesis steps for rGO-wrapped crystalline TiO_2 NPs and corresponding SEM images. (d) Photodegradation of methylene blue under visible light by (a) P25, (b) bare anatase TiO_2 NPs, (c) rGO/TiO_2 NPs (two-step hydrothermal), and (d) rGO/ crystalline TiO_2 NPs. Adapted from Ref. [275]

Hybrids of graphene with noble metals, transition metals and metal oxides are largely employed for electrocatalysis. In particular, Pt is the most used catalyst in fuel cells; however, it suffers from various drawbacks, including its low durability.[268] The combination of Pt with graphene can greatly enhance performances and durability of Pt electrocatalysts. Yoo and co-workers[278] found out that the deposition of Pt on rGO nanosheets produced nanoclusters of Pt below 0.5 nm. The nanostructuration of Pt modified its electronic structures producing a great enhancement in the electro-oxidation of methanol. Wan *et al.*[279] developed *in situ* preparation of rGO decorated with hollow Pt nanocrystals. Also in this

case, the synergic integration of Pt with rGO, and the nanostructuration provoked an enhancement in the electro-oxidation of methanol. The nanostructuration can be obtained by using templates. Tiwari *et al.*[280, 281] showed that the deposition of Pt onto rGO could be templated by ssDNA. Depending on the Pt salt precursor used both Pt nanoclusters (~1 nm) and Pt nanodendrites could be deposited (**Figure 2.3-8** a). The synthesized Pt/ssDNA/rGO hybrids displayed very high catalytic activities towards the ORR, outdoing a Pt/C commercial catalyst. Furthermore, the hybrid catalyst was stable in a wide range of pH (1-13) and presented impressive durability and stability (95 % of performances after 10000 cycles) (**Figure 2.3-8** b-c). Since Pt is highly expensive, alternative catalysts based on cheaper transition metals and metal oxides have been developed, and their combination with graphene showed promising enhancement of their performances. For instance, Co_3O_4 alone displays low catalytic activity towards ORR and OER. Dan *et al.*[282] fabricated a hybrid of amine doped rGO and Co_3O_4 NPs (**Figure 2.3-8** d). The synergic combination of the two materials produced a great enhancement in ORR and OER compared to the single component and to Pt/C catalyst. Furthermore, compared to Pt/C, the hybrid catalyst showed higher durability and stability in alkaline media (**Figure 2.3-8** e).

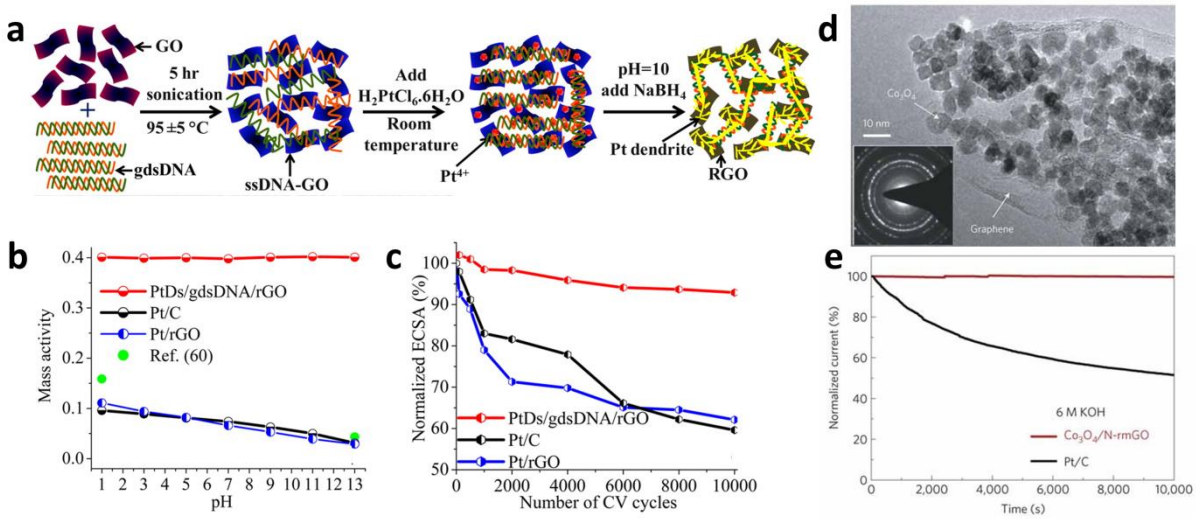

Figure 2.3-8: (a) Schematic of the synthesis of rGO/Pt Nanodendrites hybrid. (b) Mass activity of the catalysts reported in O_2-saturated solutions of various pH. (c) Electrochemically active surface area (EASA) loss for the catalysts reported, in O_2-saturated 0.1 M $HClO_4$ solution with a cyclic potential scan between 0.6 and 1.2 V at a scan rate of 50 mV/s. Adapted from Ref. [280] (d) TEM image of the N doped rGO/Co_3O_4 NPs hybrid. (e) Chronoamperometric responses of N doped rGO/Co_3O_4 NPs hybrid and Pt/C on carbon fibre paper electrodes kept at 0.70 V versus RHE in O_2-saturated 6 M KOH electrolyte. Adapted from Ref. [282]

Hybrids of graphene with TMDs have also exhibited catalytical activity and showed promising application for substituting Pt in HER. For example, Li et al.[283] reported a hybrid of rGO sheets decorated with MoS_2 NPs, synthesized through a one-step solvothermal reaction in dimethylformamide, using $(NH_4)_2MoS_4$ as MoS_2 precursor. The hybrid displayed excellent catalytic activity towards HER, being far superior to that of the single components

and similar to that of platinum (Figure 2.3-9 a-c). The high performance was attributed to the strong electronic coupling between the MoS_2 NPs and rGO. Zheng *et al.*[284] presented a hybrid rGO decorated with MoS_2 nanosheets, synthesized *via* solvent-evaporation-assisted intercalation of MoS_2 precursor in graphite oxide, followed by the exfoliation and reduction. The formation of MoS_2 nanosheets was templated by the narrow space existing between the graphite oxide layers. The hybrid exhibited excellent HER activity with small onset overpotential of 140 mV (Figure 2.3-9 d-f). These performances were attributed to the nanostructuration of MoS_2 with abundance of exposed active edge sites and to the excellent electrical conductivity of rGO. Van der Waals vertical heterostructures of MoS_2 and graphene, produced by CVD, have also displayed excellent performances in photocatalytic HER.[285] Different stacks were studied and the bilayer stack with graphene on top of MoS_2 showed the highest photoresponse with large reaction current density and lowest charge-transfer resistance toward HER, with performances far superior to Pt/C catalyst. Theoretical calculations revealed that MoS_2 induced p-type doping in graphene, facilitating the hydrogen adsorption on the graphene side, with ΔG_H close to 0 eV.

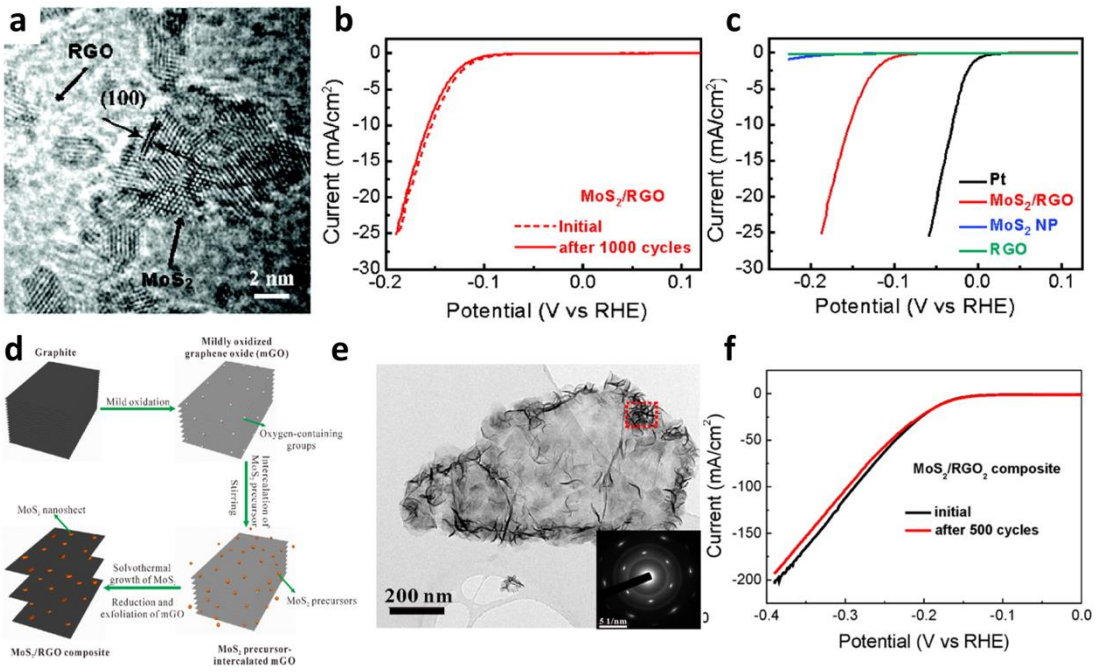

Figure 2.3-9: (a) TEM image of the rGO/MoS_2 NPs hybrid and (b) durability test of the hybrid catalyst after 1000 cycles from −0.3 to +0.7 V at 100 mV/s. (c) Polarization curves obtained with several catalysts as indicated recorded on glassy carbon electrodes with a catalyst loading of 0.28 mg/cm^2. Adapted from Ref. [283] (d) Schematic of the synthesis of rGO/ MoS_2 nanosheets hybrid and (e) TEM image of the same. (f) Durability test of hybrid after 500 cycles from 0 to +0.4 V at 100 mV/s in 0.5 M H_2SO_4 solution. Adapted from Ref. [284]

2.3.1.4. *Biomedical applications*

In addition to their capacity to sense biological molecules, graphene-based hybrids have demonstrated promising application in drug and gene delivery, bioimaging, and

photothermal/photodynamic therapy. Nonetheless, the use of graphene for medical applications still raises many concerns in the scientific community and in the general public because of the potential material's toxicity. Many studies about the toxicity of graphene have been performed; still, notably different results have been reported, mainly because of the high diversity between the available graphene types, e.g. in size and chemical composition.[224, 286, 287] Furthermore, the functionalization of graphene surface can greatly modify its toxicity. Pristine graphene is highly hydrophobic; thus, it has found limited application in the biomedical field. GO and rGO have been more extensively studied because of the easier processability in water dispersions. In particular, the GO and rGO properties of fluorescence quenching ability, surface-enhanced Raman scattering (SERS), facile non-covalent and covalent functionalization and amphiphilic behaviour make GO and rGO hybrids interesting for biomedical applications. The functionalization of the surface of GO is highly desirable in order to increase its biocompatibility. Furthermore, the availability of multiple active sites in GO and rGO allows for the parallel functionalization with drugs, chromophores, nanoparticles, and specific cellular receptors, making it a perfect versatile platform for theranostic. The first example of functionalized GO for biomedical application dates back to 2008 in a paper of Sun and co-workers.[288] The authors produced nanosheets of GO (NGO), covalently functionalized with PEG chains to increase its dispersibility in biological fluids such as serum. These nanosheets were photoluminescent in the visible and infrared regions, which is particularly useful for live-cell imaging because of the little fluorescence background in the NIR range. To this end, NGO PEG was covalently conjugated to a B-cells specific antibody (Rituxan) for the selective binding to B-cell lymphoma cells. The specific binding to B-cells was confirmed by illuminating the biological sample at 658 nm and recording its photoluminescence. Furthermore, the antibody marked NGO PEG was used for loading the cancer drug doxorubicin *via* π-π stacking and selectively killing the target cancer cells. The delivery *via* functionalized GO of potent aromatic drugs in the body has been especially investigated because their insolubility has often hampered their therapeutic use. In another example, Liu *et al.*[289] prepared an amino-PEG decorated NGO, and attached to it *via* π-π stacking the aromatic camptothecin SN38 (**Figure 2.3-10** a). They demonstrated the stability in biological liquids and high *in vitro* cell toxicity (**Figure 2.3-10** b). More importantly, no toxicity was found supplying the cells with the same concentration of functionalized NGO without SN38 (**Figure 2.3-10** c). Wang *et al.*[290] showed that rGO nanoflakes functionalized with gold nanoclusters had higher efficacy in the unloading of the drug doxorubicin in the cells, and the presence of the gold nanoclusters further inhibited the growth of the cells. In addition, the AuNPs/rGO retained IR fluorescence, which could be used for imaging of the cells. Other groups showed that the functionalization of GO/rGO drug carriers with folic acid could greatly increase their selectivity towards the cancer cells, which are known to express many folate receptors.[291] Functionalized rGO has showed also promising applications in biomedical applications; however, it is worth to note that the reduction method used has shown to influence its toxicity. In particular, GO reduced with

hydrazine or ammonia has shown higher toxicity than GO reduced thermally or chemically with milder non-toxic molecules.[292] The higher absorbance of rGO in the IR region compared to GO has been exploited for photothermal therapy. Yang et al.[293] firstly demonstrated the use of functionalized rGO for the *in vivo* photothermal treatment of a tumour in a mouse. rGO was covalently functionalized with PEG chains and labelled with a fluorescent chromophore (**Figure 2.3-10** d). By using fluorescent imaging they proved that, after administration to the mouse, the PEG-rGO was passively loaded preferentially in the cancer cells (**Figure 2.3-10** e). Then they used low-power laser IR irradiation for the photothermal treatment of the tumour, achieving ultra-efficient tumour ablation. In comparison, the PEG-rGO alone and the laser irradiation alone did not have any effect on the reduction of the tumour (**Figure 2.3-10** f). Furthermore, histological and blood analysis did not show any side-effect of the PEG-rGO. In another example, PEG functionalized GO was decorated with Fe_3O_4 and Au NPs, which allowed for the imaging of the hybrid by using magnetic resonance and X-Ray.[294] The irradiation of the tumour *in vitro* provoked its destruction resulting from the combined effect of temperature and reduction of GO, with release of CO_2. Other research groups showed that the efficiency of photothermal therapy can be increased by loading a chemotherapeutic drug on the rGO carrier.[224]

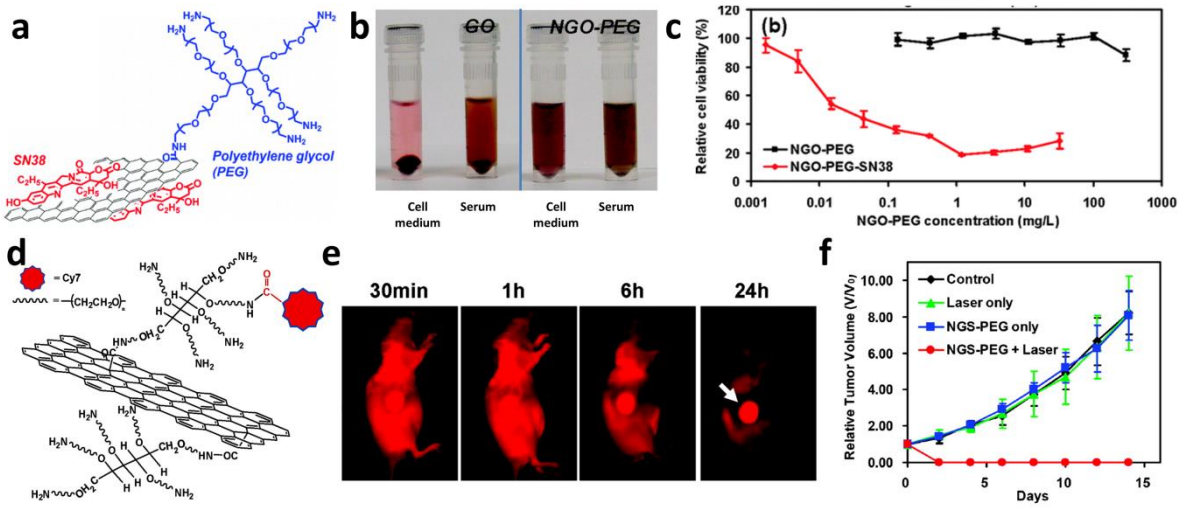

Figure 2.3-10: (a) Schematic draw of SN38 loaded NGO/NPEG. (b) Photos of GO and NGO/PEG in cell medium and serum recorded after centrifugation at 10000 g for 5 min. (c) Relative cell viability data of HCT-116 cells after incubation with NGO−PEG with (red) and without (black) SN38 loading. Adapted from Ref. [289] (d) Schematic of NGO/PEG labelled by Cy7 chromophore. (e) In vivo fluorescence images of U87MG tumour-bearing mice at different times post-injection of NGO/PEG-Cy7. (f) Tumour growth curves of different groups of untreated mice and mice after treatment with laser alone, NGO/PEG alone and NGO/PEG + laser. Adapted from Ref. [293]

Hybrids of GO and rGO have also been employed for photodynamic therapy; in these cases, GO/rGO is functionalized with a photosensitizer, and this upon irradiation gets excited and induces the formation of reactive oxygen species (ROS), which are highly toxic for the cells. GO/rGO functionalized with molecules such as porphyrin, methylene blue and

chlorin have been tested. For example, Rong *et al.*[295] attached a modified chlorin photosensitizer (Photochlor®) onto PEG-functionalized GO *via* supramolecular π-π stacking. The *in vivo* distribution and delivery were tracked by fluorescence imaging and showed a much higher loading of the GO hybrid into the cancer cells compared to the photosensitizer alone, which increased its photodynamic therapy efficacy. Functionalized GO and rGO have been also investigated for protein and gene delivery. For example, Feng and co-workers[296] have reported a non-covalent supramolecular assembly of GO and PEI, which were bonded by electrostatic interaction. The same was used to bind negatively charged plasmid DNA to the positively charged PEI (**Figure 2.3-11** a). PEI also had the function of facilitating the release of the DNA into the cell. However, while PEI alone exhibited cytotoxicity, no toxicity was observed for the assembly PEI/GO (**Figure 2.3-11** b). As aforementioned, GO has been largely employed for biomedical applications because of its easy functionalization and hydrophilicity. The downside of this higher reactivity of GO compared to pristine graphene is that GO may react with proteins and cellular structures within the body, thus leading to cellular damage and inflammation. Furthermore, GO may not stable in the reducing environment of the living cells. For this reason, Lucarelli *et al.*[297] presented recently the first example of functionalized pristine graphene as a multifunctional platform for imaging, chemotherapy and photothermal therapy. Liquid-phase exfoliated graphene nanosheets were covalently functionalized *via* diazonium salt chemistry with three different functional groups, which in turn were covalently attached to indocyanine green (ICG), PEG-folic acid and doxorubicin in a multi-step reaction (**Figure 2.3-11** c). ICG allowed for the *in vitro* fluorescence imaging of the hybrid platform, while folic acid terminated PEG provided dispersibility in water and selective targeting of the cancer cells, and doxorubicin was used as a chemotherapeutic drug. This hybrid showed *in vitro* high selective loading in the cancer cells and good cell killing ability under laser irradiation by combination of photothermal and chemotherapy properties (**Figure 2.3-11** d). Furthermore, *in vivo* toxicological studies on mice of the unfunctionalized graphene nanosheets showed no inflammatory response.

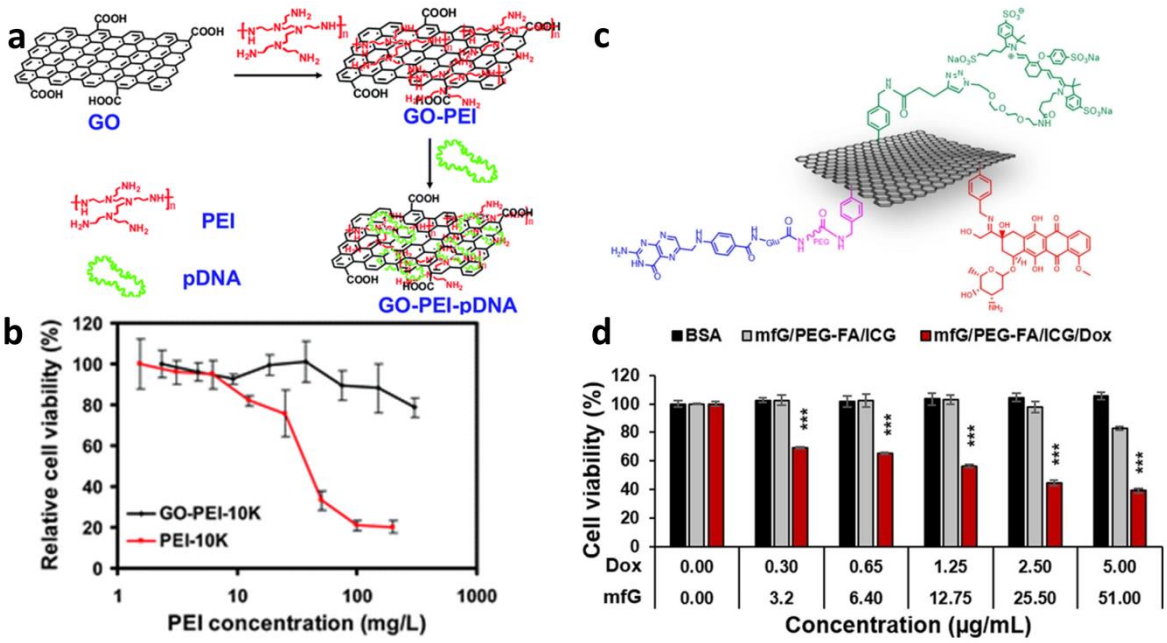

Figure 2.3-11: (a) Schematic representation of the assembling of the hybrid GO/PEI/pDNA via electrostatic interactions. (b) Relative cell viability data of HeLa cells incubated with different concentration of the GO/PEI and PEI alone (PEI molecular weight 10 KDa). Adapted from Ref. [296] (c) Schematic pf the multifunctional graphene platform functionalized with IGC, PEG-folic acid and doxorubicin (mfG/PEG-FA/ICG/Dox. (d) Relative cell viability data of HeLa cells treated with bovine serum albumin (BSA), mfG/PEG-FA/ICG and mfG/PEG-FA/ICG/Dox at different concentrations for 48 h. Adapted from Ref. [297]

2.3.1.5. *Energy storage: supercapacitors and batteries*

The growth and development of renewable electricity sources, electrical cars and portable electronic devices are strongly dependent on the development of efficient energy storage systems such as lithium ions batteries and supercapacitors. Supercapacitors and batteries are complementary devices: the former possess high power density, but low energy density, while the latter possess high energy density and low power density. In both kinds of devices, research endeavour is primarily focussed towards the enhancement of the cyclability and durability in combination with the increase in the energy density and power density, which translate into devices that deliver more current, store more energy and have faster recharge times. The search for new electrode materials for Li-ion batteries and supercapacitors has found in graphene an excellent candidate, because of its electrical conductivity, ultrahigh surface area, chemical stability and broad electrochemical window, mechanical strength joined with deformability and flexibility. The potential of graphene has emerged especially when this has been conjugated with electrochemically active nanomaterials.

Graphene-based hybrid materials are being investigated as anodes for lithium-ion batteries (LIB) and sodium-ion batteries (NIB). In particular, in sodium-ion batteries, the research for new anode materials is fundamental for the development of this technologies, since the traditional graphite based anodes employed for Li-ion batteries are completely

inefficient in storing Na ions.[298] Among these hybrid structures, graphene has the roles of increasing the electrical conductivity, accommodate the volume change of the electrode due to the Li-ions storage, stabilize and enhance the interface electrode/electrolyte, and improve the kinetic rates of the reaction with Li ions.[269]

One of the first examples of graphene-based hybrid for LIB anode was published in 2008 by Yoo and co-workers.[299] The group prepared a paper-like electrode of rGO and CNTs or C_{60} fullerenes, produced by mixing GO flakes with hydrophilic oxidized CNTs and C_{60}, followed by reduction with hydrazine and filtration. The integration of CNTs and C_{60} within the rGO structure produced an increase in the specific capacity up to 730 mAh/g and 784 mAh/g, respectively, compared to the 540 mAh/g observed in neat rGO. SnO_2 has been indicated as a possible alternative to graphite as anode in LIB, with a theoretical capacity of 782 mAh/g, being more than double to that of graphite. However, the main drawback of SnO_2 is a great change in volume during the charge/discharge cycles which causes mechanical failures in the electrode, thus shortening the battery life. For this reason, Paek *et al.*[300] fabricated a nanoporous hybrid of rGO flakes and SnO_2 NPs as anode for LIB, in which the porous nature of the hybrid and the flexibility or rGO accommodated the volume change of the SnO_2 NPs without breaking (**Figure 2.3-12** a). The hybrid exhibited a specific capacity of 810 mAh/g, and a cycling performance drastically enhanced in comparison with that of bare SnO_2 NPs (**Figure 2.3-12** b). Later Zhou *et al.*[301] prepared a hybrid anode of SnO_2 nanocrystals and N-doped rGO, by homogenizing GO and SnO_2 nanocrystals in water solution, followed by freeze-drying and reduction with hydrazine vapours. The hybrid exhibited a huge specific capacity of 1352 mAh/g and excellent retention of the performances after 500 cycles (**Figure 2.3-12** c-d). Hybrids of graphene and $TigO_2$ have also been investigated as anodes for LIB. Wang *et al.*[302] prepared a rGO/TiO_2 nanocrystals hybrid as anode for LIB. The material was prepared by *in situ* surfactant-assisted deposition of the TiO_2 nanocrystals onto rGO flakes dispersed in water. The hybrid exhibited a specific capacity more than double compared to that of bare TiO_2 nanocrystals, mainly due to its higher conductivity. Mn_3O_4 is a low-cost and abundant oxide, which however possesses little conductivity to be employed as anode in LIB. Wang *et al.*[303] developed a low cost and environmental friendly anode for LIB based on a hybrid rGO/Mn_3O_4 NPs. The material was synthesized by *in situ* one-pot deposition of the Mn_3O_4 NPs onto the surface of GO flakes and simultaneous reduction of GO to rGO under hydrothermal conditions. The hybrid exhibited a high specific capacity up to ~900 mAh/g, with good cycling stability. Silicon is another promising anode material for LIB because it has a large specific capacity, however, its great change in volume upon Li^+ insertion shortens the life of the batteries for the formation of fractures in the electrode. Graphene can accommodate the Si nanostructures deformation and protect them from the electrolyte. Lee et al.[303] reported a simple method to produce a nanocomposite paper of rGO and Si NPs obtained by mixing the two components in water phase and filtering the dispersion. The hybrid presented a specific capacity of 2200 mAh/g which decreased to 1500mAh/g after 200 cycles. Luo *et al.*[304] prepared

submicrometer-sized capsules made of Si NPs wrapped by crumpled rGO shells, that were prepared by nebulization of an aerosol of GO and Si NPs dispersion, followed by drying of the microdroplets in a tube furnace and formation of the final structure upon water evaporation (**Figure 2.3-12** e-f). The folds in the crumpled rGO coating can accommodate the volume expansion of Si NPs upon lithiation without fracture. This hybrid structure exhibited greatly improved performances compared to the bare Si NPs in terms of cycling stability and specific capacity (**Figure 2.3-12** g). Wang *et al.* presented a hierarchical multilevel architecture of Si NWs encapsulated with CVD graphene and in turn intercalated between rGO sheets.[93] Within the structure, the CVD graphene coating prevents the direct exposure of encapsulated silicon to the electrolyte enabling the structural and interfacial stabilization of silicon nanowires, while the conductive rGO sheets accommodate the volume change of embedded Si NW@G and maintain the structural and electrical integrity of the assembly. This hybrid electrode exhibited a specific capacity of 1600 mAh/g, high rate capability and 80% capacity retention after 100 cycles.

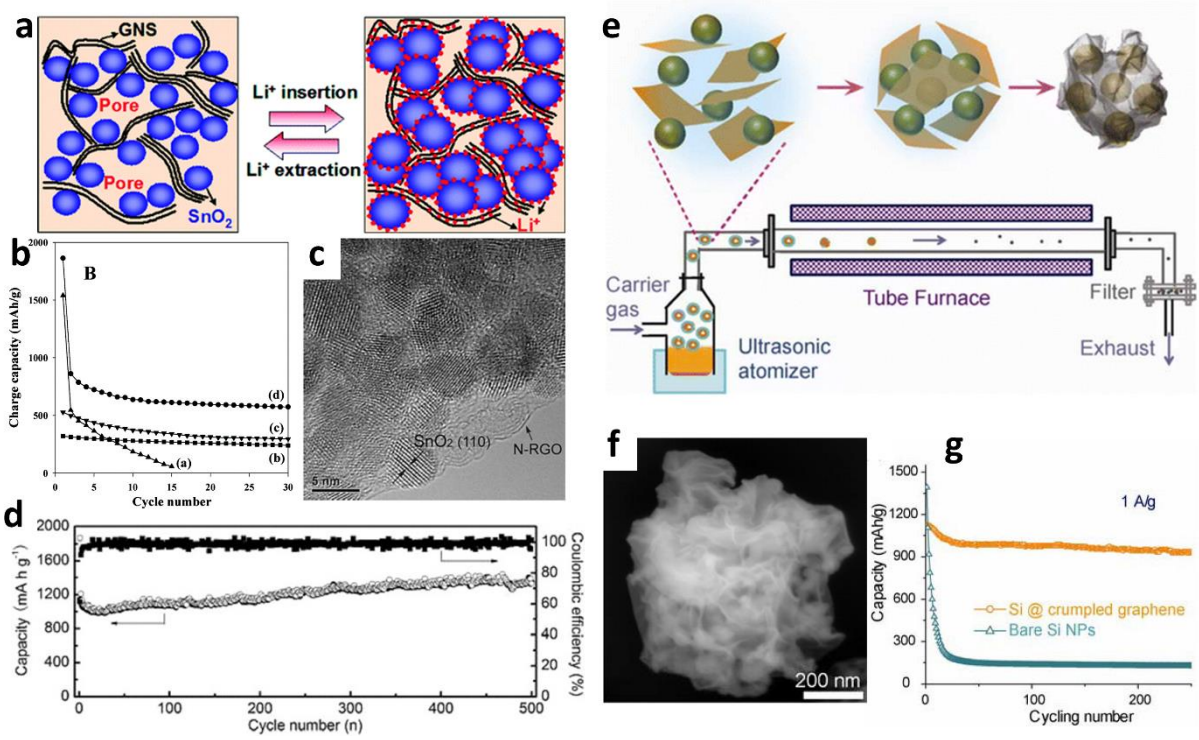

Figure 2.3-12: (a) Schematic of the structure rGO/SnO_2 NPs. (b) Cycling performances for (a) bare SnO_2 NPs, (b) graphite, (c) rGO, and (d) rGO/SnO_2. Adapted from Ref. [300] (c) TEM image of N-doped rGO/SnO_2 nanocrystals. (d) Cycling performance and Coulombic efficiency of the N-rGO/SnO_2NC electrode. Adapted from Ref. [301]. (e) Schematic of the synthesis of submicrometer-sized capsules made of Si NPs wrapped by crumpled rGO shells and (f) SEM image of one of these capsules. (g) Cycling performances of the Si NPs/rGO capsules and bare Si NPs. Adapted from Ref. [304]

Sodium-ion batteries are being developed as cheaper and safer alternatives to Li-ion batteries. Since graphite cannot be used as anode in these batteries, hybrid architectures based on graphene seem the most promising choice. In 2013 Yu *et al.* [305] deposited crystalline

Sb_2S_3 NPs onto rGO flakes and employed the material as anode for NIB. The hybrid material presented a specific capacity of 730 mAh/g, excellent rate capability and 97.2% capacitance retention after 50 cycles, compared to a 50 % capacity retention of bare Sb_2S_3. Sun et al.[123] fabricated a hybrid anode made out of few-layers phosphorene flakes sandwiched between graphene flakes, both obtained by ultrasonic-assisted liquid-phase exfoliation. In fact, phosphorene can react with sodium and lithium to form Na_3P and Li_3P. The hybrid had a specific capacity of 2440 mAh/g (calculated on the phosphorene weight) and showed a 83% capacity retention after 100 cycles. In this case, graphene principally determined an enhancement of the electrical conductivity and mechanical properties, elastically supporting the volume changes of phosphorene. Recently, Liu *et al.*[306] conceived a highly porous hierarchical flexible architecture as anode for NIB based on the structure of pillars and floors employed in modern buildings. The hybrid structure was composed by rGO layers spaced by carbon nanofibers (CNFs) interpenetrating them, all coated by MoS_2 nanoflakes, for storing the Na ions. The structure was composed by firstly mixing CNFs, GO and poly(amic acid) (PAA) as a binder, followed by directional freeze-drying and annealing under argon. Within this porous ordered architecture MoS_2 nanoflakes were grown *in* situ. The hybrid anode demonstrated a specific capacity of 598 mAh/g, long-term cycling stability up to 1000 cycles, and high rate capability up to 10 A/g (**Figure 2.3-13**).

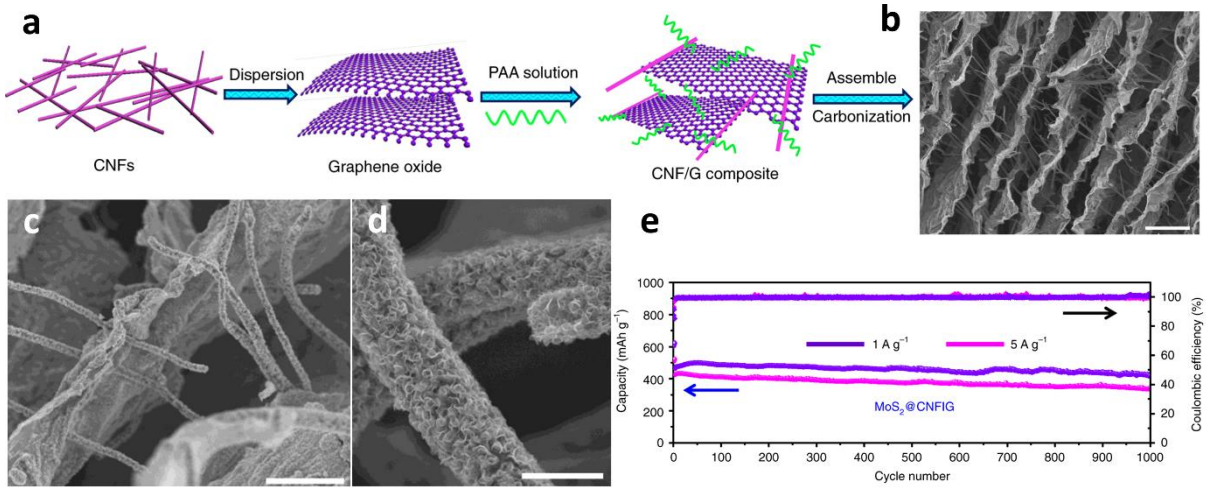

Figure 2.3-13: (a) Schematic of the synthesis of the hierarchical architecture CNFs/rGO and (b) SEM image of the structure after freeze-drying and thermal annealing. (c) and (d) SEM image of the CNFs/rGO/MoS_2 structure after the in-situ deposition of MoS_2. (d) Specific capacity and coulombic efficiency as a function of the number of cycles for the CNFs/rGO/MoS_2 anode. Adapted from Ref. [306]

Supercapacitors are devices capable of delivering high power densities and possessing short recharge and discharge times and much longer cycle life compared to batteries. In general, supercapacitors are based on two types of capacitance. One is electrostatic double-layer capacitance (EDLC), which is related to the formation of a thin region of charge separation at the interface of electrode and electrolyte. The other capacitance also called

pseudocapacitance, is related to the adsorption of ions on the electrode surface and to Faradaic redox reactions between the electrode and the electrolyte ions. In EDLCs the first process is predominant, and usually, the electrodes used are carbon electrodes with large surface area, which do not participate in redox reactions with the electrolyte. Conversely, in pseudocapacitor, the Faradaic redox processes prevail. In this case, electrochemically active electrode materials, such as metal oxides and conductive polymers are used. The two types of capacitance are present in hybrid and asymmetric supercapacitors. Hybrids of graphene with electrochemically active materials are promising electrodes for supercapacitors especially by virtue of their large surface area and high electrical conductivity, which permits fast electron transfer processes, and thus fast charging and discharging times.[269] Several metal oxides, nitrides, hydroxides and chalcogenides have been combined in hybrid with graphene, to build supercapacitors with superior performances.[13, 269] For instance, in 2010 Yan and co-workers[307] presented a hybrid electrode composed by rGO decorated with MnO_2 nanocrystals, synthesized by a one-step *in situ* deposition under microwave irradiation. The hybrid showed Faradaic pseudocapacitance, with a specific capacitance of 310 F/g at 2 mV/s, and high capacitance retention at faster charge/discharge rates (**Figure 2.3-14** a-b). A rGO/MnO_2 nanoplates hybrid electrode was presented by Peng *et al.*[308], who prepared a symmetrical in-plane flexible supercapacitor on a PET film. The material was prepared by mixing in solution rGO and MnO_2 nanoplates, which adhered to rGO *via* electrostatic interactions, and then by filtration of hybrid (**Figure 2.3-14** c-d). The film supercapacitor, with gel electrolyte, exhibited a high specific capacitance of 267 F/g at current density of 0.2 A/g and capacitance retention of 92% after 7000 operating cycles (**Figure 2.3-14** e). Xie *et al.*[309] presented a N-doped rGO decorated with MoS_2 nanoflowers, synthesized *via* a hydrothermal method. The material was then mixed with 10 % Carbon black and deposited on a Ni foam electrode. The electrochemical characterization in 1M KOH solution indicated a specific capacity up to 245 F/g at 0.25 A/g and 91.3 % capacitance retention after 1000 cycles at 2 A/g.

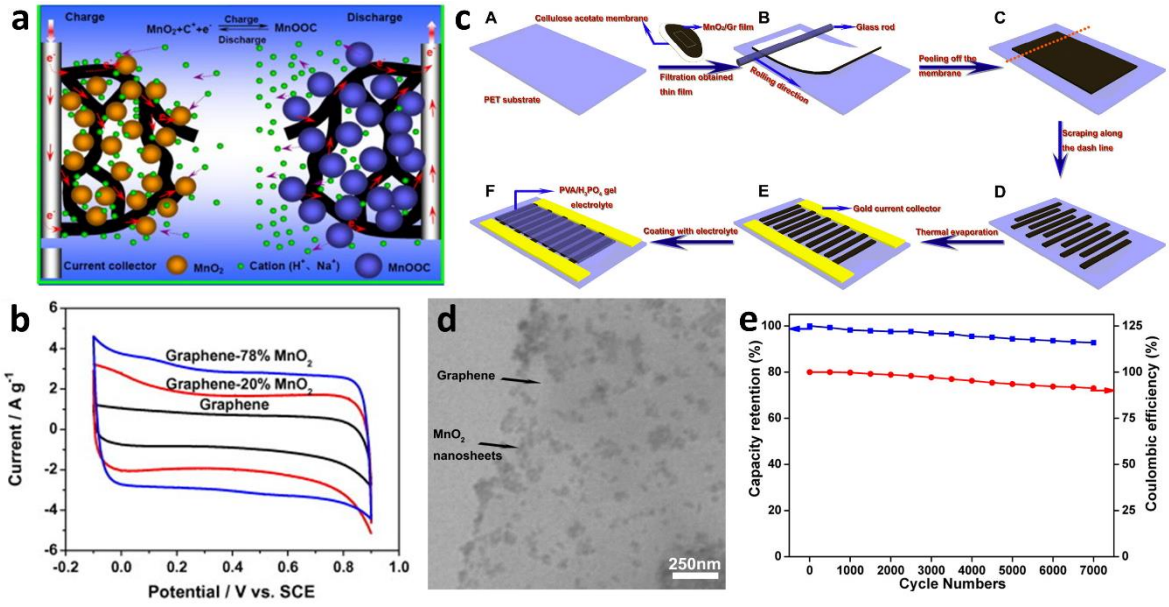

Figure 2.3-14: (a) Schematic illustration of the rGO/MnO_2 pseudocapacitor and Faradic redox reaction between MnO_2 and metallic cations. (b) CV curves of rGO alone and rGO/MnO_2 composites at 10 mV/s. Adapted from Ref. [307] (c) Schematic of the fabrication steps of the flexible in-plane supercapacitor based on a rGO/MnO_2 hybrid. (d) TEM image of the rGO/MnO_2 hybrid. (e) Capacitance retention (blue) and Coulombic efficiency (red) of the in-plane supercapacitor over 7000 charge/discharge cycles. Adapted from Ref. [308]

In order to increase the porosity of the electrode, thus increasing the available surface area and specific capacitance, Zhang and co-workers[310] prepared a hybrid electrode based on rGO decorated with Ni_3S_2 NPs and *Bacillus subtilis* bacteria, prepared by one-pot *in situ* deposition and simultaneous reduction of GO (**Figure 2.3-15**). After depositing the hybrid on a Ni foam by electrospraying the electrode was tested in a 2 M KOH aqueous solution. Thanks to the high microporosity between the RGO/ Ni_3S_2 NPs conferred by the bacteria, the electrode presented a record specific pseudo-capacitance of 1424 F/g at a current density of 0.75 A/g, with 67.5% of the capacitance retained at 15 A/g and high cyclability (89.6% capacitance retention after 3000 cycles at 15 A/g) (**Figure 2.3-15** c). Among the various strategies to increase the available surface area of the electrode, films of stacked graphene flakes intercalated by CNTs have been used.[88, 91] CNTs create voids between the graphene layers and contribute to increasing the conductivity of the electrode. For instance, Xue *et al.*[91] assembled an asymmetric flexible solid-state supercapacitor in which the positive electrode was composed by alternated layers of rGO and $Ni(OH)_2$ nanoplates and the negative electrode by rGO layers intercalated by CNTs (**Figure 2.3-15** d-e). The two free-standing flexible electrodes were then sandwiched between PET films and separated by a gel electrolyte (**Figure 2.3-15** f). The positive electrode exhibited a specific capacitance of 573 F/g and the assembled supercapacitor a volumetric capacitance of 58.5 F/cm^3, with high cycling stability. Jung et al.[88] assembled a hybrid flexible electrode composed by rGO chemically bonded to CNTs *via* amide bond formation. The electrode exhibited a volumetric capacitance

of 165 F/cm^3, which was higher than that of the hybrid formed by physical mixing (**Figure 2.3-15** g).

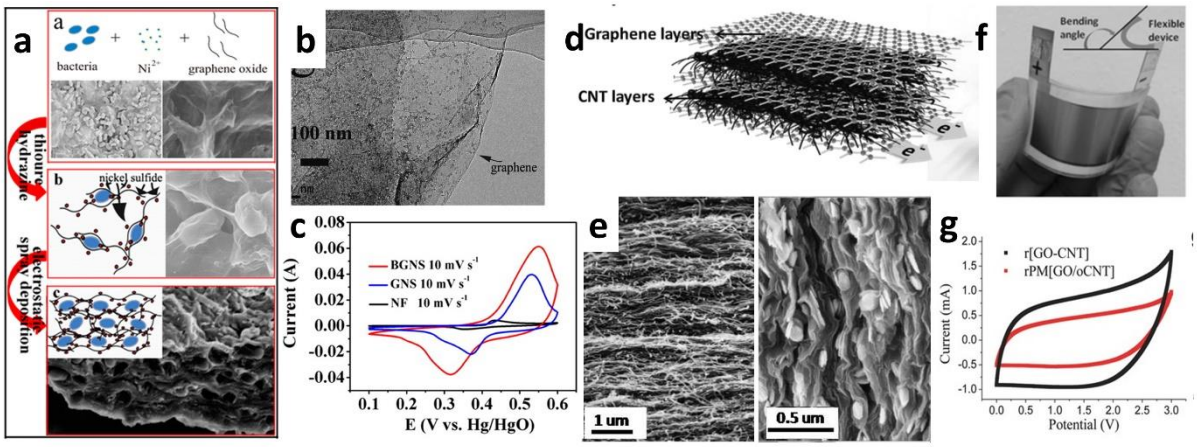

Figure 2.3-15: Schematic of the synthesis of rGO/Ni_3S_2 porous hybrid templated by bacteria and (b) TEM of the hybrid. (c) CV curves of nickel foam, rGO/Ni_3S_2 and of bacteria/rGO/Ni_3S_2. Adapted from Ref. [310] (d) Schematic of the rGO/CNTs hybrid electrode. (e) SEM images of the rGO/CNTs(left) and rGO/$Ni(OH)_2$ nanoplates (right) electrodes. (f) Photo of the flexible assembled supercapacitor. Adapted from Ref. [91] (g) CV curves of rGO chemically functionalized with CNTs (black) and rGO/CNTs physically mixed. Adapted from Ref. [88]

Hybrids of graphene with electrochemically active polymers have also found promising applications as supercapacitor electrodes. Among these polymers, hybrids with polyaniline (PANI) are the most explored because of their electrical conductivity and the fast doping-dedoping redox reactions with metallic cations. [2, 13, 269] In one of the first examples, Wu *et al*.[311] reported a free-standing rGO-PANI flexible electrode prepared by filtration method. The performances of the electrode were tested in an electrochemical cell and showed a specific capacity of 210 F/g at 0.3 A/g. An *et al*.[312] prepared a hybrid of rGO chemically functionalized with PANI chains, *via* amide bond formation between PANI and the acyl chloride derivative of GO. The hybrid was deposited on a glassy carbon electrode and tested as a supercapacitor using a 2 M H_2SO_4 aqueous electrolyte. The hybrid exhibited a high specific capacitance of 623.1 F/g at a current density of 0.3 A/g, and 510 F/g at a current density of 50 A/g and long-term cycling durability. In another example, Meng *et al*.[19] prepared a highly porous free-standing hybrid of rGO and polyaniline, with the aid of $CaCO_3$ particles as a sacrificial templating agent. The polyaniline was polymerized *in situ* on the porous 3D rGO scaffold (**Figure 2.3-16** a-b). The hybrid presented a specific capacity of 385 F/g at 0.5 A/g, with 94 % of capacitance retention at 10 A/g, and excellent cycling stability (90 % capacitance retention after 5000 cycles) (**Figure 2.3-16** c). In addition to PANI, hybrids of graphene with other polymers have been tested. Recently our group conceived a pseudocapacitor based on rGO covalently functionalized with a thiourea-formaldehyde polymer (**Figure 2.3-16** d).[313] The hybrid was processed *via* freeze-drying and presented high porosity. The pseudocapacitor performances were tested in an electrochemical cell and

revealed a high specific capacity of 400 F/g at a scan rate of 1 mV/s and 100% retention of the capacitance after 5000 cycles at 100 mV/s (**Figure 2.3-16** e).

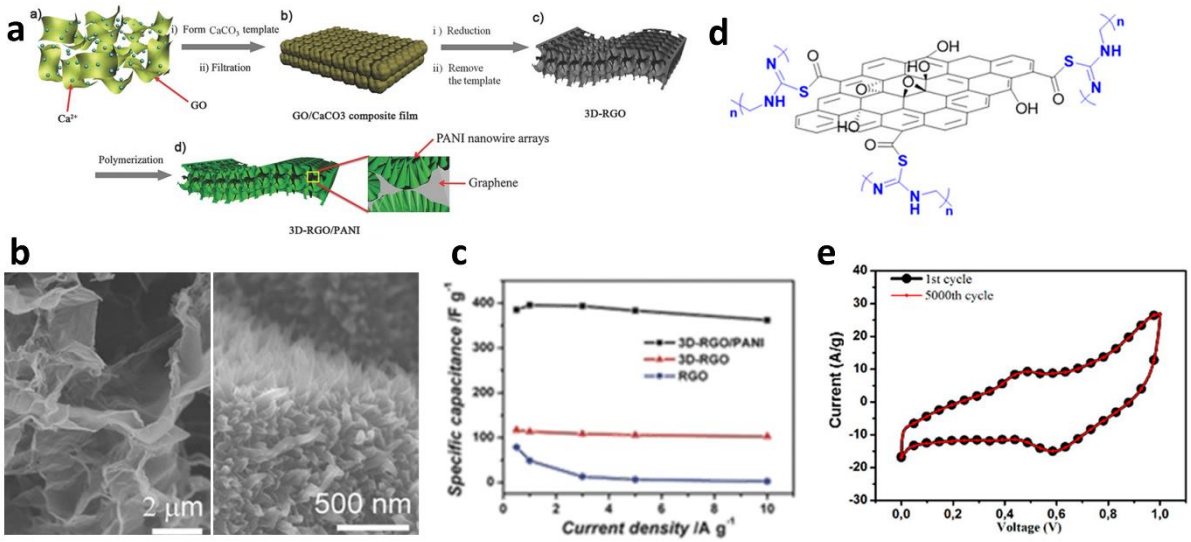

Figure 2.3-16: (a) Schematic of synthesis of rGO/PANI hybrid templated by $CaCO_3$ NPs and (b) SEM images of the same, showing the porosity of the hybrid and the PANI nanofibers. (c) Specific capacitance of rGO, porous rGO and porous rGO/PANI. Adapted from Ref. [19] (d) Structure of the hybrid rGO/thiourea-formaldehyde polymer and (d) CV of the same at the 1st and 5000th cycle at 100 mV/s showing the high stability. Adapted from Ref. [313]

2.3.2. Graphene-based hybrids as transparent electrodes for optoelectronic applications

The exceptional electronic, optical and mechanical properties of graphene have envisioned its use in optoelectronic devices as transparent conductive electrodes (TCEs). TCEs are fundamental components of several devices, including various kinds of solar cells, display technologies, organic light emitting diodes (OLEDs), touch screens and photodetectors. Nowadays the market standard for TCEs is indium tin oxide, i.e. ITO. This metal oxide, composed in large part by indium, can produce films with transmittances (T) around 93 % in the visible range and sheet resistance (R_s) as low as 15-20 Ω/sq on glass substrates.[314] Typical sheet resistances of commercially available ITO films are usually higher, especially for ITO on plastic substrates such as PET, in which the sheet resistance can raise up to 100 Ω/sq.[315] However, ITO suffers from some important drawbacks, which are the high cost and low sustainability due to the presence of the rare earth metal indium, the scarce flexibility and low electrochemical and chemical stability. Pristine single-layer graphene (SLG) is highly transparent, with a transmittance in the visible of 97.7 % and a reflectance of 0.1%, and highly conductive, with charge carrier mobilities in the order of 10^4 $cm^2V^{-1}s^{-1}$.[316] These properties make it a promising alternative of ITO. Nowadays, the largest and continuous films of graphene with the best properties in terms of transparency and conductivity are

obtained by CVD. However, even the best CVD graphene monolayer presents a T = 97 % and a sheet resistance of 600-650 Ω/sq[316-318], while for multilayer graphene the *state of the art* figures of merit are T = 84 % and R_s = 220 Ω/sq.[319] These values are quite far from the performances of ITO films. Films made of overlapped rGO flakes can have sheet resistances as low as 1000 Ω/sq at T = 80 % for films reduced with hydrazine and 800 Ω/sq at T = 82 % for films annealed at 1100 °C under Ar.[318] Despite the higher sheet resistances of rGO films, their principal appeal is due to the lower cost and much easier processability and deposition compared to CVD graphene, which needs to be transferred from the metallic substrate to the device. The sheet resistance is not the only important figure of merit of TCEs, in fact, the electrodes need to efficiently collect and inject electrons in the active material of the device, and to do so they need to have a work function that is properly aligned with that of the active material. In order to increase the conductivity and adjust the work function, CVD graphene and rGO films can be doped with small molecules.[316, 318] For instance, CVD graphene doped with p-dopant such as $AuCl_3$ and HNO_3 can exhibit R_s as low as 30 Ω/sq for T = 90 %.[316, 320] Also rGO can be made more conductive *via* chemical doping; for instance, a rGO film obtained by Langmuir Blodgett (LB) deposition and doped with $SOCl_2$ after reduction with HI exhibited a R_s = 1100 Ω/sq at T = 91 %.[321] However, the doping effect of these small molecules in most of the cases is not stable over time, leading to a degradation of the performances.[316, 317] The combination of graphene in hybrid films with bigger aromatic molecules, polymers (and especially conducting polymers) and nanostructures such as metallic nanowires and carbon nanotubes can greatly enhance the conductivity and on the same time maintain high transparency.

2.3.2.1. *Solar cells*

Graphene hybrids have found application in all the types of solar cells, including inorganic semiconductor, perovskite, organic solar cells (OSC) and dye-sensitized solar cells (DSSC). In solar cells, graphene hybrids have been used mainly as ITO replacement in the front TCE, but also as electron acceptor layer and buffer layer in OSC. Solar cells are the devices in which TCEs need the highest transparency and highest conductivity since these values have a great effect on the power conversion efficiencies (PCEs). Hybrids of CVD graphene and small doping molecules have been used to increase the conductivity of graphene and modulate its work function. For instance, Miao *et al.*[322] produced a CVD SLG doped with a layer of trifluoromethanesulfonimide and employed it as both TCE and as electron collector in a Schottky junction solar cell with n-Si. The p-doping effect on graphene from trifluoromethanesulfonimide enhanced its conductivity and led to an increase of PCE from 1.9 % of the un-doped device to 8.6 %. Hsu *et al.*[323] reported the use of a 5 layers structure of alternating single-layer CVD graphene and tetracyanoquinodimethane (TCNQ) as transparent anode for a bulk heterojunction OSC with poly(3-hexylthiophene) (P3HT) and phenyl-C61-butyric acid methyl ester (PCBM) (**Figure 2.3-17** a). The TCNQ molecules sandwiched between two graphene layers act as p-dopant, causing an increase in the work

function and a huge reduction of the sheet resistance of the electrode. The overall PCE of the solar cell constructed with the 5 layer graphene/TCNQ electrode was 2.58 %, being 6 times higher than that of the device with a single layer CVD graphene electrode (**Figure 2.3-17** b). Hybrids of graphene with conductive polymers have found application as TCEs in solar cells. In particular, poly(3,4-ethylenedioxythiophene): poly(styrene sulfonic acid) (PEDOT:PSS) has been used for its p-doping effect and the high intrinsic conductivity. Liu et al.[324] fabricated a OSC with P3HT/PCBM as active layer and CVD SLG /Au NPs/PEDOT:PSS as top TCE. The 30 nm thick layer of PEDOT:PSS increased the conductivity of the graphene layer by p-doping effect and lowered its work-function. The OSC exhibited a PCE of 2.7 %. Lee et al.[325] presented a TCE based on a bilayer CVD graphene and PEDOT:PSS and used it as top TCE in a polymer-based OSC. In this case, the PEDOT:PSS layer had a dual role, it served as a substrate for the transfer of the CVD graphene from the metal to the OSC, and then it enhanced the performance of the device through p-doping. The OSC with graphene/PEDOT:PSS on PET exhibited a PCE of 4.8 %, which was even higher than that of the same OSC with a PET/ITO electrode.

Carbon nanotubes, Ag NWs and rGO NWs have also been used in order to increase the conductivity of rGO and CVD graphene. Tung *et al.*[85] produced a TCE made of a hybrid rGO/CNTs. The two components were mixed in solution, reduced with hydrazine, and deposited by spin coating on a PET substrate. The electrode exhibited a R_s of 240 Ω/sq at 86 % transmittance. The hybrid film was used as top electrode in a P3HT/PCBM OSC, which exhibited a PCE of 0.85 %. By virtue of its good stability, a rGO/CNTs TCE was also used by Zhu *et al.*[326] to substitute platinum as counter electrode for DSSC. Ricciardulli *et al.*[101] prepared a hybrid TCE of Ag NWs/electrochemically exfoliated graphene (EEG) on different substrates *via* spray-coating of the two components from suspension (**Figure 2.3-17** c). The EEG coating on top of the Ag NWs greatly decreased the roughness of the film and the sheet resistance from 78 to 13.7 Ω/sq, and increased their stability to oxidation and to mechanical bending (**Figure 2.3-17** d). The hybrid film was integrated as top electrode in a bulk heterojunction OSC, which exhibited a PCE of 6.57% (**Figure 2.3-17** e). Dong et al.[327] prepared a TCE composed by Ag NWs network covered by CVD SLG. The hybrid electrode was prepared by spin coating of the Ag NWs on top of the transferred CVD graphene, followed by inversion of the structure *via* a second transfer step. Also in this case, the overlying graphene layer increased the resistance to corrosion of the electrode, reduced the roughness and lowered the sheet resistance (R_s = 8.06 Ω/sq at $T_{(550\ nm)}$ = 88.3%). The TCE was used as top electrode in a perovskite solar cell and outperformed a similar device with a commercial PET/ITO electrode.

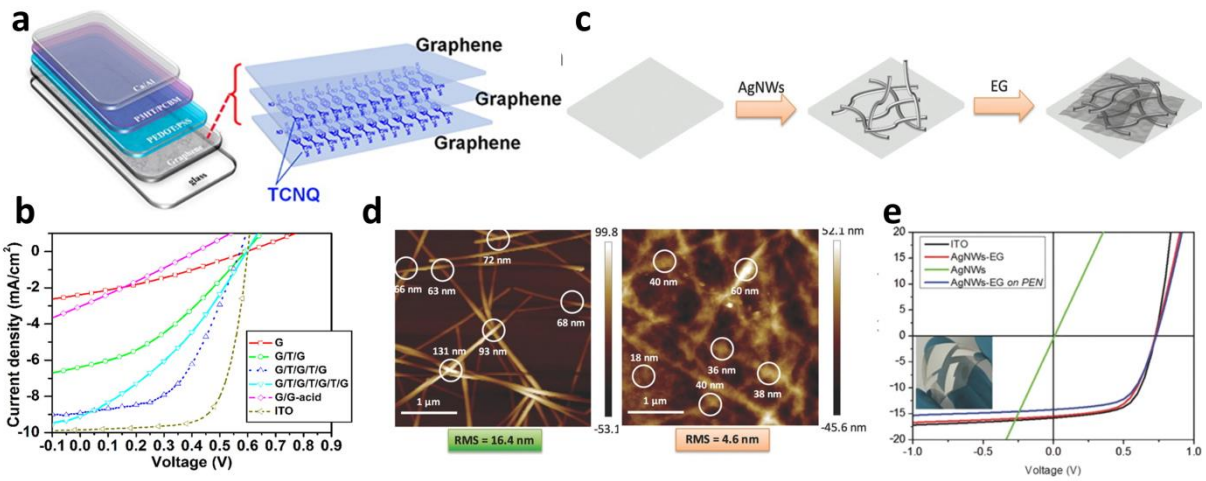

Figure 2.3-17: (a) Schematic structure of a OSC with a TCE based on a sandwiched structure of CVD graphene monolayer and TCNQ and (b) Measured current density (J)–applied bias (V) curves of the OSC devices with different TCEs. Adapted from Ref. [323] (c) Schematic of the fabrication of the hybrid TCE Ag NWs/EEG. (d) AFM images with reported the roughness (RMS) of Ag NWs and Ag NWs/EEG on glass. (e) J – V curves of the OSC device assembled with different top TCE: ITO, Ag NWs, Ag NWs/EEG on glass and PEN. Adapted from Ref. [101]

2.3.2.2. *Display technologies*

Graphene hybrids have also been employed in display technologies, such as OLEDs and electrochromic devices (ECDs), as TCE to replace ITO. In the case of OLEDs and electrochromic devices, good efficiencies can be obtained also with TCE exhibiting lower transparency in comparison to solar cells. As aforementioned, pristine CVD graphene has a low carrier concentration, that can be increased by chemical doping, thus increasing its conductivity. For instance, Li *et al.*[328] employed triethyloxonium hexachloroantimonate (OA)/dichloroethene adsorbed on a CVD graphene monolayer to enhance its conductivity by a stable p-doping (**Figure 2.3-18** a-b). The conductivity was further enhanced by depositing a layer of PEDOT:PSS on top of the p-doped graphene. The TCE on plastic substrate was used to assemble a green OLED and a white OLED, whose performances corresponded to that of the devices assembled with an ITO on glass electrode (**Figure 2.3-18** c-d). Meyer *et al.*[329] produced a TCE composed by a CVD graphene few-layers and a MoO_3 layer, thermally evaporated on top. The MoO_3 layer acts as p-dopant, lowering the sheet resistance of the film and increasing the work function of graphene. Furthermore, the doping produces an alignment of the transport levels on the two materials, favouring the charge extraction/injection. The TCE was tested in an OLED device, which showed performances slightly superior to that of a similar OLED with glass/ITO electrode. Chang *et al.*[330] presented a TCE based on a hybrid of rGO and PEDOT:PSS as addictive for increasing the conductivity. GO was exfoliated and reduced in solution with the aid of sodium dodecylbenzene sulfonate as a surfactant and then it was mixed with a solution of PEDOT:PPS and spin-coated on PET substrate. The PEDOT:PSS greatly improved the conductivity of rGO by acting as a dopant and as a conductive filler that occupied all the

empty spaces between the rGO flakes. The hybrid film was used as a transparent anode in an OLED, which performances were comparable with that of an OLED made with an ITO anode. Ruoff *et al.*[331] prepared a hybrid TCE composed of a layer of aligned metallic multi-walled CNTs coated by a continuous layer of CVD graphene deposited on top of a PET substrate. The electrode, which exhibited high bendability, was tested as top and bottom electrode in an ECD, showing good performances (**Figure 2.3-18** e-g). Interestingly, the inverted configuration of the electrode with the CNTs on top of graphene showed worse electrical, optical and mechanical performances. Assemblies of rGO and CVD graphene with Ag and Cu NWs have also been employed as TCE in OLEDs[101, 327] and ECDs.[7] In particular, the Ag NWs/EEG electrode fabricated by Ricciardulli *et al.*[101] and the Ag NWs/CVD electrode of Dong *et al.*[327] described in the previous paragraph were successfully employed also as transparent anode for OLED devices.

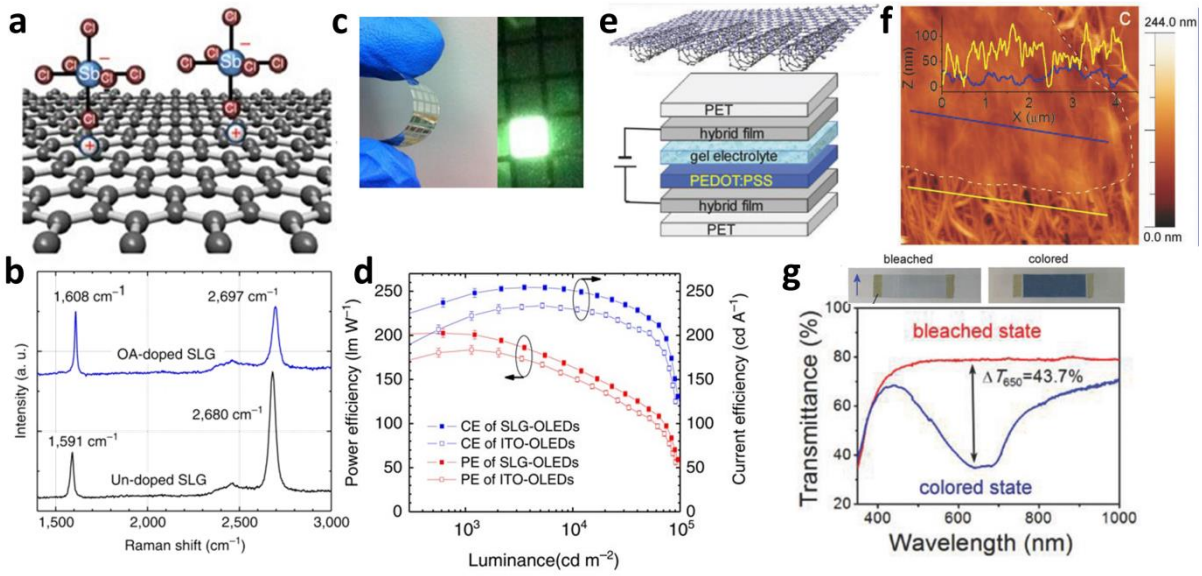

Figure 2.3-18: (a) Schematic of the doping effect of OA on graphene and (b) Raman spectra of OA-doped Single layer graphene (SLG) and undoped SLG. (c) Photos of the OLED device and (d) Power efficiency and current efficiency of OLED devices assembled with the OA-SLG electrode and ITO. Adapted from Ref. [328](e) Schematic of the electrode CNTs/SLG and of the ECD device. (f) AFM image of the CNTs partially covered by SLG and height profiles of CNTs and CNTs/SLG. (g) Photos and Transmission spectra of the ECD device in the coloured and bleached states.

2.3.2.3. *Photodetectors*

A photodetector is a transducer that absorbs photons and converts them into an electrical signal. The electrical signal generated can be a photocurrent, a difference of potential or a change in resistance. Graphene has been intensively investigated for its photonic properties and its first application as photodetector dates back to 2009.[332] A graphene monolayer absorbs as much as 2.3 % of light, being a notably large magnitude for an atom-thick material. Moreover, its light absorption is wavelength independent. Other characteristics that

make graphene so appealing for photonic applications are its zero bandgap, which allows graphene to absorb photons and generate charge carriers over an extremely wide range of frequencies, from ultraviolet to microwaves, and its high carrier mobility, which allows an extremely fast detection. [333] However, the low absorption of monolayer graphene implies that most of the incident photons do not interact with graphene. Furthermore, the zero bandgap of graphene causes a superfast charge-recombination in the ps range, which on the one hand is favourable for high-speed optoelectronics, and on the other hand, makes it difficult to separate and collect the photo-generated carriers. For these reasons, graphene is often coupled with other nanostructures, such as few layers TMDs, and QDs, which absorb the photons and generate a hole and an electron that are efficiently collected by graphene.[108] In these cases graphene acts as a transparent electrode, enabling the light to pass through and collecting and transporting the photogenerated carriers. For example, in sandwiched vertical heterostructures Graphene/TMD/Graphene the graphene layers allow the light to pass and collect immediately the photogenerated carrier in the TMD without long diffusion processes. For example, Duan and co-workers[334] developed a vertical heterostructure composed of a mechanically exfoliated 50 nm thick MoS_2 sandwiched between two CVD SLGs deposited on a Si/SiO_2 substrate (**Figure 2.3-19** a-b). The two interfaces graphene/MoS_2 produce two Schottky barriers and since the MoS_2 layer is thin, the two Schottky barriers merge together and form a monotonic band slope (**Figure 2.3-19** e). Excitons formed in the MoS_2 are separated and immediately collected by the graphene electrodes. The height of the Schottky barriers, and thus the slope of the MoS_2 bands, can be modulated by changing the doping of the bottom graphene by the application of a back gate voltage to the bottom graphene electrode, eventually leading to the modulation of the photoresponse (**Figure 2.3-19** c-e). By decreasing the thickness of the TMD, it is possible to increase the detection speed of the device, at expenses of the sensitivity.[14]

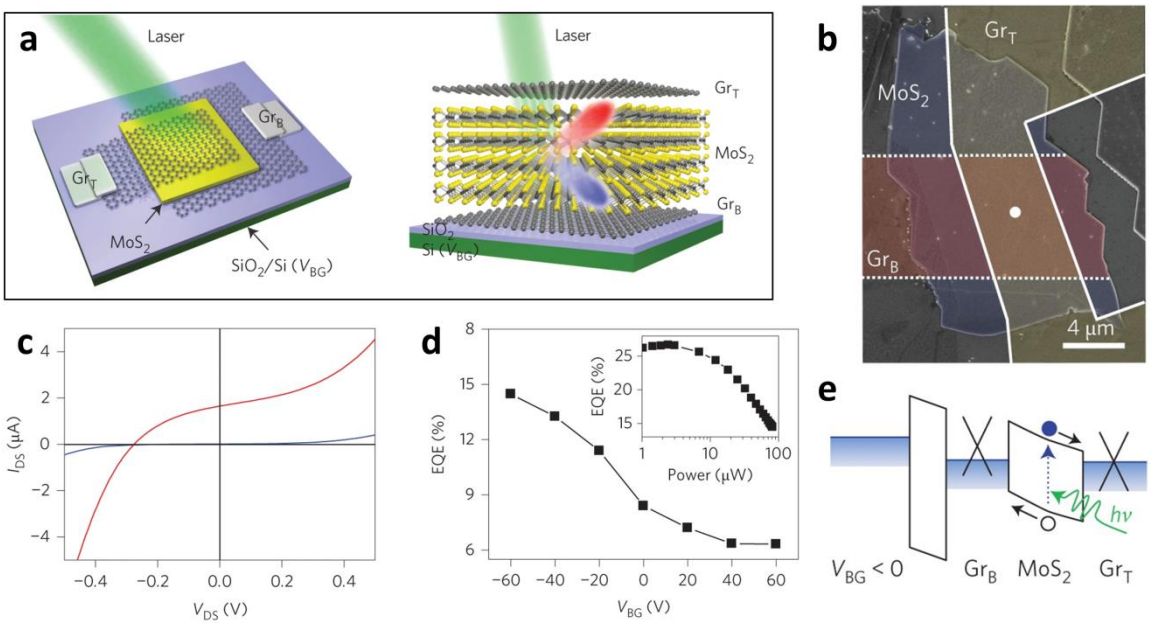

Figure 2.3-19: (a) Schematic representation of the photodetector device SLG/MoS_2/SLG view from the top and from the side and (b) SEM image in false colours of the device. (c) Current–voltage characteristic of the device in dark (blue) and under illumination (red) by a focused laser beam (λ=514 nm; 80 μW; spot size= 1 μm). External quantum efficiency as a function of the back-gate Voltage (V_{BG}) at a laser power of 80 μW and of the excitation laser power at V_{BG}= 60 V. (e) Schematic band diagrams of the vertical heterostructure with negative V_{BG}.

In order to increase the sensitivity up to the single photon detection, graphene is often coupled with photosensitive materials which absorb light efficiently, such as quantum dots.[14, 317, 333] In these cases, usually the incident light is detected by photogating effect: photons are absorbed by the photosensitizer and generate excitons, which are separated by the in-built electrical field at the interface between graphene and the photosensitizer. Eventually, one type of the charges (hole or electron) is collected by graphene, and the opposite charges remain trapped into the photosensitizer, altering the gate voltage. The longer is the lifetime of the trapped charges and the higher is the mobility of the collected charges in graphene, the higher is the modulation of the gate voltage, and thus the sensitivity. Konstantatos *et al.*[228] presented an ultrasensitive photodetector based on the photogating effect, composed by a mechanically exfoliated SLG on a Si/SiO_2 substrate coated by a 80 nm thick layer of PbS colloidal QDs, produced by LbL deposition (**Figure 2.3-20** a). The absorption of photons was detected both as a shift in the Dirac point in graphene towards more negative back gate voltages and as a decrease in the resistivity of graphene. The device exhibited great sensitivity, being able to detect light as little as 8 fW of incident light (**Figure 2.3-20** b-c). The spectral range of sensitivity of photosensitized graphene photodetectors can be modulated by changing the QDs and their optical characteristics. QDs are sensitive to the incident light if its energy is higher than the bandgap of the QDs. Bigger QDs have narrower bandgaps and absorb light from higher wavelengths. Ni et al.[335] produced a photodetector sensitive from the mid-infrared (MIR) to UV light by depositing B-doped Si QDs on CVD graphene on a Si/SiO_2 substrate. MIR light is directly absorbed by

graphene, which absorption in this region is enhanced by the localized surface plasmon resonance (LSPR) induced by the Si QDs (**Figure 2.3-20** d). The light with wavelengths from near-infrared to UV is absorbed by the QDs and is detected by photogating effect. The devices exhibited ultrahigh responsivity up to 10^9 A/W (**Figure 2.3-20** e). The photosensitizing effect may arise also from organic photosensitizers, such as porphyrins.[336] For example, Wang *et al*. produced a photodetector based on a hybrid of mechanically exfoliated SLG coated by drop-casted chlorophyll A molecules, which acted as photosensitizer. The photodetector presented a high responsivity of 10^6 A/W. Hybrids of graphene with QDs can be obtained also by solution processing. For example, Manga *et al.*[337] produced a broad-band sensitive photodetector based on a hybrid of few-layer electrochemically exfoliated graphene decorated by PbSe and TiO_2 QDs, synthesized *in situ* on the graphene surface (**Figure 2.3-20** f). The hybrid material was inserted between a transparent ITO electrode and an Al electrode. The photodetector was sensitive from IR to UV region; however, the maximum responsivity amounted only to 0.506 A/W.

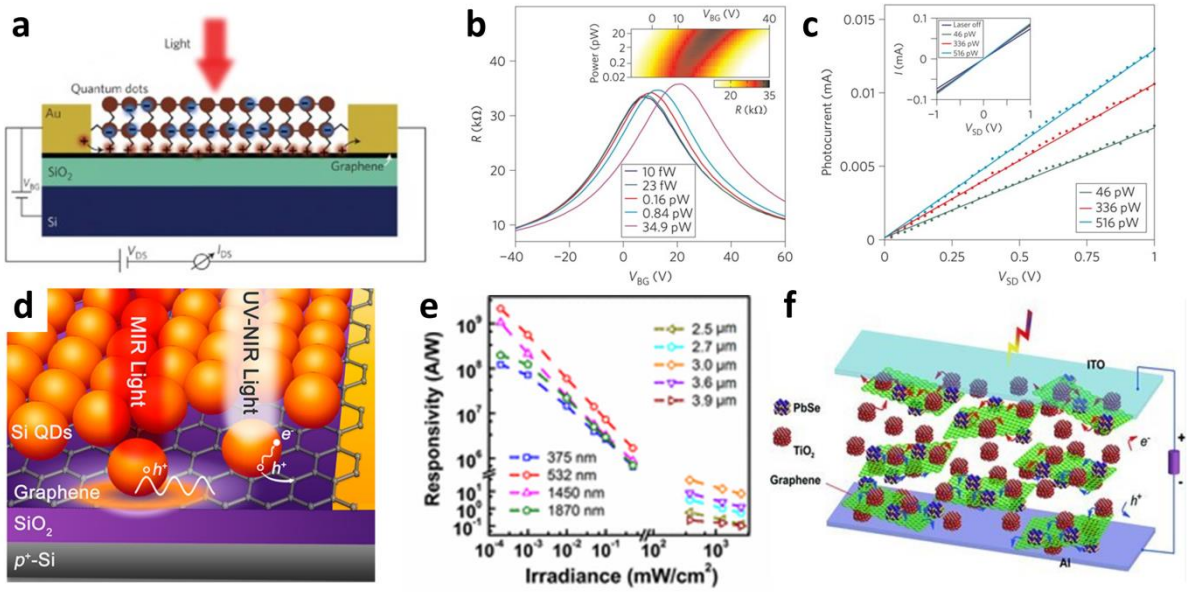

Figure 2.3-20: (a) Schematic of the SLG/PbS QDs hybrid photodetector. (b) Resistance vs V_{BG} of the device at different illumination intensities of a collimated laser (λ=500 nm, diameter= 1 mm) showing the modulation of the Dirac point. (c) Photocurrent as a function of drain-source voltage (V_{DS}) at V_{DG}=0 of the SLG/PbS QDs photodetector for different optical powers. Adapted from Ref.[228] (d) Schematic of the SLG/B-doped Si QDs photodetector and (e) Responsivity of the device as a function of the irradiance and of the incident light wavelength. Adapted from Ref.[335] (f) Schematic of the photodetector based on a hybrid FLG functionalized with PbSe and TiO_2 QDs. Adapted from Ref. [337]

2.4. Conclusion and perspectives

In this chapter, the hybrids assemblies based on graphene have been introduced and reviewed, with a particular focus on their applications. The use of graphene as a building block to assemble more complex, functional supramolecular architectures and its

functionalization with molecules was proven being a successful route to tailor the functionalities of graphene and multiply its potential applications in the most disparate fields. Hitherto, with over 35000 publications, graphene-based hybrid assemblies represent the 28 % of the total number of publications comprising graphene (**Figure 2.4-1** a). In particular, while the gold rush of graphene seems to be slowly reaching its peak, graphene-based hybrids are still steadily growing (**Figure 2.4-1** b). However, despite the great number of publications, the graphene-based hybrid structures struggle to find their use in industrial end products.

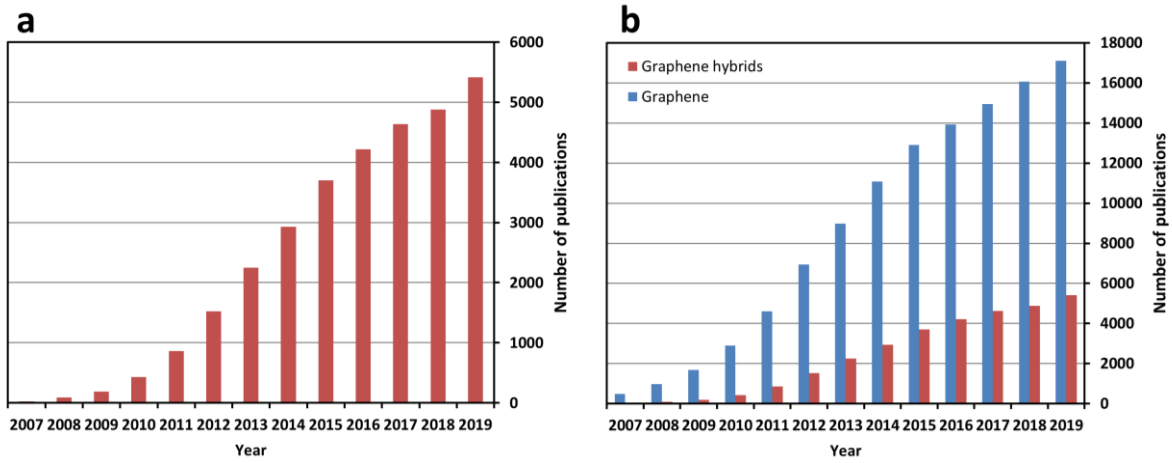

Figure 2.4-1: (a) Number of publications with subject graphene-based hybrid as a function of year and (b) comparison with the publications with subject graphene. Source: Web of Science. The results for graphene-based hybrids have been refined with the following query: TI=(graphene AND (hybrid OR nanocomposite OR functionaliz* OR nanostructur*)) OR AB=(graphene AND (hybrid OR nanocomposite OR functionaliz*)) AND TI=(graphene OR RGO)

On the contrary, composites materials in which graphene is used as nanofiller have already emerged in several products on the market.[338] The main reason is that these composites materials use cheap forms of graphene, usually obtained by liquid-phase exfoliation of graphite, which often are nothing but micrometre sized thin graphite flakes.[339, 340] These composites usually display enhanced mechanical properties, electrical and thermal conductivities and reduced weight; however, the performances of these composites do not stand out compared to that of other composite materials.[341] Before seeing graphene-based hybrids into the markets, few challenges still need to be tackled. In particular, graphene, GO and rGO are still expensive material, and their quality is highly dependent on the production method used. Furthermore, the synthetic procedures used for preparing the hybrids are often complexes and scarcely reproducible. Therefore, to meet the industrial requirements it is necessary a cost reduction, an optimization of the synthetic procedures that guarantees a higher reproducibility and an improvement of the long-term stability of the hybrids.

Chapter 3.

Materials and methods

3.1. Introduction

The scope of the present chapter is to give an overview of the experimental techniques used for the characterisation of the material and devices developed in this thesis. At the end of the chapter, the synthetic procedures employed to synthesize the copper nanowires presented in chapter 4 are also presented. A brief introduction over the theoretical concepts underlying the methods used will be given, together with the explanation on the instrumental configurations, while at the end of each section details on the experimental conditions employed will be indicated. Firstly, the chapter will focus on the techniques used to determine the composition and physical properties of the produced materials and devices: X-ray photoelectron spectroscopy (XPS), X-Ray diffraction (XRD), IR spectroscopy, Raman spectroscopy, UV-Vis spectroscopy, Thermogravimetric analysis (TGA), water contact angle and electrical measurements. Then, the microscopy techniques employed in the present work will be discussed: scanning electron microscopy (SEM), atomic force microscopy (AFM) and optical microscopy.

3.2. Characterization techniques

3.2.1. X-ray photoelectron spectroscopy

3.2.1.1. *Description of the instrument and theoretical principle*

X-ray photoelectron spectroscopy (XPS), also called "ESCA" (Electron Spectroscopy for Chemical Analysis) is an important and widely used surface analysis method and is based on the study of the energy distribution of electrons emitted from the core levels when compounds are irradiated with *X*-rays. The electrons contain information regarding chemical oxidation state, electronic structure, and atomic composition of the analyte being studied. Thus, surface composition as well as the electronic environment can be determined non-destructively. XPS gives information about the chemical composition of a thin layer (about 10 nm depth) on the surface of a specimen. XPS can detect all elements with an atomic number greater than 3, with a detection limit in the parts per thousand range (0.1 %). [342, 343]

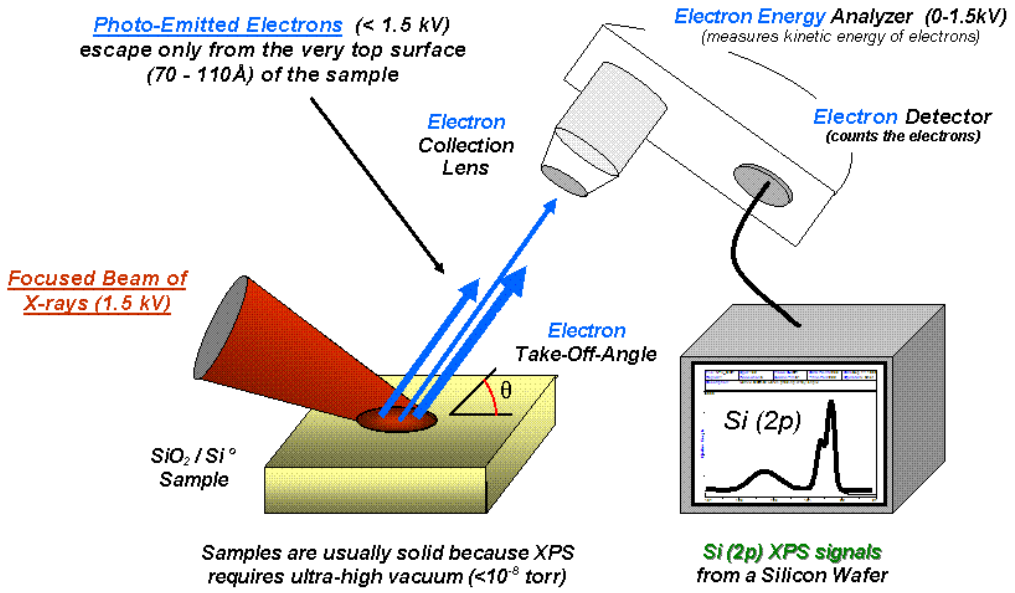

Figure 3.2-1: Schematic composition of a XPS system. Free copyright from https://commons.wikimedia.org

A modern commercial XPS instrument includes a source of X-rays, a chamber with inside the sample mounts, the electron collection optics, a concentric hemispherical analyser and an electron detector; all the system is kept under ultra-high vacuum with UHV pumps (**Figure 3.2-1**).

The electron collection optics collect and focus the electrons expelled from the sample. The concentric hemispherical analyser resolves and separates electrons with different kinetic energy, and the electron detector counts these electrons. The X-Ray source needs to be the most monochromatic possible. In commercially made XPS system X-rays are generated by bombarding a metallic anode (usually aluminium) with high-energy electrons. The radiation emitted by the aluminium contains a continuum background and a K-α line with an energy = 1486.6 eV. This radiation is rendered monochromatic by diffraction on a quartz crystal.

The XPS operates on the principle of the photoelectric effect. The photoelectric effect, or photoemission, is the ejection of electrons (also called photoelectrons) from a material when light is absorbed by the same. The kinetic energy of the ejected electrons is dependent by the wavelength of the incident radiation and the atomic number and chemical state of the atom which ejected them. The kinetic energy can be expressed as: $= h\nu - BE$, where hv is the energy of the incident radiation, which is known, and BE is the binding energy, i.e. the energy required to remove the electron from an atomic orbital to the vacuum level. Thus, the energy of the ejected electron is always lower than the energy of the incident photon.

Typical XPS spectrum is a plot of the number of electrons detected (sometimes per unit time) versus the binding energy of the same. It is comprised by a series of peaks, each one

corresponding to a specific orbital of the atoms that compose the sample, thus peaks are named according to the element and the orbital from which the electron was ejected, in particular, are expressed the principal quantum number n, the orbital quantum number ℓ and j (e.g. Au $4d_{3/2}$). The total angular momentum j is expressed because p, d and f orbitals split into two peaks for spin-orbit coupling. By measuring the ratio between the areas under the peaks it is possible to determine the quantitative composition of a surface.

The exact binding energy of an electron depends not only upon the level from which the electron is ejected but also upon the formal oxidation state of the atom and the local chemical and physical environment. Change in the binding energy of a photoelectron due to change in the chemical bonding of that element causes a shift in the peak position of the spectrum called chemical shift. Thus, measuring these shifts, it is possible to assign the chemical environment of a given element.

Summarizing, XPS has several advantages: it is not a destructive technique, is very surface sensitive and can be used to provide information about chemical bonding and accurate quantitative elemental analysis. On the other hand, it is an expensive technique, requires high vacuum and is a slow technique (collecting more points for each sample to minimize statistical errors, and more acquisition for each point to minimize background noise can take more than 8 hours per sample).

3.2.1.2. *Instrumentation and operating conditions*

In this thesis, XPS has been used to determine the atomic composition and the chemical species present in various samples, including the GO, rGO and chemically modified GO/rGO presented in chapter 4 and the Cu NWs/rGO hybrids presented in chapter 5. The XPS measurements were carried on using a Thermo Scientific™ K-Alpha™ X-ray Photoelectron Spectrometer (Thermo Fisher Scientific Inc.) with a basic chamber pressure of around 10^{-8} mbar and an Al anode as the X-ray source (x-ray radiation of 1486 eV). The measurements have been performed by averaging the spectra acquired over 3 different positions of each sample. For each analysed point, a full energy range spectrum (called survey spectrum) and the high-resolution spectra of the representative orbitals of the elements of interest (in this thesis C, N, O, Cu) were acquired. For each spectrum, between 10 and 30 acquisitions were performed to maximize the signal to noise ratio.

3.2.2. UV-vis Absorption Spectroscopy

3.2.2.1. *Description of the instrument and theoretical principles*

The absorption spectroscopy is one of the most important analytic techniques in chemistry and it is based on energetic transitions occurring when molecules or molecular assemblies absorb photons. The nature of the transition is a function of the energy of the photons. Upon

absorption of a photon with energy (hν) falling typically in the ultraviolet or visible range of the electromagnetic spectrum, a given molecular system (A) is promoted to an electronically excited state (*A), reaction which can be indicated in the general form $A + h\nu \rightarrow {}^*A$. Absorption of visible light occurs in a wide range of molecules and materials and this is the reason why the world around us appears coloured. A necessary condition for a photon to be absorbed by a molecule is that the energy of the photon hν must be equal to the energy difference between the ground state and the excited state of the molecule: $h\nu = E_f - E_i$ where E_f and E_i are respectively the energies of the excited state and the ground state of the molecule. An absorption spectrum is the fraction of incident radiation absorbed by a chemical specie over a range of frequencies. Each chemical species has its own sequence of excited states, so exhibits its own characteristic absorption spectrum.

Absorption spectroscopy can give also quantitative information about the concentration of a chemical species in solution; this is expressed by the Beer-Lambert Law which affirms that for monochromatic radiation of given energy:

$$I_t = I_0 \times 10^{-\varepsilon bc} \qquad \textit{Eq. 3.2-1}$$

Where I_t is the intensity of the radiation transmitted by the sample, I_0 is the intensity of the incident radiation, b is the optical path (in cm), c the solution molar concentration and ε the molar absorption coefficient, which is a constant for a given chemical specie and energy of the radiation (**Figure 3.2-2**).

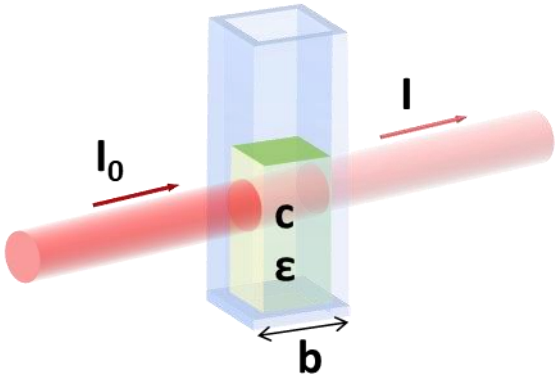

Figure 3.2-2: An illustration of light passing through a cuvette of path length b containing a sample with concentration c and molar absorption coefficient ε. Absorption is evident by the diminished intensity of the transmitted radiation I, as compared to the incident radiation I0.

The Beer-Lambert Law can be linearized introducing a quantity called *Absorbance*,

$$A = \log I_0/I_t = \varepsilon bc \qquad \textit{Eq. 3.2-2}$$

Another quantity often used in spectra is the *Transmittance*,

$$T = I_t/I_0 \qquad \textit{Eq. 3.2-3}$$

The instrument used to perform UV-Vis absorption spectroscopy is called spectrophotometer. There are two major classes of devices: single beam and double beam. The basic parts of a single-beam spectrophotometer are a polychromatic light source, a diffraction grating in a monochromator to select the measuring wavelength, a holder for the sample and a detector. The radiation source is often a deuterium arc lamp, which is continuous over the ultraviolet region (190-400 nm), and a Tungsten Lamp or a Xenon arc lamp. The detector is typically a photomultiplier tube, a photodiode, a photodiode array or a charge-coupled device (CCD). Single photomultiplier tubes or photodiode detectors are used with scanning monochromators, which filter the light so that only light of a single wavelength reaches the detector at one time. The scanning monochromator moves the diffraction grating through each wavelength so that the intensity of transmitted light may be measured as a function of wavelength. A different kind of spectrophotometer makes use of a photodiode array or CCD. In this case, the sample is probed with polychromatic light, and the transmitted light is then dispersed by a fixed monochromator before reaching the CCDs or the photodiode arrays. As both of these devices consist of many detectors grouped into one or two-dimensional arrays, they are able to collect light of different wavelengths on different pixels or groups of pixels simultaneously, so that is possible to record a complete spectrum in time as short as 12 ms.[344] In a single-beam spectrophotometer the measurement requires the alternate insertion of reference and sample cells in the sample holder, thus errors are introduced by fluctuation of the light source and drift in the detector system. To avoid these problems double beam spectrophotometers were introduced (**Figure 3.2-3**).[345] In a double beam system the analysing light beam is split into two parts after the monochromator so that the two beams pass at the same time through the sample and the reference cells and are collected at the same time by two detectors.

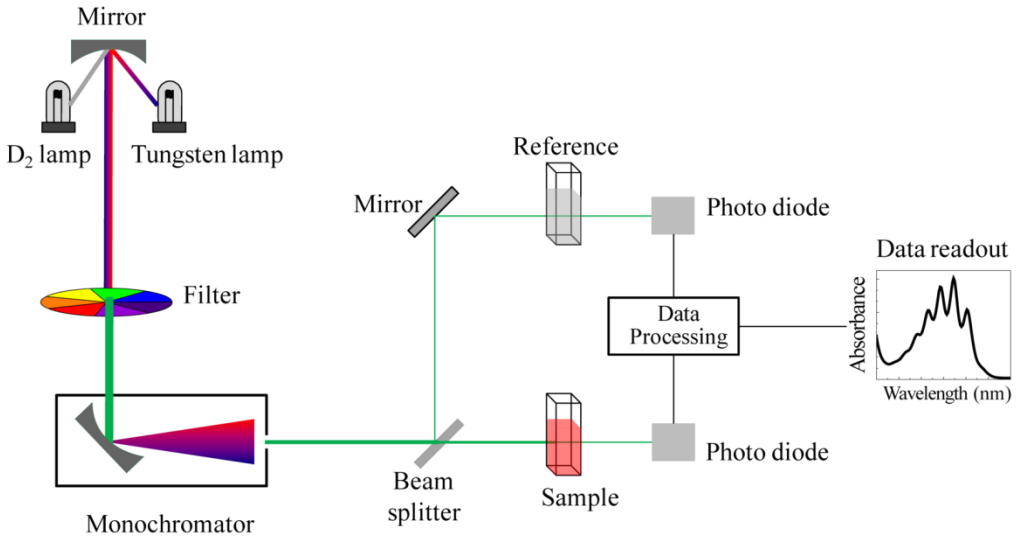

Figure 3.2-3: Schematic of a double-beam UV/Vis spectrophotometer. Adapted from [345]

3.2.2.2. *Instrumentation and operating conditions*

In this thesis, UV-Vis spectroscopy has been used to characterize the transmittance of the chemically modified GO and rGO films in chapter 3 and the transmittance of Cu NWs films and hybrid Cu NWs/rGO films in chapter 4. Spectra were acquired using a double-beam spectrophotometer Jasco V-670 UV-VIS-NIR (JASCO International Co.). Spectra were acquired in the range 200 nm to 800 nm, with a data interval of 1 nm, a UV/Vis bandwidth of 1.0 nm, a NIR bandwidth of 2.0 nm, response: Fast, scan speed: Step scan, filter exchange: Step. The light sources were a deuterium arc lamp for the UV range and a tungsten lamp for the visible. The source was changed at 340 nm.

3.2.3. Raman spectroscopy

3.2.3.1. *Description of the instrument and theoretical principles*

Vibrational spectroscopies are powerful techniques for the characterization of molecules and molecular structures. In fact, from the vibrational modes, it is possible to determine the functional groups present in the sample, as well as characteristic fingerprints of the analysed sample. Among these, Raman spectroscopy is particularly used to analyse in a non-destructive way the surface composition of the most disparate samples. The working principle of Raman spectroscopy is the inelastic scattering of light. This phenomenon is induced by excitation of matter with photons having energy not necessarily leading to an electronic excitation of the compound involved. Such photons, often leading to a "virtual state", and not to an electronically excited state induce a dipole in the molecule analysed, which yields inelastic scattering, hence the scattered light has a different energy than the incident photon used to produce the excitation. Stokes scattering occurs when the inelastically scattered photon has lower energy than the incident one, with the difference in

energy corresponding to one or more quanta of vibrational energy, hence leaving such a molecule in a vibrationally excited state. On the contrary, anti-Stokes scattering is observed when the scattered photon has higher energy than the exciting one: this happens when the molecule originally resided in a non-zero vibrational level prior to excitation (**Figure 3.2-4** a). It follows that in equilibrium conditions the intensity of the anti-Stokes Raman bands depends on the population of the vibrationally excited states (given by Boltzmann distribution).

The Raman spectrophotometer is composed by a monochromatic laser that is focussed on the sample through a lens, which also collects the laser scattered light. Then the scattered laser light passes through a filter, which removes the intense Rayleigh scatter, and is subsequently separated into the different wavelengths by passing through a spectrometer or an interferometer and finally collected by a detector (**Figure 3.2-4** b).

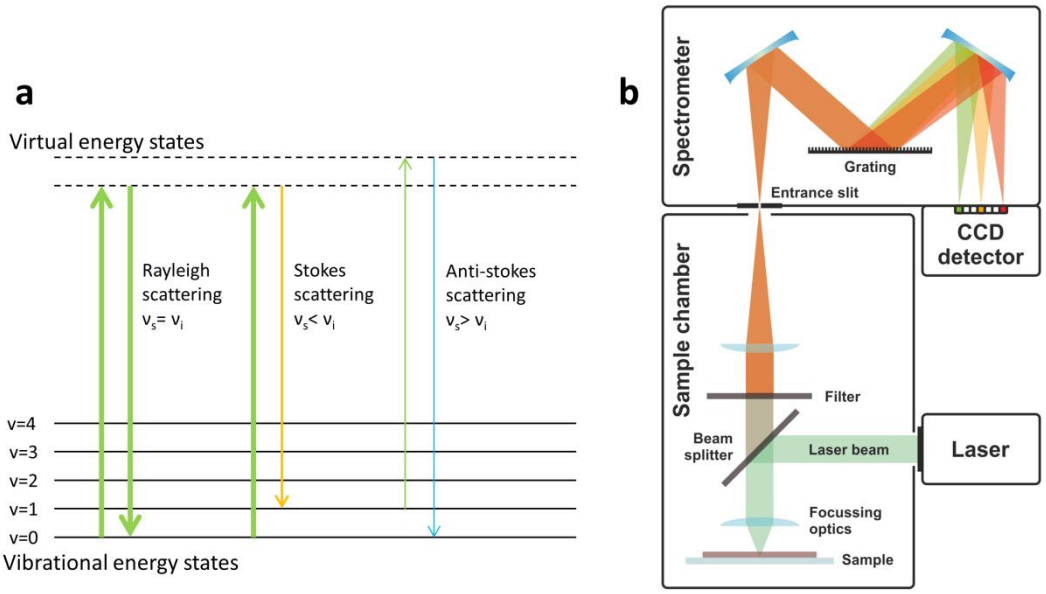

Figure 3.2-4: (a) Schematic of the mechanism of elastic and inelastic Raman scattering. (b) Schematic structure of a Raman spectrometer.

3.2.3.2. *Instrumentation and operating conditions*

In this thesis Raman spectroscopy has been employed to characterize GO, rGO and chemically modified GO/rGO presented in chapter 4. All the Raman spectra were acquired with a Renishaw InVia RE04 combined with a MS20 Encoded stage 100 nm and a 532 nm laser maintained at a power excitation below 1 mW (laser power of 1 %). The measurements were carried out in ambient conditions with a 100x lens affording a beam spot of 800 nm. The silicon 1s peak at 520.3 cm^{-1} was taken as reference for wavenumber calibration.

3.2.4. Infrared (IR) spectroscopy

3.2.4.1. *Description of the instrument and theoretical principles*

Infrared (IR) spectroscopy is one of the most common and widely used spectroscopic techniques. IR spectroscopy uses photons with energies in the infrared range. These photons do not have enough energy to excite electrons in a molecule, however, they can be absorbed by a molecule that possesses a vibrational frequency that matches the frequency of the exciting IR radiation. Upon absorption of this quantised energy, in fact, the molecule is excited to a vibrationally excited state. Almost all the structures containing covalent bonds absorb IR energy because each covalent bond behaves like a stiff spring that can be stretched or bent. In particular, a molecule composed of n atoms presents 3n-6 vibrational degrees of freedom or vibrational modes (or 3n-5 for linear molecules). Of these 3n-6 vibrational modes are active in the IR only those which are associated with a change in the dipole moment of the molecule. On the contrary, in Raman spectroscopy, the vibrational modes that produce a change in the polarizability of the molecule are active; for molecules that are centrosymmetric (e.g. benzene), the modes that are active in Raman are not active in IR and vice-versa. For this reason, the two are often considered as complementary techniques.[346]

In IR spectroscopy, the analysed sample is hit by polychromatic IR light and the intensity of the transmitted or reflected light (depending on the measurement mode) is collected and measured at each frequency and conveyed in a IR spectrum. In the spectrum the intensity is presented as a function of the energy, usually expressed as wavenumber $\tilde{\nu}$ (cm^{-1}) which is equal to $1/\lambda$ (cm). The spectrum presents as many peaks as many active vibrational modes exist in the sample. In general, bending modes are present at low wavenumbers (low energies), while stretching modes have higher energies. In particular, for stretching modes, the frequency of vibration is correlated to the mass of the atoms and the strength of the bonds involved in the vibration. The vibrational frequency of a covalent bond between two atoms of mass m_1 and m_2 respectively is expressed by the equation:[346]

$$\tilde{\nu} = \frac{1}{2\pi c}\sqrt{f \cdot \frac{m_1 + m_2}{m_1 \cdot m_2}} \qquad \textit{Eq. 3.2-4}$$

In which f is a force constant proportional to the strength of the covalent bond. Stronger bonds and lighter atoms have higher stretching frequencies. The intensities of the peaks are instead correlated to the dipolar moment change in the molecule: the higher is the dipolar moment change produced by a vibrational mode, the higher will be the corresponding peak intensity. IR spectroscopy is usually used for the qualitative determination of compounds and identification of functional groups present in the sample. However, it is possible to use IR absorbance spectroscopy for quantitative analysis of the concentration of a substance by

applying the Beer-Lambert law that we have seen in the UV-Vis absorption spectroscopy paragraph.[347]

The most diffuse IR spectrometer is the Fourier transform IR spectrometer (FT-IR), however, instruments equivalent of a UV-Vis spectrophotometer, consisting of a moving monochromator and a detector or a fixed monochromator and a photodetector array also exist. In both kinds of instruments, the light source is a globar emitting polychromatic IR light and the detectors are usually pyroelectric detectors. Semiconductive photoelectric detectors or cooled photodiodes and bolometers are also used.[348] The FT-IR is based on the working principle of Michelson interferometer (**Figure 3.2-5**). In this technique, all the polychromatic light is shined on the sample and collected by the detector simultaneously. The advantages of FT-IR spectrophotometer are a higher signal-to-noise ratio, a faster acquisition time and a higher reachable resolution. A source of coherent light is used. Before reaching the sample the light passes through a beam splitter, which reflects half of the light on a fixed mirror, while the other half is transmitted to a moving mirror; then the light beams reflected by both mirrors are recombined together, shined on the sample and transmitted (or reflected) by this to the detector. When the two beams coming from the two mirrors are combined together, these create constructive or destructive interference. In the beginning, when the two mirrors are at the same distance from the beam splitter, both the light beams have travelled the same optical path length, and the interference is constructive. However, when the moving mirror is shifted, the light that is reflected by this will have travelled a longer distance, and when will meet the light coming from the fixed mirror will create a destructive or constructive interference depending on the difference in the path length travelled by the two beams and thus by the difference in the phases of the two beams. Different wavelengths are modulated at different rates, so that at each moment the beam coming out of the interferometer is still polychromatic, but has a different spectrum. The signal is recorded as the intensity of the polychromatic light as a function of the mirror position. The IR spectrum is obtained by applying the Fourier transform to the recorded interferogram.[347, 348]

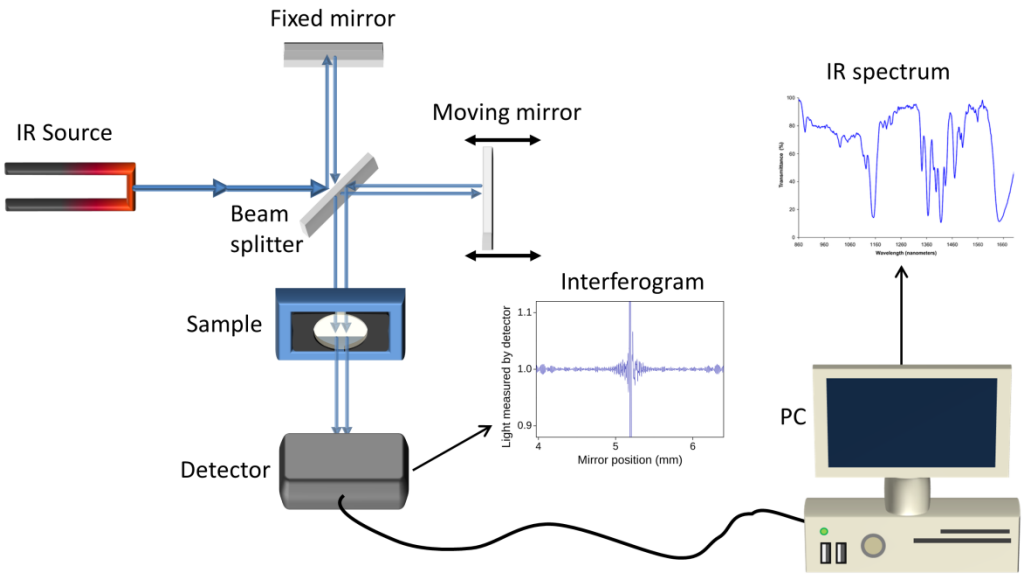

Figure 3.2-5: Schematic of a FT-IR spectrophotometer.

3.2.4.2. *Instrumentation and operating conditions*

In this thesis, IR spectroscopy was used to characterize most of the synthesized materials, including GO, rGO, chemically modified GO/rGO and the NTEG molecule presented in chapter 4 and the Cu NWs presented in chapter 5. The IR spectra were acquired with a Thermo Scientific Nicolet 6700 FT-IR spectrometer. The instrument was operated in attenuated total reflectance (ATR) mode, equipped with a diamond crystal on which the sample was deposited. The instrument was equipped with a triglycine sulfate (TGS) pyroelectric detector and a KBr beam splitter. The spectra were acquired between 400 and 4000 cm^{-1} and a resolution of 4 cm^{-1} was used. 16 scans were acquired to increase the signal-to-noise ratio.

3.2.5. X-ray diffraction

3.2.5.1. *Description of the instrument and theoretical principles*

X-ray diffraction (XRD) is a useful technique that allows determining the crystallographic structure of a material. XRD works by irradiating a material with incident X-rays and then collecting the X-ray scattered by the material at different angles. The working principle of X-Ray diffraction is based on the elastic scattering of X-ray light by the atoms of a material. Each atom that is hit by X-ray radiation generates a spherical wave of scattered radiation. In a material with a regular arrangement of atoms (i.e. a crystal) all the spherical waves scattered by each repeating unit meet and create constructive and destructive interference. In particular, the interference is destructive in most directions, except those that satisfy the Bragg's Law (**Figure 3.2-6**):

$$n\lambda = 2d \sin\theta \qquad \textit{Eq. 3.2-5}$$

where n is an integer number, representing the "order" of reflection, λ is the wavelength of the incident X-rays, d is the interplanar spacing of the crystal and Θ is the diffraction angle.[349, 350]

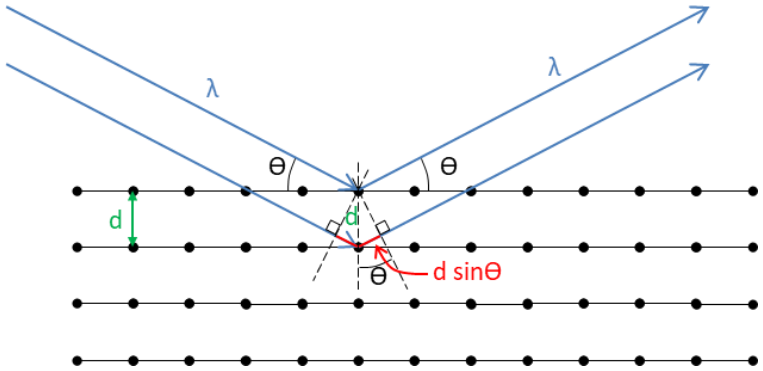

Figure 3.2-6: Schematic of the X-ray interaction with a crystal lattice: Bragg's law

We can notice from the equation that the bigger is d, the smaller is the angle θ : for studying long periodicities present in a sample, such as a nanoparticle distribution, another related technique called small-angle X-ray scattering (SAXS) is used. It is also clear from the equation the relation between the wavelength of the radiation and the length scale of the interplanar spacing d. X-rays have wavelengths in the tenths and hundredths of nanometre range, making thus possible to discern periodicities in the same range of distances, such as those of chemical bonds. If the analysed sample is a single crystal, when this is hit by the X-ray beam, it will generate a series of spots, or reflections, on a screen behind the crystal, each one corresponding to a periodic distribution of atoms within the crystal. The intensities of these spots are determined by the distribution of electrons within each repeating atom in the crystal. By rotating the crystal in different directions, it is possible to discern all the periodic planes that are present in the crystal. All the collected diffraction spots are the reciprocal space representation of the crystal lattice: by applying the Fourier transform to the collected diffraction peaks it is possible to reconstruct the electron density map within the unit cell in the crystal. For single crystals of sufficient purity and regularity, X-ray diffraction data can determine the chemical bond lengths and angles with a precision up to few thousandths of an angstrom and tenths of a degree, respectively, as well as the unit cell parameters.[350, 351]

If the sample is not a single crystal but is composed by many small crystals randomly oriented, as it happens in powders and in polycrystalline materials, the incident X-ray beam will see all the possible interatomic planes, and the diffraction pattern will transform from a series of spots to a series of concentric circles, each one corresponding to a d spacing in the crystal lattice. Actually, in powder XRD, the data are collected with a different mechanism. Usually, the reflection geometry is used. In this case, the X-ray beam is fixed, and the sample

is rotated of an angle θ respect to the incident beam, while the detector is simultaneously rotated of an angle 2θ respect to the incident beam. The sample (and the detector consequently) are scanned to a range of 2θ angles, typically from few degrees up to 90 degrees, and intensity of the scattered beam is recorded by the detector (**Figure 3.2-7**). The diffractogram reports the collected intensity of the scattered X-ray as a function of the angle 2θ. To each peak present in the diffractogram correspond a d spacing in the sample. The peak positions, intensities, widths and shapes provide important information about the composition of the sample, making possible to identify different phases and substances, the dimensions of the crystallites, the presence of amorphous phase, stress, strain and preferred orientation in the material.[348, 351]

The X-rays can be generated by either X-ray tubes or synchrotron radiation. In X-ray tubes, which are usually the X-ray source used in laboratory instruments, X-rays are generated by bombarding a metal target with an electron beam accelerated across a high voltage field. As electrons collide with the metallic atoms in the target, they produce a continuous spectrum of X-rays, called Bremsstrahlung radiation, due to the deceleration of the electrons in the target. In addition to this background radiation, when the high energy electrons hit the target atoms, X-ray photons of energy characteristic of the target material are also emitted. It is this monochromatic radiation, called K_α lines that is separated from the background radiation and focussed with a system of lenses on the analysed sample. Copper is a common target used in x-ray tubes that emits a K_α radiation with wavelengths of 1.54 Å. [348, 351]

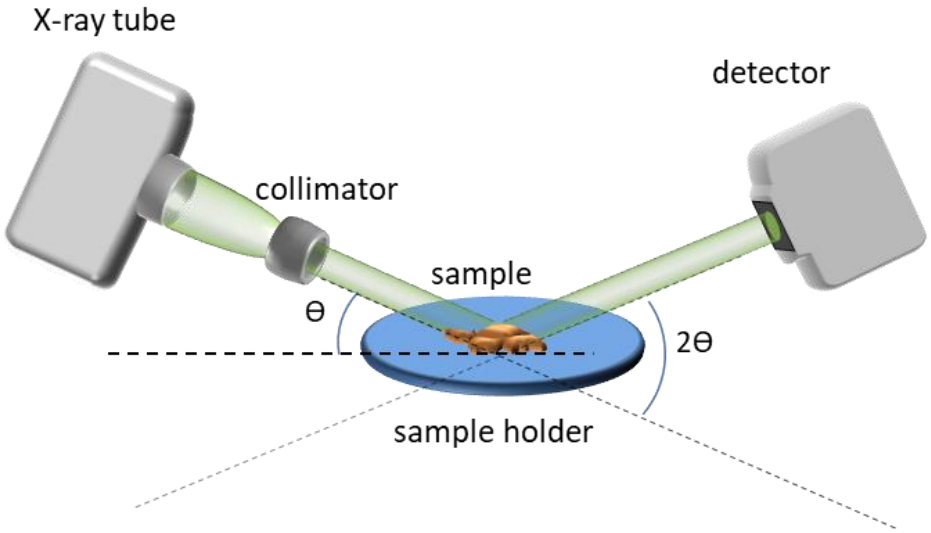

Figure 3.2-7: Schematic of a X-ray powder diffractometer.

3.2.5.2. *Instrumentation and operating conditions*

In this thesis work, XRD powder diffraction has been used to determine the interlayer distance between the different layers of GO, rGO and functionalized GO/rGO. The X-Ray Diffraction (XRD) measurements were performed in specular geometry using a SmartLab-Rigaku diffractometer equipped with a rotating anode (Cu Kα, λ = 1.54180 Å), followed by a

parabolic mirror to collimate the incident beam and a series of variable slits (placed before and after the sample position).

3.2.6. Thermogravimetric analysis (TGA)

3.2.6.1. *Description of the instrument and theoretical principles*

Thermogravimetric analysis (TGA) is a technique of thermal analysis in which the mass of a sample is monitored as a function of temperature and time as the analysed sample is subjected to a controlled temperature program in a controlled atmosphere. TGA allows evaluating and quantifying processes such as gas adsorption/desorption, solvent loss, phase transitions, thermal decomposition, pyrolysis and reaction with carrier gases (oxidation, reduction, combustion). The instrument for TGA is depicted in **Figure 3.2-8**: it consists of a sample pan that is supported by a precision balance. The pan resides in a furnace that is heated or cooled during the experiment and which atmosphere can be controlled. The mass of the sample is monitored during the experiment. A gas purge allows controlling the atmosphere inside the furnace: the inert or a reactive gas flows over the sample and exits through an exhaust. The measurements can be performed using the static, dynamic or quasi-static methods. In the static TGA, the mass of the sample is measured while keeping the temperature constant at a given value. In dynamic TGA the mass of the sample is measured while increasing or decreasing the temperature with a fixed heating rate (temperature ramp). The two methods can be combined together in the quasistatic TGA. With TGA it is possible to quantify the components of composite compounds, assess the thermal stability of a material, calculate the kinetics of reactions such as thermal decomposition, oxidation and combustion. TGA can be coupled with other instruments, such as FT-IR and mass spectrometry, to analyse and identify the gases evolved by the sample during the heating process, thus permitting a higher comprehension of the decomposition processes.[352, 353]

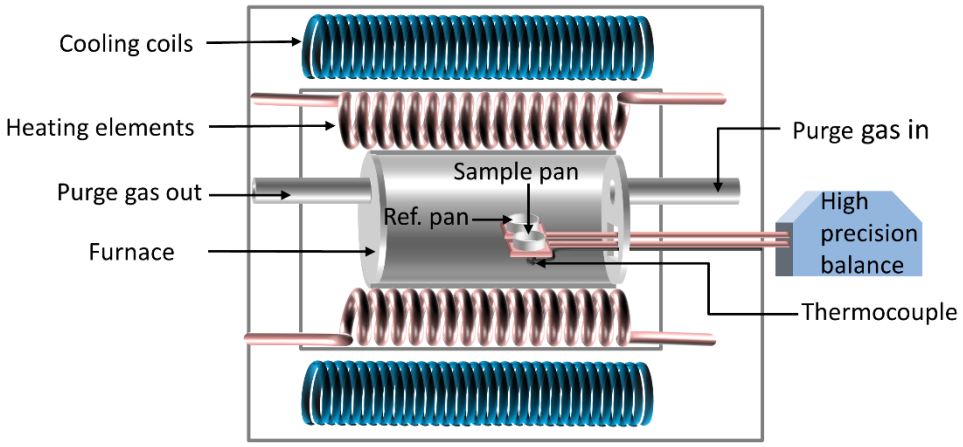

Figure 3.2-8: Schematic of a thermogravimetric analyser (TGA).

3.2.6.2. *Instrumentation and operating conditions*

In this thesis, TGA was used to assess the thermal stability and composition of GO, rGO, and chemically modified GO/rGO that are presented in chapter 4. TGA was conducted using a Mettler Toledo TGA/DSC 2 system, with a heating rate of 10 °C min^{-1} from 25 °C to 800 °C under argon atmosphere.

3.2.7. Electrical measurements

3.2.7.1. *Description of the instrument and theoretical principles*

In this thesis, electrical measurements have been used to characterize the humidity response of the humidity sensor device based on chemically modified GO presented in chapter 4 and to characterize the electrical conductivity of the transparent conductive films based on the hybrid Cu NWs/rGO presented in chapter 5. The characterization of the humidity response of the humidity sensor was performed by measuring the electrical resistance of the two-terminal device. To do so, the two electrodes of the device were electrically connected to a source-meter unit (SMU). A SMU is an electronic instrument that is capable of both sourcing and measuring at the same time. It is equipped with a highly stable direct current (DC) power source that can operate as a constant voltage source or as a constant current source, and of a high precision multimeter, that can measure with high precision and resolution differences of potential and currents simultaneously. In particular, SMUs can have a resolution as little as few fA, and few μV and can source and measure both positives and negatives currents and voltages. They can be connected to a PC and perform automated testing, with a series of programmable functions, useful for I-V characterization of devices. Typically, they can reach a sampling rate of more than 1000 samples per second. SMUs can measure currents and differences of potential, the electrical resistance (R) of the device can be extracted by applying the Ohm's law:

$$R = \frac{V}{I} \qquad \textit{Eq. 3.2-6}$$

In which V and I are the applied/read difference of potential and current, respectively.

In addition to the SMU, a four-point probe was used to measure the electrical resistance of the transparent conductive films developed in chapter 5. A four-point probe is a simple apparatus for measuring the average resistance of a thin layer or sheet. The use of a four-point probe consents the separation of current and potential to eliminate the contact resistance in a measurement. This makes measurements much more accurate since the contact resistance can often have the same magnitude as the sheet resistance. Typically, a constant current is applied to two probes, and the potential on the other two probes is measured with a high-impedance voltmeter. A geometric factor needs to be applied according to the shapes of the four-point array, which most commonly are in square and in-

line. A four-point probe consents the direct measurement of the sheet resistance, which is a special case of resistivity for a uniform sheet thickness.

The sheet resistance R_s is equal to the resistivity ρ divided by the thickness of the film.

The resistance can be written as follow:

$$R = \frac{\rho \cdot L}{A} = \frac{\rho \cdot L}{t \cdot W} \qquad \textit{Eq. 3.2-7}$$

where L is the length of the conductor (in the direction in which the current flows) and A is the cross-sectional area, which can be split into the width W and the sheet thickness t. Thus the sheet resistance can be written as :

$$R_s = R \cdot W / L \qquad \textit{Eq. 3.2-8}$$

As we can see the sheet resistance and the bulk resistance R are dimensionally equal and can be both expressed in Ohms. However, the physical meaning of the two measurements is different, for this reason, the sheet resistance is normally expressed in Ohms/square, commonly denoted Ω/sq or Ω/□, which is dimensionally equal to Ohms.

3.2.7.2. *Instrumentation and operating conditions*

The SMU used was a Keithley 2636A (Tektronix), operated in constant voltage mode. The measurements were executed in voltage sweep mode, with voltage fixed to 2 V, and the current and time points were collected with a sampling frequency of 200 Hz. The sheet resistance measurements were acquired with a Jandel Multiposition Wafer Probe with RM3000 Test Unit (BRIDGE Technology). At least 3 points of each sample were measured to evaluate the sheet resistance.

3.2.8. Water contact angle

3.2.8.1. *Description of the instrument and theoretical principles*

A contact angle is the angle that a drop of liquid creates with a solid or liquid surface on which is deposited. Contact angle is one of the common ways to measure the wettability, hydrophobicity, and the strength of contact in a solid-liquid interaction. Wettability refers to how a liquid deposited on a solid (or a different liquid) substrate spreads out and the ability of liquids to form boundary surfaces with solid states, and it is determined by the balance between the intermolecular adhesive and cohesive forces). In particular, the smaller is the contact angle, the stronger are the adhesive forces and weaker are the cohesive forces, which means that the molecules of the liquid prefer to interact with the substrate than with each other. If the liquid drop is water, as in the case of water contact angle, the more the material is hydrophilic, the lower the contact angle is. The method that we used to determine the

water contact angle is the static sessile drop. The instrument consists of a sample holder, a telescopic camera, an automated syringe and software that controls the syringe, the camera and measures the contact angle (**Figure 3.2-9**). A drop of water is deposited on the surface of a solid through the syringe. Then, the angle between the plane of the solid surface and the tangent line to the contacting edge of the drop is measured using a precision goniometer. Goniometers are telescopic imaging systems that film the behaviour of a drop from when it is deposited on a substrate. Contact angle is measured overtime during the relaxation process or spreading of the drop. In order to reduce statistical error, the measure is repeated several times.

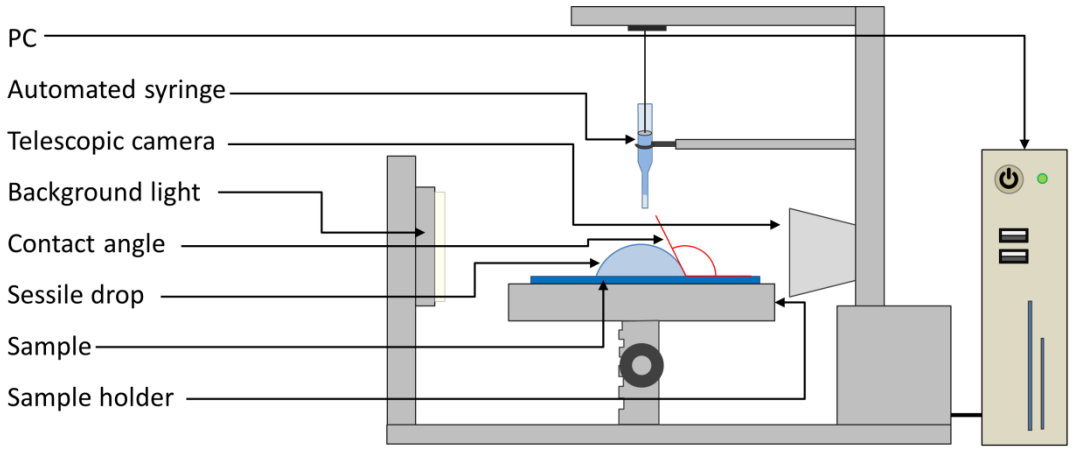

Figure 3.2-9: Schematic of a contact angle instrument

3.2.8.2. *Instrumentation and operating conditions*

The water contact angle was used to measure the hydrophilicity/hydrophobicity of spray-coated films of GO, rGO and chemically modified GOs presented in chapter 4. The measurements were performed with a Krüss DSA100S instrument. To minimize statistical error, 5 sessile drops of water were deposited for each sample. On each drop, 5 consecutive measurements (2 s delay) were performed. For each sample, the 25 drop images were fitted by the Ellipse (Tangent-1) method and the mean values and standard deviation were calculated.

3.2.9. Scanning electron microscopy (SEM)

3.2.9.1. *Description of the instrument and theoretical principles*

A scanning electron microscope (SEM) is a type of electron microscope that produces images of a sample by scanning it with a focused beam of electrons. A SEM is able to provide a high range of magnification, from about 10 times up to 300 000 times, and can achieve resolution better than 1 nanometre.[354] Another unique characteristic of this microscope is the

three-dimensional appearance of the specimen image, which can be interpreted by any observer with no prior knowledge of the instrument.[355]

The microscope is composed by two main parts: the microscope column, which is kept under vacuum by means of a series of pumps and includes the electron gun at the top, the column through which the electron beam passes, and the sample chamber at the base, and the computer that drives the microscope, with the additional bench controls (**Figure 3.2-10**). The electron gun generates free electrons and accelerates these electrons to energies in the range 1-40 keV. The simplest and cheapest gun uses a heated tungsten wire to produce electrons for thermionic emission. Other more expensive types use a crystal of lanthanum hexaboride (LaB_6), which works on the same principle, or a tungsten crystal with an extremely sharp tip, exposed to a large electrical potential, which emits electrons for field emission (FEG).[355] Then the electron beam, accelerated by an anode, enters in the column, in which a series of electromagnetic lenses focus the beam on a nanometric spot on the specimen. The scanning system uses two pairs of electromagnetic deflection coils to scan (raster) the beam across the surface of the specimen. The electrons repulsed by the specimen are collected by an electron detector. The image viewing screen is scanned in synchrony with the beam on the specimen in a one-to-one relationship between points on the specimen and points on the screen.[356, 357]

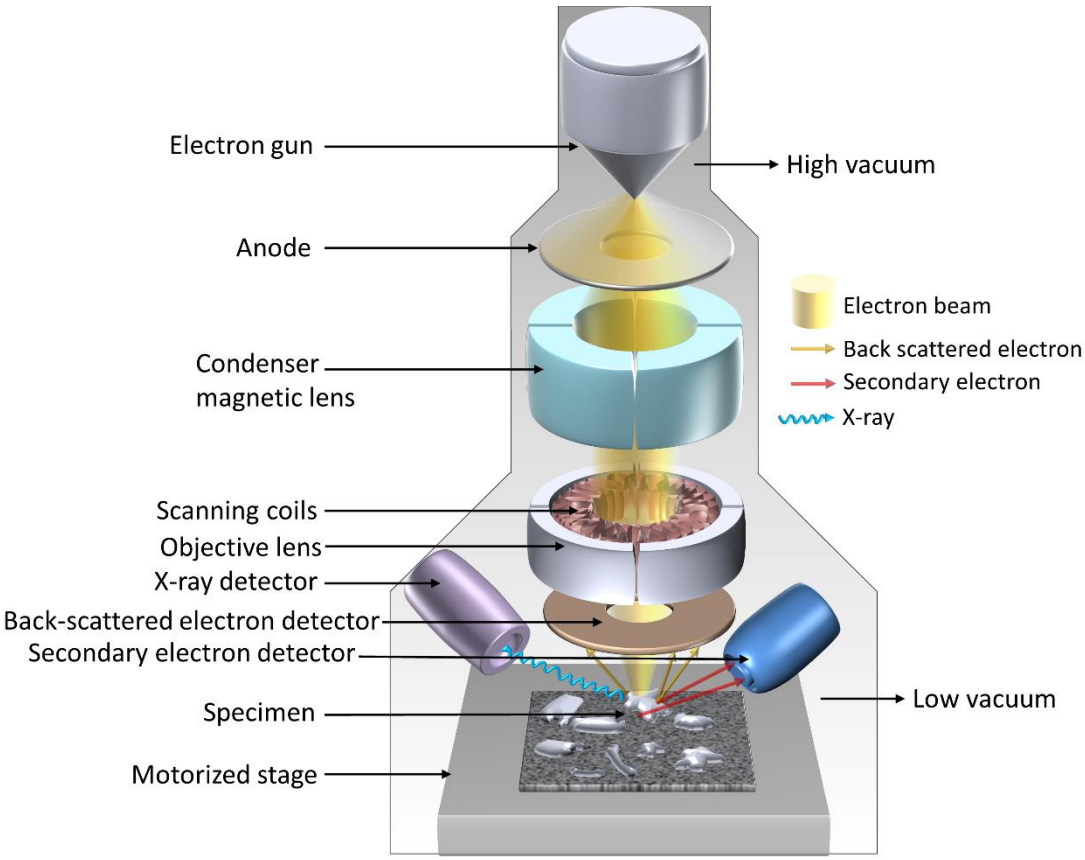

Figure 3.2-10: Schematic layout of a SEM.

Increased magnification is produced by decreasing the size of the area scanned. The electronic image formed on the screen is a result of the beam probe illuminating the sample one point at a time in a rectangular scanning pattern, with the strength of the signal generated from each point being a reflection of differences (e.g. topographical or compositional) in the sample.

When the accelerated electron beam interacts with the atoms of a specimen, it produces a variety of signals which include secondary electrons (SE), reflected or back-scattered electrons (BSE) and photons of characteristic X-rays. Secondary electrons are low energy electrons formed by inelastic scattering and have energies of less than 50eV. These electrons are emitted by the materials in all directions, and are collected by a Everhart-Thornley detector (ETD), which is equipped with a biased grid (typically at 200 – 400 V) for attracting the SE. Because secondary electrons have very low energies, only those produced on the surface of the sample are able to escape and be collected by the ETD. The number of SE produced in a point of the specimen depends on the angle of incidence between the beam and the specimen's surface. Furthermore, electrons emitted from a surface that faces away from the detector or which is blocked by the topography of the specimen will appear darker than surfaces that face towards the detector. Thus, secondary electrons are used to observe the topography and the morphology of the sample's surface. To increase the yield of SE emitted from the specimen, an extremely thin layer (~10 nm) of heavy metals such as gold or platinum is commonly applied to coat non-conductive specimens.

Backscattered electrons are high-energy electrons (>50 eV) from the primary incident beam that are ejected back out from the sample for elastic scattering. BS electrons are reflected at high angles, in direction of the scanning beam; for this reason, they are detected by a ring shaped detector placed at the base of the electron column. BSE are emitted from much greater depths and interaction volume compared to SE, consequently, the resolution of BSE images is generally poorer than SE images. BSE are sensible to the composition of the specimen; particularly in a secondary electrons image contrast tells us about the average atomic number of the sample. Inelastic collisions of high energy electrons with the specimen's atoms produce also characteristic X-rays, which can be detected by a dedicated detector. The wavelength of these X-rays is dependent by the atomic number of the atoms which emit them. The analysis of these characteristic X-rays is called energy-dispersive X-ray spectroscopy (EDS, EDX, or XEDS) or energy-dispersive X-ray analysis (EDXA) and permits the quantitative chemical characterization of the specimen.

The main advantages of SEM are the possibility to reach high resolutions, up to few nanometres and the incredible depth of field (more than 300 times the depth of field of a light microscope) that consents to obtain great topographical detail. Other advantages are the possibility to change magnification of the image without refocusing because the focal distance remains unchanged, and the easiness of the sample's preparation. The drawbacks

of SEM are that it operates under vacuum and in many SEMs the samples must be solid, stable in vacuum and conductive to be viewed. Conductivity is required to avoid that the specimen accumulates electric charge that can create artefacts in the image and degrade the specimen itself. Often it is necessary to render the specimen conductive by coating with a very thin layer of metal or graphite. However, there are a number of different types of SEMs which do not require dry or conductive samples, as “low vacuum" and "environmental" SEMs.[356, 357]

3.2.9.2. *Instrumentation and operating conditions*

SEM has been used to characterize all the surfaces of the materials and devices reported in this thesis. SEM images were recorded with a FEI Quanta FEG 250 instrument (FEI corporate, Hillsboro, Oregon, USA), operated in high vacuum mode (pressure in 10−4 Pa range) and equipped with a ETD for secondary electrons detection. An acceleration voltage between 5 and 20 kV was used.

3.2.10. Atomic force microscopy (AFM)

3.2.10.1. *Description of the instrument and theoretical principles*

Atomic force microscopy (AFM) is one of the scanning probe microscopy (SPM) techniques invented in the 1980s. It is an important technique for acquiring topographic information of conducting and insulating surfaces with high resolution that can reach the atomic scale. In addition to characterizing the surface topography of a surface, AFM can also be used in force mode, to measure local properties of a surface such as elasticity, hardness, adhesion and surface charge densities. In this case, the AFM can measure the forces between the probe and the sample as a function of their mutual distance. In imaging mode The AFM raster the surface of the sample with its probe and records the height of the sample by adjusting its height to keep constant the probe-sample interaction. As shown in **Figure 3.2-11**, an AFM consists of a tip, mounted on an oscillating cantilever, scanning the surface of the sample. The fine movements of the cantilever in height and laterally are obtained by means of accurate piezoelectric motors. In particular, the cantilever is mounted on three piezoelectric crystals, each one responsible for displacements along a given axis (x, y, z) as depicted in **Figure 3.2-11**. An alternate difference of potential applied to conductive areas of the tube determines the piezo expansion/restriction along the three axes.[358] A laser beam hits the rear side of the cantilever, causing a reflection, recorded by a photo-diode system. While scanning the sample, the tip on the extremity of the cantilever interacts with the sample surface causing a deflection of the cantilever. The deflection of the cantilever causes the laser reflected by the backside of the cantilever to change its reflection spot which is recorded by the photodiode (**Figure 3.2-11**). By mapping the deflection information of each scanned point, the sample surface morphology can be acquired.

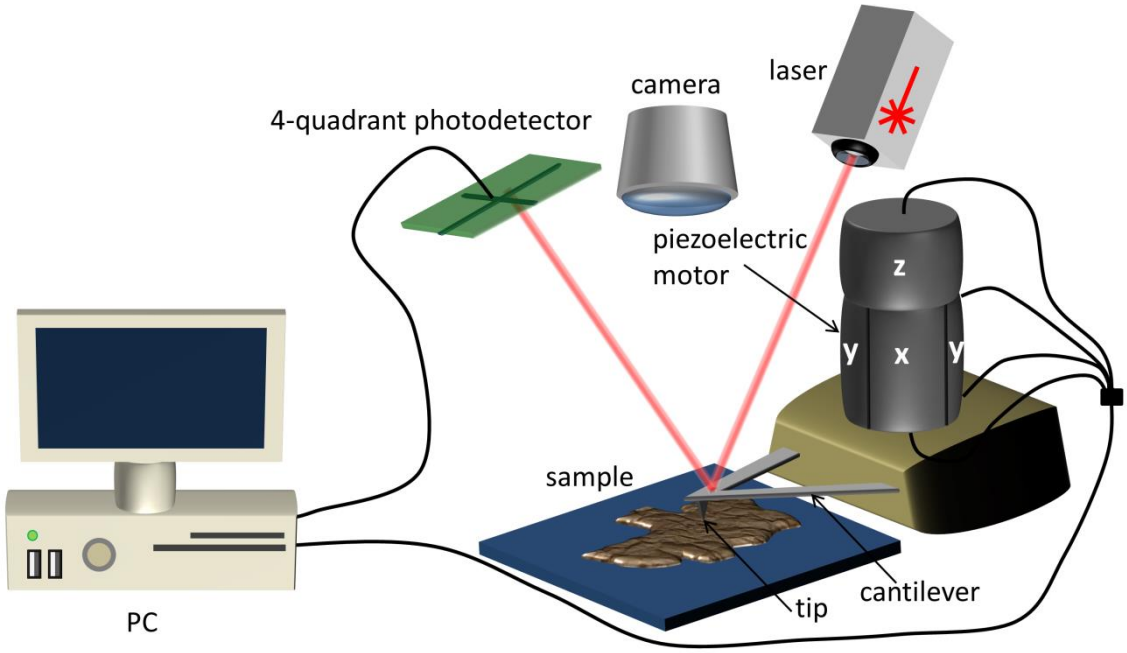

Figure 3.2-11: Schematic of an AFM

The AFM imaging can be performed in contact, tapping (i.e. intermittent contact) or non-contact mode. In contact mode, the tip of the AFM is in physical contact with the sample and "drags" the surface, thus it risks being damaged by the interaction with the substrate or pulling parts of the sample. For this reason, our experiments were always performed in the tapping mode. The topography of the surface induces changes in the amplitude and phase of the oscillation of the cantilever. These changes are measured point by point. Upon integrating measurements carried out on N × N points forming a square array, an image can be drawn providing a direct map of the topography of the surface of the studied sample. Usually, the AFM measurements are performed in constant-height mode. This means that each time that the tip distances or approaches the surface and the amplitude is consequently increased or reduced, the tip is automatically respectively lowered or raised by a system of feedbacks to keep constant the amplitude and thus the distance with the sample.[358] The constant height mode necessitates an onerous feedback mechanism but avoids either losing the interaction with the surface or damaging the tip and sample. In order to increase the quality of the results obtained during AFM experiments, each spot is being recorded and analyzed twice (trace, retrace).

3.2.10.2. *Instrumentation and operating conditions*

In this thesis, AFM was used to characterize the topography of the hybrid films used as humidity sensors in chapter 4 and as transparent conductive electrodes in chapter 5. The characterization of the devices was performed with a Bruker Dimension Icon microscope under ambient conditions, operating in tapping mode and using TESPA-V2 tips with spring constant k = 42 N/m.

3.2.11. Optical microscopy

3.2.11.1. *Description of the instrument and theoretical principles*

An optical microscope, often referred to as light microscope, is a type of microscope which uses visible light and a system of lenses to magnify images of small samples. The first examples of optical microscopes appeared in the late 17th century, and the name "microscope" firstly appeared in 1624 in a text of "Accademia dei Lincei" referred to the microscope that Galileo had invented 15 years before.[359] Basic optical microscopes can be very simple, although many complex designs exist which aim to improve resolution and sample contrast. All standard microscopes are compound microscopes. A compound microscope is composed of two lenses or a group of lenses, an objective and the eyepiece, and a light source. The objective lens, which is close to the specimen being observed, collects light and focuses a real magnified image of the specimen inside the microscope. That image is then magnified by a second lens or group of lenses, called the eyepiece, that gives the viewer an enlarged inverted image of the specimen. The image of the specimen formed inside the microscope can be captured by a digital camera to form a digital image. Modern microscopes possess exchangeable objective lenses to adjust the magnification. Since all the lenses produce various kinds of aberrations, more expensive microscopes combine several lenses inside the objective to correct these aberrations.

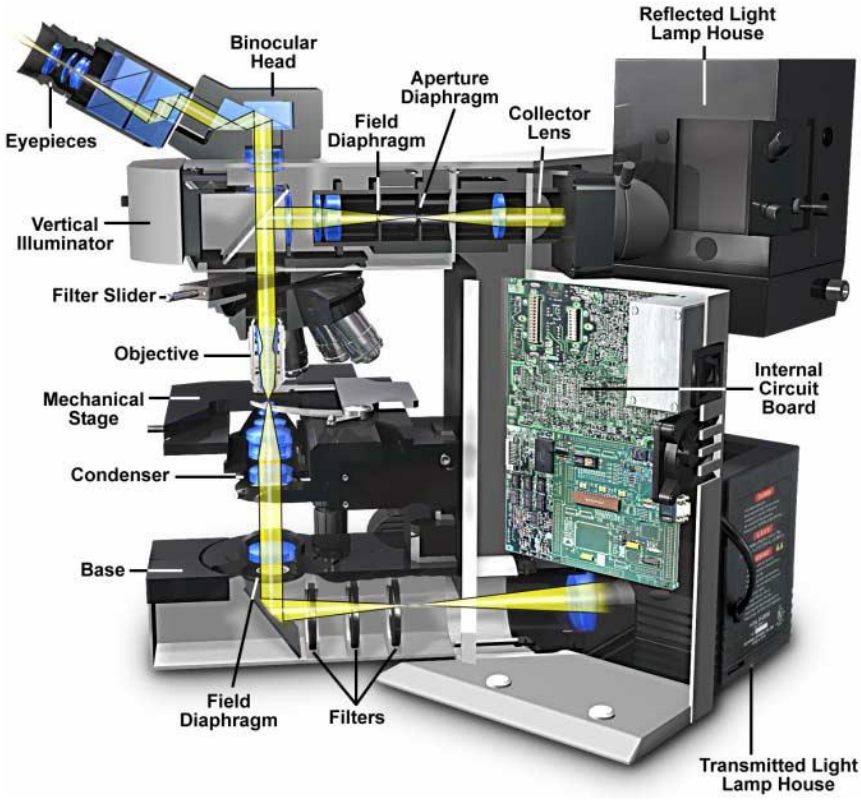

Figure 3.2-12: Scheme of a modern microscope. (Adapted from [360])

Assuming we can correct all the aberrations, the maximum resolution (e.g. the resolving power) of an optical microscope is given by the diffraction limit and can be expressed by the formula:[361]

$$R = \frac{0.61 \cdot \lambda}{N.A.} \qquad \textit{Eq. 3.2-9}$$

Where 0.61 is a geometrical term, λ = wavelength of the source of illumination and N.A. is the Numerical Aperture, which is a measure of the light-gathering capabilities of an objective lens. The more light is collected by an objective lens, the higher is N.A. and thus the resolution. For an objective in air, N.A. cannot be higher than 1.0, consequently, the maximum resolution is around 200 nm. On the other hand, a high numerical aperture produces a low depth of field (DOF), which is proportional to λ / ($N.A.$). The depth of field is the vertical distance between the highest and the lowest point in an object that appear acceptably sharp in an image.

An optical microscope can operate in transmitted light and reflected light. The most common types operate in transmitted light: the light emitted by a light source (often a halogen lamp) beneath the sample's stage is focused by a condenser onto the sample, passes through it and is collected by the objective lenses. In this kind of microscope, it is necessary that light passes, at least partially, through the sample, therefore it is not suitable for completely opaque samples.

A reflected light microscope, often referred to as incident light, overcomes this limitation, and permits to observe a wide range of specimens that includes most metals, ceramics, many polymers, semiconductors, and a wide variety of specialized materials.

The light, emitted by a lamp in the upper part of the microscope (see **Figure 3.2-12**), passes through the vertical illuminator (which has a role similar to the condenser) and is reflected by a beamsplitter through the objective to illuminate the specimen. Light reflected from the surface of the specimen re-enters the objective and generates an image that can be collected by the eyepiece or by the digital camera. Many microscope manufacturers offer models that permit the user to alternate or simultaneously conduct investigations using both reflected and transmitted illumination, like the Olympus BX51 that we used. Both kinds of microscopes can operate with various techniques which modify the light path to generate an improved contrast image from a sample. The most common technique is *bright field* illumination in which sample contrast comes from the absorbance of light in the sample. In *dark field* illumination sample contrast comes from light scattered by the sample. In *phase contrast* illumination sample contrast comes from the interference of different path lengths of light through the sample. In *cross-polarized light* illumination, sample contrast comes from the rotation of polarized light through the sample. In an epifluorescence microscope the sample

is illuminated with UV-light by means of an excitation filter interposed between the lamp and the sample; another filter, which blocks UV-light and transmits only visible light, is interposed between the objective and the eyepiece and permits to collect only light emitted from the sample by fluorescence or phosphorescence.

3.2.11.2. *Instrumentation and operating conditions*

Optical and fluorescence images were taken with an Olympus BX51 optical microscope (Olympus America Inc.) operating in reflection mode, equipped with 5 objectives M Plan Semi-Apochromat - MPLFLN-BD (5X, 10X, 20X, 50X, 100X), a X-Cite series 120 fluorescence cube 37088 U-MWBS3 (excitation wavelength from 450 to 490 nm) and a 5 Mpx CMOS camera.

3.3. Materials

3.3.1. Copper nanowires

Metal nanowires (NWs) are 1D nanostructures characterized by a thin diameter in the 1-100 nanometre range and really high aspect ratio. Metal NWs have gained great interest for applications in optoelectronics, micro/nanoelectronics, sensing and catalysis due to their excellent electrical conductivity and mechanical flexibility resulting from their nanometric dimensions. However, their major attractiveness comes from the fact that when they are uniformly randomly distributed over a substrate, they can form a conductive, yet transparent network. Such characteristic has made metal NWs among the most promising materials for transparent conductive electrodes. Their large aspect ratio allows the formation of percolation networks with a low content of NWs compared with other structures. Transparent electrodes based on Ag NWs have demonstrated performances even superior to those of conventional electrodes based on indium-tin oxide.[362] Nonetheless, the high cost of silver is the major drawback to the large-scale application of Ag NWs. Copper is 100 times cheaper and 1000 times more abundant than silver and has a similar electrical conductivity.[363] For these reasons, Cu NWs have emerged as an alternative to Ag NWs.

Copper nanowires are usually synthesized following a bottom-up approach. Methods include vacuum thermal decomposition, chemical vapour deposition (CVD), electrospinning and solution based synthesis.[364] Solution based methods are the most used because of the facile scale-up for large-scale production and possibility to choose among a wide range of precursors, reaction conditions and solvents. All the reported solution-based synthesis methods involve the reduction of copper ions (Cu^{+} or Cu^{2+}) in solution to its metallic state in the presence of a capping agent which encourages 1-dimensional growth. All the reported methods involve the use of primary alkyl amines to coordinate copper ions and direct the growth of the copper (0) crystal seed along a specific direction by selectively adsorbing on specific faces of the newly generated seeds (**Figure 3.3-1**).[365] Depending on the exact

mechanism of Cu NWs growth, these can have single-crystalline structure or polycrystalline fivefold twinned structures. The former present a lower aspect ratio, higher conductivity and oxidation resistance, while the latter have superior flexibility and higher mechanical strength and aspect ratio. In particular, single-crystalline Cu NWs grow from single-crystalline seeds, while fivefold twinned Cu NWs grow from decahedral seeds with a multiply twinned structure.

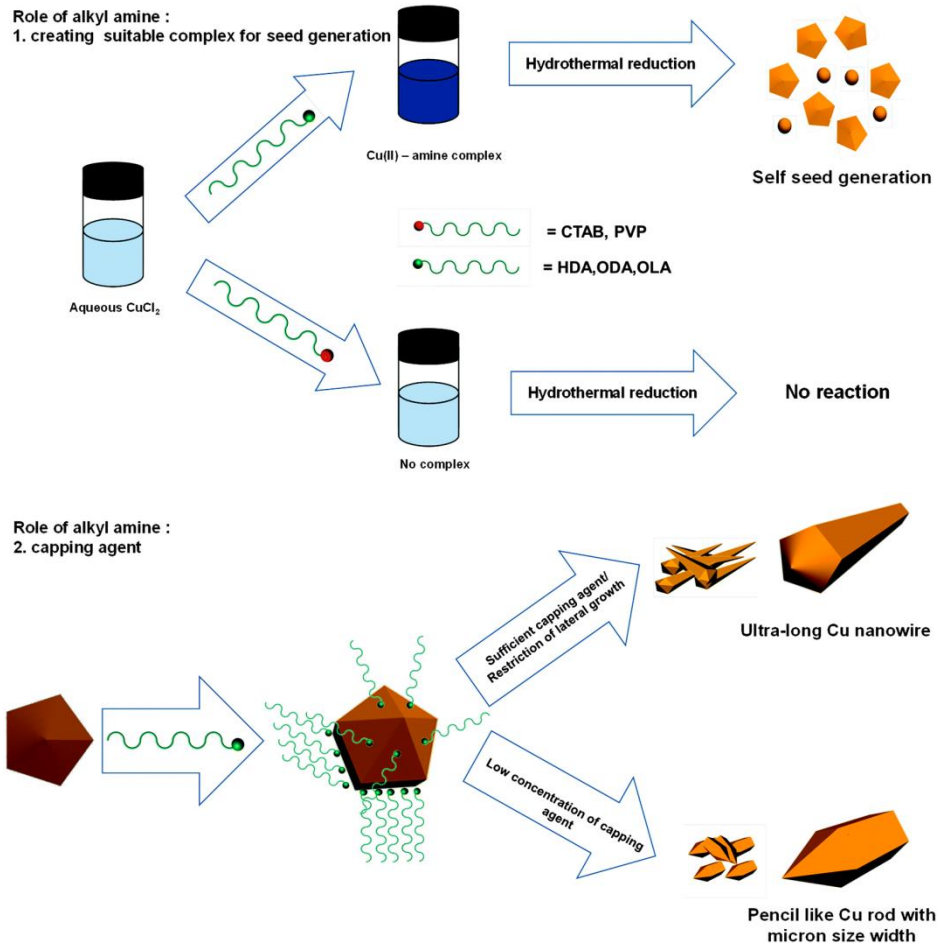

Figure 3.3-1: Schematic of the role of alkylamines in the synthesis of Cu NWs. Adapted from Ref. [365]

The first synthesis of Cu NWs was presented in 2005 by Chang and coworkers.[366] In this work $Cu(NO_3)_2$ was used as Cu salt precursor, hydrazine as reducing agent and ethylenediamine (EDA) as a capping agent. The three reactants were dissolved in water, in presence of 15 M NaOH and heated for 1h at 60 °C. The resulting Cu NWs were straight, with uniform diameters in the range of 60–160 nm and lengths greater than 40 µm. NaOH was necessary to prevent the precipitation of copper hydroxide and EDA to drive the 1D elongation along the [110] orientation. In fact, in absence of EDA, only Cu nanoparticles (NPs) were formed.[367] However, when EDA was too much disk-shaped Cu nanostructures were obtained. Wiley *et al*.[367] scaled-up this reaction to the gram grade (200 times). However, the synthesized Cu NWs had a lower aspect ratio (diameters of 90 ± 10 nm and lengths of 10

± 3 μm). Interestingly, they followed the growth of Cu NWs and observed that NPs were attached to one end of the Cu NWs at different reaction times, confirming that NWs grew from single-crystalline spherical seeds. To avoid the use of toxic hydrazine, safer alternatives have been developed. In particular, the same amines used as capping agents can reduce copper salts to copper (0) at high temperatures. For example, Huang *et al.*[368] have synthesized Cu NWs using a hydrothermal method, by heating a water emulsion of $CuCl_2$ and octadecylamine (ODA) at 120–180 °C for 48 h. In this case, ODA acted as both reductant and templating agent. These Cu NWs had diameters of 30–100 nm and lengths up to several millimetres. Polycrystalline and single-crystal Cu NWs were obtained at 120 °C and 180 °C, respectively. Han *et al.*[369] presented the synthesis of fivefold twinned Cu NWs, by the controlled disproportionation of Cu(I) in oleylamine (OLA) solution. CuCl was dissolved in OLA and heated at 200 °C to synthesize Cu NWs with diameters of ca. 50 nm and lengths > 10 μm. Another work reported the synthesis of ultralong single-crystalline Cu NWs using copper acetylacetonate [$Cu(acac)_2$] as precursor in a liquid-crystalline medium of hexadecylamine (HDA) and cetyltriamoninum bromide (CTAB) kept at 180 °C for 10 h in presence of a Pt catalyst.[370] Similarly, fivefold twinned Cu NWs have been synthesized by dissolving $CuCl_2$ in OLA in presence of $Ni(acac)_2$ as catalyst, and heating at 175 °C for 10 h.[371] Single-crystal Cu NWs have also been obtained by a polyol reduction method.[372] Cu NWs were obtained by dissolving CuCl in ethylene glycol in presence of KBr and OLA as capping agents and heating up to 198 °C for 1 h. Ethylene glycol served as reducing agent and both bromide ions and OLA in a molar ratio 1:3 were necessary to grow the Cu NWs along the [110] direction. These Cu NWs possessed an average diameter of 72 nm and length of 30 μm. By adding an external reductant, Cu NWs can be synthesized at a lower temperature and at lower reaction times. For instance, thin (width < 30 nm) fivefold twinned Cu NWs have been synthesized with Cu(II) precursors and OLA, employing tris(trimethylsilyl)silane[373] and benzoin as reductants. A higher sustainability of the Cu NWs synthesis can be obtained by using water as solvent instead of the molten alkylamines and a mild green reductant such as glucose. Mohl *et al.*[374] were the first in 2010 to synthesize Cu NWs *via* a hydrothermal process using glucose as reductant. In particular, Cu NWs were obtained by forming a water emulsion of $CuCl_2$, HDA and glucose, and then heating the emulsion in an autoclave at 120 °C for 2 h. These Cu NWs presented a diameter of 64 ± 8 nm and length of few micrometres. They observed that the ratio between glucose, HDA and Cu(II) was a key parameter for obtaining Cu NWs. One year later, Xia *et al.*[375] prepared much longer fivefold twinned Cu NWs by employing a similar procedure. In particular, $CuCl_2$, HDA and glucose were homogeneously dispersed in water and heated in a capped glass vial at 100 °C for 6 h. The obtained Cu NWs had lengths of several tens to hundreds of micrometres and diameters of 24±4 nm. They also observed that the amount of glucose and HDA were essential for the growth of Cu NWs (**Figure 3.3-2**). In particular, they found out that HDA was selectively absorbed on the twinned seeds. At high concentrations of HDA, the last prohibited the twinned seeds from being oxidized and etched by the Cl^-/O_2 pair, allowing them to grow

into Cu NWs. On the contrary, at lower concentrations, HDA was not sufficient to adsorb onto the twinned seeds and protect them from oxidation. This allowed the single crystal seeds, more resistant to the oxidation, to prevail and grow into nanocubes. Instead, when the glucose concentration was doubled, tadpole-like Cu NWs were obtained.

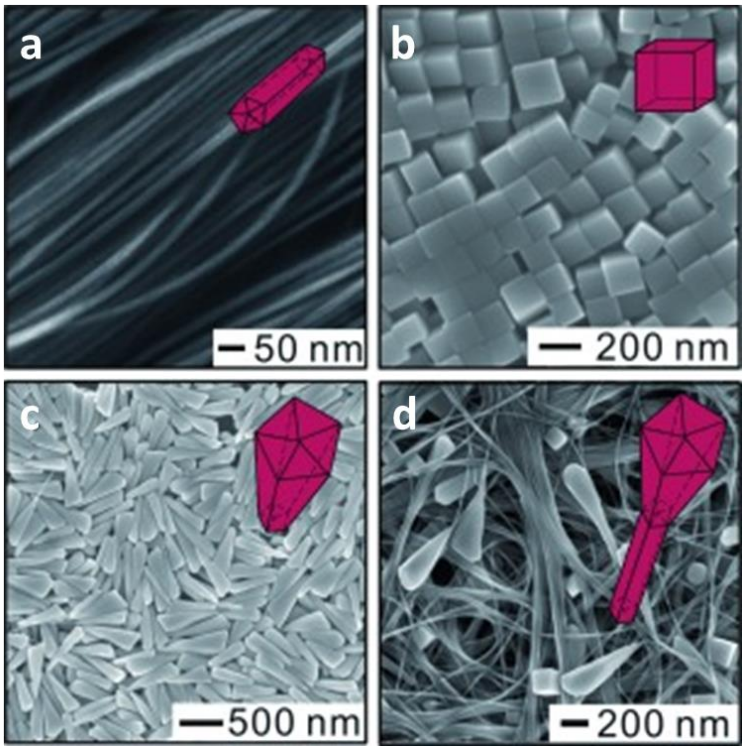

Figure 3.3-2: SEM images of (a) Cu NWs obtained in aqueous solution at 100 °C employing HDA (18 mg/mL) and glucose (5 mg/mL). (b) Cu nanocubes obtained at half concentration of HDA (9 mg/mL). (c) Tadpole-like Cu nanocrystals obtained by doubling the concentration of glucose (10 mg/mL) after 0.5 h and Tadpole-like Cu NWs obtained after 6 h. Adapted from Ref. [375]

The Cu NWs reported in chapter 4 of this thesis have been synthesised following a variation of the procedures reported by Mohl *et al.*[374], Xia *et al.*[375] and Kevin *et al.*[8]. The hydrothermal synthesis employing glucose as reducing agent was chosen among all the reported synthesis of Cu NWs because such synthesis is the most economical and eco-friendly. In fact:

- It minimizes the waste of the alkylamine, which is not used as a solvent.
- Is a water-based synthesis.
- It employs relatively low temperatures (100-120 °C).
- It makes use of a non-toxic and green reducing agent.
- It produces high aspect ratio Cu NWs in high yield.

The synthetic procedure that we developed differs from those reported by Mohl *et al.*[374], Xia *et al.*[375] and Kevin *et al.*[8] because we employed ODA instead of HDA and we scaled-up

the reaction of 18 times the reaction reported by Xia *et al.*[375] (2 times the quantities reported by Mohl *et al.*[374], and 12 times the quantities reported by Kevin *et al.*[8]). As a result, the concentration of reactants in water was enhanced and the ratio between the different reagents was optimized to increase the yield of Cu NWs and minimize the formation of Cu nanocubes and other Cu nanocrystals. The detailed synthetic procedures are reported in chapter 5 of this thesis.

Chapter 4.

High-performance humidity sensors based on a graphene-molecules hybrid*

Humidity sensors allow monitoring the mutable water vapour content in the atmosphere. Such devices are gaining crescent attention in numerous fields and applications. Nowadays metal oxides and ceramic materials dominate the market of humidity sensors, yet new cheaper and more efficient materials are emerging. Within the race for new cost-efficient materials with superior performances, graphene oxide (GO) based humidity sensors are becoming more and more important because of their low-cost and high sensitivity. However, current GO-based sensors suffer from some important drawbacks including slow response and recovery, and poor stability. Interestingly, reduced GO (rGO) exhibits higher stability, yet accompanied by lower sensitivity to humidity due to its hydrophobic nature. With the aim of improving the sensing performances of rGO, in this chapter we report on a novel generation of humidity sensors based on a simple chemical modification of rGO with selective receptors of water molecules, i.e. triethylene glycol chains. A facile procedure was adopted to chemically functionalize GO with a dangling triethylene glycol. Such hybrid material exhibits a notably improved sensing performance compared to pristine rGO such as high sensitivity (31 % increase in electrical resistance when humidity is shifted from 2 to 97%), an ultrafast response (25 ms) and recovery in the sub-second timescale, low hysteresis (1.1 %), excellent repeatability and stability as well as high selectivity towards moisture.

* A large part of the work presented within this chapter has been published: 1. Anichini, C.; Aliprandi, A.; Gali, S. M.; Liscio, F.; Morandi, V.; Minoia, A.; Beljonne, D.; Ciesielski, A.; Samorì, P. Ultrafast and Highly Sensitive Chemically Functionalized Graphene Oxide-Based Humidity Sensors: Harnessing Device Performances via the Supramolecular Approach. *ACS Appl. Mater. Interfaces* **2020,** *12* (39), 44017-44025.

4.1. Introduction

Sensors capable of measuring the relative humidity with high precision are key devices for monitoring the environment and are playing an important role in our daily life, industry, agriculture, bio-medical and environmental fields. In general, humidity sensors can be divided into two categories: *i*) resistive-type humidity sensors, [376, 377] which measure the variation in relative humidity (RH) as a function of the electrical resistance or impedance, and *ii*) capacitive-type humidity sensors[378] in which a variation of the capacitance is measured. The vast majority of commercially available humidity sensors are based on ceramics[379] (in particular, Al_2O_3, Si_3N_4), metal oxides like SnO_2, GaN, polyelectrolytes, and conducting polymers.[376, 380] These sensors suffer from various drawbacks including poor sensitivity, slow response and recovery time, and narrow range of humidity detection. For this reason, carbon nanomaterial-based humidity sensory materials, such as carbon nanotubes (CNTs),[381] graphene oxide (GO),[382-384] and reduced graphene oxide (rGO)[385] are attracting great attention in the last few years due to their excellent humidity-sensing capabilities resulting from the high surface-to-volume ratio making their physical and chemical properties extremely susceptible on their environment. Compared to traditional humidity sensors, those based on carbon-nanomaterials typically display higher mechanical and chemical stability, faster response, and high scalability.[386] In particular, GO and rGO have aroused remarkable interest due to their industrially scalable production, low-cost of the starting material, simplicity in their preparation and processability in green solvents, and high chemical stability, rendering them most suitable for applications in humidity sensing. [71, 172, 382-385, 387] The remarkable humidity sensing capabilities of GO originate from the presence of numerous hydrophilic functional groups on its surface (e.g., epoxide rings, hydroxyl and carboxyl groups) that can efficiently interact with water molecules from the environment. However, since the interactions between the water molecules and the aforementioned functional groups of GO are rather strong, GO-based humidity sensors suffer from large hysteresis and incoherent behaviour over time.[388] Moreover, their sensing performances are often characterized by slow response and recovery times.[71, 389, 390] Furthermore, because of the poor conductivity of GO ($1 \cdot 10^{-4}$ S/m and lower),[52] high potentials need to be applied in order to reach readable currents, thus resulting in increased power consumption.[391, 392] On the other hand, rGO is 6-7 orders of magnitude more conductive than GO,[393] allowing the fabrication of power-efficient devices.[394] To overcome the poor conductivity of GO electrochemical impedance spectroscopy (EIS), which require a complex and expensive analyzing device, is also employed.[3] Nonetheless, the main drawback of rGO is its hydrophobic nature; due to the elimination of the oxygen-containing functional groups during the reduction processes of GO, its surface becomes hydrophobic, which causes a lower interaction with the water molecules and ultimately lower response to humidity.[385, 389] Chemical functionalization of

rGO repristinate some functional groups, which through their interaction with water may enhance rGO sensitivity. For instance Lee's et al.[395] functionalized GO with terminating amines by using ethylenediamine, and demonstrated that the presence of amine groups improved the sensitivity towards humidity, but provoked unneglectable hysteresis due to the strong interaction between water molecules and the terminating amines.

In this chapter, we demonstrate that the sensitivity of rGO to humidity can be enhanced by its chemical functionalization with hydrophilic moieties that by design specifically and reversibly interact at the supramolecular level with water molecules. We have focused our attention to triethylene glycol, whose etheric oxygens can interact with water molecules forming weak, thus reversible, hydrogen bonding when compared to carbonyls, carboxylic acids and hydroxyls.[4] To demonstrate our rational, a comparative test has been carried out also *via* the functionalization of GO with an aliphatic chain which, on the contrary, is more hydrophobic and should feature lower interactions with moisture. The performances towards humidity sensing of these two chemically modified rGO (rCMGO) were benchmarked also with the pristine rGO, and the mechanism at the basis of the different responses to humidity changes was elucidated with the aid of force field molecular dynamics simulations.

4.2. Materials and methods

4.2.1. Experimental procedures

All the chemicals and reagents were purchased from Sigma-Aldrich and used without further purification. Graphene oxide (GO) (4 mg/ml, water dispersion) was purchased from Graphenea. 2-[2-(2-methoxyethoxy)ethoxy]ethylamine (NTEG) was synthesized as described in the following paragraph.

4.2.1.1. *Synthesis of 2-[2-(2-methoxyethoxy)ethoxy]ethylamine (NTEG)*

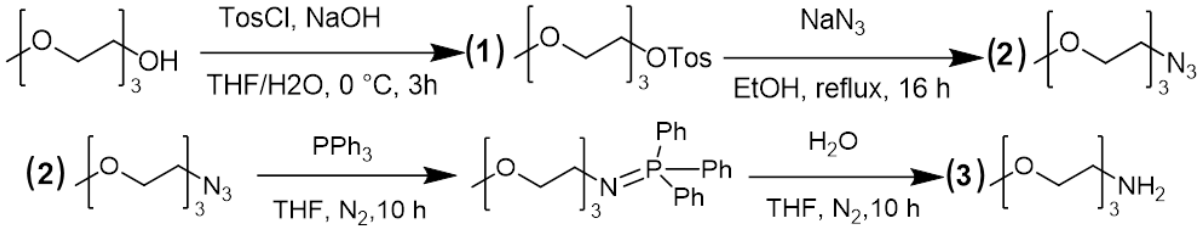

Figure 4.2-1: Reaction scheme of the synthesis of N,triethylene glycol aminomethyl ether (NTEG), 1st step: formation of TEG- Tosylate (**1**). 2nd step: formation of TEG-azide (**2**). 3rd step: reaction of **2** with triphenylphosphine and formation of the phosphanimine intermediate, followed by workup with water to obtain NTEG (**3**).

The synthesis of NTEG consists in a three-step reaction (**Figure 4.2-1**): the first step is the synthesis of 2-[2-(2-Methoxyethoxy)ethoxy]ethoxy]p-toluenesulfonate (TEG-Tosylate, **1**) that was synthesized following the procedure reported by Ki Duk Park *et al.*[396] Triethylene glycol monomethyl ether (TEG) (8.0 g; 48.7 mmol; 1 eq) was dissolved in 4 mL of THF. An aqueous NaOH (1.8 g; 45 mmol, 0.9 eq) solution (4 mL) was added to the reactant at 0 °C and then a THF solution (15 mL) of *p*-toluenesulfonyl chloride (TosCl) (8.6 g; 46 mmol; 0.9 eq) was added while stirring (1 h). After stirring at 0 °C (2 h), the reaction mixture was diluted with cold water (60 mL). The organic layer was separated, and the aqueous layer was extracted with DCM (3 × 50 mL). The combined organic layers were extracted 3 times with H_2O (50 mL). The organic layer was dried with Na_2SO_4 and evaporated in vacuum to obtain the TEG-Tosylate (**1**) (10.45 g, yield = 67 %). ^{1}H NMR (400 MHz, $CDCl_3$) δ 7.77 (d, *J* = 8.3 Hz, 2H), 7.32 (d, *J* = 8.7 Hz, 2H), 4.16 – 4.10 (m, 2H), 3.68 – 3.63 (m, 2H), 3.62 – 3.53 (m, 6H), 3.52 – 3.48 (m, 2H), 3.34 (s, 3H), 2.42 (s, 3H).

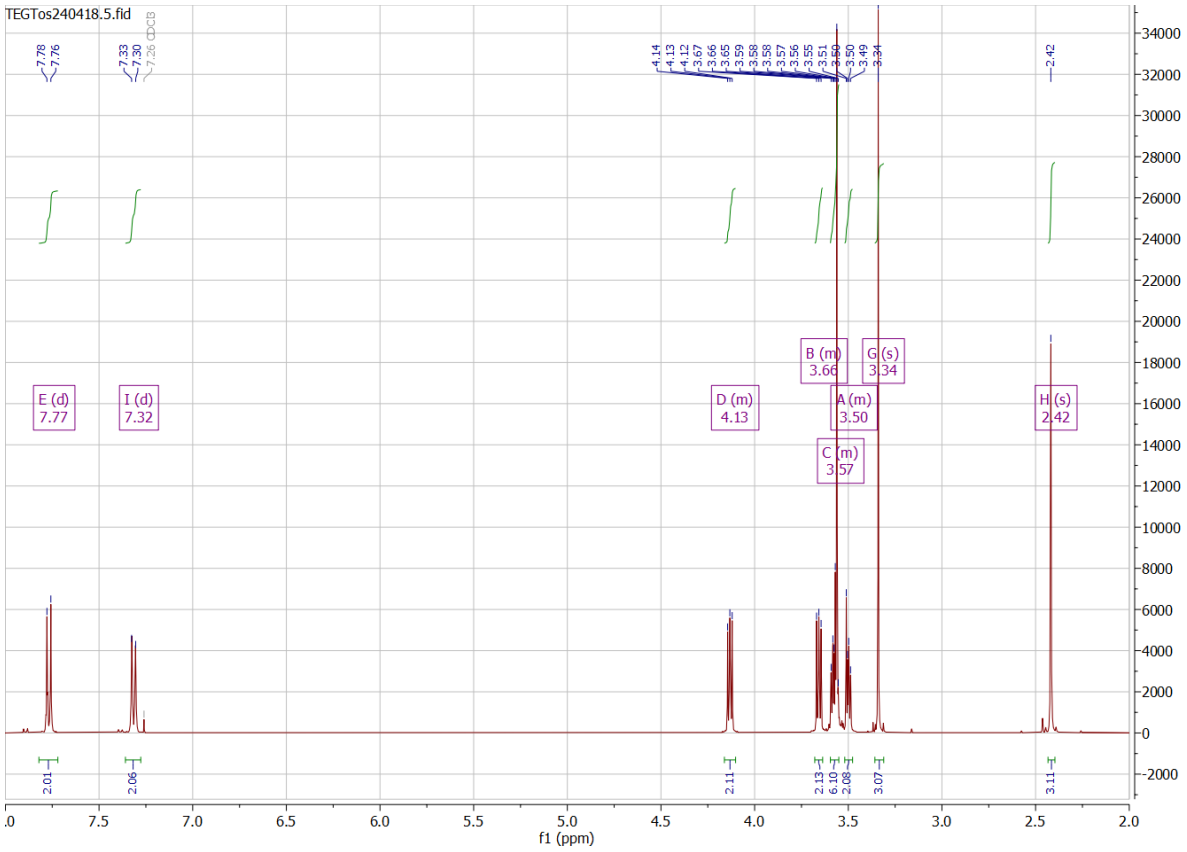

Figure 4.2-2: ^{1}H-NMR of the first intermediate TEG-Tosylate (**1**).

The second and third steps of the reaction, aimed at the production of TEG-azide (**2**) and finally NTEG (**3**), were performed following the procedure reported by Hyunkyu Kim *et al.*[397] TEG-Tosylate (**1**; 5 g; 15.7 mmol; 1 eq) and sodium azide (1.8 g; 25.2 mmol, 2 eq) were dissolved in 70 mL of EtOH and the solution was stirred at reflux for 16 h. Eventually, the solution was concentrated to 1/3 of volume and 80 mL of water was added, then the EtOH was completely removed in vacuum. The remaining water solution was extracted with

dichloromethane 4 times. The organic layer was dried with Na_2SO_4 and evaporated in vacuum to obtain TEG-azide (**2)** as a yellow oil (2.98 g, 100 % yield).

In a two-neck flask were added 80 mL of anhydrous THF and triphenylphosphine (5.9 g, 23.6 mmol, 1.5 eq) under N_2 at 0 °C; then the TEG-azide (2.98 g, 15.7 mmol, 1 eq) was added dropwise under stirring and the reaction was conducted overnight under N_2. Then 50 mL of water was added, and the mixture was stirred for 8 additional hours, at the end of which the organic phase was evaporated and the water phase extracted 3 times with toluene. Finally, the water phase was concentrated to obtain the compound **3** (NTEG) in form of a pale-yellow oil (1.93 g, yield = 75.4 %). ^{1}H NMR (400 MHz, $CDCl_3$) δ 3.68 – 3.62 (m, 6H), 3.55 (dd, *J* = 5.7, 3.6 Hz, 2H), 3.51 (t, *J* = 5.2 Hz, 2H), 3.38 (s, 3H), 2.86 (t, *J* = 5.2 Hz, 2H).

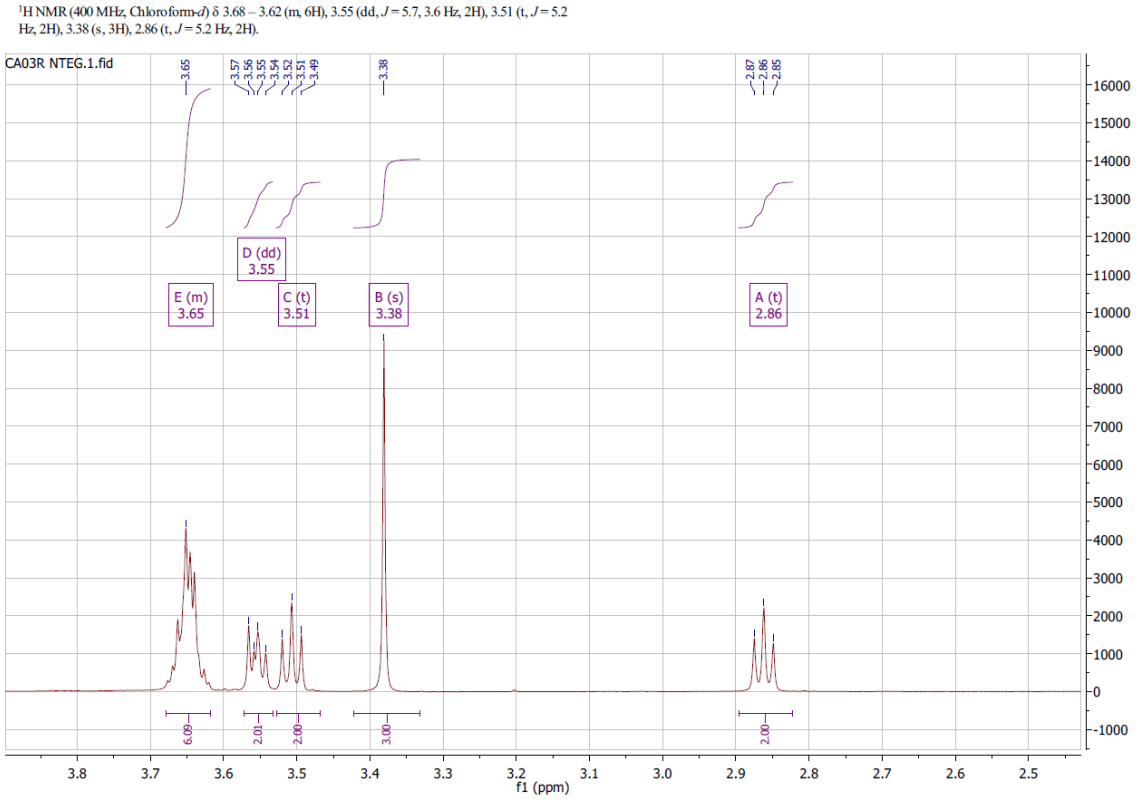

Figure 4.2-3: ^{1}H-NMR of the synthesized NTEG (**3**).

4.2.1.2. *Synthesis of Chemically Modified GO and preparation of the devices*

1.0 mL NTEG and 10 mL of GO aqueous dispersion (4 mg/mL from Graphenea) were added to 50 mL of ethanol (EtOH) and the resulting mixture was refluxed for 12 h. Then the mixture was cooled down and centrifuged 5 times in EtOH (6000 rpm, 10 min), each time eliminating the supernatant to remove the excess of the unreacted NTEG. The solid was dispersed again in 80 mL of EtOH to obtain the CMGO-1 suspension (0.5 mg/mL). The same procedure was repeated adding 1 mL of decylamine instead of NTEG to prepare CMGO-2

and without the addition of any amine for GO. The suspensions of CMGOs and GO were diluted 10 times in EtOH and sonicated 10 minutes until stable and clear suspensions were formed. These suspensions were spray-coated on freshly cleaned solid substrates (glass or Si/SiO2) pre-heated at 100 °C. A commercial airbrush gun for modelling and painting with a 0.3 mm needle and nozzle was used. The airbrush was supplied with compressed nitrogen at 1.5 bar. Typically microscope glass slides cut in 1.2 x 1.2 cm^2 squares were used. Finally, the samples were annealed under nitrogen at 240 °C for 10 minutes to obtain rCMGO-1/-2 and rGO. Electrical contacts were fabricated by depositing two strips of 30 nm gold layer spaced by a 2 mm channel on the CMGO films with a thermal evaporator and a shadow mask.

4.2.2. Characterization of the devices

The performance of humidity sensors has been investigated by connecting the two electrical contacts to a source measure unit (SMU) Keithley 2636A. To measure the sensitivity, the response and recovery time a constant bias of 2 V was applied to the device and the current intensity was acquired for 30 s, with a sampling frequency of 80 Hz, while a pulsed flow of humid air was spilt on the sample. To do so a glass stopcock, connected to a balloon filled with humid air and fixed at 10 cm from the sample, was cyclically and manually opened. The values of initial humidity were included between 36 and 42 % RH. The response and recovery times were calculated on the humidity pulses as the time interval between the 10 % and 90 % of the distance between the maximum response and the baseline. The values of response and recovery time reported in the text are the arithmetic mean of 5 different pulses. The calibration of the humidity response of the devices was performed including the devices connected to the SMU into a closed chamber, in which humidity levels have been controlled by filling it with dry nitrogen. High levels of humidity in the chamber were obtained introducing into the chamber the N_2 gas that was previously passed through a saturated aqueous solution of potassium sulfate (RH = 98%). The values of the RH inside the chamber were measured with two independent commercial hygrometers. The response of the device was calibrated by reading the resistance and the corresponding RH values registered by the hygrometers, while the level of humidity inside the chamber was increased from RH = 0 % to 98% and vice-versa (**Figure 4.2-4** a). The stability over time and the cyclability of the devices were gauged alternating for 10 times the RH in the chamber between 10 and 90 % and recording the resistance. The calibration of the sensitivity to different vapours (ethanol, methanol, acetone and chloroform) were performed inside a glove-box by exposing alternatively the device to the environment of the gloves-box and to a close chamber saturated with vapours of the analytes, obtained by placing in the chamber a small beaker with the anhydrous liquid analyte and continuously measuring the resistance with the source-meter. The long-term stability of the rCMGO-1 device was evaluated placing the device connected to the SMU in a sealed chamber in which a beaker containing a saturated solution of respectively LiCl, NaCl and K_2SO_4). The high humidity and temperature tests were performed by acquiring the calibration curve for the humidity of

rCMGO-1 device before and after the exposure of the device to the temperature of 80 °C and humidity of 79 % RH. These conditions were obtained by placing the device and a small beaker containing a saturated solution of KBr inside a sealed container and this was placed into an oven at 80°C for 3 days. The vapour pressures of the saturated salt solution used were obtained from the article of Lewis Greenspan.[398] The calibration of the rCMGO-1 sensor response to the temperature was performed by placing the device connected to the SMU inside a glove-box with water-free atmosphere, a thermocouple glued to the device was used to control the temperature. For measuring the response to temperatures above RT the device was placed on top of an electrical heater with temperature control, whose temperature was increased with a ramp of 5 °C/min. The temperature read from the thermocouple and the resistance read from the SMU were acquired at 5 °C intervals until 90 °C. Likewise, to acquire the response to temperatures lower than RT the device was placed on top of a thermoelectric cooler and cooled to -5 °C while the temperature and resistance were acquired. All the measurements were performed in a temperature range between 20 and 24 °C unless differently reported.

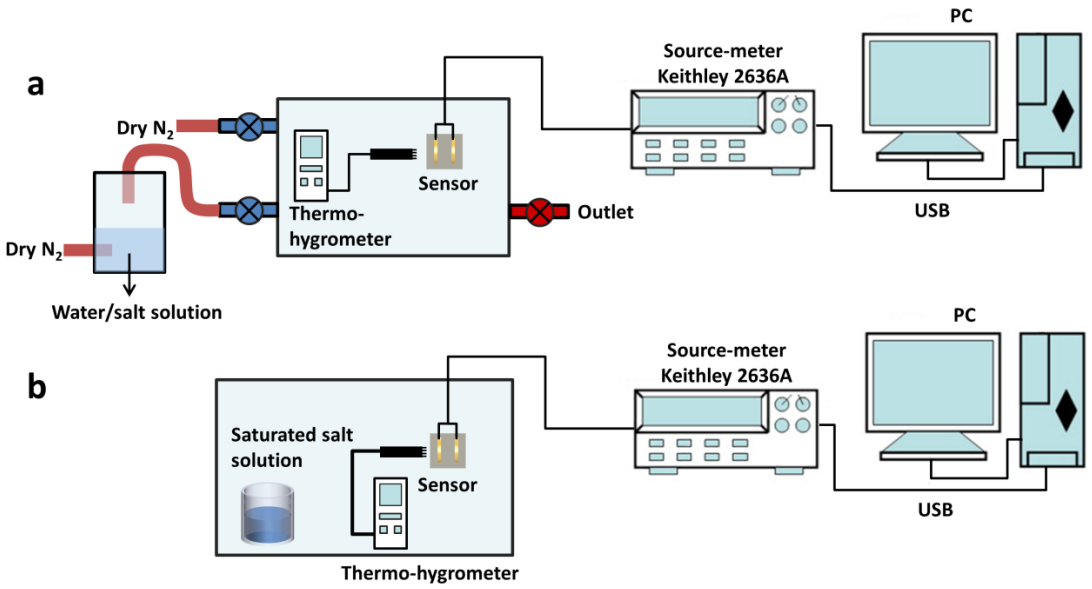

Figure 4.2-4: Schematic image of the two sensing setup used for the humidity calibration and cycling tests (a) and for the long-term stability test.

4.2.3. Instrumental methods

The X-Ray Photoelectron Spectroscopy (XPS) measurements were carried out using a Thermo Scientific KAlpha X-ray Photoelectron Spectrometer system equipped with an Al Kα X-Ray source (photon energy Eph = 1486.6 eV, beam spot size ~100 µm). Transmittance UV-Vis spectra were recorded on the Jasco V-670 spectrophotometer. Raman spectra were recorded by a Renishaw microscope with a 50x objective, laser excitation wavelength of 532 nm and laser power of 1%. The silicon peak at 520.3 cm-1 was taken as reference for wavenumber calibration. The FTIR-ATR measures were performed with a Thermo Scientific

Nicolet 6700 FT-IR spectrometer. TGA was conducted using a Mettler Toledo TGA/DSC 2 system, with a heating rate of 10 °C min^{-1} from 25 °C to 800 °C under argon atmosphere. The X-Ray Diffraction (XRD) measurements were performed in specular geometry using a SmartLab-Rigaku diffractometer equipped with a rotating anode (Cu Kα, λ = 1.54180 Å), followed by a parabolic mirror to collimate the incident beam and a series of variable slits (placed before and after the sample position). The sample was mounted inside a box having two Kapton windows to let pass the incident and diffracted beam through and a thermo-hygrometer to measure RH and temperature in real-time. RH was varied by changing the hydration of nitrogen flux inside the box. The flux rate was fixed to maintain the pressure constant. The water contact angle measurements were performed with a Krüss DSA100S instrument by depositing on spray-coated films of rCMGO-1, rCMGO-2 and rGO on glass 5 sessile drops of water (for each sample and performing 5 consecutive measurements (2 s delay) for each drop. For each sample, the 25 drop images were fitted by the Ellipse (Tangent-1) method and the mean values and standard deviation were reported. Atomic force microscopy (AFM) characterization of the devices was performed with a Bruker Dimension Icon microscope under ambient conditions, operating in tapping mode and using TESPA-V2 tips with spring constant k = 42 N/m. The thickness of the spray-coated materials was calculated by levelling at 0 nm the substrate and calculating the average height of the image after subtracting the substrate area. Scanning Electron Microscopy (SEM) was performed with a FEI Quanta 250 FEG instrument, operated in high vacuum mode (pressure in the 10^{-4} Pa range).

4.2.4. Molecular dynamics simulations

Molecular dynamic (MD) simulations were performed in the group of Prof. David Beljonne, by Dr Sai Manoj Gali, and Dr Andrea Minoia, who are greatly acknowledged. Firstly, model structures of rGO, rCMGO-1 and r-CMGO-2 were constructed. rGO was constructed as a 11X11 honeycomb carbon lattice (C286), functionalized with hydroxyl moieties, such that its atomic composition is comparable to the experimental composition measured by XPS. CMGO-1 was constructed by grafting 2-[2-(2-methoxyethoxy)ethoxy]ethylamine (NTEG) chains to the rGO layer, such that, the atomic composition and the surface (density) coverage are identical to that obtained from experimental XPS rCMGO-1 data. rCMGO-2 was constructed by grafting decylamine chains to the rGO surface, with a density equal to rCMGO-1. Two more CMGO structures were constructed by reducing the density of coverage to half of rCMGO-1/ rCMGO-2 (hitherto referred to as rCMGO-1H and rCMGO-2H). The atomic compositions of these structures are reported in Table 4.2-1.

Table 4.2-1: Atomic composition (in %) considered for MD simulations.

Atomic composition (%)					
Element/Name	rGO	rCMGO-2H	rCMGO-2	rCMGO-1H	rCMGO-1
C	80.0	88.1	90.0	87.0	75.0
O	20.0	8.5	5.0	9.25	20.0
N	0.0	3.4	5.0	3.75	5.0
C/N	0.0	26.0	18.0	23.5	15.0

All these surfaces were then immersed in a water box containing 9000 water molecules and subjected to molecular dynamics (MD) preparation and sampling runs. Molecular Dynamics (MD) simulations were performed using NAMD software with General AMBER force field (GAFF),[399] employing periodic boundary conditions. Geometry optimizations and electrostatic potential fitted (ESP) atomic charges for NTEG and decylamine chains were obtained with the Møller–Plesset perturbation theory at the second order (MP2) and a 6-311+G(d,p) basis set using the Gaussian software. Then, these charges between chains and the connected GO surfaces were redistributed following the procedure described elsewhere.[400] For water the well-known and reliable "modified TIP3P" force field was used. MD simulations on rGO and rCMGOs surfaces were performed in three stages, first, simulations were performed at 100 bar and 300 K (high pressure) for 10 ns to obtain appropriate densities, then simulations were performed in isothermal–isobaric (NPT) ensemble (1 bar and 300 K) for 10 ns to enable sufficient equilibration of the systems, followed by an MD production run of 50 ns in NPT ensemble. Pair Interaction (PI) energy between water molecules and respective rCMGOs and rGO surfaces was computed with the Particle mesh Ewald (PME) grid, using the MD trajectories from the production cycle of 50 ns, to specifically accounting the electrostatic and van der Waals interactions between the respective residues (water-rCMGOs/rGO). Potential of Mean Force (PMF) profiles were computed by lifting the water molecule perpendicular to the surface of rGO and rCMGO surfaces (taking sp2 surface carbon atoms as reference). The centre of mass movement of the water molecule is unconstrained in the 'XY' plane (free movement in the plane parallel to the rGO/rCMGO surface) but constrained along the 'Z' axis (perpendicular to the rGO and rCMGO surfaces) with 2 Å and 16 Å employed as lower and upper boundaries. PMF profiles were computed using the Adiabatic Biasing Force (ABF) method,[401] with 75 ns of MD simulation time. Relative orientations of water molecules with respect to Z axis (perpendicular to rCMGO-1/2 surface) at distances of 4 and 6 Å were computed by taking the three angles based on the vectors passing through atoms in the selected water molecule: O-H1, O-H2 and H1-H2, wherein 'O', 'H1' & 'H2' are atoms of a selected water molecule.

4.3. Results and discussion

4.3.1. Synthesis of chemically modified GO and preparation of the devices

The surface of GO sheets possesses numerous reactive oxygen-rich functional groups such as hydroxyls, carboxylic acids and epoxides which can react with various organic molecules, including amines.[49, 402, 403] Noteworthy, while the hydroxyls and carboxylic acid groups of GO need to be first activated to react with amines,[404-406] ring-opening reactions take place on epoxides even without any catalyst under mild experimental conditions.[49, 163, 403] Because of this reason, the functionalization of GO with amines was conducted primarily by exploiting the epoxide ring-opening reaction, yet not excluding the possibility of amide formation on some of the carboxylic groups.[49, 403, 407-409] The mechanism of epoxide ring-opening in GO is illustrated in **Figure 4.3-1** and consist in a S_N2 nucleophilic attack on the electrophilic carbon of the epoxide by the amine. We decided to carry out the condensation reaction of GO in an ethanolic solution of the amines under reflux to minimize reagent waste. GO was functionalized with two different primary amines, i.e. 2-[2-(2-methoxyethoxy)ethoxy]ethylamine (NTEG) and decylamine. These two chemically modified GO were named hereafter CMGO-1 and CMGO-2, respectively. The two amines have similar molecular length, yet the former is highly hydrophilic, while the latter is strongly hydrophobic. In parallel, we refluxed neat GO in ethanol, which served as reference sample and allowed comparison with CMGOs. The ethanolic suspensions of CMGOs and GO were processed into thin films on glass substrates by the spray-coating. Subsequently, GO films were partially reduced by a short (10 min) thermal annealing under nitrogen atmosphere at 240 °C. The employed annealing conditions were chosen based on previously reported works, as they are sufficiently high to increase the conductivity of the GO-based materials,[410, 411] and mild enough to preserve the amine bond to CMGOs.[412] Finally, top gold electrodes were patterned via sublimation in high vacuum through a shadow mask with electrodes distance of 5 mm. A representation of the CMGOs synthesis and device preparation and a photo of the assembled device are portrayed in **Figure 4.3-2**.

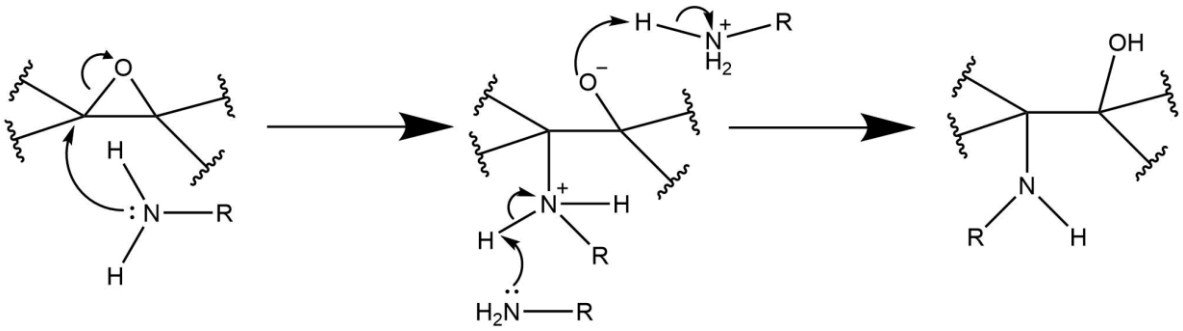

Figure 4.3-1: Schematic mechanism of epoxide ring opening of GO with a primary amine (NTEG, decylamine).

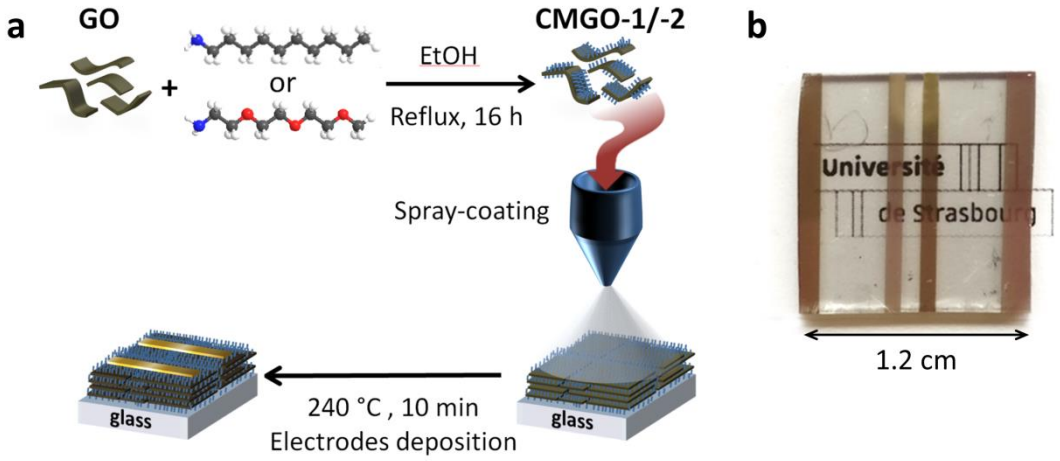

Figure 4.3-2: (a) Schematic of the GO functionalization with NTEG and decylamine, followed by spray-coating on glass substrates, thermal annealing and electrodes deposition. (b) Actual photo of the final rCMGO-1/-2 device.

4.3.2. Characterization of the materials

The materials were characterized prior and after annealing to prove the successful functionalization and stability. X-ray photoelectron spectroscopy (XPS) was used to gain quantitative insight into the chemical composition of hybrid materials by identifying the relevant chemical elements present in GO and CMGOs. The C 1s, N 1s, O 1s and survey spectra of each material before and after annealing were acquired. The C1s XPS spectrum of the neat GO, reported in **Figure 4.3-3**a shows the typical two peaks at 284.6 eV (C-C) and 286.7 eV (C-O) due to the abundant oxygen functionalities (oxygen content up to 50 %). Compared to GO, the C1s deconvoluted spectra of the functionalized CMGO-1 and CMGO-2 hybrid materials show lower C-O component intensities, due to a partial reduction of GO (**Figure 4.3-3** b-c). Furthermore, such peaks exhibit a hump at 285.9 eV which indicate the C-N bond formation,[413, 414] as evidence in the deconvoluted peaks. The C-N component is also present in the spectra of rCMGO-1 and rCMGO-2 (yet with lower intensity for rCMGO-2), while is completely absent in rGO, indicating the retention of the functionalization after the annealing (**Figure 4.3-3** d-f). Simultaneously, the spectral features associated with the various C-O bonds are drastically less intense in all the annealed species, in accordance with the effects of the thermal reduction of GO.[415]

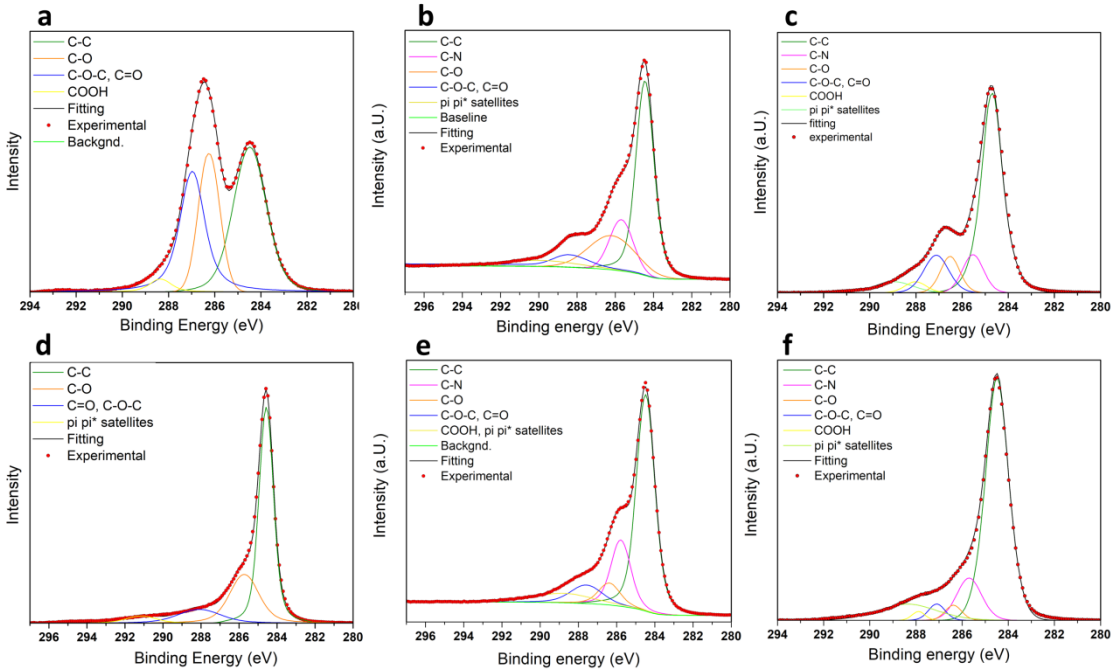

Figure 4.3-3: XPS spectra of C1s peaks of GO (a), CMGO-1 (b), CMGO-2 (c) and of the thermally annealed rGO (d), rCMGO-1 (e) and rCMGO-2 (f).

In **Figure 4.3-4** are reported the N 1s deconvoluted spectra of the materials. As expected, N 1s peaks are negligible in GO and rGO, while in CMGOs and rCMGOs they are strong. In rCMGO-2 is possible to observe a hump at 401.7 eV due to the presence of some free amine not bound to GO (primary amines); however, the contribution of the secondary amines is much more important for all the functionalized species. Furthermore, after the annealing, the amines not bonded to CMGO-2 are removed (**Figure 4.3-4** f). From the deconvoluted peaks, it is possible to discern a minor component at 398.2 eV, which indicates the presence of a small fraction of the amines bonded to the carboxylic groups of GO. The deconvoluted oxygen spectra of (r)GO and (r)CMGOs are reported in **Figure 4.3-5**. However, the oxygen spectra provide little information about the composition of the samples because of the difficulty of discerning the oxygens of epoxide, ethers and hydroxyls that are present in all the samples. XPS can also provide semi-quantitative information concerning the composition:[416] for this purpose, survey spectra of the different materials were acquired (**Figure 4.3-6**). Qualitatively, it is possible to observe a reduction of the intensities of the O 1s peaks in all the annealed samples and the presence of the nitrogen peaks in the functionalized hybrids (CMGOs and rCMGOs). Furthermore, by fitting the XPS survey spectra, the atomic relative abundance of carbon, nitrogen and oxygen were obtained (**Table 4.3-1**).

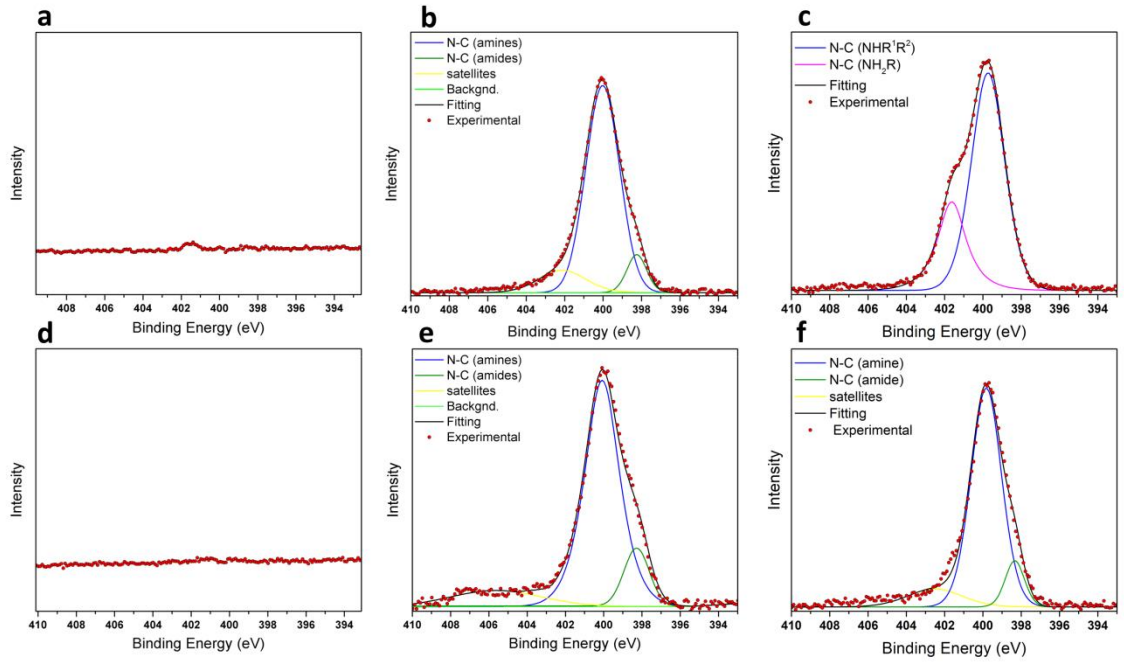

Figure 4.3-4: XPS spectra of N1s peaks of GO (a), CMGO-1 (b), CMGO-2 (c) and of the thermally annealed rGO (d), rCMGO-1 (e) and rCMGO-2 (f).

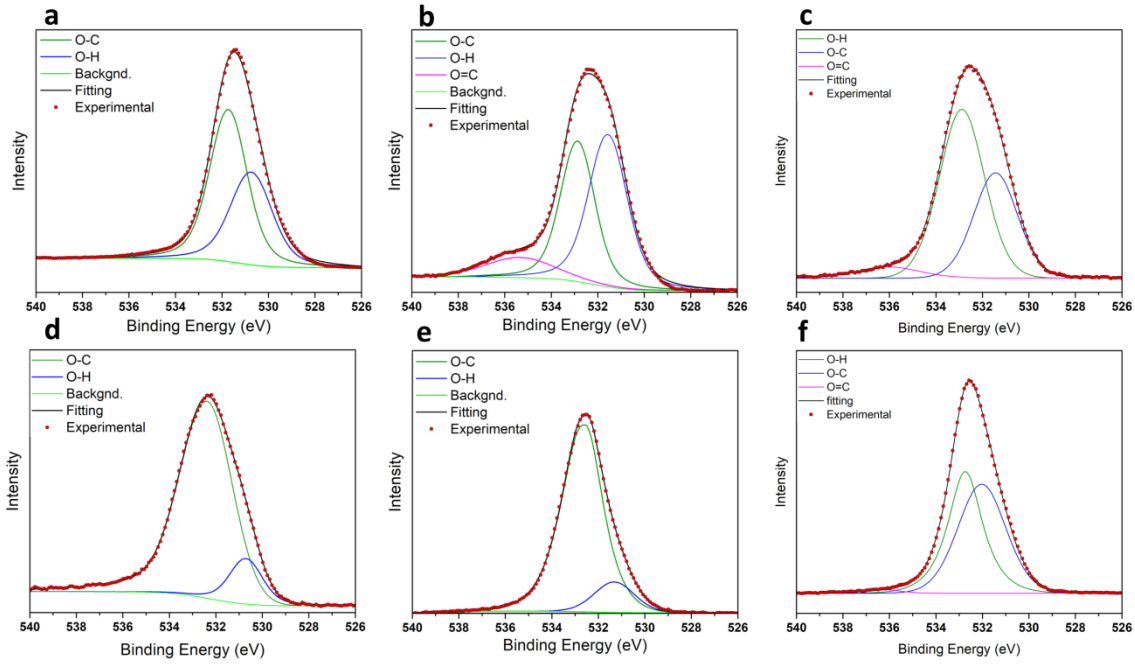

Figure 4.3-5: XPS spectra of O1s peaks of GO (a), CMGO-1 (b), CMGO-2 (c) and of the thermally annealed rGO (d), rCMGO-1 (e) and rCMGO-2 (f).

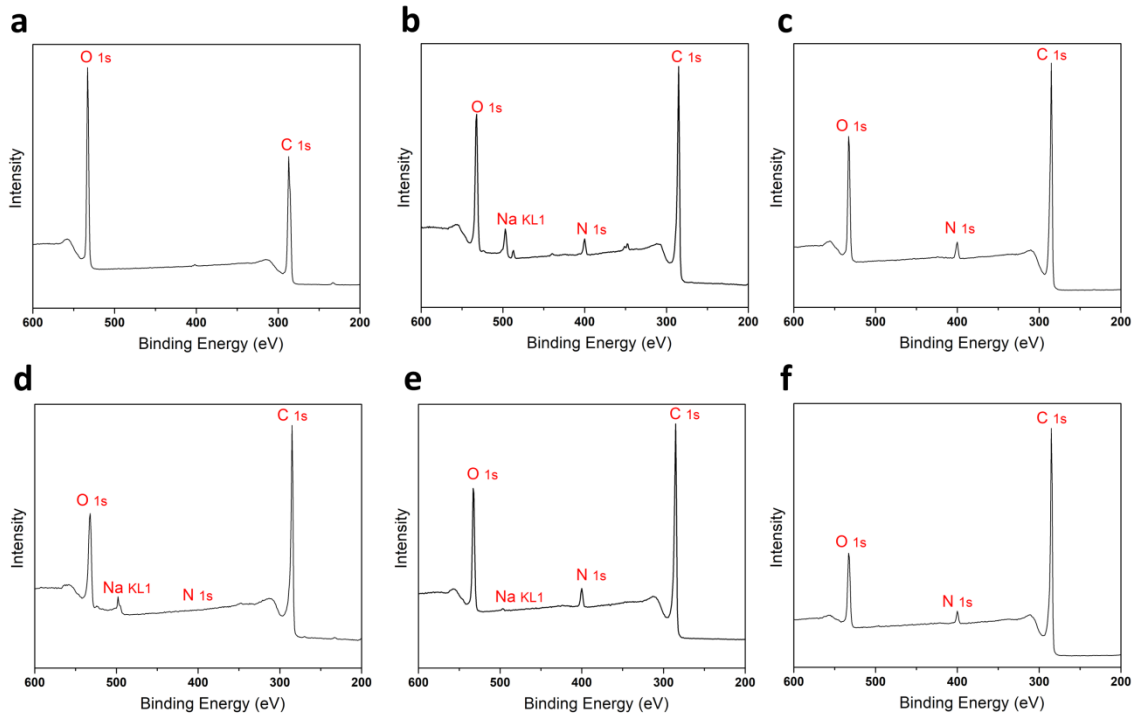

Figure 4.3-6: XPS survey spectra of GO (a), CMGO-1 (b), CMGO-2 (c) and of the thermally annealed rGO (d), rCMGO-1 (e) and rCMGO-2 (f).

Table 4.3-1: Elemental atomic abundance of C, N, O obtained from the XPS survey spectra for GO and CMGO before and after the thermal annealing.

	GO	rGO	CMGO-1	rCMGO-1	CMGO-2	rCMGO-2
Element				Atomic %		
C (1s)	67.31	79.97	73.60	75.57	80.66	83.94
N (1s)	0.11	0.14	4.36	4.49	3.75	3.62
O (1s)	32.45	19.59	22.04	19.94	15.58	12.44

From the atomic percentage reported in **Table 4.3-1** the degree of functionalization was assessed. In particular, the number of NTEG and decylamine molecules in rCMGO-1 and rCMGO-2 per number of carbon atoms of GO was estimated considering that any NTEG or decylamine molecule contributes to the total number of carbon atoms "seen" by the XPS. For any nitrogen atom of the NTEG molecule, there are 7 carbon atoms and for any nitrogen atom of decylamine, there are 10 carbon atoms. Therefore, the ratio of the number of carbon atoms of graphene over the number of NTEG and decylamine molecules can be expressed as follows:

$$\frac{C\ graphene}{NTEG\ molecules} = \frac{C\%_{tot} - 7 \times N\%_{tot}}{N\%_{tot}} = \frac{75.57 - 7 \times 4.49}{4.49} = 9.83 \qquad Eq.\ 4.3\text{-}1$$

$$\frac{C\ graphene}{decylamine\ molecules} = \frac{C\%_{tot} - 10 \times N\%_{tot}}{N\%_{tot}} = \frac{83.94 - 10 \times 3.62}{3.62} = 13.18 \qquad Eq.\ 4.3\text{-}2$$

The results show that the functionalization degree is slightly higher for rCMGO-1 than for rCMGO-2. Nevertheless, the abundance of nitrogen in rCMGO-1 and rCMGO-2 differs by 0.8%, which is very close to the XPS accuracy. Therefore, we should consider the data presented as a rough approximation on the structure of the hybrid materials, and the functionalization degree being nearly identical for both systems.

The preservation of the chemical functionalization under the annealing conditions combined with a reduction of the GO scaffold evidenced by the loss of hydroxyls moieties are highlighted by TGA analysis, reported in **Figure 4.3-7**a. It is possible to observe that GO presents a first mass loss at 100 °C, the corresponds to the release of the water molecules absorbed, and two more weight loss steps at 150 °C and 260 °C corresponding to the removal of the oxygen-containing functional groups.[417, 418] Conversely CMGO-1 and CMGO-2 are thermally more stable, being already partially reduced during the reaction with the amine. At 60-100 °C, they both present a first small mass loss which is again due to the absorbed water and at 185- 190 °C a second, more pronounced mass loss corresponds to the removal of the unreacted oxygen-containing groups (in particular hydroxyls) and the effective reduction of CMGOs. [410, 411, 415, 419] Finally both CMGOs present a third major weight loss at 320-350 °C that corresponds probably to the elimination of the covalent functionalization and to a higher reduction of graphene. The partial reduction of the GO scaffold is also evidenced by the decrease in transmittance of the films (**Figure 4.3-7** b). The reduction of GO and functionalized GO is accompanied by an increase of the aromatization of GO. The increased conjugation of rGO produces a decrease of the energy of the π-π* transition and thus a redshift of the π-π* peak and an increased absorbance over all the visible region.[420] It is worth noting that the final devices are rather transparent (transmittance at 550 nm of 64 ± 3 %).

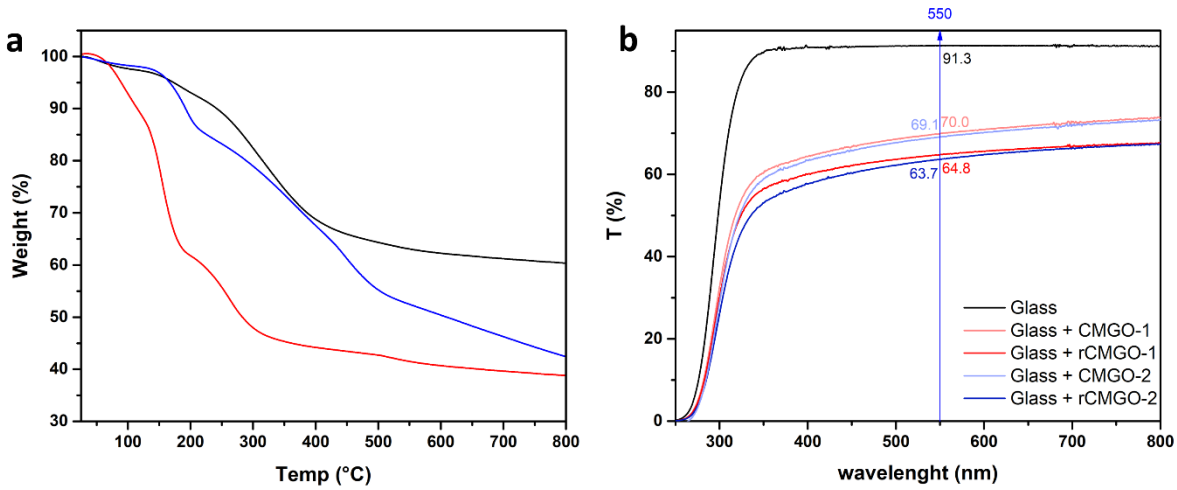

Figure 4.3-7: (a) Thermogravimetric analysis (TGA) of GO (red), CMGO-1 (black) and CMGO-2 (blue). (b) Transmittance spectra of the glass substrate (black), the substrate with spray-coated CMGO-1 and CMGO-2 before (light red and light blue) and after the thermal annealing (dark red and dark blue).

The successful functionalization of GO was also confirmed by the IR spectroscopy attenuated total reflection (FTIR-ATR). The IR spectra of the amine NTEG, decylamine, GO, CMGO-1 and CMGO-2 are reported in **Figure 4.3-8**a. The spectrum of GO shows a broad band at 3390 cm^{-1}, which belongs to the stretching of OH groups of carboxylic and hydroxyl groups and a strong peak at 1626 cm^{-1} due to the stretching C=C. The further peaks at 1729, 1213 and 1051 cm^{-1} correspond respectively to the stretching modes of C=O, C–OH and C–O. The spectrum of NTEG shows a strong peak at 2865 cm^{-1} due to the stretching of CH_2. The two peaks at 3370 and 3307 cm^{-1} belong to NH_2 stretching, while the peak at 1598 cm^{-1} is characteristic of NH_2 bending. The peak at 1198 cm^{-1} is due to C-N stretching. The strong peak at 1098 cm^{-1} is characteristic of C-O-C stretching. The spectrum of CMGO-1 shows at 3432 cm^{-1} the peak corresponding to the stretch of OH. The peaks at 2853 cm^{-1} and 1084 cm^{-1} are indicative of the success of the functionalization; in fact, they belong respectively to the stretching of CH_2 and the stretching of C-O-C introduced by the NTEG molecules. The spectrum of decylamine shows two strong peaks at 2850 and 2912 cm^{-1} due to the stretching of CH_2. The two peaks at 3332 and 3248 cm^{-1} belong to NH_2 stretching, while the peak at 1568 cm^{-1} is characteristic of NH_2 bending. The peak at 1461 cm^{-1} is due to CH_2 scissor bending. The spectrum of CMGO-2 shows fewer features; however, the few peaks visible are diagnostic of the functionalization. In fact, it is possible to discern clearly two peaks at 2842 cm^{-1} and 2913 cm^{-1} belonging to the stretching of CH_2 of the aliphatic chains and a peak at 1452 cm^{-1} caused by the bending of CH_2 groups.

Raman spectroscopy is an important technique to evaluate the presence of defects and disorder in graphene and GO. The comparative Raman spectra of GO and CMGOs before and after the thermal reduction are shown in **Figure 4.3-8**b. All the spectra exhibit two

characteristic peaks at around 1350 and 1560 cm^{-1}, corresponding to the D and G bands, respectively. The former, also known as defective band is ascribed to structural imperfection. In fact, this peak corresponds to a breathing mode of the honeycomb graphitic structure which symmetry is forbidden for Raman selection rules in pristine graphite and graphene, while only becomes active in the presence of defects.[421] G peak is instead related to the presence of pairs of sp^2 carbon atoms, yet does not require the presence of 6-membered aromatic rings. Therefore, such a peak is characteristic of graphene and graphite, but also of amorphous carbon. However, since GO is a highly defective form of graphene, the ratio between the intensities of D and G peaks (I_D/I_G) decreases at the introduction of more defects because of the decrease in the aromaticity, which is necessary for the appearance of the D band. In the present case, this ratio was found being superior in CMGOs and reduced CMGOs compared to GO and rGO samples, which originates from the higher defectiveness of CMGOs as a result of the chemical functionalization.[422] Conversely, such ratio decreases after thermal reduction for all samples, due to the growth of sp^2-hybridized regions.

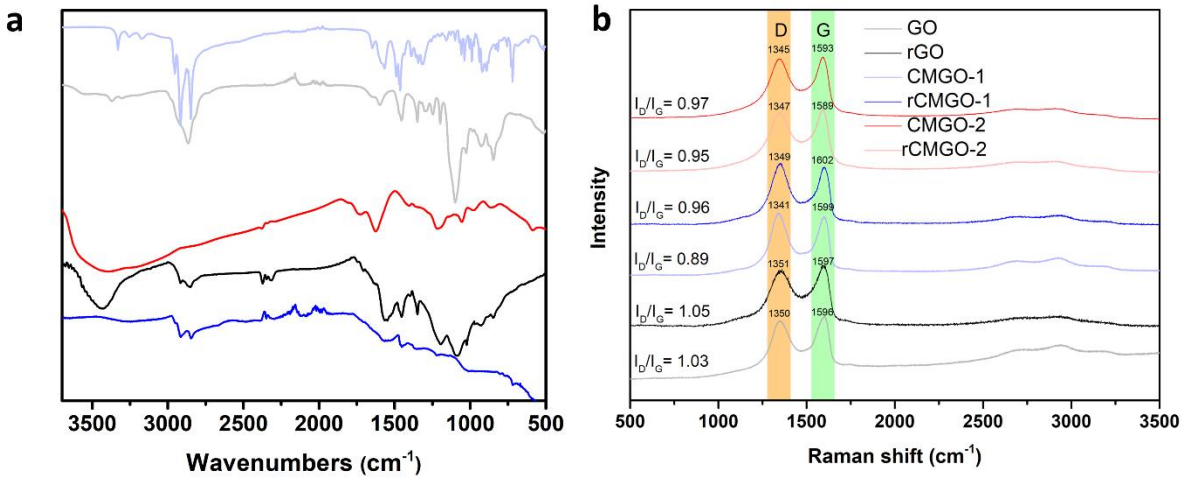

Figure 4.3-8: (a) FTIR-ATR of CMGO-1 (black), CMGO-2 (blue) and GO (red), decylamine (light blue) and NTEG (gray). (b) Raman spectra of GO, CMGO-1 and CMGO-2 before and after the thermal annealing.

The deposited and annealed films were also investigated through Scanning Electron Microscopy (SEM) and Atomic Force Microscopy (AFM) to evaluate the morphology, roughness, and film thickness. The SEM images are reported in **Figure 4.3-9**. The films appear uniform and continuous all over the substrate. All the samples look quite similar, with flat surfaces in which the GO flakes stuck one over the other in a layered motif. However, compared to rGO, both rCMGO-1 and rCMGO-2 display more wrinkles and jutting edges.

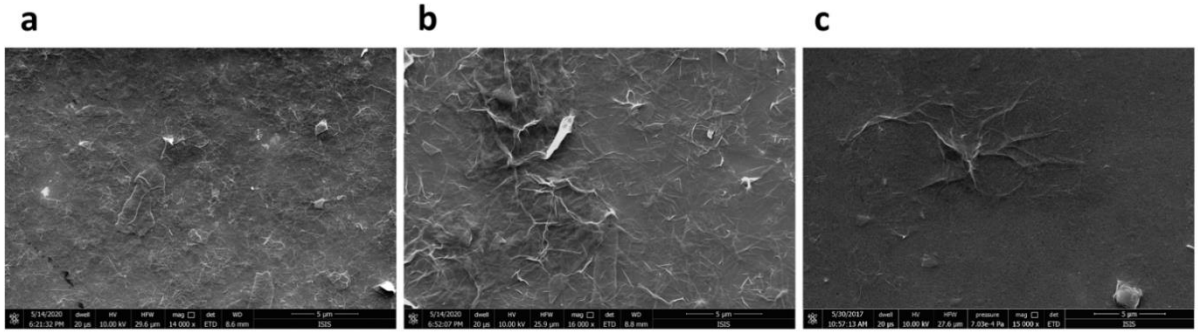

Figure 4.3-9: SEM images of rCMGO-1(a), rCMGO-2 (b) and rGO(c). The scale bar is 5 μm.

A more detailed analysis of the morphology of the samples is offered by AFM, which provides a map of the topography of the surface. Once again, the surface appears uniformly covered by the flakes of rGO and rCMGOs, whose characteristic folds and wrinkles are clearly visible (**Figure 4.3-10**). The surface roughness (Rq) calculated from the AFM images follows the trend rGO (4.49 nm) < rCMGO-1 (7.21 nm) < rCMGO-2 (14.29 nm). We ascribe such a difference to the diverse dispersibility of GO, CMGO-1 and CMGO-2 in ethanol which follows the same trend, being GO the most dispersible. Even though the suspension was sonicated for 15 minutes before the coating, small aggregates of CMGO-1 and CMGO-2 not visible to the naked eye could still be present. The film thickness was also evaluated by AFM, by scratching the film surfaces to expose the substrate and imaging the scratch edge. The results as well as the height profiles are reported in **Figure 4.3-11**. In the case of rCMGO-2 for simplicity, we imaged a small hole present in the surface of the film. The average film thicknesses, calculated over the entire image, were 23.7 nm for rCMGO-1, 22.9 nm for rGO, and 39.5 nm for rCMGO-2.

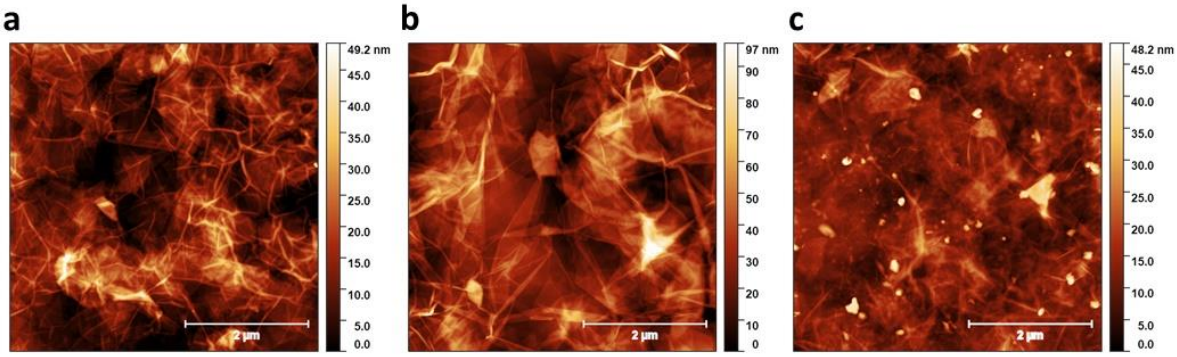

Figure 4.3-10: AFM images (5 μm x 5 μm) of films of rCMGO-1 (a), rCMGO-2 (b) and rGO (c) spray-coated on glass substrates.

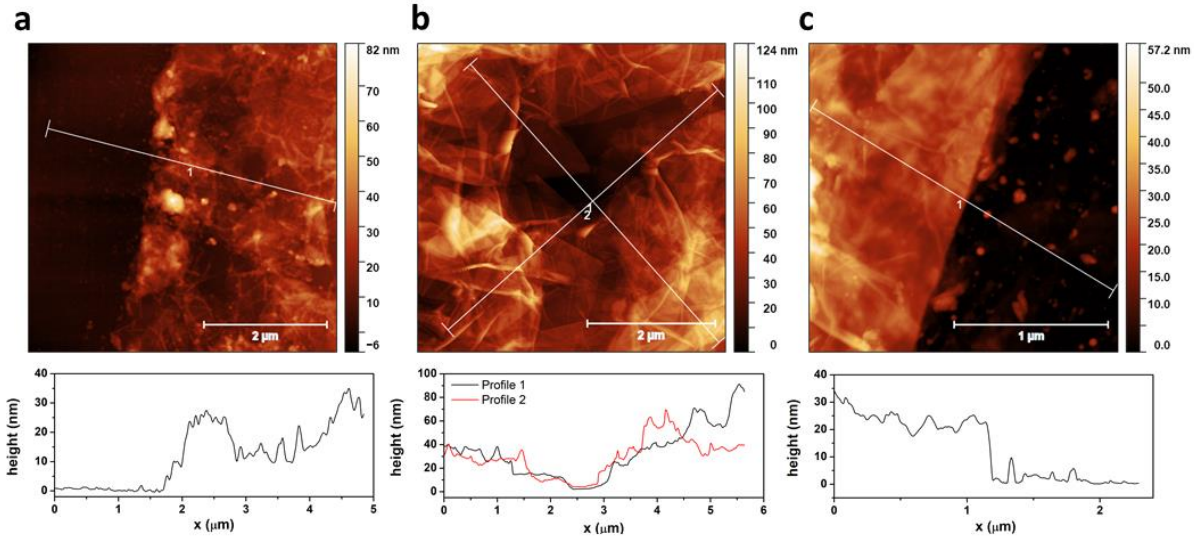

Figure 4.3-11: AFM images of films of rCMGO-1 (a), rCMGO-2 (b) and rGO (c) in which the substrate is exposed (in a and c the film was mechanically scratched). The corresponding height profiles pointed out in the AFM images are reported under each image.

The hydrophilicity of the different spray-coated films was quantified by water contact angle (C.A.) measurements, which are reported in **Figure 4.3-12**. Before the reduction, GO results obviously in the most hydrophilic material (C.A. = 35.1°± 1.2°), followed at a short distance by CMGO-1 (C.A. = 51.8°± 5.2°), while CMGO-2 is much more hydrophobic (C.A. = 87.1°± 1.8°). On the contrary, after the annealing, rCMGO-1 results in the most hydrophilic (C.A. = 63.1°± 3.4°), while rGO and rCMGO-2 appear more hydrophobic (with a C.A of 87.3°±1.7° and 92.4°±1.0°, respectively).

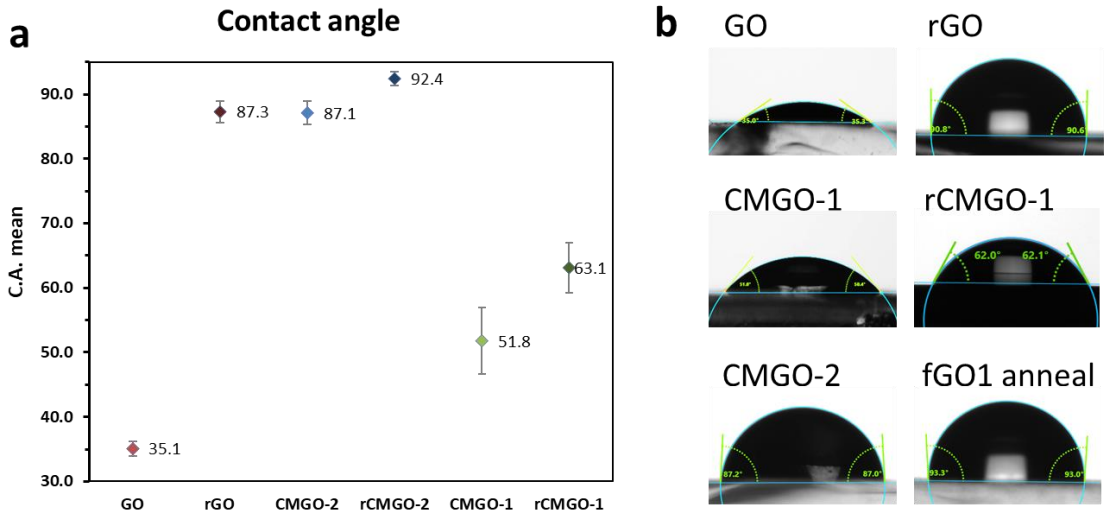

Figure 4.3-12: Water contact angle measurements. a) Contact angle of (r)GO, (r)CMGO-1, (r)CMGO-2 and b) corresponding photos of the water sessile drop on the material with the fitted contact angle represented.

The X-ray diffraction (XRD) spectra recorded *in situ* by systematically changing the RH provided information about the structure and the stability of (r)CMGOs and (r)GO films under humidity exposure (**Figure 4.3-13**). The XRD measurements were performed by Dr Fabiola Liscio and Dr Vittorio Morandi, who are greatly acknowledged. Interlayer spacing in dried CMGO-1 and CMGO-2 samples, calculated following Bragg's law, is 10.02 Å and 12,24 Å, respectively, according to the presence of NTEG and decylamine molecules in stand up configuration. Conversely, GO has a lower spacing of 6.93 Å. XRD patterns carried out on CMGO-1, CMGO-2 and GO samples show a dependence of interlayer spacing from RH. GO in particular exhibits a strong interlayer increase from 6.93 Å to 8.46 Å at RH = 80%, as already observed in the literature,[423] due to the intercalation of water molecules, absorbed by hydrophilic sites and then driven through the empty space between non-oxidized regions.[247] CMGO-1 and CMGO-2 exhibit a lower increase of the interlayer spacing of 5 % in the RH range 0 - 80 %. The spacing variation is smaller compared to GO sample, probably due to the steric effect of the functional molecules which reduces the free space for the water molecules.

The XRD spectra of rCMGOs reveal that at RH = 0 % the 001 peaks of rCMGOs shifts towards a smaller 2θ angle compared to rGO (**Figure 4.3-13** d-f). The corresponding interlayer distance changes from 4.82 Å of rGO to 8.38 Å of rCMGO-1 and 8.37 Å of rCMGO-2, indicating that the presence of TEG and decylamine chains imposes higher inter-flakes distances in rCMGOs. Furthermore, a subtle change in the crystallinity of the materials is observed upon exposure to humidity: the spacing between rCMGO-1 and rGO layers increases by only 0.16 Å when RH increases from 0 % to 80 % (Figure 2d,f) whereas such a small increase is negligible for rCMGO-2 with an interlayer spacing enhancement of only 0.09 Å (Figure 2e). Noteworthy, the expansion of rGO films is similar to those of rCMGO-1 because, despite the higher hydrophilicity of rCMGO-1 compared to rGO, in the former, the water molecules have less free space between the layers due to the steric effect of the dangling molecules. Such interlayer expansion is minimal for rCMGO-2 because of both its high hydrophobicity and few empty spaces between layers.

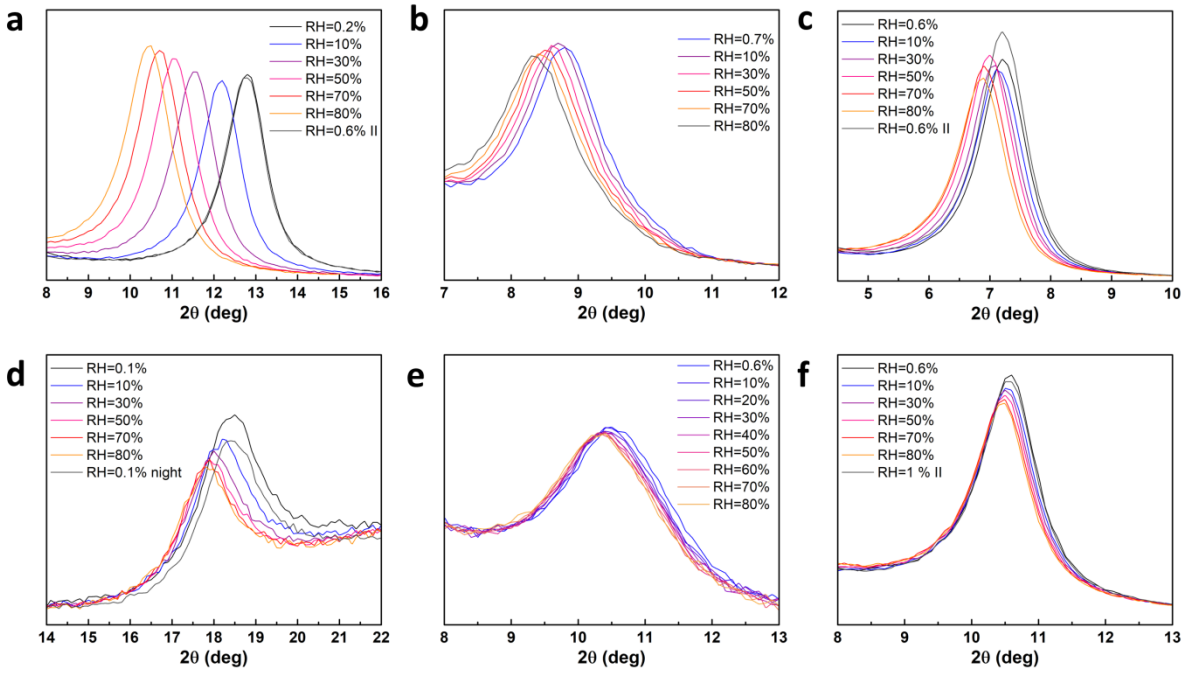

Figure 4.3-13: Variation of the XRD patterns upon exposure to humidity of the (a) CMGO-1, (b) CMGO-2, (c) GO, (d) rCMGO-1, (e) rCMGO-2, and (f) rGO films.

4.3.3. Humidity sensing performances of rGO, rCMGO-1 and rCMGO-2

Once the successful functionalization was confirmed, different electrical measurements were performed on the devices fabricated from the three reduced materials to gain quantitative insight into the key performance indicators of the humidity sensor, i.e. sensitivity, response and recovery time, reversibility, long term stability and selectivity. The response to ΔRH was defined as the ratio between the change in resistance ΔR and the initial resistance R_0 in percentage upon exposure of the devices to humidity or to vapour whereas the sensitivity as the response over a specific variation in relative humidity.

$$Response = \frac{\Delta R}{R_0}\% = \frac{(R - R_0)\cdot 100}{R_0} = \left(1 - \frac{R}{R_0}\right)\cdot 100 \qquad Eq.\ 4.3\text{-}3$$

$$Sensitivity = \frac{\Delta R}{R_0 \cdot \Delta RH}\% = \frac{(R - R_0)\cdot 100}{R_0 \cdot (RH - RH_0)} \qquad Eq.\ 4.3\text{-}4$$

Firstly, the response of the devices as a function of time was measured while sending a pulsed flow of humid air over the sample while applying a constant bias of 2 V, and measuring the electrical current to evaluate the response intensity and stability. **Figure 4.3-14** a portrays the response of rCMGO-1 and rCMGO-2 and rGO once exposed to a series of 100 pulses. It shows that the response is almost constant for the rCMGO-1 device, even after 100 pulses and the small variations are more likely caused by the rough approach employed to provide the humid pulses. In addition, the baseline of this device is particularly stable; in

fact, by keeping the humidity constant the resistance of the device shows fluctuations below the 0.01 % (**Figure 4.3-14** b). Conversely, the rGO sensor exhibits a more instable behaviour (**Figure 4.3-14** a). In fact, the intensity of the response varies from a maximum of 1 % to just the 0.07 %, and it becomes progressively weaker after several pulses. Such a trend may be due to the progressive saturation of the oxygen containing moieties of the rGO with water molecules. Furthermore, instability of the baseline has been monitored, revealing a dramatic increase during the first 10 pulses, then stabilizing and finally decreasing slowly to the initial values. On the other hand, the sensor based on rCMGO-2 shows a more stable response than the one comprising rGO; however, its baseline reveals a similar instability to rGO, with an initial rapid increase followed by a more stable behaviour.

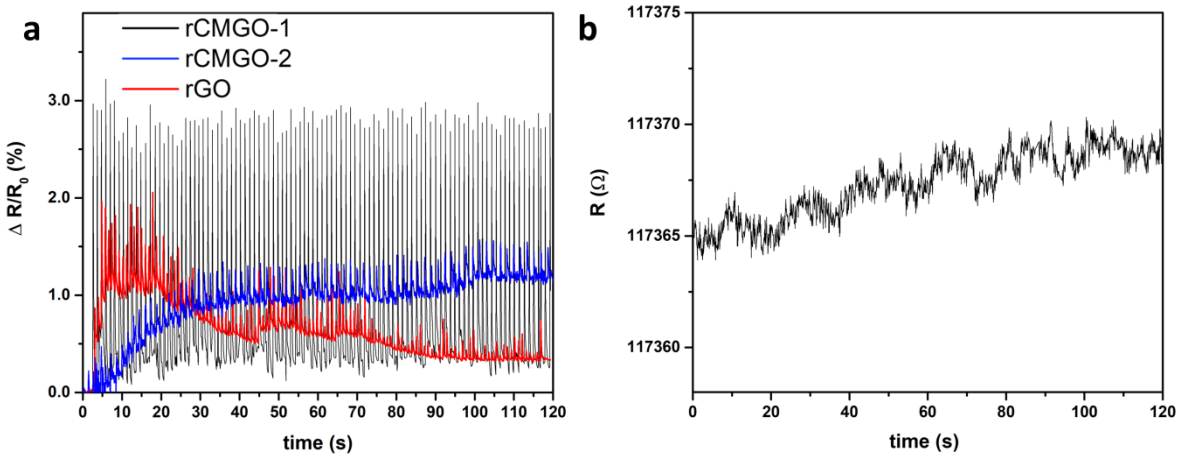

Figure 4.3-14: (a) Variation of the resistance expressed in % (response) of the devices rCMGO-1 (black), rCMGO-2 (blue) and rGO (red) when these are exposed to 100 pulses of humid air during the application of a constant bias of 2 V. (b) Resistance as a function of time of the rCMGO-1 device at constant temperature (24 °C) and RH (37 %).

To monitor the response to single humidity pulses the devices were also subjected to a lower frequency of pulses (**Figure 4.3-15** a). The rCMGO-1 sensor displays the highest sensitivity (being almost three and seven times greater than rGO and rCMGO-2, respectively), a constant and completely reversible response. This is not the case of rGO and rCMGO-2, whose baselines increase over time because of a not complete recovery. **Figure 4.3-15** c-e shows magnifications of single pulses of humidity for the three devices, from which the response and recovery times of the devices were calculated. Significantly, the rCMGO-1 device responds in just 25 ms and fully recovers in 127 ms. Conversely, the rGO sensor exhibits a 5-fold increase in the response and a not complete recovery which is 15 times longer, and the rCMGO-2 device exhibits a response and recovery time respectively 4 and 6 times longer. For comparison, the commercial sensor Sensirion SHT31, when exposed to a similar pulse of humid air, shows a response and recovery time of 0.5 and 3 s respectively (**Figure 4.3-15** b).

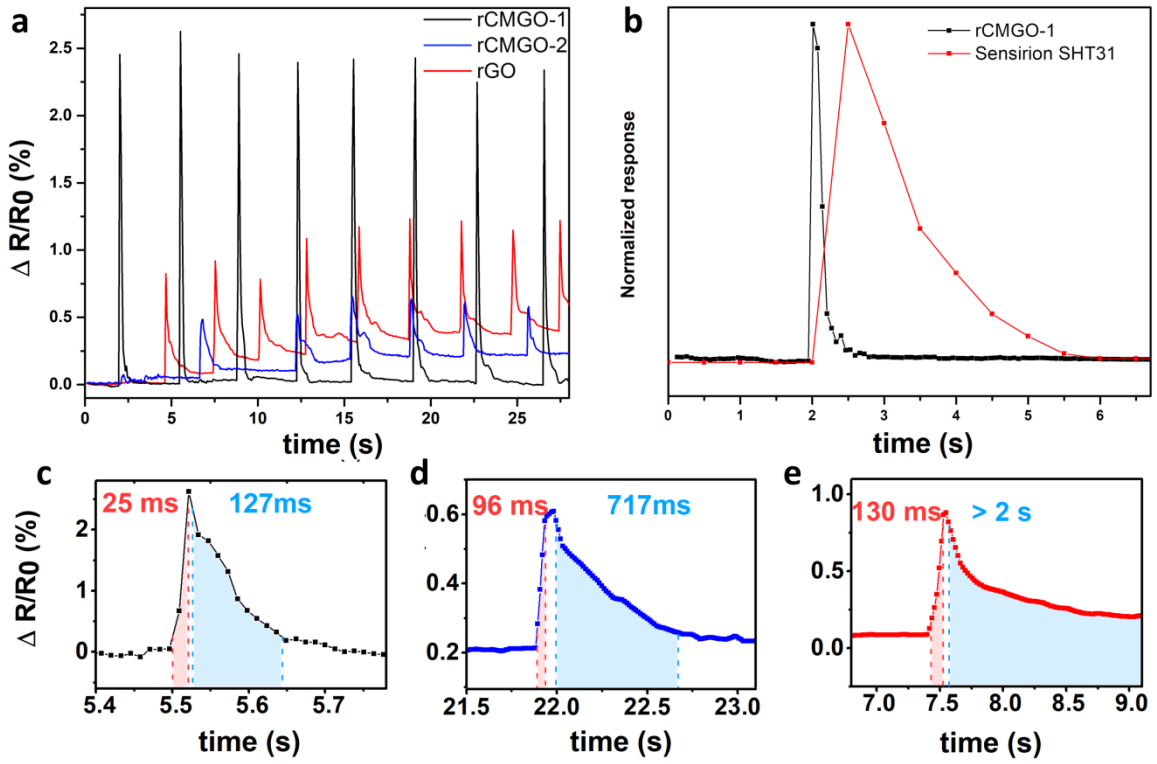

Figure 4.3-15: (a) Response of the devices rCMGO-1 (black), rCMGO-2 (blue) and rGO (red) exposed to a few pulses of humid air. (b) Comparison of the normalized responses of rCMGO-1 (black line) and of the commercial sensor Sensirion SHT31 (red line) to the same short pulse of humid air. (c-e) Magnification of the response of (c) rCMGO-1, (d) rCMGO-2 and (e) rGO to a single pulse of humid air with reported response time (in red) and recovery time (in light blue), which correspond to the highlighted regions

The response of the three devices to different humidity levels was calibrated by measuring the electrical output of the devices while increasing the relative humidity from 2 % to 97 % and then decreasing it (**Figure 4.3-16** a). It is possible to observe that the sensitivity of the rCMGO-1 sensor over the entire range of RH is around 30 % and the response data can be perfectly fitted with a negative exponential curve ($y= y_0+A_0e^{Ax}$, with $A<0$), ($R^2 = 0.9987$). Noteworthy, there is no threshold of the response and that the maximum sensitivity is observed for low RH values. Furthermore, the device exhibited low hysteresis (1.1 %). On the contrary, the rGO and rCMGO-2 samples showed a lower sensitivity, being less than half compared to rCMGO-1. Additionally, the response of rGO has a different trend upon increasing the RH respect to the rCMGO-1, and it can be fitted by a positive exponential. However, in the return curve, the trend is again a negative exponential, which results in a large hysteresis (around 67 % of $\Delta R/R_0$). Such behaviour suggests that a high resistance is retained even after the humidity level has decreased because of a more difficult release of the water molecules absorbed in the rGO sample. The rCMGO-2 sensor exhibits an intermediate behaviour, with a response that can be fitted with a negative exponential in both direction and a lower, but still fairly important hysteresis (21%). Significantly, the r-CMGO-1 sensor retains a stable response even after 10 cycles between 10 and 90 % of RH; conversely, the

response of rGO and rCMGO-2 is not stable after different cycles since the devices showed a continuous increase in resistance (**Figure 4.3-16** b). The devices were also cycled between low and high humidity by plotting continuously the change in resistance over time. These results are reported in **Figure 4.3-16** c-d and confirm the higher stability and sensitivity of rCMGO-1.

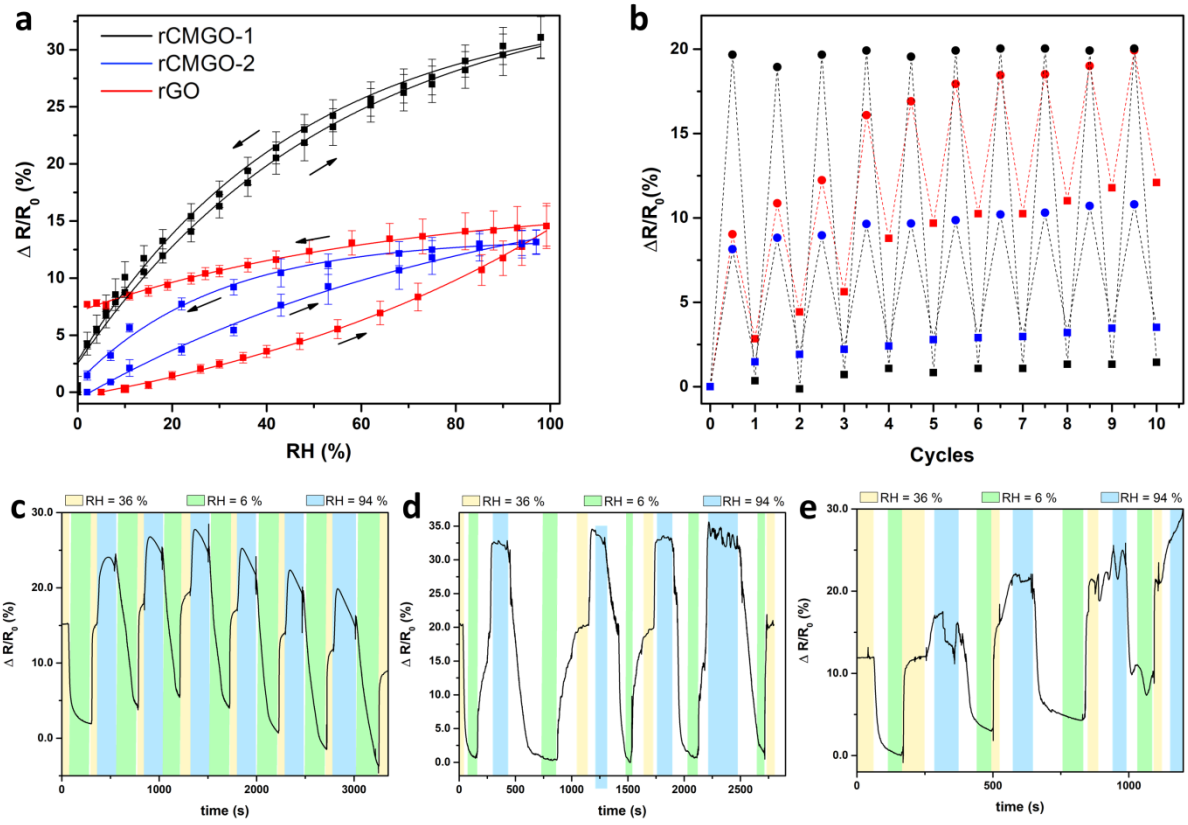

Figure 4.3-16: (a) Response as a function of the measured RH (%) of the devices rCMGO-1 (black), rCMGO-2 (blue) and rGO (red) when the humidity is gradually increased and decreased in the range 0 – 98% RH. b) Response of the same devices upon cycling the RH between 10 % (squares) and 90 % (circles) 10 times. (c-e) Continuous measurements of the response of (c) rGO, (d) rCMGO-1 and (e) rCMGO-2 while the RH was cycled between 6 %, 36 % and 94 %.

4.3.4. Cross-sensitivity to volatile organic compounds (VOCs) of the devices

The cross-sensitivity of the devices to vapours of volatile organic compounds (VOCs) was also evaluated. In particular, the sensitivity towards dehydrated ethanol, methanol, acetone and chloroform was tested by recording the response of the devices while exposing them subsequently to nitrogen gas and to the equilibrium vapour pressure of the selected VOCs for two cycles. The results are plotted in **Figure 4.3-19** a-c. They unambiguously show that the response of rCMGO-1 to all the VOCs is the lowest. In order to compare the sensitivity of all sensory materials to the different VOCs and to RH, we considered that all the analyzed VOCs are more volatile than water, thus can reach higher concentration at saturation. For

this reason, the responses of the devices to the saturated vapours of the analytes were normalized dividing them by the saturation vapour pressure of each analyte at 20 °C, expressed in kPa. The results are reported in **Table 4.3-2** and graphically in **Figure 4.3-19** d. All the sensors exhibit the highest response to methanol and ethanol, which can both donate and accept hydrogen bond, thus being the most similar to water. Furthermore, ethanol and methanol dipole moments are also similar to the one of water, which can explain the relatively high sensitivity to these vapours. In particular, rCMGO-2 displays the highest response to ethanol (3.19 $\%kPa^{-1}$), whereas rGO shows the highest response to methanol (2.81$\%kPa^{-1}$). The sensitivity to acetone, which can only accept hydrogen bonds, is lower for all the devices and the sensitivity to chloroform is comprehensibly even lower, being unable to form hydrogen bonds. However, while rCMGO-1 has negligible sensitivity to chloroform (0.07 $\%kPa^{-1}$), the aliphatic chains which decorate the surface of rCMGO-2 determine a higher affinity for chloroform, resulting in a 0.43 $\%kPa^{-1}$ response to its vapour. rCMGO-2 also shows a continuous increase in the response for high concentrations of methanol and ethanol, which may be due to a disruption of the alkyl chains packing at high concentrations of these vapours. Interestingly, rCMGO-1 alongside being the most sensitive to humidity possesses also the lowest cross-sensitivity to each one of the analyzed VOCs. In particular, rCMGO-1 is at least 9 times more sensitive to water than to any other analyte.

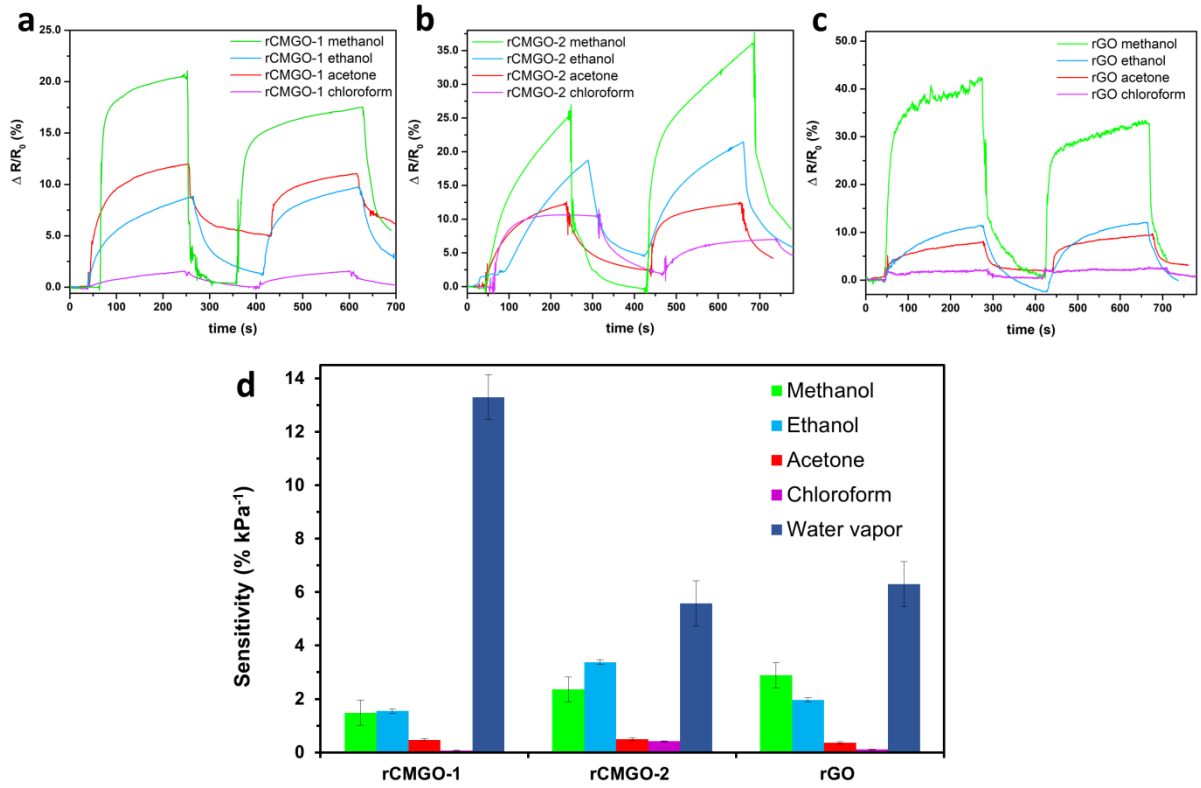

Figure 4.3-17: Selectivity response as a function of time when a) rCMGO-1, b) rCMGO-2 and c) rGO are exposed alternatively to nitrogen and to saturated vapours of methanol (green line), ethanol (blue line), acetone (red line) and chloroform (purple line). d) Sensitivity of the devices (% kPa^{-1}) to the same vapours and to humidity (100 % RH) obtained dividing the maximum response to the analytes by its saturation vapor pressure at 20 °C expressed in kPa.

Table 4.3-2: Sensitivity of the three sensors rCMGO-1, rCMGO-2 and rGO to VOCs and water vapour, obtained by normalizing the average response to the analytes for the vapour pressure of each analyte at 20 °C.

	Methanol %(kPa^{-1})	Ethanol %(kPa^{-1})	Acetone %(kPa^{-1})	Chloroform %(kPa^{-1})	Humidity %(kPa^{-1})
rCMGO-1	1.41 ± 0.16	1.51 ± 0.11	0.45 ± 0.03	0.07 ± 0.00	**13.30** ± 0.79
rCMGO-2	2.34 ± 0.61	3.19 ± 0.32	0.49 ± 0.01	0.43 ± 0.12	**5.58** ± 0.46
rGO	2.81 ± 0.46	2.02 ± 0.08	0.37 ± 0.04	0.12 ± 0.02	**6.30** ± 0.84
Vapor pressure (kPa) at 20 °C	13.0	5.95	24.47	21.17	2.33

4.3.5. Long term stability, temperature calibration and benchmarking of the performances of rCMGO-1

The best-performing device, namely rCMGO-1, was also further characterized to assess the long term stability and robustness. The rCMGO-1 sensor was left at the extreme conditions of RH = 11 % and RH = 98 % for 10 days, and its resistance was measured daily (**Figure 4.3-18** a). Impressively, the resistance of the device remained nearly constant during the evaluated time interval (changes < 1.5 %). To assess further the robustness of our device, it was also exposed to the harsh environment of 80 °C and 80 % RH for 3 days, being considered as the standard extreme conditions to assess the robustness of a humidity sensor. The response of rCMGO-1 to different levels of humidity was acquired before and after the extreme environment test and showed a small decrease in the resistance of 3.4 % after the test (**Figure 4.3-18** b). However, the response remained constant (0.7 % increase), thus the rCMGO-1 sensor can be exposed to extreme conditions without requiring recalibration.

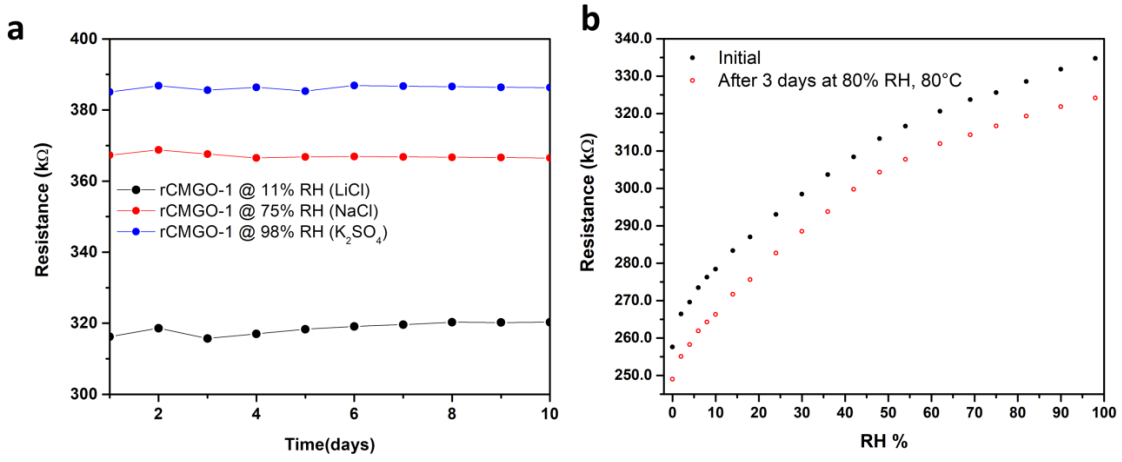

Figure 4.3-18: Long term stability of rCMGO-1 sensor.a) Resistance changes over 10 days when the sensor is stored in a low humidity (RH=11%, black dots) and a high humidity (RH=75 %, red

dots and RH=98%, blue dots). b) Resistance as a function of the RH of rCMGO-1 sensor before (black dots) and after the exposure to 80 °C at 80 % RH (red empty dots).

The effect of temperature on the resistance of rCMGO-1 was also evaluated, by keeping constant the humidity at 0 % RH and varying the temperature from 0 °C to 80° C (**Figure 4.3-19**). The resistance decreases when the temperature increases and the points can be well fitted by an exponential equation in the form $R = R_0 \exp(k/T)$ indicating a thermally activated band-like conductivity in the sample.[424]

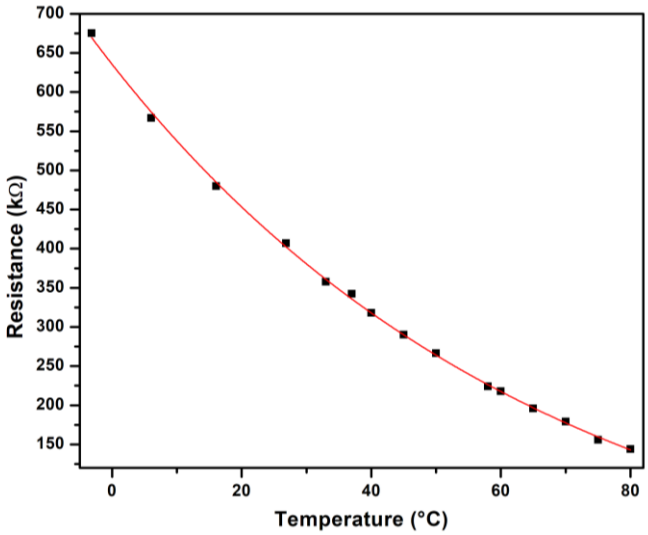

Figure 4.3-19: Resistance of the rCMGO-1 device as a function of the device temperature in the range 0 °C – 80 °C at constant RH = 0%.

Finally, the key performance indicators of rCMGO-1 were benchmarked against commercial relative humidity sensors and to the *state-of-the-art* rGO and GO based sensors that are reported in the literature (Table 4.3-3). It is clear that rCMGO-1 outperforms most of the commercial sensors that show similar performances in terms of sensitivity, but slower response and recovery while it performs better than all the rGO based sensors for sensitivity, response speed and recovery. Only GO sensors seem to have higher sensitivity at the expense of the conductivity of the material, that on the one hand obliges to operate the device with high-frequency alternating currents, thus complicating the measurement and on the other hand, restricts the sensing range because of the insulating behaviour of GO at low humidity and low reversibility when GO is exposed to high humidity.[388]

Table 4.3-3: Comparison of the performances of selected commercial humidity sensors and those based on GO/rGO which are described in the literature.

Type	Sensor	Sensitivity %(%RH^{-1})	Hysteresis	Response time	Recovery time	Humidity range (%RH)
C (commercial)	IST P14-W	0.17 %	< 1.5 %	5 s		0 - 100 %
C (commercial)	E+E Elektronik HCT01	0.35 %	< 1.85 %	6 s		0 - 100 %
C (commercial)	Sensirion SHT10	6 %	1%	6 s		0 - 100 %
R (commercial)	Sensirion SHT31	8 %	0.8 %	8 s		0 - 100 %
C (article)	GO [391]	472 %		10 s	41 s	15 - 95 %
Z (article)	GO [382]	25 %		20 ms	30 ms	40 - 80 %
R (article)	dGO-PVA [390]	11.5 %		> 60 s	> 60 s	40 - 95 %
R (article)	rGO [385]	0.04 %				40 - 95 %
R (article)	GO-aniline [392]	43 %		50 ms	50 ms	10- 90 %
R (article)	PDDA/rGO [220]	0.31 %	2 %	94 s	133 s	11 - 97 %
R (this work)	**rCMGO-1**	**0.33 %**	**1.1 %**	**25 ms**	**127 ms**	**0 - 100 %**

R : resistive, C : capacitive, Z : impedance, dGO : poly(dopamine) coated GO, PVA : poly(vinyl alcohol), PDDA : poly(diallyldimethyammonium) chloride

4.3.6. Molecular Dynamics simulations

Molecular dynamics (MD) simulations were performed to gain further insight into the nature of the interaction between water molecules and rGO/rCMGOs surfaces and reveal the origin of the different response of the latter. Force field MD simulations were performed in the presence of explicit water molecules, on rGO and rCMGO-1 layers built according to the experimental atomic composition and surface coverage (for rCMGO-1). To ease a quantitative comparison between the three surfaces, a model for rCMGO-2 was constructed by replicating the surface density of rCMGO-1, whose density of side chains is comparable to that measured in rCMGO-2 sample (**Figure 4.3-20** a). However, we also considered that in the functionalized monolayers the number of side chains should be equally distributed on the two faces of the monolayer, hence we also built two additional surfaces (hitherto referred as rCMGO-1H and rCMGO-2H) with half the surface coverage of rCMGO-1. All of these surfaces were then immersed in a water box and subjected to MD preparation and sampling runs. Final MD configurations, taken as the average of 100 MD frames along the 50 ns production run are represented in **Figure 4.3-20** b. In rCMGO-2(H) a de-wetting layer between the water molecules and the graphene surface is present, whereas the water

molecules penetrate the surface of rCMGO-1(H), demonstrating the hydrophilic nature of NTEG groups. The higher hydrophilicity of the latter is confirmed also by the lower mean distance of water molecules measured with respect to the 2D-graphene surface in rCMGO-1(H), compared to rCMGO-2(H) (**Table 4.3-4**).

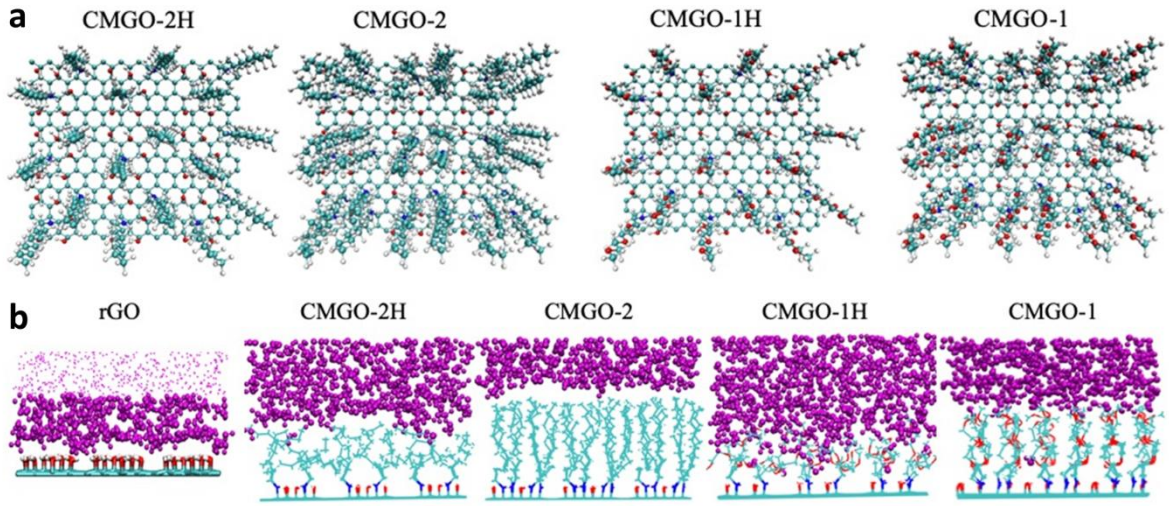

Figure 4.3-20: (a) Schematic representation of rCMGO surfaces considered for MD simulations. (b) Final MD configurations of rGO and rCMGO surfaces, taken as an average of 100 MD frames along the production cycle.

Table 4.3-4: Average distance of water molecules from the graphene surface.

Name	Height (Å)	Distance: water (Å)
rCMGO-2	14.31 ± 0.17	15.07 ± 0.31
rCMGO-1	13.22 ± 0.34	10.17 ± 2.61
rCMGO-2H	10.19 ± 0.65	8.47 ± 1.27
rCMGO-1H	10.77 ± 0.63	5.11 ± 2.32

The distances are computed as a mean of 100 MD frames taken over 50 ns of production cycle.

The Pair Interaction (PI) energies between water molecules and the (functionalized) layers were computed (**Figure 4.3-21** a). PI energies follow the trend rCMGO-1(H) > rGO > rCMGO-2(H), in line with the changes in hydrophobic/hydrophilic character of the surface and explain the trend in sensitivity of the three materials. Although reduced surface coverage of rCMGO-2 (i.e. rCMGO-2H surface) enables water penetration onto the surface, the interaction of rCMGO-2H surface is significantly smaller in comparison to rCMGO-1(H) and/or rGO surfaces.

Subsequently, Potential of Mean Force (PMF) profiles of water molecules (selected at random) with respective rGO/rCMGOs surfaces were computed, as reported in **Figure 4.3-21** b. These PMF energy profiles are composed of three distinct regions, a repulsive part

at distance < 4 Å, an interacting part where water molecules are physisorbed on rGO/rCMGO surfaces and/or surrounded by the alkyl chain of rCMGOs, comprised between 4 Å and 14 Å, and the global minima with a PMF energy ~ 0 kcal/mol, where the selected water molecule is surrounded by other solvent water molecules.

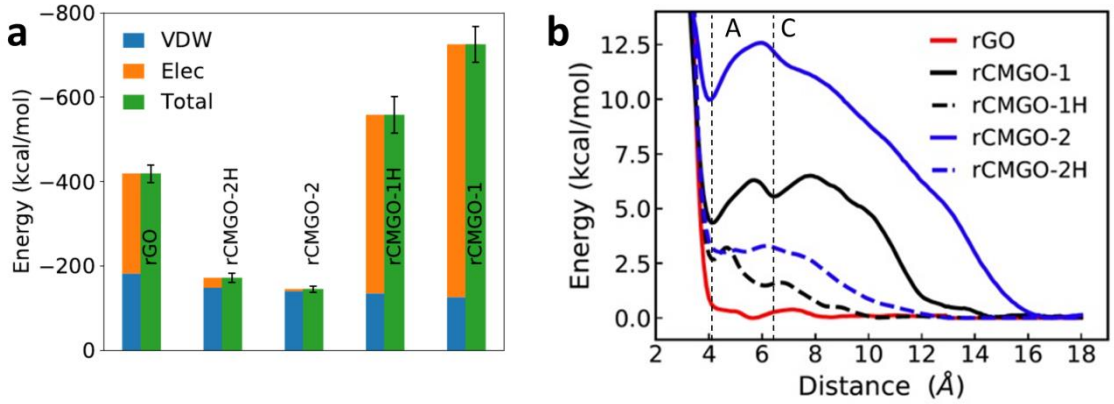

Figure 4.3-21: (a) Average pair interaction energy between water molecules and respective rGO/rCMGO surfaces. VDW, Elec energies correspond to van der Waals and electrostatic contributions to the total (Total) energies. (b) PMF energy profile of water molecules with rGO (red), rCMGO-1/rCMGO-1H (black) and rCMGO-2/rCMGO-2H (blue) surfaces, with indicated the local minima A and C.

The PMF free energy profile for rGO is very flat (likely because the enthalpic gain due to interaction between water molecules and the rGO layer is compensated by entropic losses as the molecules land on the surface), suggesting that water molecules can adsorb/desorb freely from the rGO surface. While the free energy shows a more pronounced surge in proximity to the surface in rCMGO-2 compared to rCMGO-1, both profiles feature a local minimum at around 4 Å (position A). This minimum, which is absent for rGO, is mostly associated with 'mechanical' trapping of water molecules in nano-pockets formed around the anchoring groups. This is borne out by results obtained for the half-coverage simulations showing a repulsive PMF profile all the way from 2D-surface to bulk water in CMGO-2H (and to a lesser extent in CMGO-1H). Most importantly, at both low and high coverage, the rCHGO-1(H) surfaces equipped with glycolated side chains are characterized by an additional local minimum on the PMF curve at around 6 Å (position C), which results from the interaction between water molecules and the NTEG-oxygen atoms. As a matter of fact, this minimum is completely absent for the decylamine-decorated rCMGO-2(H) surfaces. The picture that emerges from these calculations is that the favourable interactions between water and the glycolated chains grafted on the surface enable a dynamic equilibrium in rCMGO-1, where the water molecules can be stored into metastable configurations at a distance from the 2D graphene layer (~6 Å) that is sufficiently close to perturb charge transport while still being able to desorb through crossing a small energy barrier (~0.8 and 0.2 kcal/mol for rCMGO-1 and rCMGO-1H surfaces, respectively) and thereby switching the system back to its original electrical response. We furthermore speculate that the instability

and hysteresis behaviour observed experimentally for rGO and rCMGO-2 arise because of the completely flat surface energy potential in the former case (hence it is impossible to desorb all water molecules from the surface) and local inhomogeneity in the surface coverage density in the latter case (with trapping of water molecules at van der Waals contact with the surface in densely grafted regions). Furthermore, the orientations of selected water molecules in the micro-states at distance 4 and 6 Å were computed (**Figure 4.3-22** and **Table 4.3-5**). While rCMGO-1 shows a specific orientation of the water molecules in the two discrete micro-states, rCMGO-2 exhibits partially defined orientation of water molecules only at distance 4 Å, while rGO shows an isotropic distribution of the orientations of the water molecules in the quasi-continuous ensemble of microstates. The set of discrete microstates with low energy barriers and a constrained orientation of water molecules at the micro-states in rCMGO-1 lead to the higher and faster response of this material.

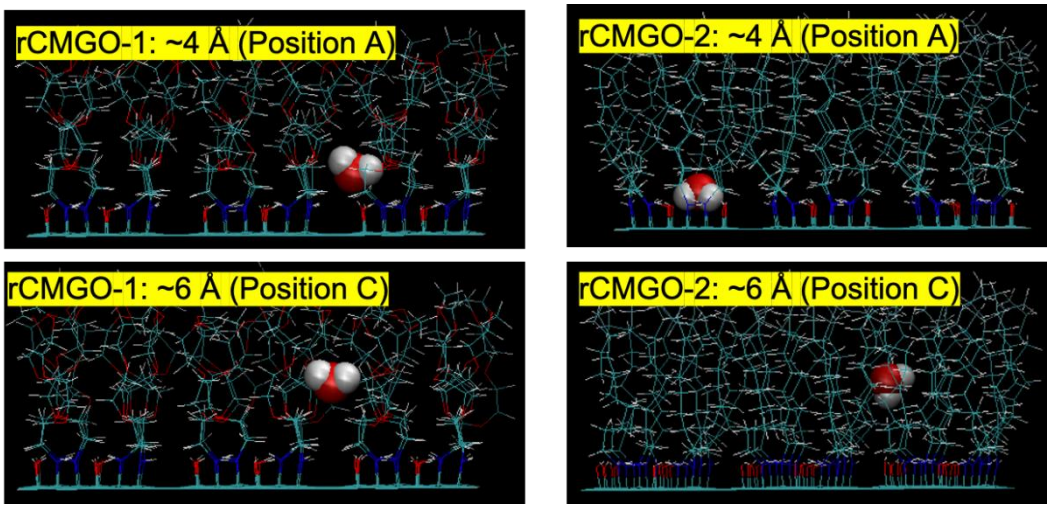

Figure 4.3-22: Orientation of water molecules at positions A & C for rCMGO-1 and rCMGO-2 surfaces.

Table 4.3-5: Acute angle formed by the vectors passing through the atoms (O, H1 and H2) of selected water molecule: O-H1, O-H2 , H1-H2 and Z axis (perpendicular to rCMGO-1/2 surface) for rCMGO-1 and rCMGO-2 surfaces, in positions 'A' and 'C'.

Surface	Moiety/Vector	Angle at Position A	Angle at Position C
rCMGO-1	O-H1	61 ± 11	72 ± 15
	O-H2	63 ± 10	70 ± 14
	H1-H2	87 ± 10	88 ± 10
rCMGO-2	O-H1	21 ± 31	10 ± 26
	O-H2	25 ± 30	12 ± 25
	H1-H2	75 ± 21	20 ± 30

In liquid water, the angles between O-H1, O-H2, H1-H2 and Z-axis are ~ 0 ± 40, indicating an isotropic orientation of water molecules.

4.4. Conclusions

In summary, we have investigated the effect of the hydrophilicity of rGO and its chemically modified analogues over the humidity sensing capabilities. In particular, we produced two novel hydrophilic and hydrophobic materials based on the chemical modification of rGO with triethylene glycol and decane derivatives, respectively. These two materials and rGO were processed in thin and transparent resistive-type humidity sensors and exposed to humidity. We proved that the device comprising the most hydrophilic material, namely the glycolated rCMGO-1, possesses the best sensing performances towards humidity. This device shows an interesting positive response with a remarkable sensitivity (up to 31 % when the RH is shifted from 2 to 97 %), high stability of the signal after 100 humid pulses, complete reversibility, fast response and recovery time (respectively 25 ms and 127 ms), and long-term stability thereby outperforming many of the commercial devices and other rGO based resistive type devices. Our sensor displays also high selectivity to humidity when compared to representative small polar organic molecules. Conversely, the alkyl decorated rCMGO-2 and the non-functionalized rGO exhibit worse sensitivity, longer response and recovery times and unstable behaviour. The use of humidity dependent XRD and Force Field MD simulations made it possible to unravel the physical origin of the better performances of rCMGO-1 based devices. While the functional groups present on the rGO surface have a low impact on the structural changes of the materials when they are exposed to a humid environment, the presence of chemically attached molecules can favour or disfavour the interaction of water molecules with the graphene surface, leading to different electronic behaviour. In particular, the interaction force with water is the highest in rCMGO-1 due to its functionalization with TEG, resulting in the highest sensitivity. Furthermore, we demonstrated that the water molecules need to overcome a small energy barrier to escape from the surface of rCMGO-1, leading to a fast and complete reversible sensing. These water molecules are instead trapped on rCMGO-2 and rGO surface, thus leading to a slow and incomplete recovery which ultimately yielding to poorly responsive nature of the device. Overall, we have demonstrated that the ad hoc chemical functionalization of GO with suitably designed molecules enables it to reach the highest performances in humidity sensing and ensures the highest selectivity to water molecules. We can anticipate that the analogous functionalization of GO and other 2D materials with the specific receptor of the analyte of choice, wisely chosen by exploiting the well-established library provided by supramolecular chemistry, will make it possible to fabricate highly performing chemical sensors of the analyte of interest. Finally, we believe that our sensor matches all the technological requirements to be integrated into portable, low-cost and low-consumption devices which potentially can be supported on flexible and transparent substrates.

Chapter 5.

Reduced graphene oxide-copper nanowires hybrid transparent electrodes for optoelectronic devices‡

Transparent conductive films (TCFs) are key-components as electrodes in many electronic devices. Nowadays most TCFs are made of indium tin oxide (ITO) because it combines high stability and conductivity with a transparency in the visible range. However, ITO is also expensive and brittle; therefore many efforts are being made to develop new TCFs which could be also flexible, less expensive and that can be processed using methods which potentially allow large-area coatings. TCFs based on copper nanowires (Cu NWs) are promising for their transparency and conductivity similar to the one of ITO, their easiness of deposition on larges and arbitrary surfaces and flexibility. Nevertheless, Cu NWs are prone to oxidation. To enhance their chemical stability different strategies have been proposed, including their coating with reduced graphene oxide (rGO), which is cheap, sufficiently transparent and conductive. In this chapter, we report a novel green chemistry approach to assemble Cu NWs/reduced graphene oxide hybrid coatings onto a wide range of supports via spray-coating. The method involves the preparation of dispersions in environmentally friendly solvents and avoids the use of harmful reagents. The resulting films combine sheet resistances (< 30 Ω/sq) and transparencies in the visible region (transmittance > 70 %) which are rivalling those of ITO. Furthermore, these electrodes show high flexibility (4 % resistance change after 10000 bending cycles at a bending radius of 1 cm) and robustness, with long-term stability in air and washability in common household detergents. Such hybrid transparent electrodes have been used to assemble high-performance electrochromic devices, which showed stability of thousands of cycles. This hybrid conductive coating holds the potential for being exploited as transparent electrode in numerous optoelectronic applications such as solar cells, light-emitting diodes and displays.

‡ A part of the work presented within this chapter have been published: Aliprandi, A.; Moreira, T.; Anichini, C.; Stoeckel, M. A.; Eredia, M.; Sassi, U.; Bruna, M.; Pinheiro, C.; Laia, C. A.; Bonacchi, S. Hybrid Copper-Nanowire–Reduced-Graphene-Oxide Coatings: A "Green Solution" Toward Highly Transparent, Highly Conductive, and Flexible Electrodes for (Opto) Electronics. *Adv. Mater.* **2017,** *29* (41), 1703225.

5.1. Introduction

Transparent conducting electrodes are fundamental components in a wide range of optoelectronic devices including organic light emitting diodes (OLED), liquid crystal (LCD) displays, touch-screens, photovoltaic cells, luminescent lamps, and electrochromic devices. Indium tin oxide (ITO) is currently the most widely used transparent conductor because of its unique property of being at the same time highly conductive and transparent.[17] However, ITO features a number of drawbacks: (*i*) it is brittle, thus poorly suitable for flexible electronics, (*ii*) it has limited chemical and electrochemical stability, (*iii*) it is expensive and barely sustainable, due to the high preparation costs and the scarcity of indium in the earth's crust. In particular, the latter point is the most alarming, because more than the 75 % of refined indium is used to produce ITO,[425] and by 2050 the world reserves of this element may run out.[426] Therefore, the development of new, low-cost, stable, sustainable and large-area transparent electrodes represents one among the major challenges in material sciences and engineering. Alternatives to ITO include other transparent metal oxides such as fluorine doped tin oxide (FTO), metal nanowires, graphene, carbon nanotubes, conductive polymers such as PEDOT:PSS and composites based on these materials. In particular, films made of random meshes of copper and silver nanowires (NWs) have gained considerable attention because of their high electrical conductivity and optical transmittance that are comparable to those of ITO.[427] Furthermore, NWs can be readily dispersed into solution and deposited onto different substrates by spray coating or using a Meyer rod, [428] which represent big advantages for industrial production. Among them, silver nanowires are the most used because of the higher oxidation resistance compared to copper. However, the cost of silver is 100 times greater than that of copper, and its abundance in the earth crust is 1000 lower. [5] Thus, copper nanowires (Cu NWs) represent the most affordable alternative. Moreover, "green" large-scale hydrothermal synthesis of high-quality Cu NWs relying on the use of hydrophobic amines and glucose as reducing agent has been recently reported. [8, 375, 429]

Nevertheless, the practical applicability of Cu NWs is hindered by their limited chemical stability and propensity to undergo oxidation which results in a degradation of the conductive properties of the film. Furthermore, the as-synthesized Cu NWs are scarcely conductive because of the presence on their surface of a layer of the adsorbed alkylamines used in their synthesis and a thin layer of CuO, which is readily formed once the NWs are exposed to air. To remove this oxide layer and the adsorbed ammines, harsh methods are typically employed. Such methods include a post-deposition treatment based on high temperature annealing (> 175 °C) in reducing hydrogen atmosphere or annealing-free processes consisting of acid etching[11] and photonic sintering.[430] In parallel, a great effort has been devoted to protect Cu NWs from further oxidation including nickel alloying[431] and the use of inorganic shells. [432] However, the latter approach requires cumbersome additional steps such as atomic layer deposition (ALD)[433] or the electrodeposition of a metal (Zn, Sn, or

In) onto the surface of Cu NWs network, followed by oxidation to create a transparent oxide shell.[432] Moreover, albeit the protection of Cu NWs through inorganic (semiconducting or insulating) oxide shell can impart them good stability, such surface passivation can impede the heterogeneous electron transfer with the active materials, making the NWs no longer suitable as electrodes in electrochemical and other optoelectronic devices. To address such a problem, graphene has been proposed as an effective barrier against oxidation of NWs by virtue of its high transparency, electrical conductivity and impermeability.[434, 435] For this purpose, CVD graphene has been used; however, the high cost of CVD graphene sheets and the tedious and time-consuming transfer process from the growth substrate to the NWs film make such approach poorly suitable for the generation of large-area and low cost electrodes.[436] Conversely, graphene oxide (GO) has received large attention in the past decade because of its low production cost and its high processability from polar solvents. While GO is electrically insulating, once it is chemically or thermally reduced to reduced graphene oxide (rGO) the conjugated structure is partially restored and so is the electrical conductivity. However, films of rGO typically have sheet resistances > 1000 Ω/sq which is nearly two orders of magnitude higher than that of ITO films,[393] thus making rGO alone not suitable as electrode for optoelectronics.[420] Recently, Ruoff *et al.*[7] have proposed the use of Cu NWs covered by a rGO film as transparent electrodes. However, the main drawback of this electrode was the complicated dry transfer process through a sacrificial poly(methylmethacrylate) (PMMA) layer required to move the rGO film on top of the Cu NWs, thereby limiting the large-scale scalability. Furthermore, in order to obtain conductivity, reduction with hydrazine and three thermal annealing steps in H_2/Ar up to 400 °C were used, which increased considerably the environmental and energetic impact of the productive cycle. Overall, there is a great technological demand to produce highly transparent and highly conductive electrodes using green and low-cost preparation approaches that are potentially suitable for any kind of substrates, making them applicable as transparent electrodes for different types of electronic devices.

In this work, we have conceived a straightforward method for the preparation of Cu NWs/rGO films which relies on the bottom-up formation of Cu NWs suspensions by means of the Maillard reaction[8] and on the use of commercial GO. These two components are processed into thin transparent conductive films onto any arbitrary substrate through spray-coating from ethanolic suspensions of the two components, followed by their simultaneous chemical reduction in a diluted water solution of $NaBH_4$. The rGO coating provides effective protection against the oxidation of Cu NWs making it possible to produce highly stable transparent and flexible electrodes. The use of cheap materials and of a chemically mild approach and the elimination of any additional treatments such as metal electrodeposition[432] reduce the cost and the environmental impact of the electrode and make it suitable for industrial scale-up. Finally, we have exploited the hybrid Cu NWs/rGO electrodes to fabricate high-performance electrochromic devices.

5.2. Materials and methods

5.2.1. Experimental procedures

All the chemicals and reagents were purchased from Sigma-Aldrich and used without further purification. Graphene oxide (GO) (4 mg/ml, water dispersion) was purchased from Graphenea.

5.2.1.1. *Synthesis of copper nanowires (Cu NWs)*

Cu NWs were synthesized following a modification of the methods reported in Ref. [8, 374, 375]. In particular, in a round bottom flask $CuCl_2 \cdot 2H_2O$ (380 mg, 2.23 mmol) was dissolved in 110 mL of deionized water, followed by the addition of octadecylamine (2600 mg, 9.64 mmol). The suspension was sonicated for 15 min until a light blue emulsion was obtained. Then D-(+)-glucose (850 mg, 0.55 mmol) was added to the emulsion. To obtain a homogeneous emulsion, this was heated at 50 °C, while stirring for 3 hours. Then the emulsion was transferred into a steel autoclave and heated at 110 °C for 10 hours. The resulting reaction product containing the Cu NWs was cooled and transferred to 45 mL plastic vials and centrifuged several times (each time discarding the supernatant) before with pure water, then with ethanol/water mixture 1/1, and finally with pure ethanol (5000 rpm, 8 min). Finally, the resulting pure Cu NWs were dispersed into 80 mL of ethanol (Cu NWs concentration ≈ 1.2 mg/mL, yield 67 %).

Alternatively, the Cu NWs were extracted from hexane to increase the ratio between Cu NWs and Cu NPs, which represent an unavoidable by-product. The procedure was inspired by the work of F. Quian *et al.* [437]. After the synthesis, the Cu NWs were precipitated by centrifugation (4000 rpm, 8 min) and re-dispersed in water. This procedure was repeated 4 times until the water solution remained clear. Then the water Cu NWs suspension was sonicated for 1 minute and then transferred to a separatory funnel and hexane in equal amount was added. The two phases were mixed vigorously and let to separate. The lower water phase was eliminated and put apart. Deionized water was added to the hexane phase in the funnel and the procedure was repeated. Then the hexane phase was let decanted and the Cu NWs precipitated on the bottom, the upper hexane part was removed. Finally, the Cu NWs were collected and precipitated by centrifugation (5000 rpm 8 min) firstly from hexane, then from acetone, twice from ethanol and then finally dispersed in 80 mL of ethanol (Cu NWs concentration ≈ 1.0 - 1.1 mg/mL). The water phase was also centrifuged to precipitate the NPs (6000 rpm, 8 min) and the Cu NPs collected.

5.2.1.2. *Preparation of the Cu NWs/rGO hybrid electrodes*

PET foils (of different sizes, thickness = 0.175 mm) were cleaned by sonication in ethanol for 10 min, followed by washing with ethanol and drying under a stream of air. Microscope glass slides, Si/SiO_2 and Si substrates were cleaned with a sonication bath in acetone and 2-propanol for 15 min respectively, followed by UV ozone treatment (10 min) to further remove the surface contaminant. In order to improve the affinity of GO for the glass substrate, an interlayer of (3-aminopropyl) triethoxysilane (APTES) (30 µL in 20 mL ethanol) was sprayed on top of the glass supports. The schematic assembly procedure is reported in **Figure 5.2-1**. The ethanolic dispersion of Cu NWs was diluted 20 times in ethanol (Cu NWs concentration ≈ 0.05 % mg/mL), homogenized by vortexing and short sonication (1 min max) and sprayed onto the surface of the different substrates. Subsequently, GO dispersion in water (4 mg/ mL, Graphenea©) was diluted with ethanol 40 times and sonicated 30 min. The clear yellow dispersion was then sprayed onto the top of Cu NWs. A commercial airbrush gun for modelling and painting with a 0.3 mm needle and nozzle was used for all the spray-depositions. The airbrush was supplied with compressed nitrogen at 1.5 bar and the substrates were heated at 90 °C during the spray-coating. Finally, the substrates were dipped into a fresh aqueous solution of $NaBH_4$ (0.1% w/w) for 2 hours at room temperature (RT). Then the substrates were washed with water and ethanol and dried with nitrogen.

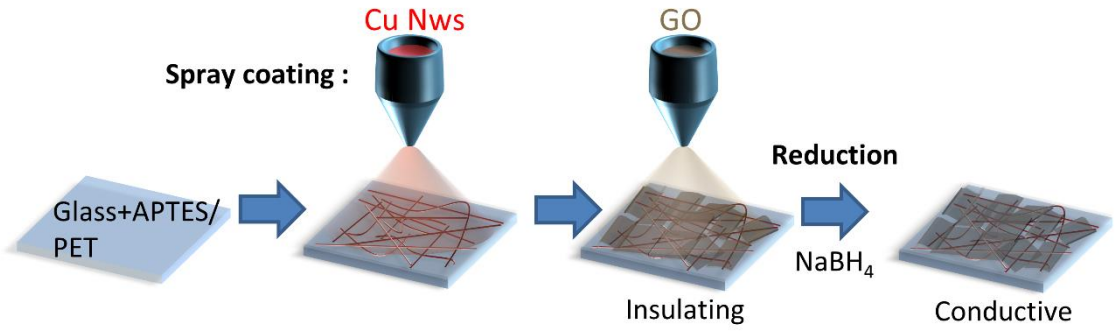

Figure 5.2-1: Schematic of the preparation of the hybrid Cu NWs/rGO transparent electrode.

5.2.1.3. *Effect of the reducing agent*

In addition to NaBH4, other reducing agents were also tested. In particular, the Cu NWs/GO films on glass and PET were reduced chemically by soaking them in the solutions **1-6**. The microscopic aspect, the sheet-resistance and the transmittance of the film were checked every 30 minutes.

Solution 1: acetic acid (0.1 mL) and hydrazine monohydrate (0.133 mL) in 20 mL of ethanol at RT.

Solution 2: hydrazine monohydrate (0.100 mL) in 20 mL of ethanol at RT.

Solution 3: hydrazine monohydrate (0.150 mL) in 20 mL of water at RT.

Solution 4: $SnCl_2$ (15 mg) in 20 mL of ethanol at RT.

Solution 5: L-ascorbic acid (45 mg) in 20 mL of water at 55 °C.

Solution 6: dispersion of zinc powder (20 mg) and acetic acid (10 μL) in 20 mL of water at RT.

5.2.1.4. *Evaluation of the sheet resistance as a function of the Cu NWs density*

To evaluate the sheet resistance of the electrodes as a function of the network density of Cu NWs samples with an increasing quantity of Cu NWs were assembled.

The samples were assembled using clean glass substrates, preheated at 100 °C, on which were deposited via spray-coating in the order: APTES (30 μL in ethanol) and increasing quantity Cu NWs (0.05 mg/mL in ethanol). The samples were soaked in a reducing solution of $NaBH_4$ in water (1 mg/mL) at room temperature for 2.5 hours to reduce the coating layer of oxide over the Cu NWs and restore the conductivity. Each sample was characterized *via* an optical microscope to check the Cu NWs network, UV-Vis to measure the transmittance and four-point probe to measure the sheet resistance.

5.2.1.5. *Bending tests of the Cu NWs/rGO hybrid films on PET*

Electrical contacts are fabricated on a reduced Cu NWs/rGO film by depositing Cr/Au (5 nm / 60 nm) with a thermal evaporator and a shadow mask, providing a film area to be investigated of 5 x 10 mm^2. The contact resistance is measured by using a Keithley 2410 source meter in a four-terminal configuration and it is estimated to be <1 Ω. (i.e. ~10 Ω/mm). The bending tests on the hybrid electrodes were performed in the Nokia Bell Labs (Cambridge) by Dr Ugo Sassi and Dr Matteo Bruna, who are greatly acknowledged. The mechanical stability of the film was first characterized by performing sheet resistance measurements under different bending radii, using a calibrated mandrel tester with cylinders having different diameters. The electrical resistivity was measured in situ with the film kept at the desired bending radius. Resistance of the material to fatigue bending has been carried out by performing thousands of bending cycles using a Bose Electroforce LM1 in a three-point bending configuration (**Figure 5.2-2**). The sample was placed face-down to prevent surface damages by the central actuator and the bottom holders were covered by a Kapton tape to minimise scratching effects with the metal electrodes. The bending radius r_b is calculated as:

$$r_b = \frac{h^2 + \left(\frac{L_b}{2}\right)^2}{2h} \qquad \textit{Eq. 5.2-1}$$

where L_b is the distance between the bottom holders of the bending system and h the maximum height displaced by the central actuator, as indicated in **Figure 5.2-2**.

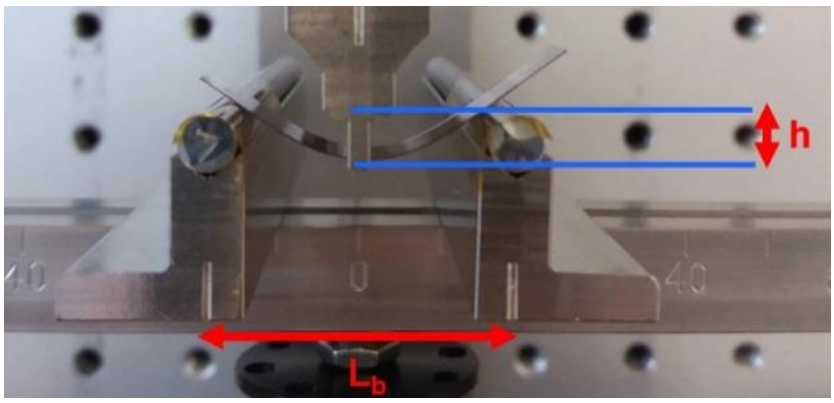

Figure 5.2-2: Photo of the fatigue bending setup with the PET/Cu NWs/rGO facing down. The distances h and L_b are reported in the figure.

5.2.1.6. *Washing tests of the Cu NWs/rGO hybrid transparent electrodes*

Samples of Cu NWs/rGO and Cu NWs alone on PET (3 x 2 cm^2) were produced (both reduced with $NaBH_4$ aqueous solution). The first washing solution was prepared by dissolving 0.8 mL of a commercial washing machine detergent (Ariel™, Procter & Gamble) in 400 mL tap water at 30 °C stirred with a magnetic stirrer with a speed such as to form a vortex deep 1/5 of the total height of the liquid. The solution presented a pH= 7.4. Then a sample of Cu NWs on PET and a sample of Cu NWs/rGO on PET were soaked in the agitated washing solution for 9 min, after which the samples were placed in equally agitated tap water for rinsing. Subsequently, the samples were dried and the sheet resistance, as well as the morphological aspect, checked. The same procedure was repeated for a higher concentration of washing machine detergent (4 mL, pH = 8, 30 °C) and for a higher washing temperature (4 mL, 60 °C). The second washing solution was prepared by using a commercial dishwashing liquid soap (Fairy™, Procter & Gamble) and repeating the exact procedure used for the washing machine detergent. The diluted and concentrated solutions had a pH of 6.5 and 6.0 respectively. For the direct contact tests, the samples of Cu NWs and Cu NWs/rGO on PET were soaked alternatively in a hard surface cleaner (generic brand), in a multi-purpose spray-cleaner with hypochlorite (Cif™, Unilever) (pH=12) and in H_2O_2 solution in water at 2 % v/v. Then the samples were rinsed and dried as described before, and the sheet resistance and microscopic appearance were checked.

In particular, the formulations of the tested detergents were as follows:

- Washing machine detergent: 5-15% anionic surfactants, <5% non-ionic surfactants, fatty acid soaps, phosphonates, enzymes, benzisothiazolinone, methylisothiazolinone (preservatives), perfumes, NaOH, NaCl, CaCl.

- Dishwashing liquid soap. 15-30% anionic surfactants, 5-15% non-ionic surfactants, phenoxyethanol, methylisothiazolinone (preservative), perfumes, NaOH, NaCl, Na_2SO_4.
- Hard surface cleaner: <5% non-ionic surfactants, C12-C14 alkyltrimethylendiamine (0.3g/100g), benzisothiazolinone (preservative), perfumes, denatonium benzoate
- Multi-purpose spray-cleaner with hypochlorite. Anionic surfactants <5%, sodium hypochlorite 1 %, methylisothiazolinone, methylchloroisothiazolinone, perfumes.

5.2.1.7. *Assembly of the electrochromic device (ECD)*

The Cu NWs/rGO electrodes on PET were used as electrodes in electrochromic devices (ECDs). The devices were assembled and characterized by Tiago Moreira in the group of Prof. César A. T. Laia (Universidade Nova de Lisboa) who are greatly acknowledged. The devices were assembled in collaboration with the company Ynvisible, that supplied the materials and shared their *know-how*. A poly(3,4-ethylenedioxythiophene) (PEDOT) ink, whose formulation is reported after, was deposited on the Cu NWs/rGO electrodes by spray-coating. The electrodes were placed over a heating plate at 60 °C. The 2 layers of PEDOT ink were spray-coated subsequently, and the electrode was left to dry for 2 min at 60 °C in-between the two depositions. The PEDOT ink used on spray-casting contained poly(3,4-ethylenedioxythiophene) polystyrene sulfonate (PEDOT:PSS from Clevios®), dimethyl sulfoxide, miliQ water and Brij 30® from Sigma-Aldrich as a surfactant. The formulation is property of Ynvisible®, all the chemicals were used as bought with no purification. The ECDs were assembled with the *know-how* of the company Ynvisible®. The Cu NWs/GO + PEDOT electrodes were used as the working electrode and a substrate of PET-ITO was used as a counter-electrode. Between the two electrodes is placed an UV curable electrolyte Li^+ based denominated Ynv.El.® property of Ynvisible® with the patent nº 20140361211. A bi-adhesive plastic spacer is placed around the frame of the device, interposed between the two electrodes, with the double function of separating the electrodes and sealing the device. Electrical contacts with the two electrodes are enabled with copper tape. Alternatively, an ITO free electrode composed of PEDOT ink spray-coated on PET was used as a counter-electrode. A schematic of the assembly procedure and cross-section of the ECD are reported in **Figure 5.2-3**.

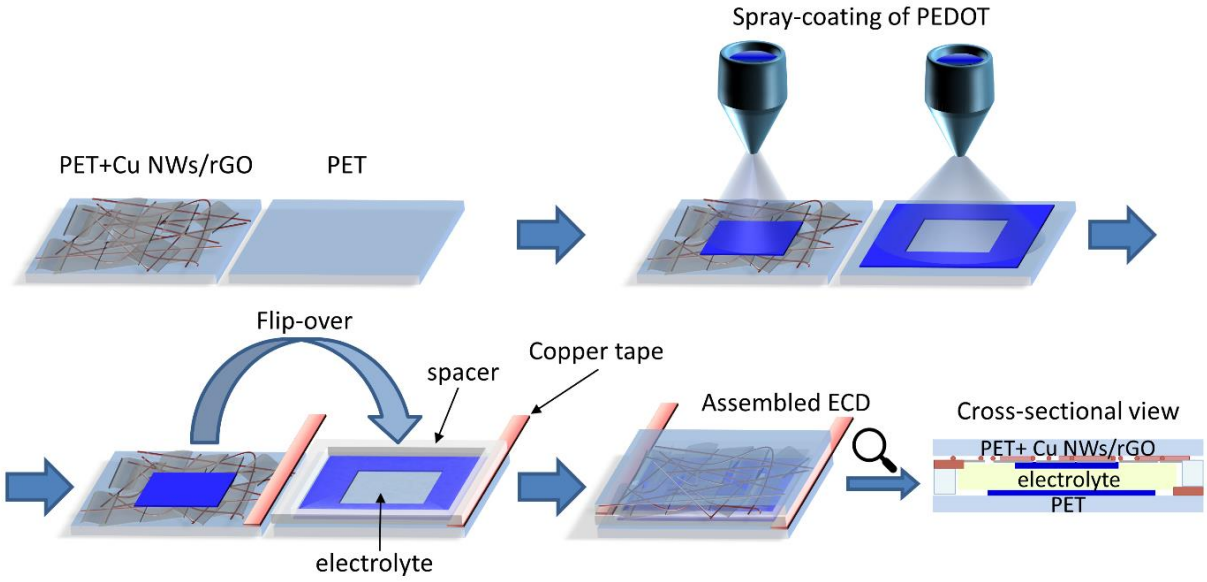

Figure 5.2-3: Schematic of the assembly of the ECD, and cross-sectional view of the device.

5.2.1.8. *Characterization of the ECD*

The EC devices were electrically connected to a potentiostat and placed inside a UV-Vis spectrophotometer for the acquisition of the absorption spectra. The applied potential was -1.5 V for reduction (blue state) and 0 V for the neutral state.

The cycling measurements of the devices were made in a homemade cycling box (**Figure 5.2-4**). A digital camera, a cold-cathode fluorescent lamp to control the luminosity and a ColorChecker® accessory (colour pattern) were placed inside an isolated chamber. The device was electrically connected to a function generator (Tektronix AFG2000) and placed inside the box. The device was operated cyclically between -1.5 V and 0 V, each cycle was 5 s long. The camera, equipped with an intervalometer, acquired every 100 ms pictures of the device in the *on* and *off* states. Then, the acquired pictures were treated with a MatLab function to convert the RGB coordinates to CIE L*a*b* colour coordinates, using the ColorChecker® as reference.

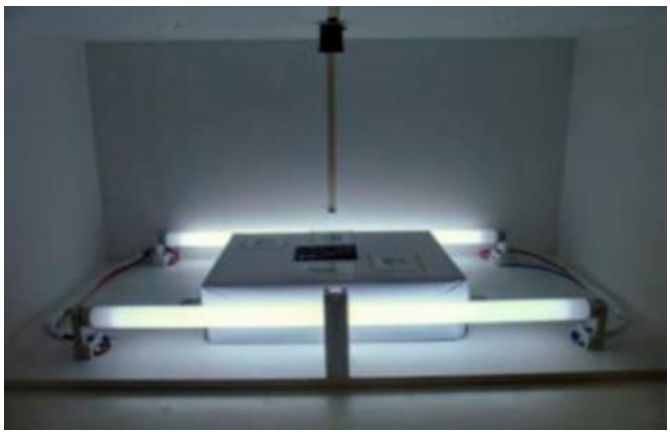

Figure 5.2-4: Photo of the Cycling box created by Ynvisible® to monitor the durability of the ECDs.

5.2.2. Instrumental methods

X-Ray Photoelectron Spectroscopy (XPS) measurements were carried out using a Thermo Scientific KAlpha X-ray Photoelectron Spectrometer system equipped with an Al Kα X-Ray source (photon energy Eph = 1486.6 eV, beam spot size ~100 μm). The samples for the XPS analysis were deposited on Silicon substrates *via* drop-casting. 10 scans were acquired for the survey, C 1s, O 1s, Cu 1s spectra, while 30 scans were acquired for N 1s spectra. For each sample, three different points were measured and averaged. Transmittance UV-Vis spectra of the films were recorded on the Jasco V-670 spectrophotometer. The FTIR-ATR measures were performed with a Thermo Scientific Nicolet 6700 FT-IR spectrometer. TGA was conducted using a Mettler Toledo TGA/DSC 2 system, with a heating rate of 10 °C/min from 25 °C to 800 °C under argon atmosphere. Atomic force microscopy (AFM) characterization of the devices was performed with a Bruker Dimension Icon microscope under ambient conditions, operating in tapping mode and using TESPA-V2 tips with spring constant k = 42 N/m. Scanning Electron Microscopy (SEM) was performed with a FEI Quanta 250 FEG instrument, operated in high vacuum mode (pressure in 10^{-4} Pa range). The characterization of the absorbance of the ECD device was performed with an Agilent Cary 300 bio UV-Vis spectrometer, coupled with a Metrohm Autolab PGSTAT 100N potentiostat. Photoelectron spectroscopy in air (PESA) was measured with a AC-2 Photoelectron Spectrometer (from Riken-Keiki Co.). The UV light intensity used for the measurements was 40 nW with a counting time of 10 seconds per point. The thickness of the samples used for the PESA measurements was estimated through a Alpha step IQ surface profiler, by scratching a small part of the films to expose the surface of the substrate and measuring the corresponding height profile.

5.3. Results and discussion

5.3.1. Synthesis and characterization of copper nanowires

Among several methods reported so far for the synthesis of Cu NWs[367, 428], we have focused our attention on the Maillard reaction[8] approach since it relies on the use of green reagents and mild conditions that are essential for industrial application. The reaction was conducted in water, heated at 110 °C, employing $CuCl_2$ was employed as copper source, octadecylamine (ODA) as surfactant and capping agent, and glucose as reducing agent in water. Actually, it was demonstrated by Kevin *et al.*[8] that Cu(II) is reduced to Cu(0) by the reaction products between glucose and the aliphatic amine, which include aldehydes, aldoles and reductones, since glucose and the amine alone do not have sufficient reducing strength to reduce Cu(II) at 110 °C. Hence, after the reaction, the Cu NWs need to be separated from the reaction products between glucose and the amine, and the large excess of amine. After the purification, the synthesized Cu NWs were dispersed in ethanol and drop-casted onto glass and silicon substrates for a first characterization. **Figure 5.3-1** displays optical micrographs and SEM images of the synthesized Cu NWs. The diameter of the nanowires, averaged over 50 of them, amounts to 75±17 nm and their length is higher than 50 μm, as it can be appreciated from the optical micrographs. Such values correspond to an aspect ratio exceeding 650. In the micrographs and in the low magnification SEM image is it possible to identify also some copper nanocrystals; these objects have mostly cubic, tetrahedral and pyramidal shapes, and dimensions between 100 and 300 nm. These copper nanocrystals are always produced as a bi-product due to difficulties in the control of the seeding process and usually represent up to 20 % of the total Cu yield.[363, 364, 438]

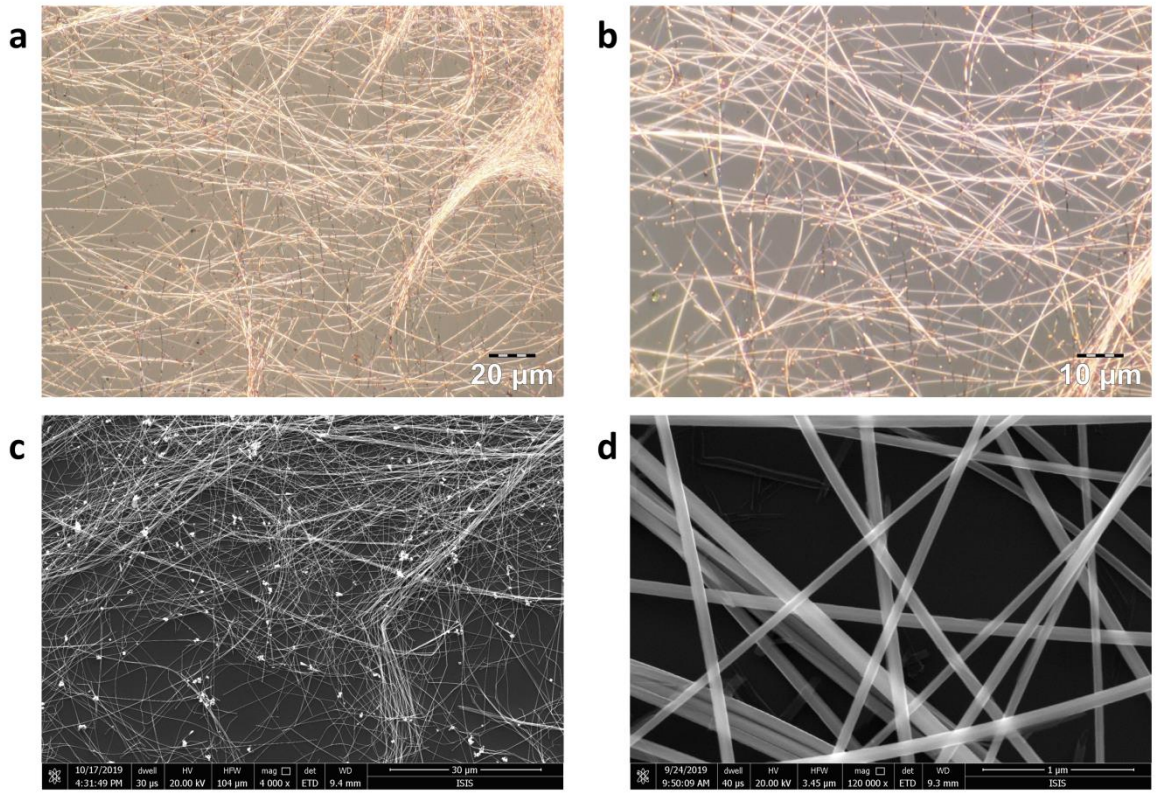

Figure 5.3-1: Characterization of the synthesized Cu NWs. (a-b) Optical micrographs of the Cu NWs on glass at different magnifications. (c-d) SEM images of the Cu NWs on Si substrate at different magnifications.

In most of the cases, their presence is not problematic, however, because of their considerable diameter, they may increase the roughness of the film and decrease the transmittance of the films without contributing to creating electrical percolation. Several methods to separate metal nanoparticles them from the metal nanowires have been proposed, including cross-flow filtration,[439] multi-phase centrifugation,[440] and selective precipitation.[441] However, these methods are not suitable for large scale synthesis and produce poor results with Cu NWs. Recently, a method for the extraction of Cu NWs and NPs in different phases, which exploits the different affinities of the two nanostructures for organic hydrophobic solvents has been developed by Quian *et al.* [437]. The Cu NWs in particular, have a higher affinity for the organic phase in comparison with the Cu nanocrystals. We took inspiration from this method to separate Cu NWs from the nanocrystals. The mixture of the two was dispersed in water and extracted with hexane. After the extraction and decantation, the nanowires are separated in the hexane phase, while the nanocrystals are retained in the water phase (**Figure 5.3-2** a-b). The results of the separation are excellent, as it can be appreciated from **Figure 5.3-2** c-d.

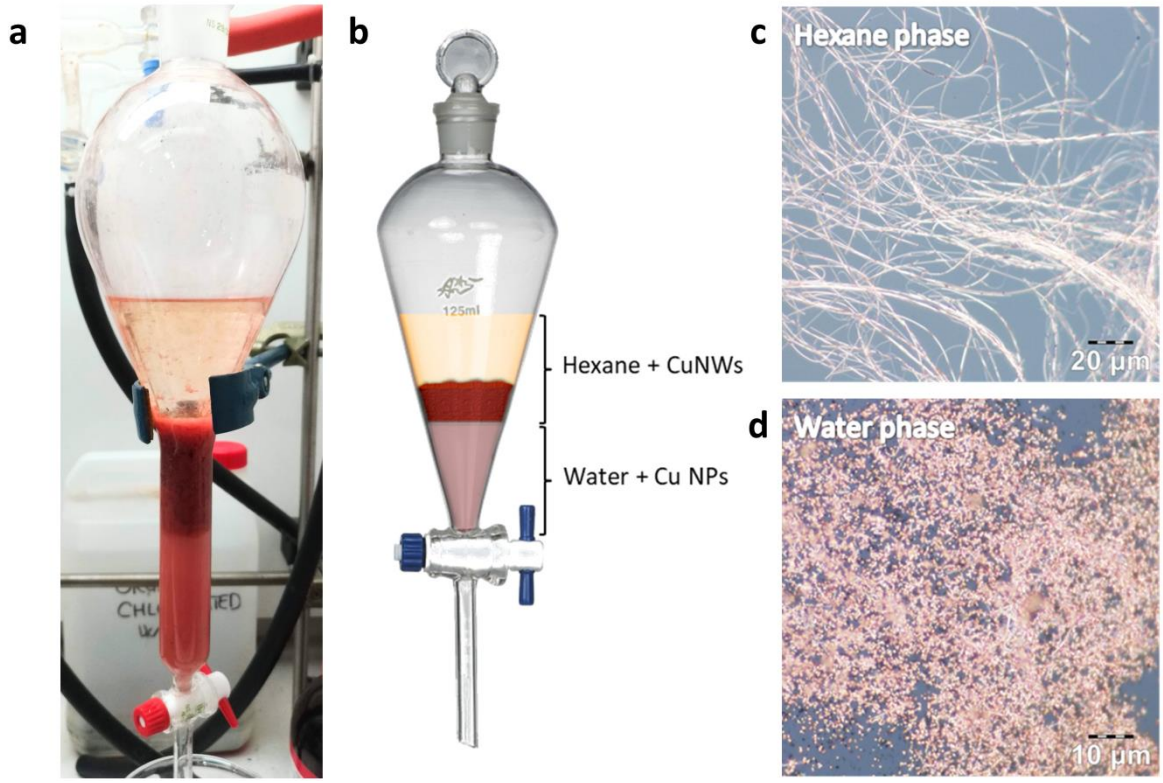

Figure 5.3-2: (a) Photograph and (b) schematic of the separatory funnel with the hexane phase containing Cu NWs and the water phase containing Cu NPs after the extraction. Optical micrograph of the Cu NWs deposited from the hexane phase (c) and of the fraction containing Cu NPs deposited from the water phase (d).

The Cu NWs dispersed in ethanol were deposited on glass and polyethylene terephthalate (PET) substrates *via* spray-coating, using a commercial airbrush. Such technique was chosen because it is suitable for large areas, is easily industrially scalable and allows obtaining a homogeneous distribution of randomly oriented nanowires, which are required to have simultaneously conductivity and transparency of the film. However, the spray-coated film, although being composed of an interconnected network of Cu NWs, in which percolative pathways are present, exhibited a very low electrical conductivity (sheet resistance ~50 MΩ/sq) due to the presence of a thin CuO passivation layer and adsorbed ODA monolayer on the Cu NWs surface, which was confirmed by XPS and IR characterization. The presence of CuO is confirmed by the XPS of Cu 2p region (**Figure 5.3-3** a). Electrons expelled from Cu 2p orbitals have two different energies due to spin-orbit splitting, thus producing two peaks Cu $2p_{1/2}$ and Cu $2p_{3/2}$ with a ratio intensity of 1:2. In the spectrum of the as-synthesized Cu NWs, two more broad satellite peaks are visible, due to the presence of Cu(II). The presence of adsorbed ODA is confirmed by the XPS spectra of C 1s and N 1s regions (**Figure 5.3-3** b-c). In C 1s spectrum of the Cu NWs after the work up an intense peak at 284.8 eV corresponding to the aliphatic sp_2 carbons of ODA is clearly visible and the N 1s region shows undoubtedly a peak at 400 eV due to the amine nitrogen. Furthermore, the presence of ODA is also confirmed by IR of the Cu NWs (**Figure 5.3-3** d), which shows two small peaks at 2850 and

2916 cm^{-1} appertaining to the CH stretching of the aliphatic chain of ODA (ODA IR spectrum, exhibiting the two strong CH stretching, is reported in blue).

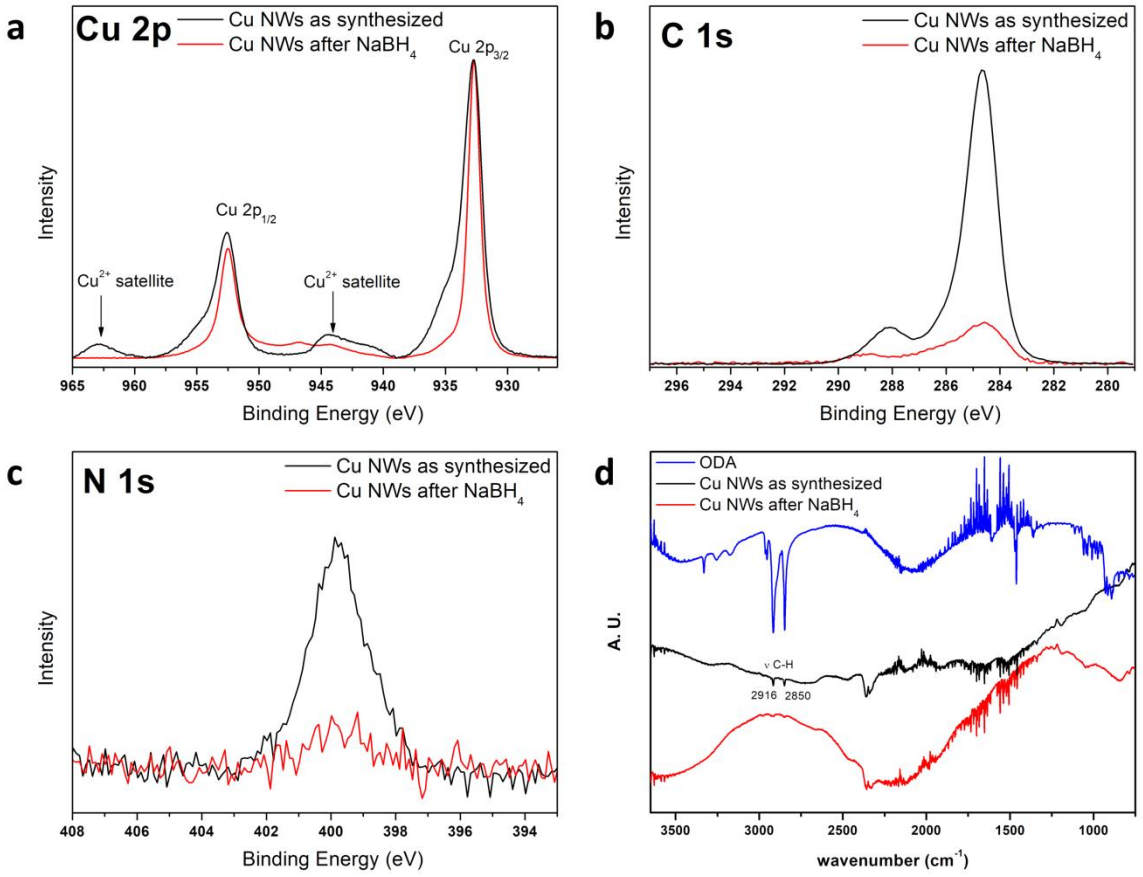

Figure 5.3-3: (a-c) Cu 2p (a), C 1s (b) and N 1s (c) spectra of (black) and Cu NWs (red). (d) IR spectra of ODA (blue), as-synthesized Cu NWs (black) and Cu NWs after reduction with $NaBH_4$ (red).

Various treatments for restoring the conductivity of Cu NWs have been proposed, which include the use of harsh dangerous chemicals such hydrazine,[7, 367] and annealing steps under a hydrogen atmosphere at 200-300 °C.[7, 371, 442, 443] With the aim of avoiding dangerous chemicals, we tested various mild reducing agents (which are discussed below) and we found out that the conductivity of the network of Cu NWs could be restored by treatment with an aqueous solution of $NaBH_4$ at 0.1 % at room temperature, that reduced CuO to Cu(0) and removed the adsorbed amines. The Cu 2p spectrum of the reduced Cu NWs in fact shows the disappearance of the Cu^{2+} satellites of CuO (**Figure 5.3-3** a). The desorption of ODA is highlighted by the almost complete disappearance of the C and N peaks, which appertained to ODA, respectively in the C 1s and N 1s XPS spectra of the nanowires after reduction. (**Figure 5.3-3** b-c). Also, the IR spectrum shows the disappearance of the two peaks appertaining to the CH stretching of ODA (**Figure 5.3-3**d).

The kinetics of the reduction of Cu NWs with $NaBH_4$ at room temperature can be followed by measuring the sheet resistance of the Cu NWs spray-coated film as a function of the

dipping time (**Figure 5.3-4**). The reduction goes to completeness in ca. 90 min, during which the sheet resistance dramatically drops of over 6 orders of magnitude, from 45 MΩ/sq down to 30 Ω/sq.

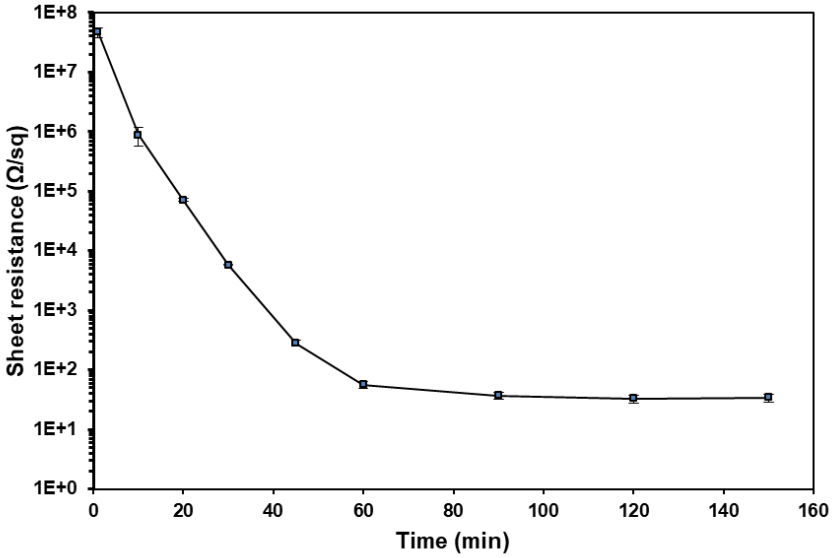

Figure 5.3-4: Kinetics of reduction of Cu NWs with a $NaBH_4$ solution 0.1 %. The sheet resistance of the Cu NWs film is measured as a function of the soaking time in the $NaBH_4$ solution.

As aforementioned, spray-coating allows finely tuning the Cu NWs network density, and thus the electrical conductivity and transmittance of the film. It is known that in random networks of metallic nanowires the transmittance decreases linearly with the increase of the nanowires density, while the sheet resistance decreases following a power low.[6] To precisely evaluate the best compromise between sheet resistance of the film and transmittance we prepared five different samples of spray-coated Cu NWs on glass with increasing density. The macroscopic and microscopic aspect of the film is reported in **Figure 5.3-5** a-b, which shows clearly the increase in the film density and the decrease in transmittance. The corresponding transmittance spectra are reported in **Figure 5.3-5** c. The sheet resistance of such films decreases from 440 of the least dens film to 7 Ω/sq of the densest film, which exhibit transmittances at 550 nm of 84.6 % and 55.8 %, respectively (**Figure 5.3-5** d).

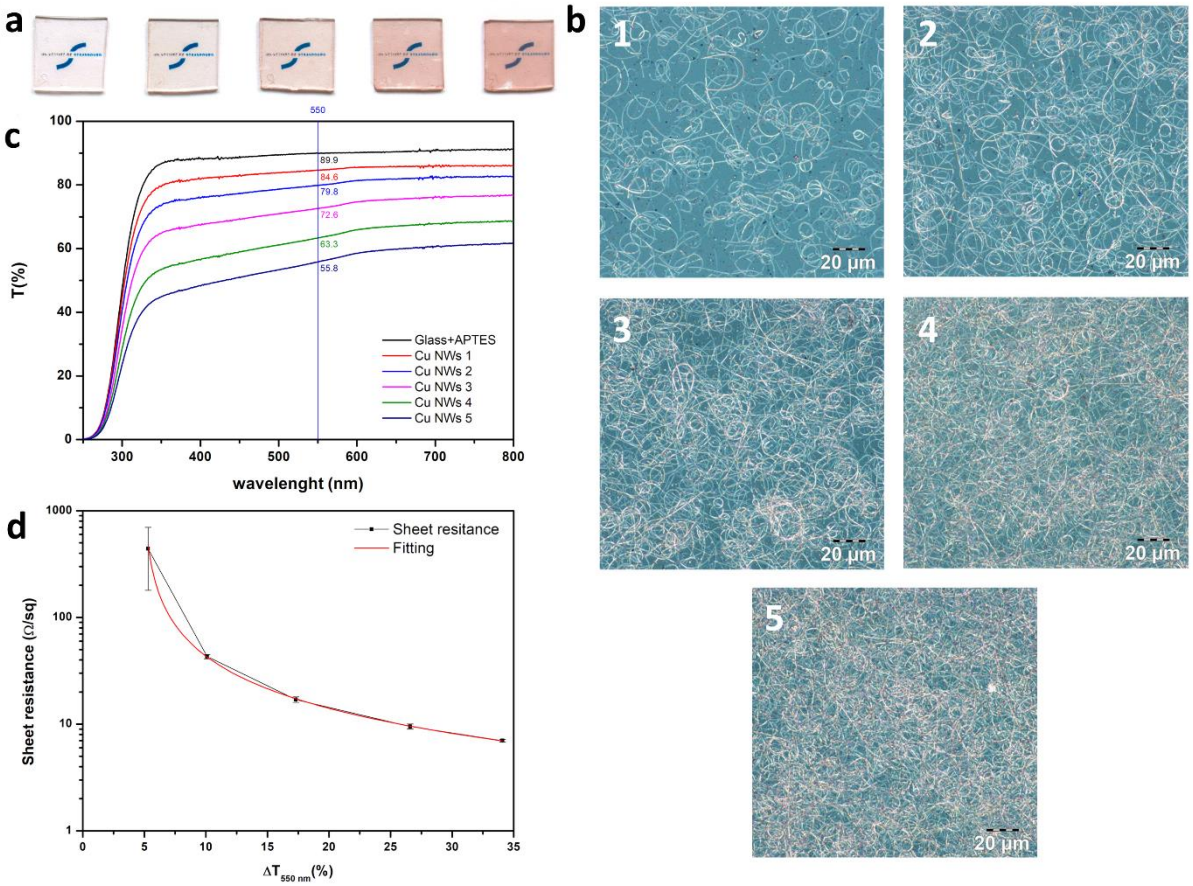

Figure 5.3-5: Transmittance and sheet resistance of Cu NWs films as a function of the network density. (a) Photos and (b) micrographs of the five different films of Cu NWs on glass with crescent density. (c) Transmittance spectra of the substrate and the 5 Cu NWs films, with reported the T at 550 nm. (d) Sheet resistance of the Cu NWs films as a function of the decrease in transmittance at 550 nm.

It can be seen that the sheet resistance decreases not linearly, and can be fitted by a potential equation expressed by Eq. 4.2-2, in agreement with the existing literature.[6, 444]

$$y = \frac{1}{a + bx^c} \qquad Eq.\ 5.3\text{-}2$$

According to the experimental curve, at T = 78 % (ΔT = 12 %), the sheet resistance is ca. 30 Ω/sq, being a value comparable to commercial ITO films on glass (Sigma-Aldrich).

5.3.2. Assembly of the hybrid Cu NWs/rGO transparent conductive film

The so fabricated Cu NWs films possess high conductivity and transparency. However, the high tendency of copper(0) towards oxidation, hampers the long term stability and the application of such films as electrodes in optoelectronic devices. To tackle this problem, we deposited *via* spray-coating a thin layer of graphene oxide on top of the Cu NWs starting from an ethanolic suspension of commercial GO. Also in this case, spray-coating was chosen

to finely tune the amount of GO deposited on top of Cu NWs. The spray-coated GO film acts as an insulating barrier on top of the Cu NWs (Rs > 1 GΩ/sq), thus it must be reduced to rGO. We firstly verified that GO could be reduced efficiently with the same sodium borohydride solution that was used for Cu NWs. The sheet resistance of a thin (ca. 10 nm) GO film decreases during the reduction from 1.2 GΩ/sq to ca 320 kΩ/sq after 2 h of soaking in the aqueous $NaBH_4$ solution. At the same time, the transmittance of the film decreases by 8.8 % because of the higher absorbance of rGO in the visible range compared to GO.[420] The reduction goes to completeness in ca. 120-150 min (**Figure 5.3-6** a). To minimize the number of steps, we decided to simultaneously reduce both Cu NWs and GO by soaking the substrate with the deposited Cu NWs/GO film in the $NaBH_4$ solution. Interestingly, when we reduced the hybrid film, the reduction kinetics of GO, followed by the decrease in UV-Vis transmittance, was faster than for GO alone (**Figure 5.3-6** b). This was probably due to a catalytic effect of metallic copper, which was pointed out by the increased production of hydrogen.[445] The formation of small hydrogen bubbles on the film surface caused the partial delamination of the Cu NWs/GO film from the glass substrates. This problem was totally avoided using glass substrates coated with a thin layer of APTES. Interestingly, we never observed the delamination of the film on PET, even without APTES layer. The mechanism of this stabilization is not clear, though APTES can form strong interaction with GO,[446] and probably interact also with Cu NWs through the amine groups. In the case of PET, the higher hydrophobicity and stronger interaction with rGO probably are sufficient to avoid the delamination.

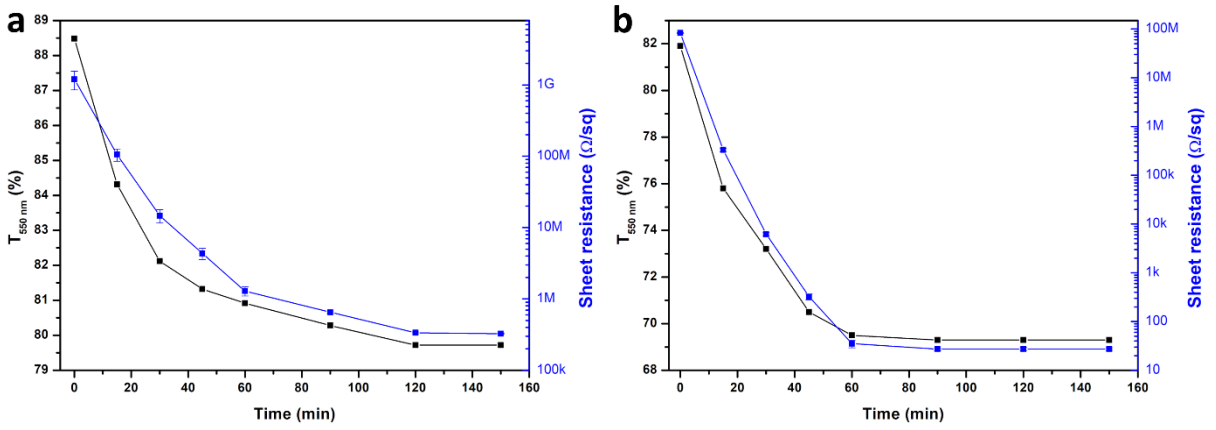

Figure 5.3-6: (a) Transmittance (at 550 nm) and sheet resistance as a function of the soaking time in aqueous $NaBH_4$ solution 0.1% for (a) GO spray-coated on glass+APTES, and (b) glass+APTES/Cu NWs/rGO.

In addition to the increase in conductivity and decrease of the transmittance, the reduction of both components was confirmed by XPS. **Figure 5.3-7**a shows the Cu 2p XPS spectra of the Cu NWs/(r)GO film before and after the reduction. In particular, after 2 hours of immersion in $NaBH_4$ solution, the broad satellite peaks of Cu(II) at 940-945 eV and 965 eV disappear whereas only the typical peaks of metallic Cu at 932 and 952 eV appear. The spectra of Cu

appear noisier in this case because XPS has an average depth analysis of few nanometers and Cu NWs are located under the (r)GO layer. The XPS analysis of C peaks is displayed in **Figure 5.3-7** b: before the reduction, it shows the typical spectrum of GO, with two bands, one at 284.8 eV of C sp^3 and a second at 286 eV of C-O. After the reduction, the spectrum acquires the typical aspect of rGO, with a strong decrease of the C-O band intensity and a shift of the main peak to 284 eV, due to the increase of C sp^2.

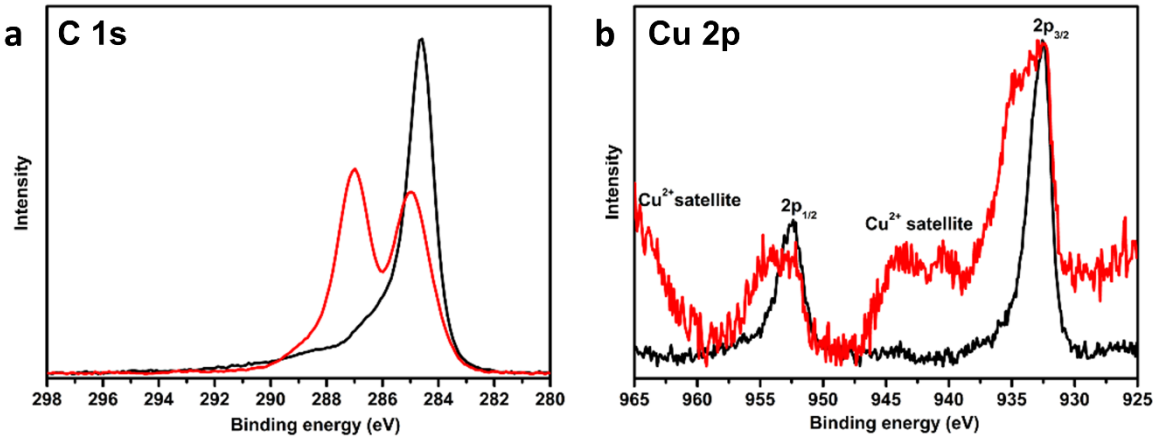

Figure 5.3-7: XPS spectra of (a) C 1s and (b) Cu 2p of the Cu NWs/GO film on Si before the reduction with $NaBH_4$ (red) and Cu NWs/rGO film after the reduction (black).

Figure 5.3-8 portrays the SEM images and optical micrographs of the hybrid electrode Cu NWs/(r)GO as deposited and after the reduction with $NaBH_4$. The SEM images reveal that the Cu NWs are clearly covered by the GO/rGO layer, both before and after the reduction. Furthermore, after the reduction with $NaBH_4$ the nanowires are perfectly intact (**Figure 5.3-8** b). The micrographs show the microscopic appearance of the hybrid electrode, with randomly distributed Cu NWs covered by GO flakes. The last becomes more visible after the reduction because rGO reflects and scatters more light.

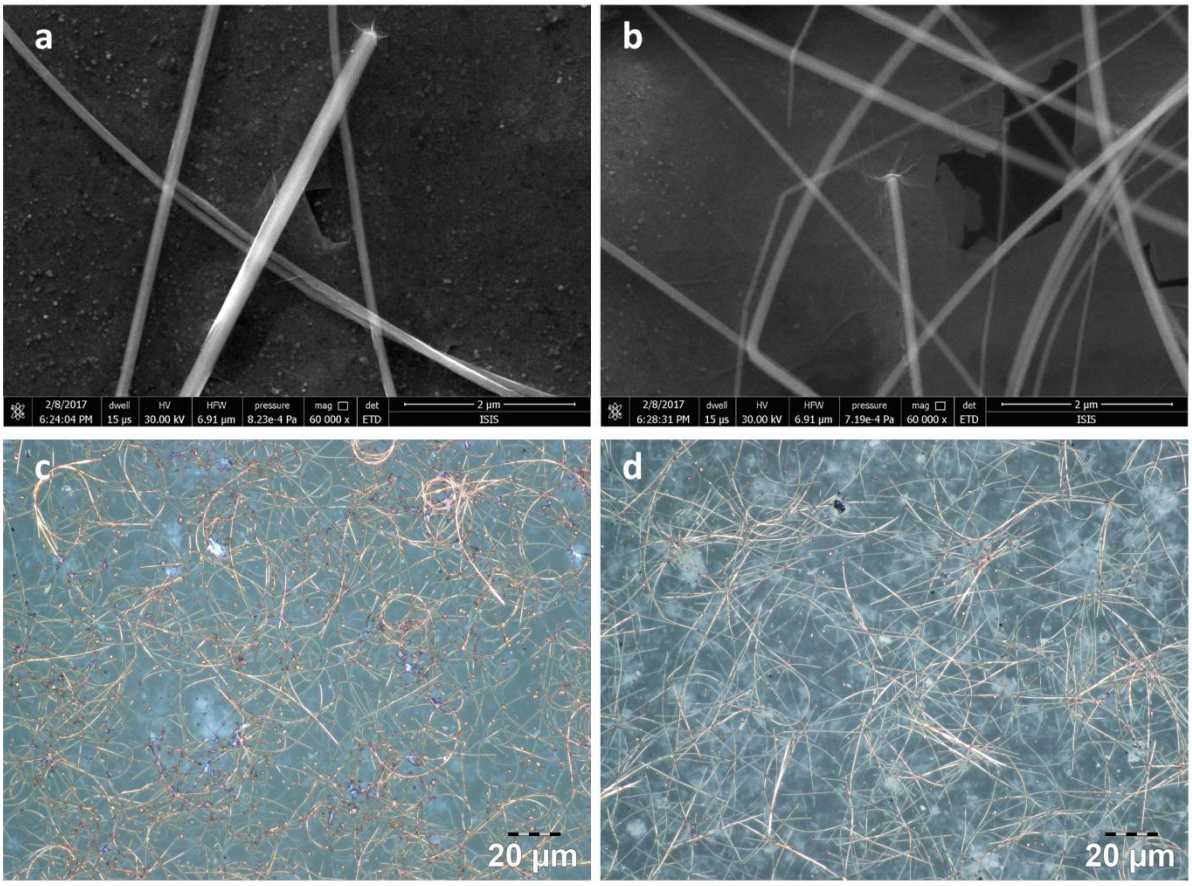

Figure 5.3-8: SEM images of the hybrid Cu NWs/GO on Si+APTES before reduction (a) and Cu NWs/rGO after reduction with $NaBH_4$ (b). Micrographs of the hybrid Cu NWs/GO on glass+APTES before reduction (c) and after reduction with $NaBH_4$.

5.3.3. Effect of different reducing agent on the Cu NWs/GO films

Effectively, before testing $NaBH_4$ as reductant, other reducing agents were also tested. In particular, hydrazine, L-ascorbic acid, $SnCl_2$ and metallic zinc were tested. The reduction of the sample with hydrazine in EtOH caused the destruction of the nanowires, after just 30 minutes of reduction (**Figure 5.3-9** b). Probably hydrazine coordinates Cu(I)/(II) ions in acidic medium, dissolving the protective Cu_xO layer and favouring the conversion of Cu NWs in Cu NPs, whose stability is higher in absence of the capping agent ODA. The blue crystals visible in the micrograph are probably complexes of Cu^{2+} ions with hydrazine and its ammonia derivatives. The reduction of the sample in a solution of hydrazine in EtOH without acetic acid produced the same results. In water the stability of Cu NWs with hydrazine is higher, however, these were fragmented in multiple points after 2 hours of reduction (**Figure 5.3-9** c). For shorter soaking times (30 min and 1 h) the GO was not sufficiently reduced yet, and the Cu NWs appeared already damaged at SEM (**Figure 5.3-9** d). Probably in water solution the nanowires are attacked slowly because water solutions of hydrazine are basic and the insolubility of CuO layer in basic media protects the nanowires

from further oxidation. Similarly, the reduction of the sample with ascorbic acid for 2 hours produced the complete dissolution of the nanowires for a coordinating effect of the ascorbic acid, which was highlighted by the blue colouration of the solution (**Figure 5.3-9** e). Tin(II) chloride demonstrated to be a weak reducing agent for GO, and for this reason, the Cu NWs/rGO sample was soaked in the $SnCl_2$ solution for 2 h, after which the Cu NWs were destroyed (**Figure 5.3-9** f). On the contrary, the sample reduced for 2 hours with an aqueous Zn dispersion presented a sheet resistance of 77 Ω/sq and the nanowires appeared intact, yet the reduction was not uniform over the entire sample and some particles of zinc remained attached to the surface of the film (**Figure 5.3-9** g). Such results demonstrated that sodium borohydride was the most effective reducing agent. Samples of Cu NWs/rGO left in the $NaBH_4$ solution for 20 h were perfectly intact and conductive, demonstrating the high stability of Cu NWs in this medium (**Figure 5.3-9** h). Interestingly, the pH of such 0.1 % $NaBH_4$ solution was 13. However, the basicity alone was not sufficient to protect the nanowires from the oxidation, because another sample left in a solution of NaOH 0.1 M for 20 hours showed the corrosion of the nanowires (**Figure 5.3-9** e). Probably the basicity protects the oxide layer on the nanowires from the dissolution, while $NaBH_4$ reduces such a layer to Cu(0) and counteracts the oxidizing action of oxygen dissolved in solution.

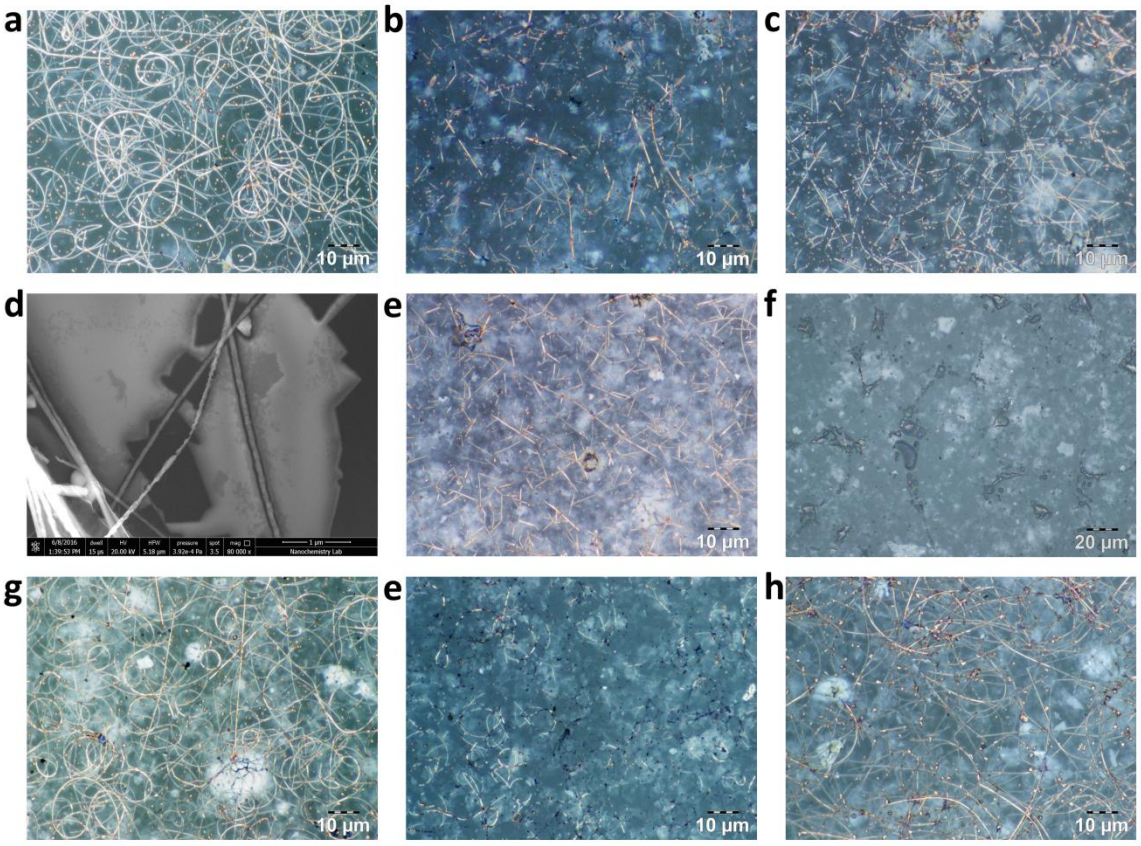

Figure 5.3-9: (a-c and e-f) Micrographs and (d) SEM image of (a) Cu NWs/GO on glass+APTES before reduction and after the following conditions. (b) Hydrazine monohydrate (5 µL/mL), ethanol, RT, 30 min. (c) Hydrazine monohydrate (7.5 µL/mL), water, RT, 120 min and (d) 30 min.

(e) L-ascorbic acid (2.3 mg/mL), water, 55 °C, 120 min. (f) $SnCl_2$ (0.75 mg/mL), ethanol, RT, 120 min. (g) Zn powder (1 mg/mL), water, RT, 120 min. (e) NaOH 0.1 M, water, RT, 20 h. (h) $NaBH_4$ (1 mg/mL), water, RT, 20 h.

5.3.4. Characterization of the Cu NWs/rGO conductive films

The hybrid Cu NWs/rGO transparent conductive films were further characterized physically, morphologically, and electrically. In **Figure 5.3-10** are reported the transmittance spectra of two Cu NW/rGO films on glass and PET. The two films have respectively transmittances at 550 nm of 71.4 and 66.7 %. The transmittance of the film on PET is slightly lower also because PET is less transparent than glass (transmittances at 550 nm of 90 and 87 % for glass and PET, respectively). The spectra after each step of production are also reported. Noteworthily, the APTES layer on glass is completely transparent, and the transmittance decreases of around 9-10 % after the deposition of Cu NWs and after the deposition of GO and following reduction. The sheet resistances of these hybrid films on glass and PET were 36 ± 2 and 32 ± 3 Ω/sq, respectively.

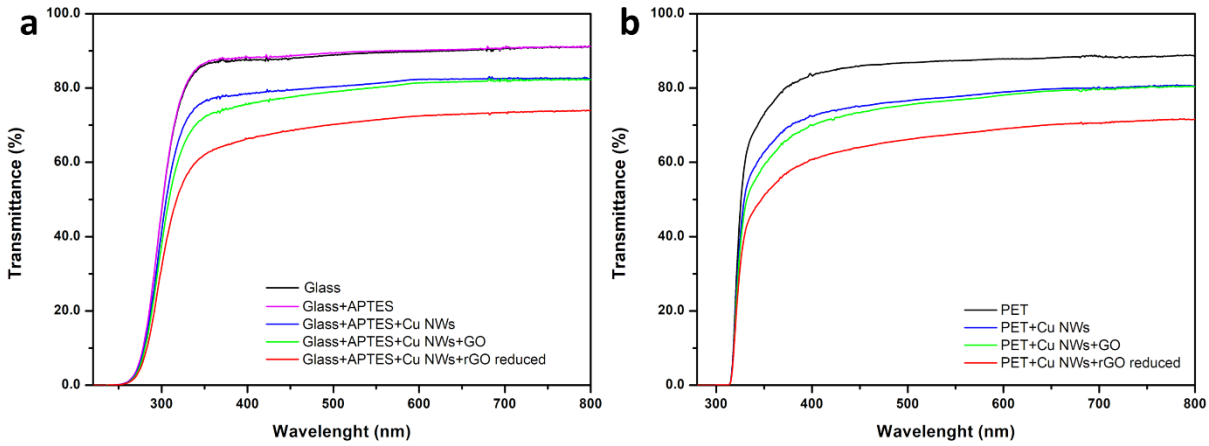

Figure 5.3-10: Transmittance spectra of the Cu NWs/rGO film on (a) glass, and (b) PET. The transmittance spectra at the different steps of production are reported.

By AFM we examined the topography of the hybrid film and compared to the one of the bare Cu NWs film (**Figure 5.3-11**). In **Figure 5.3-12** is reiterated a higher scale topographic image of the hybrid film. In particular, after the coating with rGO, the height of the film, averaged over 10 images, decreases from 216 ± 22 nm to 135 ± 5 nm and the roughness decreases from 24.8 ± 3.7 to 11.4 ± 1.8 nm. From the height images of the hybrid film, it is clear how the rGO flakes on top of the nanowires decrease the apparent height and sharpness of the latter (**Figure 5.3-11** c, e and **Figure 5.3-12**). In the height images of both Cu NWs and Cu NWs/rGO film are visible also some Cu nanocrystals, which are responsible for the increased height and roughness of both films. The heights of the individual Cu NWs are between 60 and 80 nm, in accordance with the SEM characterization. Only a few rGO flakes can be easily recognized in the topographic images of the hybrid film. However, from

the phase images (**Figure 5.3-11** d, f) it is clear that rGO covers almost completely the Cu NWs and the substrate surface. In fact, only a tiny spot of the surface is visible, which is pointed out by an arrow in **Figure 5.3-11** d.

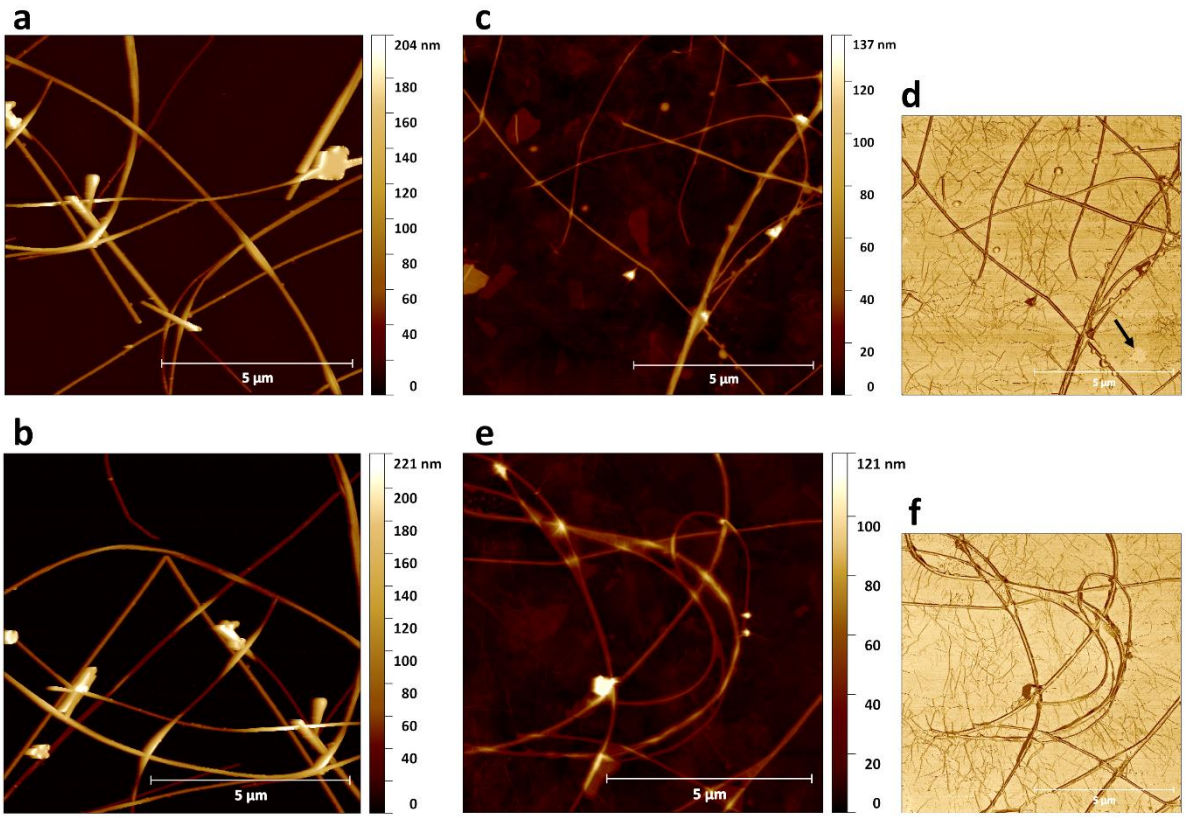

Figure 5.3-11: AFM images of (a, b) Cu NWs on Si/SiO_2 and (c, e) Cu NWs/rGO on Si/SiO_2 with the respective phase images (d, f). The arrow in (d) indicates a small surface of the exposed substrate.

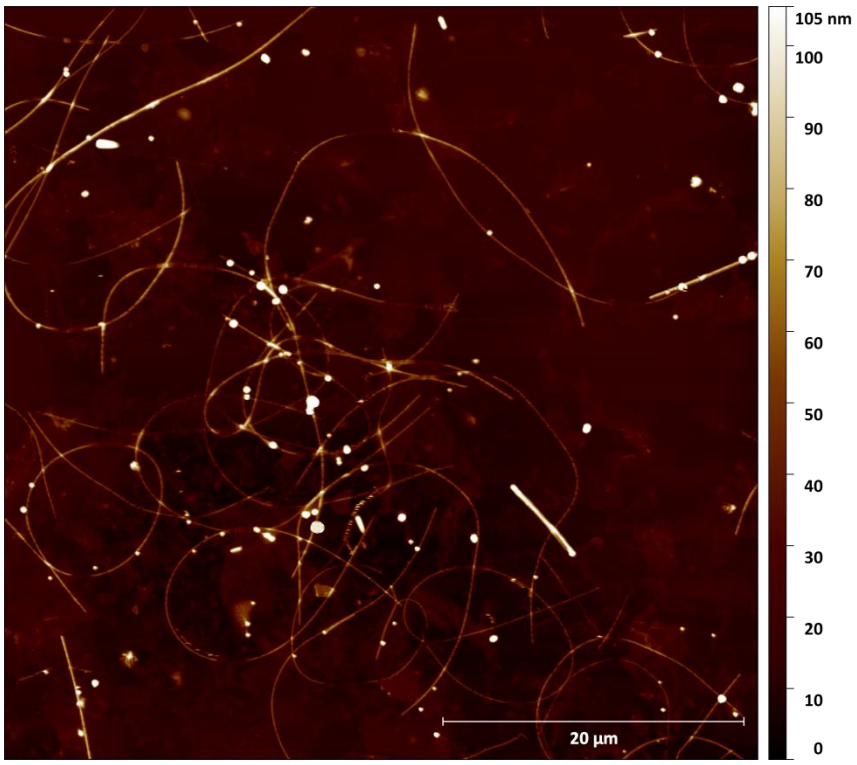

Figure 5.3-12: AFM images of Cu NWs/rGO on Si/SiO_2 on a larger scale.

The stability of our reduced Cu NWs/rGO film on PET under bending both in static and dynamic configuration was tested by measuring the variation of the electrical resistance. **Figure 5.3-13**a shows the sheet resistance of the film for different bending radii. It reveals the sheet resistance is stable up to a r_b of 5 mm and then increases up to ~73 Ω/sq for a bending radius of 1.5 mm. Furthermore, the stability under repeated bending was tested (**Figure 5.3-13** b). Impressively, after 10000 bending cycles at a bending radius of 1 the sheet resistance change was below 4%.

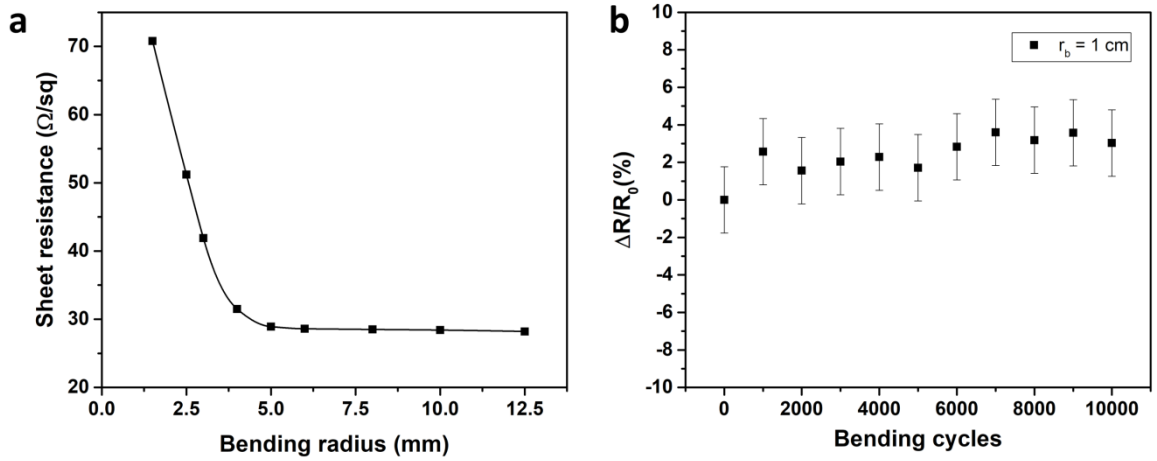

Figure 5.3-13: (a) Sheet resistance of a hybrid Cu NWs/rGO electrode on PET as a function of the bending radius. (b) Variation of resistance in % of the Cu NWs/rGO electrode as a function of the number of cycles, with a bending radius of 1 cm.

The I-V characteristic of the hybrid film on PET was also characterized (**Figure 5.3-14** a). For this purpose, two parallel gold electrodes 8 mm long and distanced by 6 mm were evaporated on top of the Cu NWs/rGO film. The voltage applied to the electrode was shifted between 3 and -3 V and vice versa at 0.1 V/s. The electrode shows almost perfect Ohmic behaviour, and exhibits a resistance of 27.34 Ω, corresponding to a sheet resistance of 43.7 Ω/sq.

In addition, the work function of the hybrid electrode was also calculated with photoelectron spectroscopy in air and compared to that of Cu NWs and rGO separately. In **Figure 5.3-14** b are reported the photoemission spectra of the three materials, in which the number of photoelectrons emitted by the material is reported as a function of the energy of the incident UV radiation. The values of the ionization energies (IE) correspond to the threshold energies at which the materials start to emit photoelectrons. The IE values, which are equal to the work function, were 4.90 ± 0.02 eV, 4.82 ± 0.02 eV and 4.83 ± 0.04 eV for Cu NWs/rGO, Cu NWs and rGO, respectively.

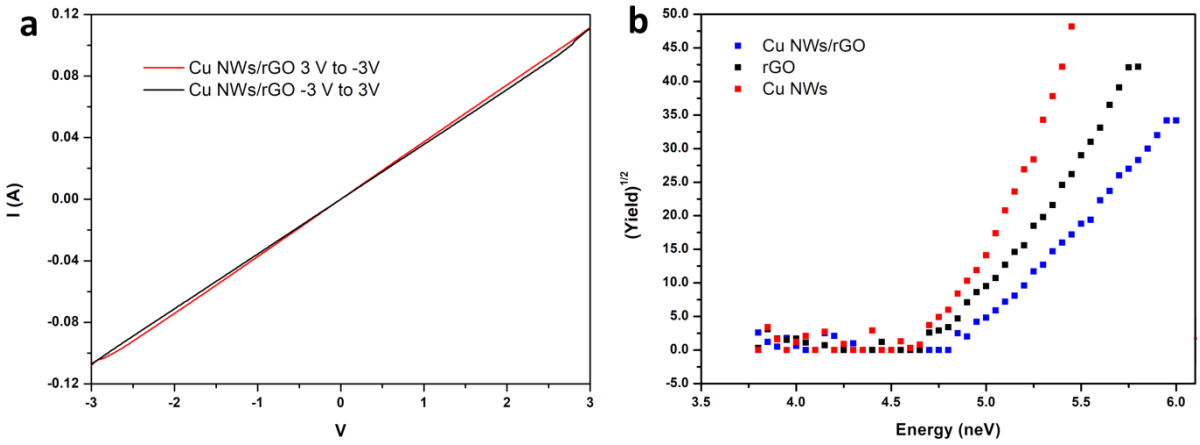

Figure 5.3-14: (a) Current vs voltage characteristic of Cu NWs/rGO electrode. (b) Measurements of the ionization energy for Cu NWs (red), rGO (black) and the hybrid Cu NWs/rGO (blue) by photoemission spectroscopy in air (PESA).

5.3.5. Stability of the hybrid Cu NWs/rGO electrode to air and to washing cycles

The stability of the hybrid Cu NWs/rGO electrode was evaluated. In particular, the electrode was left exposed to air and its sheet resistance was checked periodically. The results, displayed in **Figure 5.3-15** show high stability of the electrode, with a small variation of the sheet resistance of 17 % after 100 days.

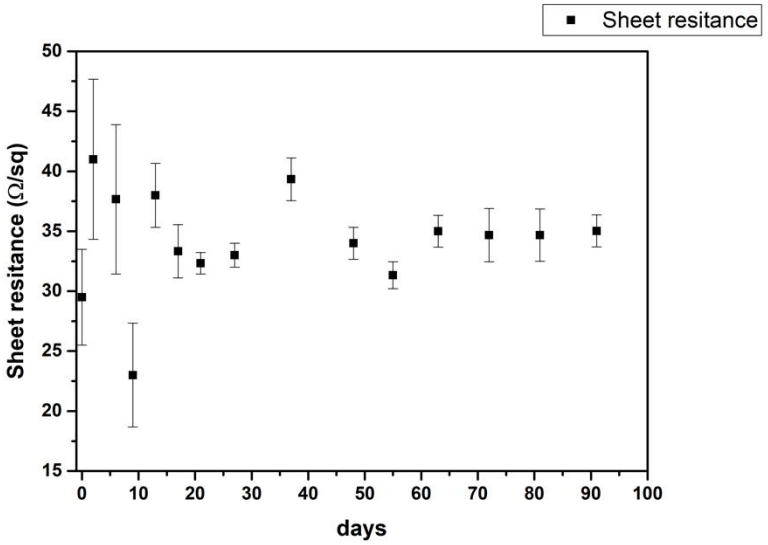

Figure 5.3-15: Change of the sheet resistance of the Cu NWs/rGO hybrid onto a glass substrate over time in ambient conditions.

To further explore the stability of the hybrid electrode we tested its durability to washing. In fact, washability is an important requisite for flexible and wearable electronics. However, this aspect is still not much explored in the literature. Imagining that these transparent electrodes could be integrated into wearable devices and fabrics, and in domestic objects and furniture, we test the resistance of the Cu NWs/rGO film on PET to washing cycles with laundry detergent and with dishwashing soap. Furthermore, we also tested the resistance of the electrodes to direct contact with three surface detergents: a hard surface detergent containing alkyltrimethylendiamine, a hypochlorite-based detergent and diluted (2 %) hydrogen peroxide solution. In particular, for the dishwashing detergent and laundry detergent, 3 different washing cycles were simulated, denominated delicate, normal and intense, with respectively decreased detergent concentration for the delicate cycle, and increased temperature to 60 °C for the intense cycle. The behaviour of the Cu NWs/rGO hybrid was compared to that of bare Cu NWs. In **Figure 5.3-16** and **Figure 5.3-17** are reported respectively the micrographs and the sheet resistances of both films before and after the different washing tests.

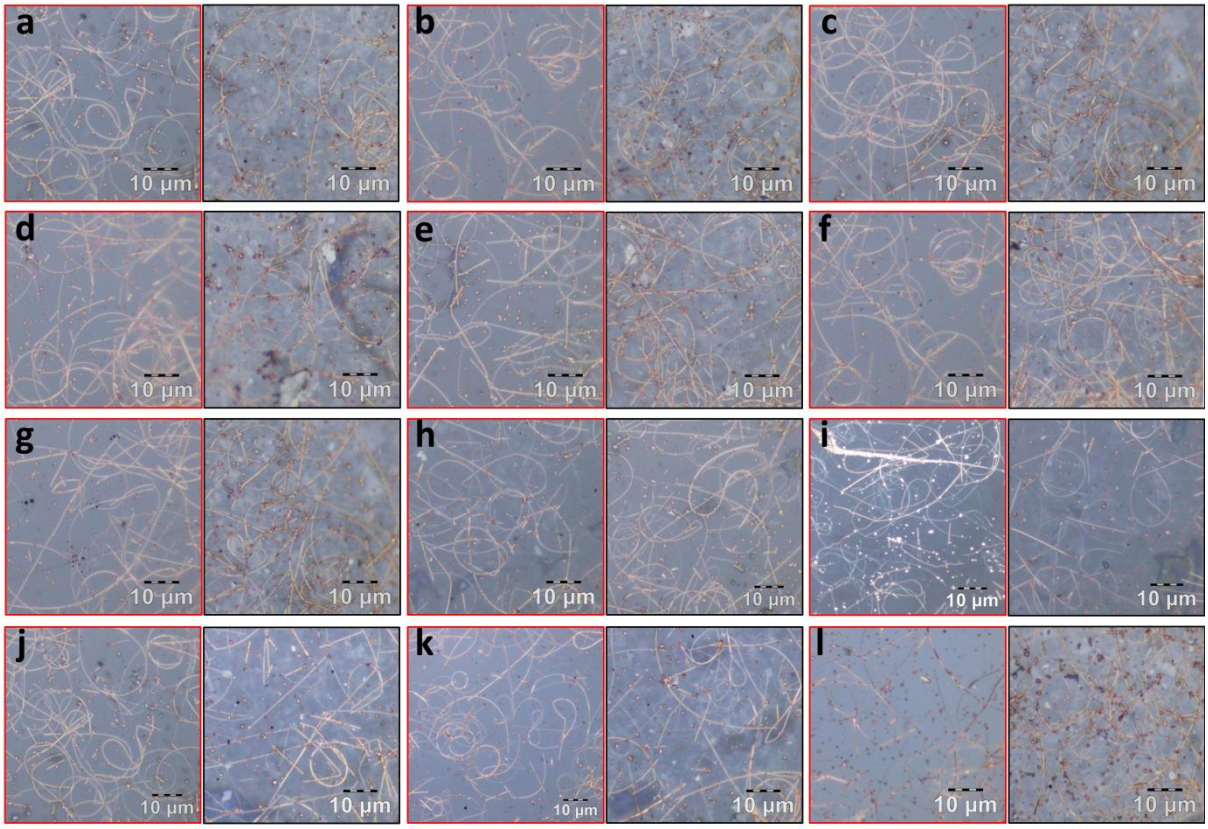

Figure 5.3-16: Micrograph of Cu NWs on PET (red frames) and Cu NWs/rGO on PET (black frames)before washing (a) and (b-d) after the washing cycles with laundry detergent (b: 30°C – conc. 0.2 % v/v, c: 30°C – conc. 1 % v/v, d: 60°C – conc. 1 % v/v); (e-g) after the washing cycles with dishwashing detergent (e: 30°C – conc. 0.2 % v/v, f: 30°C – conc. 1 % v/v, g: 60°C – conc. 1 % v/v); after (h) 2 min and (i) 20 min of soaking in a hard surface detergent; after (j) 2 min and (k) 20 min of soaking in a hypochlorite based detergent; (l) after 10 min of soaking H_2O_2 water solution (2 % v/v).

After the three cycles with laundry and the dishwashing detergent, the micrographs exhibit no visible differences in the microscopic appearance for any of the samples. However, the sheet resistance displays a small increase in the resistance after the normal and intensive washing cycles with laundry detergent for the not protected Cu NWs sample, while the film of Cu NWs protected by rGO does not show any increase in the resistance. In the case of the dishwashing detergent, the resistance increases already after the first delicate cycle and becomes more than double after the intensive washing for the not protected Cu NWs sample, while the Cu NWs protected by rGO display a 20 % increase in the sheet resistance after the more intense washing cycle. Both films exhibit lower stability to the hard surface detergent. In particular, a 6-fold increase in the sheet resistance of bare Cu NWs has been observed after 2 minutes of soaking in the detergent and 12-fold after 20 minutes of soaking. The corresponding micrograph (**Figure 5.3-16** j) reveals that the unprotected Cu NWs are partially fragmented and covered by a white layer. The Cu NWs/rGO sample shows higher stability, with a doubling of the sheet resistance after 20 min of soaking. The lower stability

of both films to this detergent is likely caused by the presence of alkyltrimethylendiamine. Impressively, we could not observe any macroscopic or microscopic difference and any change in the sheet resistance in both the samples Cu NWs and Cu NWs/rGO after the soaking in a hypochlorite based detergent for 2 and 20 min, despite hypochlorite is a strong oxidant. On the contrary, a H_2O_2 solution in water at 2 % v/v destroyed completely the unprotected Cu NWs after 10 minutes of soaking (**Figure 5.3-16** l), whose sheet resistance increased by 3 orders of magnitude. The Cu NWs/rGO sample withstood much better the oxidizing action of H_2O_2, showing an increase of the sheet resistance of just 80 %. It is worth noting that in any case, we observed a macroscopic or microscopic detachment of the film from the PET surface. These results confirm that Cu NWs are more stable in basic conditions, such as those of the hypochlorite-based detergent. Furthermore, all the tests show higher stability of the hybrid Cu NWs/rGO, confirming the protective action of rGO.

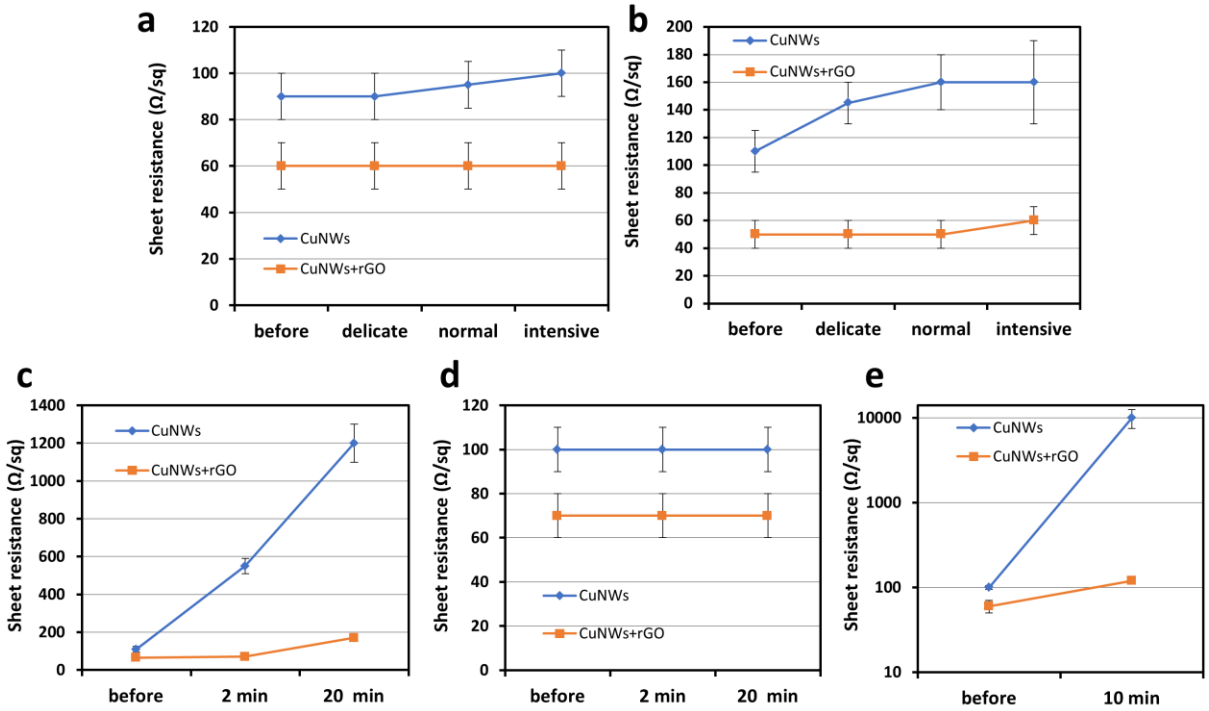

Figure 5.3-17: Measured sheet resistances with relative error bars of Cu NWs and Cu NWs/rGO films before and after each of 3 washing cycles (delicate, normal and intensive) with (a) laundry detergent and (b) dishwashing detergent, before and after 2 and 20 min of soaking in (c) hard surface cleaner and (d) hypochlorite based detergent and (e) before and after 10 min of soaking in a 2% aqueous solution of H_2O_2.

5.3.6. Implementation of the hybrid Cu NWs/rGO electrode into electrochromic devices

Finally, we have exploited our hybrid Cu NWs/rGO films on PET, as transparent electrodes in electrochromic devices. Poly(3,4-ethylenedioxythiophene) (PEDOT) was chosen as electrochromic material because it is cost-effective and easily accessible, exhibits very high

colour contrast and large colouration efficiencies,[447] and can be processed using printing techniques typical of industrial scale onto different types of substrates.[448, 449] These features make PEDOT ideal component for large-scale electrochromic devices applications. We have spray-coated a PEDOT ink on the surface of complementary electrodes which were then assembled using the established architecture for electrochromic devices (ECD)[450, 451] with a UV-curable electrolyte layer. Once assembled, the ECD was characterized by spectroelectrochemical analysis. Then, we applied -1.5 V and 0 V to the ECD to respectively reduce (coloured state) and oxidize (almost uncoloured) PEDOT (**Figure 5.3-18** a). The assembled ECD shows the usual colour development of PEDOT, *i.e.* the appearance of an intense blue colour at -1.5 V with an absorption spectrum peaking at 623 nm, with an absorption change amounting to 0.16 (**Figure 5.3-18** b). Significantly, our device exhibited a rather fast switching (about 0.5 s) for both colouration and bleaching processes, which can be ascribed to the high electronic coupling between the conducting layer and PEDOT (**Figure 5.3-18** c). The colouration efficiency (CE), defined as the ratio between the difference in absorbance of the coloured and bleached state and the injected charge per unit area, is remarkably high (948 $cm^2\ C^{-1}$) for a spray-casted ECD, in line with the best results reported using glass/ITO systems (maximum values are about 1000 $cm^2\ C^{-1}$).[452, 453] Coloration (Q_c) and bleaching (Q_b) electric currents are experimentally the same, being a mandatory characteristic for stable ECD, to avoid secondary electrochromic reactions.

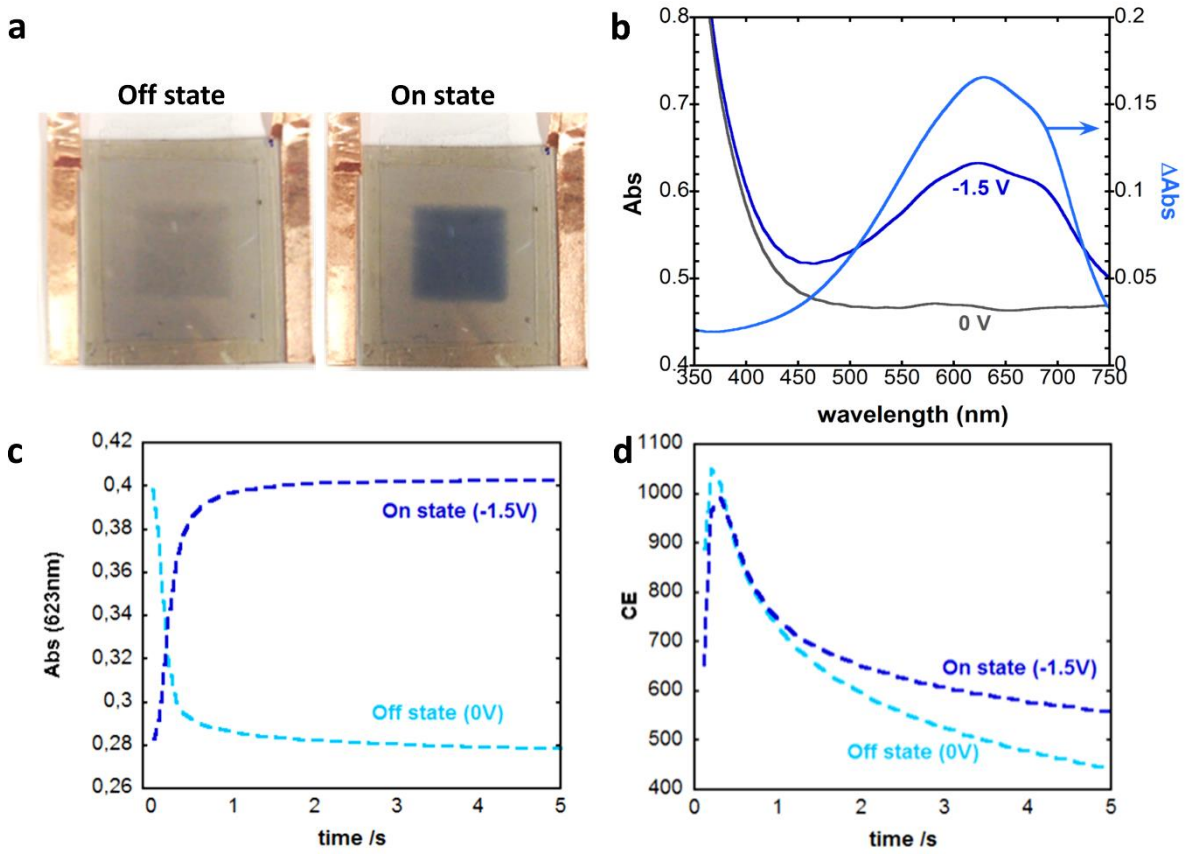

Figure 5.3-18: (a) Photos of the electrochromic device (ECD) in the coloured and bleached state. (b) Absorbance spectra of the ECD in the bleached and coloured state and reported ΔAbsorbance

between the two states. (c) Absorbance at 623 nm as a function of the time after the application of 0 V and -1.5 V. (d) Coloration efficiency (CE) as a function of time after the application of -1.5 V and 0 V.

To prove the relevance of our devices for technological applications, and in particular to test its resistance to its operation, we have run the device for several days by performing 5 seconds electrochemical cycles in a custom-made chamber[452] described in the experimental section. Digital photographic images of the devices were acquired over time with a frequency of 100 ms. To analyse those images, colourimetric CIE L*a*b coordinates are determined for the region where the electrochromism develops on the device, which renders 3 different coordinates (L^* for luminosity, a^* for red/green colour balance, and b^* for yellow/blue colour balance). Colour contrast is then measured between *off* (bleached) and *on* (coloured) states for a given electrochromic cycle. The so-called colour contrast parameter, ΔE*, is a root-mean squared colour deviation from the *off* state and can be expressed by the following equation.

$$\Delta E^* = \sqrt{(L_2^* - L_1^*)^2 + (a_2^* - a_1^*)^2 + (b_2^* - b_1^*)^2} \qquad Eq.\ 5.3\text{-}3$$

ΔE* is in close correlation to what the human eye experiences: if it is higher than 3 (ΔE*>3) the colour change is detectable.[451, 452] This parameter can be followed during the switch, enabling the calculation of switching times for some given cycle number (**Figure 5.3-19** b). Significantly, after 1000 cycles of operation of our ECD its performances in terms of colour contrast ΔE* and switching times remain basically the same as those of the pristine ECD, thus being a remarkable result. After 1000 cycles, the ECD still operates with fast switching times and good colour contrasts. Outstandingly, at about 20000 cycles the colour contrast was about 50% of the initial value, which ensures very high stability of the electrodes. The colouration efficiency amounts to 174 $cm^2\ C^{-1}$ after 20000 cycles, being still very high even when compared even with pristine ECDs, providing unambiguous evidence for the robustness of our device. It is worth noting that a comparative ECD assembled with a Cu NWs on PET electrode without rGO on top presented much worse performances, exhibiting a ΔE^* of 4.5 after just 3 cycles.

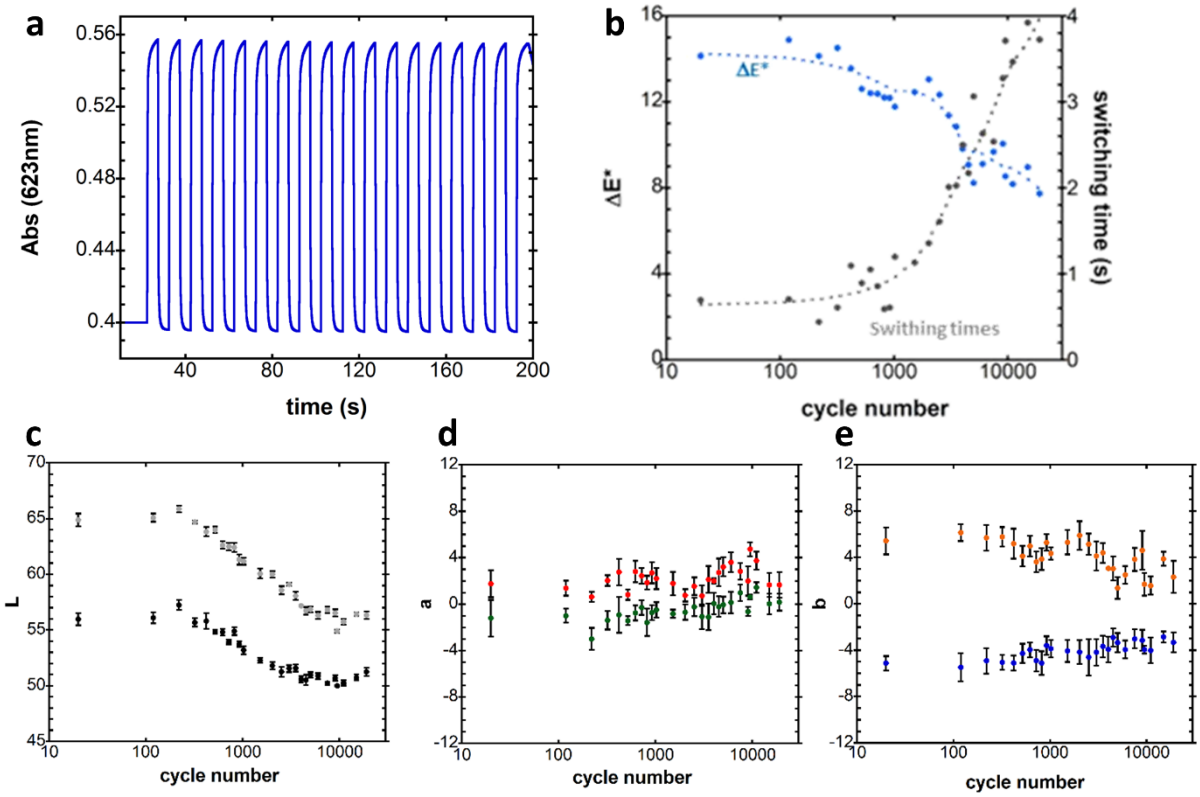

Figure 5.3-19: (a)) electrochemical cycling between -1.5 V and 0 V of the ECD followed by optical transmittance at 623 nm, and (b) colour contrast (ΔE*) and switching times of the ECDs measured during the durability test. (c) L^*, (d) $a^*$and (e) b^* coordinate evolution as a function of the number of cycles.

Table 5.3-1: Figures of merits of the Cu NWs/rGO based electrochromic device.

Number of cycles	ΔAbs^{max}	Q_c (mC/cm²)	Q_b (mC/cm²)	CE (cm²/C)	τ_c (s)	τ_b (s)
20	0.160	0.14	0.14	948	0.4	0.4
20000	0.086	1.04	0.45	174	18.9	8.4

ΔAbs^{max} is the maximum absorbance change at 623 nm, colouration (Q_c) and bleaching (Q_b) electric current, colouration efficiency (CE, measured after 95% change of optical transmittance) and switching time for coloured (τ_c) and bleached (τ_b) states of the ECDs (also measured after 95% change of optical transmittance).

Besides, a completely ITO free ECD was also prepared. In this case, the Cu NWs/rGO on PET was used as the working electrode, and PEDOT deposited onto PET as the counter electrode. Apart from this difference, the device was assembled as the previous one. The device was switched between 0 V and – 1.5 V. The ΔAbsorbance of this device was equal to 0.44, a value impressively higher compared to the first ECD device. However, the switching times were longer (1.9 s in oxidation and 3.9 s in reduction) and the colouration efficiency consequently lower (427 and 241 cm²/C, for oxidation and reduction, respectively). After the optical characterization using spectroelectrochemistry and the measurement of the switching

time, the experiments were extended performing cycling measurements of the fully ITO-free device, which showed good durability up to 30000 cycles with colour retention above 50%.

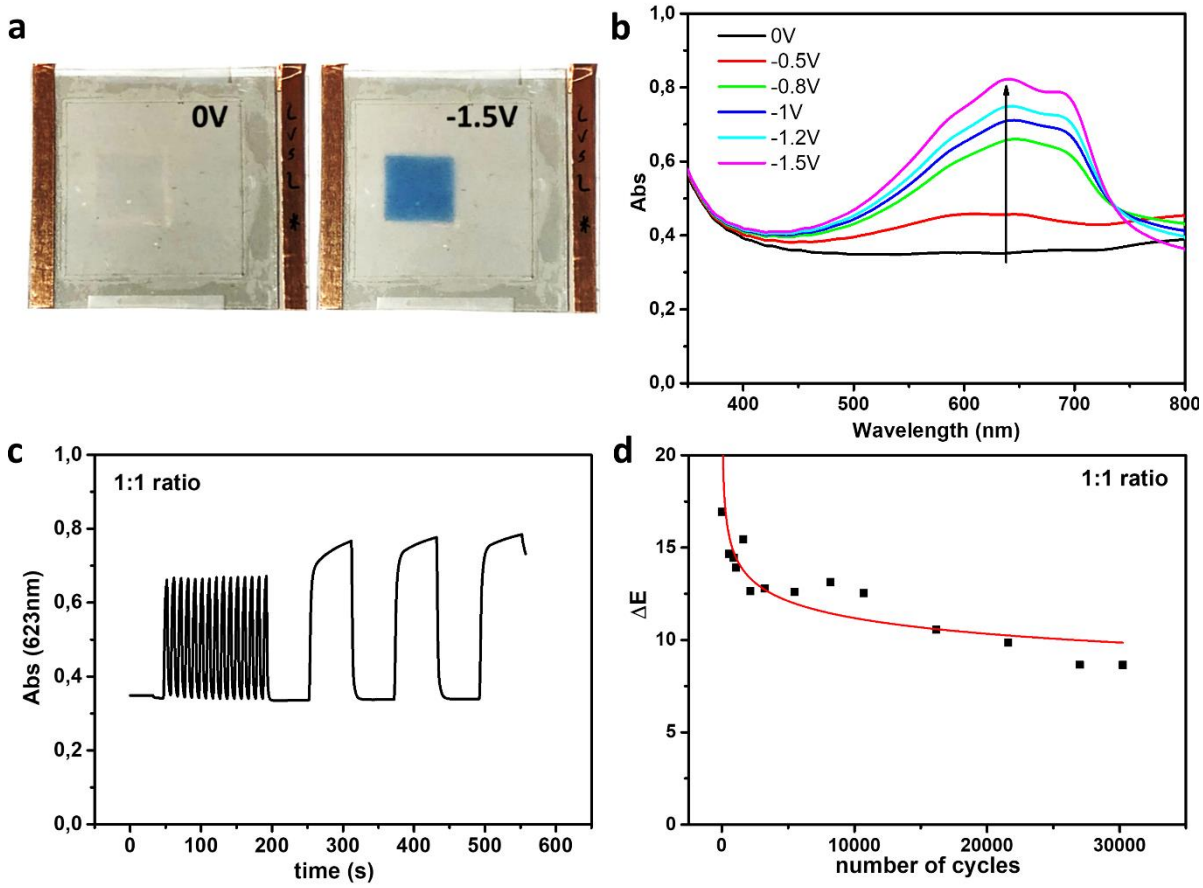

Figure 5.3-20: (a) Photos of the fully ITO free ECD in the coloured and bleached state. (b) Absorbance spectra of the ECD in under application of different potentials between 0 V and -1.5 V. (c) Absorbance at 623 nm as a function of the time after the application of 0 V and -1.5 V. (d) Colour contrast (ΔE*) of the ECD as a function of the number of operating cycles.

Table 5.3-2: Figures of merits of the fully ITO-free Cu NWs/rGO based electrochromic device.

ΔT (%)	ΔAbs_{max}	Q_c (mC/cm²)	Q_b (mC/cm²)	CE (cm²/C)	τ_c (s)	τ_b (s)
28 %	0.44	1.03	1.82	241	1.9	3.9

5.4. Conclusions

The objective of this chapter was the development of highly performing transparent electrodes based on the hybrid assembly of rGO and copper nanowires. In particular, we focussed on the use of low cost and abundant materials and green synthetic procedures. We found that homogenous films can be obtained through spray-coating of all the components onto different substrates. The assembly of the electrodes via spray-coating has the advantage

to be fast and easily industrially scalable. We demonstrated that a mild reduction with sodium borohydride in water at room temperature can be successfully used to reduce in one-step both the GO and the oxide layer coating the Cu NWs, enabling the conduction. This hybrid Cu NWs/rGO transparent electrode exhibited a transmittance of 71 % (at 550 nm) and sheet resistance of ca. 30 Ω/sq. We demonstrated that the rGO layer increases the durability of the film, which was stable in environmental conditions up to at least 100 days and withstood several washing cycles with various kinds of household products. Furthermore, the hybrid electrode compared to bare Cu NWs showed a more uniform and higher conductivity and a lower roughness, as confirmed by AFM characterization. The hybrid Cu NWs/rGO electrode supported on PET exhibited also high flexibility, with a small 4 % change in the resistance after 10000 bending cycles with a bending radius of 1 cm. As a proof-of-concept, high performance ECDs based on the hybrid electrode have been fabricated and characterized. These devices showed excellent optical contrast, switching time and colouration efficiency and good durability up to 10000 cycles. The robustness and chemical stability of the electrodes also after several operating cycles when in contact with an electrolyte, promotes these hybrid materials for the replacement of ITO in different opto-electronic applications such as organic light emitting diodes (OLEDs) and organic photovoltaics (OPVs), but also as low-cost electrodes for biomedical applications such as disposable electrodes for electrochemiluminescence (ECL) biosensing and immunoassay applications.

Chapter 6.

Conclusion and perspectives

In conclusion, this thesis work has been focussed on the development of two different types of hybrids based on reduced graphene oxide (rGO), by making use of either covalent functionalization with molecules or non-covalent assembly with metallic nanostructures, for application in humidity sensing or as transparent conductive electrodes. In particular, we have focussed on the use of facile, reproducible and scalable procedures and the use of low-cost and "green" reagents, thus making such hybrids environmentally sustainable and industrially relevant. In this regard, among the various forms of graphene we decided to use (reduced) graphene oxide because of its lower cost, larger volume production and more straightforward functionalization.

In the first experimental chapter, we have developed a hydrophilic hybrid based on rGO covalently functionalized with molecules and used it as the active material of a high performing humidity sensor. In particular, we have demonstrated that the sensitivity of rGO to humidity can be enhanced via its chemical functionalization with hydrophilic moieties designed to specifically and reversibly interact at the supramolecular level with water molecules. In particular, amine-terminated triethylene glycol, whose etheric oxygens can interact with water molecules forming weak, thus reversible, hydrogen bonding have been employed.[4] In parallel, to demonstrate our rational, we developed a hydrophobic rGO hybrid, by functionalizing GO with decylamine chains. Amine terminated molecules were chosen because they can easily react with the epoxide functional groups exposed on the basal plane of GO by the epoxide-ring opening reaction. Ethanolic dispersions of these two materials and of GO were processed in thin and transparent films by spray-coating and subjected to mild thermal annealing to partially reduce GO and increase the electrical conductivity while maintaining its chemical functionalization. We have carried out a full and multiscale characterization of these hybrid films to confirm the successful functionalization and its retention after the annealing and investigate the hydrophilicity, topography, and morphology of such films. Then, we assembled resistive-type humidity sensors by evaporating two gold electrodes onto such films and we exposed them to humidity. We proved that the device comprising the most hydrophilic triethylene glycol functionalized rGO (rCMGO-1) exhibited the best sensing performances towards humidity. This device showed an interesting increase in resistance with the growing humidity, with a remarkable sensitivity (up to 31 % when the RH is shifted from 2 to 97 %), high stability of the signal after 100 pulses of humid air, complete reversibility, fast response and recovery time (respectively 25 ms and 127 ms), high robustness and long-term stability, thereby

outperforming many of the commercial devices and other rGO based resistive type devices. Furthermore, rCMGO-1 sensor displayed also high selectivity to humidity when compared to representative polar volatile organic compounds (with sensitivity to humidity at least 9 times superior to that of the other vapours). Conversely, the decylamine decorated rGO (rCMGO-2) and the non-functionalized rGO exhibited lower sensitivity to humidity, being less than half those of rCMGO-1, longer response and recovery times (at least 4 and 6 times longer, respectively), incomplete recovery, large hysteresis (67 and 21 % for rGO and rCMGO-2, respectively) and unstable behaviour. Their selectivity to humidity was also lower, with increased cross-sensitivity to methanol, ethanol and chloroform compared to rCMGO-1.

With the help of humidity dependent XRD measurements and Force Field MD simulations we shed light onto the physical origin of the response to the humidity of the devices and onto the reasons for the better performances of rCMGO-1. Humidity dependent XRD data revealed that the functional groups present on the basal plane of rGO have a low impact on the structural changes of the materials when they are exposed to a humid environment. The presence of humidity determines an increase in the interlayer distance of the three materials, but such an increase is quite small and the differences between the materials too limited to explain the major differences in performances. The different electronic behaviours of the three materials when they interacted with humidity, and thus their different performances were explained by Force Field MD. In particular, the interaction force with water was the highest in rCMGO-1 due to its functionalization with triethylene glycol, resulting in the highest sensitivity. Furthermore, we demonstrated that the water molecules need to overcome a small energy barrier to escape from the surface of rCMGO-1, leading to fast and completely reversible sensing. These water molecules are instead trapped in a quasi-continuous ensemble of microstates on the surfaces of rCMGO-2 and rGO, causing a slow and incomplete recovery which ultimately yields to the poorly responsive nature of these devices.

Overall, we have demonstrated that the ad hoc chemical functionalization of GO with suitably designed molecules, acting as water molecules receptors, enables to reach highest performances in humidity sensing and ensures the highest selectivity to water molecules. We believe that our sensor matches all the technological requirements to be integrated into portable, low-cost and low-consumption devices which potentially can be supported on flexible and transparent substrates. We foresee that flexible devices could easily be obtained using either polymeric substrates with high melting temperatures, such as polysulfone, or by reducing the annealing temperature while increasing the annealing time, or employing a chemical reduction before the deposition of the hybrid material. We believe that the same strategy of functionalization of GO can be used to graft to GO other chosen molecules capable of interacting with other target analytes by exploiting the well-established library provided by supramolecular chemistry. This general strategy will make it possible to

fabricate highly performing chemical sensors of a wide range of different analytes. For example, GO could be functionalized with different crown-ethers to interact selectively with different metal ions.[454] On the same time, the functionalization of GO with a different molecule bearing more units capable to interact with water molecules *via* weak hydrogen bonding, such as polyethyleneimine (PEI) may increase even further its response to humidity. In fact, with simple linear molecules, it will be hard to increase further the response since the degree of functionalization that we obtained is around the maximum allowed when exploiting the epoxide-ring opening reaction.[168] Longer (poly)ethylene glycol chains may also be used, however, probably the sensitivity of the hybrid would not be increased because only the molecules of water interacting with the etheric oxygens that are close to the GO surface will perturb its electronic states.

The second experimental chapter has been focused on the design and fabrication of a transparent conductive film based on the hybrid assembly of copper nanowires (Cu NWs) and rGO and on its implementation as an electrode for electrochromic devices. Cu NWs were chosen by virtue of their low cost and high conductivity and transparency when processed into thin films. Their proneness to oxidation has been addressed by covering them with a thin film of rGO on top as a protective transparent and conductive layer. In particular, we developed a simple method for the preparation of Cu NWs/rGO films which relies on the bottom-up formation of Cu NWs suspensions by means of the Maillard reaction[8, 375] (since it implies green reagents and mild conditions) and on the use of commercial GO. Hybrid films were prepared by sequentially depositing *via* spray-coating ethanolic suspensions of the two components on PET and glass substrates. Then the conductivity of the hybrid Cu NWs/GO was enabled by treating it with a sodium borohydride water solution to simultaneously reduce the CuO layer coating the Cu NWs and GO to rGO. At the end of the treatment, the films displayed sheet resistance of 30 Ohm/sq and transmittance of ca. 70 %. Other reducing agents were also tested, showing that most of them brought to the dissolution of Cu NWs. The films of Cu NWs, rGO and the hybrid Cu NWs/rGO were fully characterized. The reduction of both components was confirmed by XPS. Noteworthily, the rGO layer coating the Cu NWs network contributes also to decrease its roughness, as confirmed by AFM imaging. The hybrid film exhibited stability in air for at least 3 months and washability in the most common household detergents. On the contrary, the bare Cu NWs film exhibited lower stability to the exposure to the same household detergents. Furthermore, the hybrid film on PET demonstrated high flexibility, being able to stand to 10000 cycles of bending at 1 cm radius without any drop in the performances.

Finally, the hybrid film was employed as a transparent electrode to assemble flexible electrochromic devices (ECD). These devices showed excellent optical contrast between the coloured and bleached states (up to 0.44 of ΔAbsorbance), fast switching times (between 1 and 3 s) and high colouration efficiency, being comparable to the performances of similar

ECD devices employing ITO electrodes. Furthermore, to test the industrial relevance of the devices, these were run for several days by performing continuous on-off cycles. The devices showed unaltered performances up to 1000 cycles and maintained satisfactory performances even after 20000 cycles. Currently, we are testing A4 size devices, to demonstrate the scalability of our approach. The facile, scalable, low-cost and sustainable procedures used open up the use of such electrodes as disposable electrodes for electrochemiluminescence biosensing and immunoassay applications and for disposable low consumption ECD, to be used for example as interactive tags for packaging or as small artistic gadgets. Furthermore, we foresee the use of this low-cost and sustainable hybrid electrode for the replacement of ITO electrode also in different optoelectronic applications such as organic light-emitting diodes and photovoltaic cells.

However, these electrodes can still be improved to display higher industrial relevance. In particular, actions can be taken in order to (i) decrease further the roughness and increase the uniformity of the Cu NWs network, (ii) increase the transparency, while maintaining high conductivity and stability, (iii) increase further the stability to oxidative environment and electrical potentials. Aggregates of Cu NWs and larger Cu nanocrystals are often present on the surface of the film; these objects, which are much higher than the single Cu NWs, could cause short-circuits of the devices. To address this problem, the uniformity of the film may be increased by optimizing the spray-coating parameter and by increasing the stability of Cu NWs ink with the aid of surfactants. Other deposition techniques, such as Meyer road, may also be used. Furthermore, a reduction of the roughness of the hybrid film can be obtained either by pressing the film at elevated pressures under heating,[455] or by depositing and additional transparent, conductive and smoothing layer on top of the hybrid such as PEDOT:PSS or MoO_3.[456, 457] Another technique consists in embedding the Cu NWs in a polymeric matrix. To do so, Cu NWs should be deposited onto a rigid substrate, then a liquid polymer precursor should be poured on top of the Cu NWs network in order to form a thin film. Once the polymer is solidified, it can be peeled away, together with the nanowires, from the rigid surface.

The transparency of the film may be increased by coating the Cu NWs individually with a graphitic layer, instead of having a rGO film covering the entire surface of the electrode. This technique should increase the transmittance of the film of around 10 %. Towards this end, nanoflakes of (r)GO could be selectively adsorbed onto the surface of Cu NWs in solution, before the deposition.[436] Binders, such as PEI, may be used to favour the interaction between the Cu NWs and GO flakes. The problem of this approach may be the presence of some discontinuity on the (r)GO coating which would expose the Cu NWs to oxidation. Another approach consists in the coating of Cu NWs with a polymer in solution such as polythiophene, polypyrrole or polydopamine,[458-460] followed by the deposition of the coated Cu NWs and thermal annealing to graphitize the polymer. However, in this case, the thermal annealing would increase the cost and environmental impact of this method.

Finally, the oxidation resistance of the Cu NWs could be further increased by coating the Cu NWs with a metal more resistant to oxidation, such as Ni, Ag or Au,[461-463] or by forming an alloy with copper.[464-466] However, in this case, the use of Ag or Au would increase the cost of the electrode. Another approach may be the use of a semi-conductive metal oxide coating, such as MnO_3, TiO_2, ZnO. Small molecular corrosion inhibitors may also be used.[467] Molecules terminating with amines or carboxylic acids could be used because of the tendency of these to adsorb onto the Cu NWs surface. However, such molecules should be small enough to not hinder the electron transfer between the Cu NWs and the active material.

Overall, we have demonstrated the versatility of GO/rGO which can be combined with an immense library of molecules and other nanostructures, by exploiting a wide range of covalent and non-covalent interactions. We have also demonstrated that these hybrid assemblies based on rGO possess new properties and enhanced performances compared to the single components and that these properties can be tailored at will by choosing the properly designed molecule or nanostructure.

The research on graphene-based hybrid assemblies is still on an early stage and there is still plenty of room for improving the performances, reducing the costs and ultimately allowing products with a revolutionary impact in the years to come. New technologies indeed necessitate several decades for implanting into society.[468] For example, it took 15 years for silicon-based semiconductors to appear in the first commercial products, and more than 20 years to completely supplant other existing technologies.[469] We believe that graphene-based hybrids possess the qualities to emerge as disruptive technologies in optoelectronics, water purification, energy, biomedical applications, as well as sensing, with the ultimate goal of providing a decisive step forward in the major challenges our society is facing, i.e. energy, water and quality of life.

References

1 K. S. Novoselov, A. K. Geim, S. V. Morozov, D. Jiang, Y. Zhang, S. V. Dubonos, I. V. Grigorieva and A. A. Firsov, *Science*, 2004, **306**, 666.

2 V. Georgakilas, M. Otyepka, A. B. Bourlinos, V. Chandra, N. Kim, K. C. Kemp, P. Hobza, R. Zboril and K. S. Kim, *Chem. Rev.*, 2012, **112**, 6156.

3 C. Lv, C. Hu, J. Luo, S. Liu, Y. Qiao, Z. Zhang, J. Song, Y. Shi, J. Cai and A. Watanabe, *Nanomaterials*, 2019, **9**, 422.

4 T. Steiner, *J. Chem. Soc., Chem. Commun.*, 1994, DOI: Doi 10.1039/C39940002341, 2341.

5 C. J. M. Emmott, A. Urbina and J. Nelson, *Sol. Energy Mater. Sol. Cells*, 2012, **97**, 14.

6 T. Sannicolo, M. Lagrange, A. Cabos, C. Celle, J.-P. Simonato and D. Bellet, *Small*, 2016, **12**, 6052.

7 I. N. Kholmanov, S. H. Domingues, H. Chou, X. Wang, C. Tan, J.-Y. Kim, H. Li, R. Piner, A. J. G. Zarbin and R. S. Ruoff, *ACS Nano*, 2013, **7**, 1811.

8 M. Kevin, G. Y. R. Lim and G. W. Ho, *Green Chem.*, 2015, **17**, 1120.

9 M. Hofmann, H. Hofmann, C. Hagelüken and A. Hool, *Sustainable Mater. Technol.*, 2018, **17**, e00074.

10 A. K. Geim and K. S. Novoselov, *Nat. Mater.*, 2007, **6**, 183.

11 K. S. Novoselov, V. I. Fal'ko, L. Colombo, P. R. Gellert, M. G. Schwab and K. Kim, *Nature*, 2012, **490**, 192.

12 O. C. Compton and S. T. Nguyen, *Small*, 2010, **6**, 711.

13 X. Huang, X. Qi, F. Boey and H. Zhang, *Chem. Soc. Rev.*, 2012, **41**, 666.

14 X. Chen, K. Shehzad, L. Gao, M. Long, H. Guo, S. Qin, X. Wang, F. Wang, Y. Shi, W. Hu, Y. Xu and X. Wang, *Adv. Mater.*, 2019, **32**, 1902039.

15 V. Georgakilas, J. N. Tiwari, K. C. Kemp, J. A. Perman, A. B. Bourlinos, K. S. Kim and R. Zboril, *Chem. Rev.*, 2016, **116**, 5464.

16 L. Peng, Y. Zhu, H. Li and G. Yu, *Small*, 2016, **12**, 6183.

17 S. Ye, A. R. Rathmell, Z. Chen, I. E. Stewart and B. J. Wiley, *Adv. Mater.*, 2014, **26**, 6670.

18 J. Liu, S. Li, B. Zhang, Y. Wang, Y. Gao, X. Liang, Y. Wang and G. Lu, *J. Colloid Interface Sci.*, 2017, **504**, 206.

19 Y. Meng, K. Wang, Y. Zhang and Z. Wei, *Adv. Mater.*, 2013, **25**, 6985.

20 P. Xue, S. Liu, X. Shi, C. Sun, C. Lai, Y. Zhou, D. Sui, Y. Chen and J. Liang, *Adv. Mater.*, 2018, **30**, 1804165.

21 S. Deng, V. Tjoa, H. M. Fan, H. R. Tan, D. C. Sayle, M. Olivo, S. Mhaisalkar, J. Wei and C. H. Sow, *J. Am. Chem. Soc.*, 2012, **134**, 4905.

22 K. S. Novoselov, A. K. Geim, S. V. Morozov, D. Jiang, M. I. Katsnelson, I. V. Grigorieva, S. V. Dubonos and A. A. Firsov, *Nature*, 2005, **438**, 197.

23 A. S. Mayorov, R. V. Gorbachev, S. V. Morozov, L. Britnell, R. Jalil, L. A. Ponomarenko, P. Blake, K. S. Novoselov, K. Watanabe, T. Taniguchi and A. K. Geim, *Nano Lett.*, 2011, **11**, 2396.

24 C. Lee, X. Wei, J. W. Kysar and J. Hone, *Science*, 2008, **321**, 385.

25 R. R. Nair, P. Blake, A. N. Grigorenko, K. S. Novoselov, T. J. Booth, T. Stauber, N. M. R. Peres and A. K. Geim, *Science*, 2008, **320**, 1308.

26 J. S. Bunch, S. S. Verbridge, J. S. Alden, A. M. van der Zande, J. M. Parpia, H. G. Craighead and P. L. McEuen, *Nano Lett.*, 2008, **8**, 2458.

27 K. Nagashio, T. Yamashita, T. Nishimura, K. Kita and A. Toriumi, *J. Appl. Phys.*, 2011, **110**, 024513.

28 A. C. Ferrari, F. Bonaccorso, V. Fal'ko, K. S. Novoselov, S. Roche, P. Bøggild, S. Borini, F. H. L. Koppens, V. Palermo, N. Pugno, J. A. Garrido, R. Sordan, A. Bianco, L. Ballerini, M. Prato, E. Lidorikis, J. Kivioja, C. Marinelli, T. Ryhänen, A. Morpurgo, J. N. Coleman, V. Nicolosi, L. Colombo, A. Fert, M. Garcia-Hernandez, A. Bachtold, G. F. Schneider, F. Guinea, C. Dekker, M. Barbone, Z. Sun, C. Galiotis, A. N. Grigorenko, G. Konstantatos, A. Kis, M. Katsnelson, L. Vandersypen, A. Loiseau, V. Morandi, D. Neumaier, E. Treossi, V. Pellegrini, M. Polini, A. Tredicucci, G. M. Williams, B. Hee Hong, J.-H. Ahn, J. Min Kim, H. Zirath, B. J. van Wees, H. van der Zant, L. Occhipinti, A. Di Matteo, I. A. Kinloch, T. Seyller, E. Quesnel, X. Feng, K. Teo, N. Rupesinghe, P. Hakonen, S. R. T. Neil, Q. Tannock, T. Löfwander and J. Kinaret, *Nanoscale*, 2015, **7**, 4598.

29 S.-M. Lee, J.-H. Kim and J.-H. Ahn, *Mater. Today*, 2015, **18**, 336.

30 R. Raccichini, A. Varzi, S. Passerini and B. Scrosati, *Nat. Mater.*, 2015, **14**, 271.

31 J. M. Cai, P. Ruffieux, R. Jaafar, M. Bieri, T. Braun, S. Blankenburg, M. Muoth, A. P. Seitsonen, M. Saleh, X. L. Feng, K. Mullen and R. Fasel, *Nature*, 2010, **466**, 470.

32 A. Narita, X. Feng and K. Müllen, *Chem. Rec.*, 2015, **15**, 295.

33 C. Berger, Z. M. Song, X. B. Li, X. S. Wu, N. Brown, C. Naud, D. Mayou, T. B. Li, J. Hass, A. N. Marchenkov, E. H. Conrad, P. N. First and W. A. de Heer, *Science*, 2006, **312**, 1191.

34 C. Riedl, C. Coletti and U. Starke, *J. Phys. D: Appl. Phys.*, 2010, **43**, 374009.

35 Y. Zhang, L. Zhang and C. Zhou, *Acc. Chem. Res.*, 2013, **46**, 2329.

36 C. Mattevi, H. Kim and M. Chhowalla, *J. Mater. Chem.*, 2011, **21**, 3324.

37 H. Xin and W. Li, *Appl. Phys. Rev.*, 2018, **5**, 031105.

38 N. Woehrl, O. Ochedowski, S. Gottlieb, K. Shibasaki and S. Schulz, *AIP Adv.*, 2014, **4**, 047128.

39 M. Chen, R. C. Haddon, R. Yan and E. Bekyarova, *Mater. Horiz.*, 2017, **4**, 1054.

40 Y. Wang, Y. Zheng, X. Xu, E. Dubuisson, Q. Bao, J. Lu and K. P. Loh, *ACS Nano*, 2011, **5**, 9927.

41 F. Pizzocchero, B. S. Jessen, P. R. Whelan, N. Kostesha, S. Lee, J. D. Buron, I. Petrushina, M. B. Larsen, P. Greenwood, W. J. Cha, K. Teo, P. U. Jepsen, J. Hone, P. Bøggild and T. J. Booth, *Carbon*, 2015, **85**, 397.

42 A. Ciesielski and P. Samorì, *Chem. Soc. Rev.*, 2014, **43**, 381.

43 Y. Xu, H. Cao, Y. Xue, B. Li and W. Cai, *Nanomaterials*, 2018, **8**, 942.

44 A. Ciesielski and P. Samorì, *Adv. Mater.*, 2016, **28**, 6030.

45 A. M. Abdelkader, A. J. Cooper, R. A. W. Dryfe and I. A. Kinloch, *Nanoscale*, 2015, **7**, 6944.

46 M. Cai, D. Thorpe, D. H. Adamson and H. C. Schniepp, *J. Mater. Chem.*, 2012, **22**, 24992.

47 *Philos. Trans. R. Soc. London*, 1997, **149**, 249.

48 W. S. Hummers and R. E. Offeman, *J. Am. Chem. Soc.*, 1958, **80**, 1339.

49 D. R. Dreyer, S. Park, C. W. Bielawski and R. S. Ruoff, *Chem. Soc. Rev.*, 2010, **39**, 228.

50 A. Lerf, H. He, M. Forster and J. Klinowski, *J. Phys. Chem. B*, 1998, **102**, 4477.

51 K. Erickson, R. Erni, Z. Lee, N. Alem, W. Gannett and A. Zettl, *Adv. Mater.*, 2010, **22**, 4467.

52 S. Gilje, S. Han, M. Wang, K. L. Wang and R. B. Kaner, *Nano Lett.*, 2007, **7**, 3394.

53 Y. Wang, Y. Chen, S. D. Lacey, L. Xu, H. Xie, T. Li, V. A. Danner and L. Hu, *Mater. Today*, 2018, **21**, 186.

54 H. Conrad, G. Ertl and E. E. Latta, *Surf. Sci.*, 1974, **41**, 435.

55 A. Kaniyoor, R. Imran Jafri, T. Arockiadoss and S. Ramaprabhu, *Nanoscale*, 2009, **1**, 382.

56 M. G. Chung, D.-H. Kim, D. K. Seo, T. Kim, H. U. Im, H. M. Lee, J.-B. Yoo, S.-H. Hong, T. J. Kang and Y. H. Kim, *Sens. Actuator B-Chem.*, 2012, **169**, 387.

57 W. Li, X. Geng, Y. Guo, J. Rong, Y. Gong, L. Wu, X. Zhang, P. Li, J. Xu, G. Cheng, M. Sun and L. Liu, *ACS Nano*, 2011, **5**, 6955.

58 L. Huang, Z. Wang, J. Zhang, J. Pu, Y. Lin, S. Xu, L. Shen, Q. Chen and W. Shi, *ACS Appl. Mater. Interfaces*, 2014, **6**, 7426.

59 S. Mao, S. Cui, G. Lu, K. Yu, Z. Wen and J. Chen, *J. Mater. Chem.*, 2012, **22**, 11009.

60 L. Zhou, F. Shen, X. Tian, D. Wang, T. Zhang and W. Chen, *Nanoscale*, 2013, **5**, 1564.

61 G. Singh, A. Choudhary, D. Haranath, A. G. Joshi, N. Singh, S. Singh and R. Pasricha, *Carbon*, 2012, **50**, 385.

62 R. K. Mishra, S. B. Upadhyay, A. Kushwaha, T.-H. Kim, G. Murali, R. Verma, M. Srivastava, J. Singh, P. P. Sahay and S. H. Lee, *Nanoscale*, 2015, **7**, 11971.

63 Q. Huang, D. Zeng, H. Li and C. Xie, *Nanoscale*, 2012, **4**, 5651.

64 R. K. Mishra, S. B. Upadhyay, A. Kushwaha, T. H. Kim, G. Murali, R. Verma, M. Srivastava, J. Singh, P. P. Sahay and S. H. Lee, *Nanoscale*, 2015, **7**, 11971.

65 W. Peng, H. Li, Y. Liu and S. Song, *J. Mol. Liq.*, 2017, **230**, 496.

66 K. C. Kemp, H. Seema, M. Saleh, N. H. Le, K. Mahesh, V. Chandra and K. S. Kim, *Nanoscale*, 2013, **5**, 3149.

67 V. Chandra, J. Park, Y. Chun, J. W. Lee, I.-C. Hwang and K. S. Kim, *ACS Nano*, 2010, **4**, 3979.

68 J. Zhu, S. Wei, H. Gu, S. B. Rapole, Q. Wang, Z. Luo, N. Haldolaarachchige, D. P. Young and Z. Guo, *Environ. Sci. Technol.*, 2011, **46**, 977.

69 H.-P. Cong, X.-C. Ren, P. Wang and S.-H. Yu, *ACS Nano*, 2012, **6**, 2693.

70 X. Yang, C. Chen, J. Li, G. Zhao, X. Ren and X. Wang, *RSC Adv.*, 2012, **2**, 8821.

71 C. Anichini, W. Czepa, D. Pakulski, A. Aliprandi, A. Ciesielski and P. Samorì, *Chem. Soc. Rev.*, 2018, **47**, 4860.

72 Z. S. Qian, X. Y. Shan, L. J. Chai, J. R. Chen and H. Feng, *Biosens. Bioelectron.*, 2015, **68**, 225.

73 H. Dong, W. Gao, F. Yan, H. Ji and H. Ju, *Anal. Chem.*, 2010, **82**, 5511.

74 M. Kaur, A. Umar, S. K. Mehta and S. K. Kansal, *Appl. Catal., B*, 2019, **245**, 143.

75 J. Gong, T. Zhou, D. Song and L. Zhang, *Sens. Actuator B-Chem.*, 2010, **150**, 491.

76 J. Li, J. Yang, Z. Yang, Y. Li, S. Yu, Q. Xu and X. Hu, *Anal. Methods*, 2012, **4**, 1725.

77 T. Zeng, X.-l. Zhang, Y.-r. Ma, H.-y. Niu and Y.-q. Cai, *J. Mater. Chem.*, 2012, **22**, 18658.

78 L. Yang, W. Luo and G. Cheng, *ACS Appl. Mater. Interfaces*, 2013, **5**, 8231.

79 X. J. Lv, W. F. Fu, H. X. Chang, H. Zhang, J. S. Cheng, G. J. Zhang, Y. Song, C. Y. Hu and J. H. Li, *J. Mater. Chem.*, 2012, **22**, 1539.

80 Q. Li, B. Guo, J. Yu, J. Ran, B. Zhang, H. Yan and J. R. Gong, *J. Am. Chem. Soc.*, 2011, **133**, 10878.

81 F.-X. Xiao, J. Miao and B. Liu, *J. Am. Chem. Soc.*, 2014, **136**, 1559.

82 J. Kim, M.-S. Lee, S. Jeon, M. Kim, S. Kim, K. Kim, F. Bien, S. Y. Hong and J.-U. Park, *Adv. Mater.*, 2015, **27**, 3292.

83 I. N. Kholmanov, C. W. Magnuson, A. E. Aliev, H. Li, B. Zhang, J. W. Suk, L. L. Zhang, E. Peng, S. H. Mousavi, A. B. Khanikaev, R. Piner, G. Shvets and R. S. Ruoff, *Nano Lett.*, 2012, **12**, 5679.

84 M.-S. Lee, K. Lee, S.-Y. Kim, H. Lee, J. Park, K.-H. Choi, H.-K. Kim, D.-G. Kim, D.-Y. Lee, S. Nam and J.-U. Park, *Nano Lett.*, 2013, **13**, 2814.

85 V. C. Tung, L.-M. Chen, M. J. Allen, J. K. Wassei, K. Nelson, R. B. Kaner and Y. Yang, *Nano Lett.*, 2009, **9**, 1949.

86 A. Aliprandi, T. Moreira, C. Anichini, M. A. Stoeckel, M. Eredia, U. Sassi, M. Bruna, C. Pinheiro, C. A. Laia and S. Bonacchi, *Adv. Mater.*, 2017, **29**, 1703225.

87 Q. Zhang, Y. Di, C. M. Huard, L. J. Guo, J. Wei and J. Guo, *J. Mater. Chem. C*, 2015, **3**, 1528.

88 N. Jung, S. Kwon, D. Lee, D.-M. Yoon, Y. M. Park, A. Benayad, J.-Y. Choi and J. S. Park, *Adv. Mater.*, 2013, **25**, 6854.

89 D. Yu and L. Dai, *J. Phys. Chem. Lett.*, 2009, **1**, 467.

90 Q. Cheng, J. Tang, J. Ma, H. Zhang, N. Shinya and L.-C. Qin, *Phys. Chem. Chem. Phys.*, 2011, **13**, 17615.

91 M. Li, Z. Tang, M. Leng and J. Xue, *Adv. Funct. Mater.*, 2014, **24**, 7495.

92 Z. Li, Q. He, X. Xu, Y. Zhao, X. Liu, C. Zhou, D. Ai, L. Xia and L. Mai, *Adv. Mater.*, 2018, **30**, 1804089.

93 B. Wang, X. Li, X. Zhang, B. Luo, M. Jin, M. Liang, S. A. Dayeh, S. T. Picraux and L. Zhi, *ACS Nano*, 2013, **7**, 1437.

94 S. Woo, Y. R. Kim, T. D. Chung, Y. Piao and H. Kim, *Electrochim. Acta*, 2012, **59**, 509.

95 Q. He, J. Liu, X. Liu, G. Li, D. Chen, P. Deng and J. Liang, *Electrochim. Acta*, 2019, **296**, 683.

96 S. Chen, Y. Wei, S. Wei, Y. Lin and L. Liu, *ACS Appl. Mater. Interfaces*, 2016, **8**, 25563.

97 Z. Chen, Z. Wang, X. Li, Y. Lin, N. Luo, M. Long, N. Zhao and J.-B. Xu, *ACS Nano*, 2017, **11**, 4507.

98 P. Z. Sun, Q. Yang, W. J. Kuang, Y. V. Stebunov, W. Q. Xiong, J. Yu, R. R. Nair, M. I. Katsnelson, S. J. Yuan, I. V. Grigorieva, M. Lozada-Hidalgo, F. C. Wang and A. K. Geim, *Nature*, 2020, **579**, 229.

99 P. Kumar, K. L. Woon, W. S. Wong, M. S. Mohamed Saheed and Z. A. Burhanudin, *Synth. Met.*, 2019, **257**, 116186.

100 L. He, C. Liao and S. Tjong, *Nanomaterials*, 2018, **8**, 224.

101 A. G. Ricciardulli, S. Yang, G.-J. A. H. Wetzelaer, X. Feng and P. W. M. Blom, *Adv. Funct. Mater.*, 2018, **28**, 1706010.

102 J. Liang, L. Li, K. Tong, Z. Ren, W. Hu, X. Niu, Y. Chen and Q. Pei, *ACS Nano*, 2014, **8**, 1590.

103 L. Dou, F. Cui, Y. Yu, G. Khanarian, S. W. Eaton, Q. Yang, J. Resasco, C. Schildknecht, K. Schierle-Arndt and P. Yang, *ACS Nano*, 2016, **10**, 2600.

104 W. K. Chee, H. N. Lim, Z. Zainal, N. M. Huang, I. Harrison and Y. Andou, *J. Phys. Chem. C*, 2016, **120**, 4153.

105 H. Y. Jeong, D.-S. Lee, H. K. Choi, D. H. Lee, J.-E. Kim, J. Y. Lee, W. J. Lee, S. O. Kim and S.-Y. Choi, *Appl. Phys. Lett.*, 2010, **96**, 213105.

106 J. Yi, J. M. Lee and W. I. Park, *Sens. Actuator B-Chem.*, 2011, **155**, 264.

107 T. V. Cuong, V. H. Pham, J. S. Chung, E. W. Shin, D. H. Yoo, S. H. Hahn, J. S. Huh, G. H. Rue, E. J. Kim, S. H. Hur and P. A. Kohl, *Mater. Lett.*, 2010, **64**, 2479.

108 P. Solís-Fernández, M. Bissett and H. Ago, *Chem. Soc. Rev.*, 2017, **46**, 4572.

109 H. Wang, F. Liu, W. Fu, Z. Fang, W. Zhou and Z. Liu, *Nanoscale*, 2014, **6**, 12250.

110 A. K. Geim and I. V. Grigorieva, *Nature*, 2013, **499**, 419.

111 C. R. Dean, A. F. Young, I. Meric, C. Lee, L. Wang, S. Sorgenfrei, K. Watanabe, T. Taniguchi, P. Kim, K. L. Shepard and J. Hone, *Nat. Nanotechnol.*, 2010, **5**, 722.

112 K. S. Novoselov, A. Mishchenko, A. Carvalho and A. H. Castro Neto, *Science*, 2016, **353**, aac9439.

113 Q. Li, M. Liu, Y. Zhang and Z. Liu, *Small*, 2016, **12**, 32.

114 M. Kan, Y. Li and Q. Sun, *Wiley Interdiscip. Rev. Comput. Mol. Sci.*, 2016, **6**, 65.

115 M. Yankowitz, Q. Ma, P. Jarillo-Herrero and B. J. LeRoy, *Nat. Rev. Phys.*, 2019, **1**, 112.

116 C. R. Dean, L. Wang, P. Maher, C. Forsythe, F. Ghahari, Y. Gao, J. Katoch, M. Ishigami, P. Moon, M. Koshino, T. Taniguchi, K. Watanabe, K. L. Shepard, J. Hone and P. Kim, *Nature*, 2013, **497**, 598.

117 M. Yankowitz, J. M. Xue, D. Cormode, J. D. Sanchez-Yamagishi, K. Watanabe, T. Taniguchi, P. Jarillo-Herrero, P. Jacquod and B. J. LeRoy, *Nat. Phys.*, 2012, **8**, 382.

118 L. Britnell, R. V. Gorbachev, R. Jalil, B. D. Belle, F. Schedin, A. Mishchenko, T. Georgiou, M. I. Katsnelson, L. Eaves, S. V. Morozov, N. M. R. Peres, J. Leist, A. K. Geim, K. S. Novoselov and L. A. Ponomarenko, *Science*, 2012, **335**, 947.

119 S. J. Haigh, A. Gholinia, R. Jalil, S. Romani, L. Britnell, D. C. Elias, K. S. Novoselov, L. A. Ponomarenko, A. K. Geim and R. Gorbachev, *Nat. Mater.*, 2012, **11**, 764.

120 L. Wang, I. Meric, P. Y. Huang, Q. Gao, Y. Gao, H. Tran, T. Taniguchi, K. Watanabe, L. M. Campos, D. A. Muller, J. Guo, P. Kim, J. Hone, K. L. Shepard and C. R. Dean, *Science*, 2013, **342**, 614.

121 P. J. Zomer, S. P. Dash, N. Tombros and B. J. van Wees, *Appl. Phys. Lett.*, 2011, **99**, 232104.

122 G. Gao, W. Gao, E. Cannuccia, J. Taha-Tijerina, L. Balicas, A. Mathkar, T. N. Narayanan, Z. Liu, B. K. Gupta, J. Peng, Y. Yin, A. Rubio and P. M. Ajayan, *Nano Lett.*, 2012, **12**, 3518.

123 J. Sun, H.-W. Lee, M. Pasta, H. Yuan, G. Zheng, Y. Sun, Y. Li and Y. Cui, *Nat. Nanotechnol.*, 2015, **10**, 980.

124 S. Sinha, Jyotsna and S. K. Arora, *Mater Today-Proc*, 2020, **21**, 1840.

125 Z. Liu, L. Song, S. Zhao, J. Huang, L. Ma, J. Zhang, J. Lou and P. M. Ajayan, *Nano Lett.*, 2011, **11**, 2032.

126 X. Ding, G. Ding, X. Xie, F. Huang and M. Jiang, *Carbon*, 2011, **49**, 2522.

127 Z. Yan, Z. Peng, Z. Sun, J. Yao, Y. Zhu, Z. Liu, P. M. Ajayan and J. M. Tour, *ACS Nano*, 2011, **5**, 8187.

128 X. Song, T. Gao, Y. Nie, J. Zhuang, J. Sun, D. Ma, J. Shi, Y. Lin, F. Ding, Y. Zhang and Z. Liu, *Nano Lett.*, 2016, **16**, 6109.

129 X. Ling, Y.-H. Lee, Y. Lin, W. Fang, L. Yu, M. S. Dresselhaus and J. Kong, *Nano Lett.*, 2014, **14**, 464.

130 K. Roy, M. Padmanabhan, S. Goswami, T. P. Sai, G. Ramalingam, S. Raghavan and A. Ghosh, *Nat. Nanotechnol.*, 2013, **8**, 826.

131 Y. Tsuboi, F. Wang, D. Kozawa, K. Funahashi, S. Mouri, Y. Miyauchi, T. Takenobu and K. Matsuda, *Nanoscale*, 2015, **7**, 14476.

132 S. Bertolazzi, D. Krasnozhon and A. Kis, *ACS Nano*, 2013, **7**, 3246.

133 F. Withers, O. Del Pozo-Zamudio, A. Mishchenko, A. P. Rooney, A. Gholinia, K. Watanabe, T. Taniguchi, S. J. Haigh, A. K. Geim, A. I. Tartakovskii and K. S. Novoselov, *Nat. Mater.*, 2015, **14**, 301.

134 E. Pomerantseva and Y. Gogotsi, *Nat. Energy*, 2017, **2**, 17089.

135 M. A. Bissett, I. A. Kinloch and R. A. W. Dryfe, *ACS Appl. Mater. Interfaces*, 2015, **7**, 17388.

136 W. S. V. Lee, E. Peng, T. A. J. Loh, X. Huang and J. M. Xue, *Nanoscale*, 2016, **8**, 8042.

137 Y. Teng, H. Zhao, Z. Zhang, Z. Li, Q. Xia, Y. Zhang, L. Zhao, X. Du, Z. Du, P. Lv and K. Świerczek, *ACS Nano*, 2016, **10**, 8526.

138 L. Ci, L. Song, C. Jin, D. Jariwala, D. Wu, Y. Li, A. Srivastava, Z. F. Wang, K. Storr, L. Balicas, F. Liu and P. M. Ajayan, *Nat. Mater.*, 2010, **9**, 430.

139 Z. Liu, L. Ma, G. Shi, W. Zhou, Y. Gong, S. Lei, X. Yang, J. Zhang, J. Yu, K. P. Hackenberg, A. Babakhani, J.-C. Idrobo, R. Vajtai, J. Lou and P. M. Ajayan, *Nat. Nanotechnol.*, 2013, **8**, 119.

140 Y. Gong, G. Shi, Z. Zhang, W. Zhou, J. Jung, W. Gao, L. Ma, Y. Yang, S. Yang, G. You, R. Vajtai, Q. Xu, A. H. MacDonald, B. I. Yakobson, J. Lou, Z. Liu and P. M. Ajayan, *Nat. Comm.*, 2014, **5**, 3193.

141 X. Ling, Y. Lin, Q. Ma, Z. Wang, Y. Song, L. Yu, S. Huang, W. Fang, X. Zhang, A. L. Hsu, Y. Bie, Y.-H. Lee, Y. Zhu, L. Wu, J. Li, P. Jarillo-Herrero, M. Dresselhaus, T. Palacios and J. Kong, *Adv. Mater.*, 2016, **28**, 2322.

142 M. Zhao, Y. Ye, Y. Han, Y. Xia, H. Zhu, S. Wang, Y. Wang, D. A. Muller and X. Zhang, *Nat. Nanotechnol.*, 2016, **11**, 954.

143 M. H. D. Guimarães, H. Gao, Y. Han, K. Kang, S. Xie, C.-J. Kim, D. A. Muller, D. C. Ralph and J. Park, *ACS Nano*, 2016, **10**, 6392.

144 E. Bekyarova, M. E. Itkis, P. Ramesh, C. Berger, M. Sprinkle, W. A. de Heer and R. C. Haddon, *J. Am. Chem. Soc.*, 2009, **131**, 1336.

145 L.-H. Liu and M. Yan, *J. Mater. Chem.*, 2011, **21**, 3273.

146 A. Sinitskii, A. Dimiev, D. A. Corley, A. A. Fursina, D. V. Kosynkin and J. M. Tour, *ACS Nano*, 2010, **4**, 1949.

147 S. Niyogi, E. Bekyarova, M. E. Itkis, H. Zhang, K. Shepperd, J. Hicks, M. Sprinkle, C. Berger, C. N. Lau, W. A. Deheer, E. H. Conrad and R. C. Haddon, *Nano Lett.*, 2010, **10**, 4061.

148 H. T. Liu, S. M. Ryu, Z. Y. Chen, M. L. Steigerwald, C. Nuckolls and L. E. Brus, *J. Am. Chem. Soc.*, 2009, **131**, 17099.

149 V. Georgakilas, A. B. Bourlinos, R. Zboril, T. A. Steriotis, P. Dallas, A. K. Stubos and C. Trapalis, *Chem. Commun. (Cambridge, U. K.)*, 2010, **46**, 1766.

150 X. Zhang, L. Hou, A. Cnossen, A. C. Coleman, O. Ivashenko, P. Rudolf, B. J. van Wees, W. R. Browne and B. L. Feringa, *Chem. - Eur. J.*, 2011, **17**, 8957.

151 S. Vadukumpully, J. Gupta, Y. P. Zhang, G. Q. Xu and S. Valiyaveettil, *Nanoscale*, 2011, **3**, 303.

152 T. A. Strom, E. P. Dillon, C. E. Hamilton and A. R. Barron, *Chem. Commun. (Cambridge, U. K.)*, 2010, **46**, 4097.

153 X. Zhong, J. Jin, S. W. Li, Z. Y. Niu, W. Q. Hu, R. Li and J. T. Ma, *Chem. Commun. (Cambridge, U. K.)*, 2010, **46**, 7340.

154 C. Gómez-Navarro, R. T. Weitz, A. M. Bittner, M. Scolari, A. Mews, M. Burghard and K. Kern, *Nano Lett.*, 2007, **7**, 3499.

155 Y. Liu, J. Zhou, X. Zhang, Z. Liu, X. Wan, J. Tian, T. Wang and Y. Chen, *Carbon*, 2009, **47**, 3113.

156 D. Yu, Y. Yang, M. Durstock, J.-B. Baek and L. Dai, *ACS Nano*, 2010, **4**, 5633.

157 Y. F. Xu, Z. B. Liu, X. L. Zhang, Y. Wang, J. G. Tian, Y. Huang, Y. F. Ma, X. Y. Zhang and Y. S. Chen, *Adv. Mater.*, 2009, **21**, 1275.

158 J. Shen, M. Shi, B. Yan, H. Ma, N. Li, Y. Hu and M. Ye, *Colloids Surf., B*, 2010, **81**, 434.

159 F. Liu, J. Y. Choi and T. S. Seo, *Biosens. Bioelectron.*, 2010, **25**, 2361.

160 N. Mohanty and V. Berry, *Nano Lett.*, 2008, **8**, 4469.

161 Z. Liu, J. T. Robinson, X. M. Sun and H. J. Dai, *J. Am. Chem. Soc.*, 2008, **130**, 10876.

162 H. J. Salavagione, M. A. Gomez and G. Martinez, *Macromolecules*, 2009, **42**, 6331.

163 O. C. Compton, D. A. Dikin, K. W. Putz, L. C. Brinson and S. T. Nguyen, *Adv. Mater.*, 2010, **22**, 892.

164 H. R. Thomas, A. J. Marsden, M. Walker, N. R. Wilson and J. P. Rourke, *Encyclopedia of imaging science and technology*, 2014, **53**, 7613.

165 S. Chakraborty, S. Saha, V. R. Dhanak, K. Biswas, M. Barbezat, G. P. Terrasi and A. K. Chakraborty, *RSC Adv.*, 2016, **6**, 67916.

166 I. A. Vacchi, S. Guo, J. Raya, A. Bianco and C. Ménard-Moyon, *Chem. - Eur. J.*, 2020, **26**, 6591.

167 S. Guo, Y. Nishina, A. Bianco and C. Ménard-Moyon, *Angew. Chem., Int. Ed.*, 2020, **59**, 1542.

168 I. A. Vacchi, C. Spinato, J. Raya, A. Bianco and C. Ménard-Moyon, *Nanoscale*, 2016, **8**, 13714.

169 C. Shan, H. Yang, D. Han, Q. Zhang, A. Ivaska and L. Niu, *Langmuir*, 2009, **25**, 12030.

170 W. Yuan, A. Liu, L. Huang, C. Li and G. Shi, *Adv. Mater.*, 2013, **25**, 766.

171 N. Hu, Y. Wang, J. Chai, R. Gao, Z. Yang, E. S.-W. Kong and Y. Zhang, *Sens. Actuator B-Chem.*, 2012, **163**, 107.

172 N. L. Teradal, S. Marx, A. Morag and R. Jelinek, *J. Mater. Chem. C*, 2017, **5**, 1128.

173 R. Seenivasan, W.-J. Chang and S. Gunasekaran, *ACS Appl. Mater. Interfaces*, 2015, **7**, 15935.

174 C. J. Madadrang, H. Y. Kim, G. Gao, N. Wang, J. Zhu, H. Feng, M. Gorring, M. L. Kasner and S. Hou, *ACS Appl. Mater. Interfaces*, 2012, **4**, 1186.

175 S. H. Lee, D. R. Dreyer, J. An, A. Velamakanni, R. D. Piner, S. Park, Y. Zhu, S. O. Kim, C. W. Bielawski and R. S. Ruoff, *Macromol. Rapid Commun.*, 2010, **31**, 281.

176 B. Das, K. E. Prasad, U. Ramamurty and C. N. R. Rao, *Nanotechnology*, 2009, **20**.

177 M. Fang, K. G. Wang, H. B. Lu, Y. L. Yang and S. Nutt, *J. Mater. Chem.*, 2009, **19**, 7098.

178 T. Ramanathan, A. A. Abdala, S. Stankovich, D. A. Dikin, M. Herrera-Alonso, R. D. Piner, D. H. Adamson, H. C. Schniepp, X. Chen, R. S. Ruoff, S. T. Nguyen, I. A. Aksay, R. K. Prud'homme and L. C. Brinson, *Nat. Nanotechnol.*, 2008, **3**, 327.

179 G. Gonçalves, P. A. A. P. Marques, A. Barros-Timmons, I. Bdkin, M. K. Singh, N. Emami and J. Grácio, *J. Mater. Chem.*, 2010, **20**, 9927.

180 K. P. Pramoda, H. Hussain, H. M. Koh, H. R. Tan and C. B. He, *J. Polym. Sci., Part A: Polym. Chem.*, 2010, **48**, 4262.

181 Y. Yang, Y. Xie, L. Pang, M. Li, X. Song, J. Wen and H. Zhao, *Langmuir*, 2013, **29**, 10727.

182 Y. Li, M. Zhou, Y. Wang, Q. Pan, Q. Gong, Z. Xia and Y. Li, *Carbon*, 2019, **147**, 519.

183 R. Li, Y. Yang, D. Wu, K. Li, Y. Qin, Y. Tao and Y. Kong, *Chem. Commun. (Cambridge, U. K.)*, 2019, **55**, 1738.

184 S. K. Yadav, R. Kumar, A. K. Sundramoorthy, R. K. Singh and C. M. Koo, *RSC Adv.*, 2016, **6**, 52945.

185 Z.-F. Li, H. Zhang, Q. Liu, Y. Liu, L. Stanciu and J. Xie, *Carbon*, 2014, **71**, 257.

186 J. Lehn, *Science*, 1993, **260**, 1762.

187 X.-F. Zhang and X. Shao, *J. Photochem. Photobiol., A*, 2014, **278**, 69.

188 J. Wang, Z. Chen and B. Chen, *Environ. Sci. Technol.*, 2014, **48**, 4817.

189 Q. Su, S. Pang, V. Alijani, C. Li, X. Feng and K. Müllen, *Adv. Mater.*, 2009, **21**, 3191.

190 A. Schlierf, H. Yang, E. Gebremedhn, E. Treossi, L. Ortolani, L. Chen, A. Minoia, V. Morandi, P. Samorì, C. Casiraghi, D. Beljonne and V. Palermo, *Nanoscale*, 2013, **5**, 4205.

191 Z. Chen, Y. Wang, Y. Shang, A. Umar, P. Xie, Q. Qi and G. Zhou, *Sci. Rep.*, 2017, **7**, 2713.

192 S. Qu, M. Li, L. Xie, X. Huang, J. Yang, N. Wang and S. Yang, *ACS Nano*, 2013, **7**, 4070.

193 X. Tian, J. Xu and X. Wang, *J. Phys. Chem. B*, 2010, **114**, 11377.

194 S. M. Kozlov, F. Viñes and A. Görling, *Adv. Mater.*, 2011, **23**, 2638.

195 W. Zhang, C.-T. Lin, K.-K. Liu, T. Tite, C.-Y. Su, C.-H. Chang, Y.-H. Lee, C.-W. Chu, K.-H. Wei, J.-L. Kuo and L.-J. Li, *ACS Nano*, 2011, **5**, 7517.

196 W. Chen, S. Chen, D. C. Qi, X. Y. Gao and A. T. S. Wee, *J. Am. Chem. Soc.*, 2007, **129**, 10418.

197 J. Mao, H. Zhang, Y. Jiang, Y. Pan, M. Gao, W. Xiao and H. J. Gao, *J. Am. Chem. Soc.*, 2009, **131**, 14136.

198 S. K. Hämäläinen, M. Stepanova, R. Drost, P. Liljeroth, J. Lahtinen and J. Sainio, *J. Phys. Chem. C*, 2012, **116**, 20433.

199 Y. Xu, L. Zhao, H. Bai, W. Hong, C. Li and G. Shi, *J. Am. Chem. Soc.*, 2009, **131**, 13490.

200 B.-P. Jiang, L.-F. Hu, D.-J. Wang, S.-C. Ji, X.-C. Shen and H. Liang, *J. Mater. Chem. B*, 2014, **2**, 7141.

201 Y. Guo, L. Deng, J. Li, S. Guo, E. Wang and S. Dong, *ACS Nano*, 2011, **5**, 1282.

202 R. Verdejo, M. M. Bernal, L. J. Romasanta and M. A. Lopez-Manchado, *J. Mater. Chem.*, 2011, **21**, 3301.

203 J. Liu, J. Tang and J. J. Gooding, *J. Mater. Chem.*, 2012, **22**, 12435.

204 B. Li, A. V. Klekachev, M. Cantoro, C. Huyghebaert, A. Stesmans, I. Asselberghs, S. De Gendt and S. De Feyter, *Nanoscale*, 2013, **5**, 9640.

205 R. Phillipson, C. J. Lockhart de la Rosa, J. Teyssandier, P. Walke, D. Waghray, Y. Fujita, J. Adisoejoso, K. S. Mali, I. Asselberghs, C. Huyghebaert, H. Uji-i, S. De Gendt and S. De Feyter, *Nanoscale*, 2016, **8**, 20017.

206 M. Gobbi, S. Bonacchi, J. X. Lian, Y. Liu, X.-Y. Wang, M.-A. Stoeckel, M. A. Squillaci, G. D'Avino, A. Narita, K. Müllen, X. Feng, Y. Olivier, D. Beljonne, P. Samorì and E. Orgiu, *Nat. Comm.*, 2017, **8**, 14767.

207 M. Gobbi, S. Bonacchi, J. X. Lian, A. Vercouter, S. Bertolazzi, B. Zyska, M. Timpel, R. Tatti, Y. Olivier, S. Hecht, M. V. Nardi, D. Beljonne, E. Orgiu and P. Samorì, *Nat. Comm.*, 2018, **9**, 2661.

208 M. Gobbi, A. Galanti, M.-A. Stoeckel, B. Zyska, S. Bonacchi, S. Hecht and P. Samorì, *Nat. Comm.*, 2020, **11**, 4731.

209 T. Premkumar and K. E. Geckeler, *Prog. Polym. Sci.*, 2012, **37**, 515.

210 B. G. Choi, H. Park, T. J. Park, M. H. Yang, J. S. Kim, S.-Y. Jang, N. S. Heo, S. Y. Lee, J. Kong and W. H. Hong, *ACS Nano*, 2010, **4**, 2910.

211 H. Bai, Y. Xu, L. Zhao, C. Li and G. Shi, *Chem. Commun. (Cambridge, U. K.)*, 2009, **13**, 1667.

212 D.-W. Wang, F. Li, J. Zhao, W. Ren, Z.-G. Chen, J. Tan, Z.-S. Wu, I. Gentle, G. Q. Lu and H.-M. Cheng, *ACS Nano*, 2009, **3**, 1745.

213 A. J. Patil, J. L. Vickery, T. B. Scott and S. Mann, *Adv. Mater.*, 2009, **21**, 3159.

214 J. Liu, Y. Li, Y. Li, J. Li and Z. Deng, *J. Mater. Chem.*, 2010, **20**, 900.

215 Y. Xu, Q. Wu, Y. Sun, H. Bai and G. Shi, *ACS Nano*, 2010, **4**, 7358.

216 Y. Liang, D. Wu, X. Feng and K. Müllen, *Adv. Mater.*, 2009, **21**, 1679.

217 X. Zhao, Q. Zhang, Y. Hao, Y. Li, Y. Fang and D. Chen, *Macromolecules*, 2010, **43**, 9411.

218 M. Hu and B. Mi, *J. Membr. Sci.*, 2014, **469**, 80.

219 J. Zou and F. Kim, *Nat. Comm.*, 2014, **5**, 5254.

220 D. Zhang, J. Tong and B. Xia, *Sens. Actuator B-Chem.*, 2014, **197**, 66.

221 S. Dervin, D. D. Dionysiou and S. C. Pillai, *Nanoscale*, 2016, **8**, 15115.

222 B. F. Machado and P. Serp, *Catal. Sci. Technol.*, 2012, **2**, 54.

223 Y. Zhang, T. R. Nayak, H. Hong and W. Cai, *Nanoscale*, 2012, **4**, 3833.

224 S. Syama and P. V. Mohanan, *Nano-Micro Lett.*, 2019, **11**.

225 M. Haniff Wahid, U. H. Stroeher, E. Eroglu, X. Chen, K. Vimalanathan, C. L. Raston and R. A. Boulos, *J. Colloid Interface Sci.*, 2015, **443**, 88.

226 S. Zhu, J. Zhang, C. Qiao, S. Tang, Y. Li, W. Yuan, B. Li, L. Tian, F. Liu, R. Hu, H. Gao, H. Wei, H. Zhang, H. Sun and B. Yang, *Chem. Commun. (Cambridge, U. K.)*, 2011, **47**, 6858.

227 J. Peng, W. Gao, B. K. Gupta, Z. Liu, R. Romero-Aburto, L. Ge, L. Song, L. B. Alemany, X. Zhan, G. Gao, S. A. Vithayathil, B. A. Kaipparettu, A. A. Marti, T. Hayashi, J.-J. Zhu and P. M. Ajayan, *Nano Lett.*, 2012, **12**, 844.

228 G. Konstantatos, M. Badioli, L. Gaudreau, J. Osmond, M. Bernechea, F. P. G. de Arquer, F. Gatti and F. H. L. Koppens, *Nat. Nanotechnol.*, 2012, **7**, 363.

229 M.-H. Jung and M.-J. Chu, *Nanoscale*, 2014, **6**, 9241.

230 F. Schedin, A. K. Geim, S. V. Morozov, E. W. Hill, P. Blake, M. I. Katsnelson and K. S. Novoselov, *Nat. Mater.*, 2007, **6**, 652.

231 C. Wang, L. Yin, L. Zhang, D. Xiang and R. Gao, *Sensors*, 2010, **10**, 2088.

232 W. Yang, P. Wan, X. Zhou, J. Hu, Y. Guan and L. Feng, *ACS Appl. Mater. Interfaces*, 2014, **6**, 21093.

233 L. Al-Mashat, K. Shin, K. Kalantar-zadeh, J. D. Plessis, S. H. Han, R. W. Kojima, R. B. Kaner, D. Li, X. Gou, S. J. Ippolito and W. Wlodarski, *J. Phys. Chem. C*, 2010, **114**, 16168.

234 X. Huang, N. Hu, R. Gao, Y. Yu, Y. Wang, Z. Yang, E. Siu-Wai Kong, H. Wei and Y. Zhang, *J. Mater. Chem.*, 2012, **22**, 22488.

235 H. Bai, K. Sheng, P. Zhang, C. Li and G. Shi, *J. Mater. Chem.*, 2011, **21**, 18653.

236 T. Zhang, Z. Cheng, Y. Wang, Z. Li, C. Wang, Y. Li and Y. Fang, *Nano Lett.*, 2010, **10**, 4738.

237 H. G. Sudibya, Q. He, H. Zhang and P. Chen, *ACS Nano*, 2011, **5**, 1990.

238 J. H. An, S. J. Park, O. S. Kwon, J. Bae and J. Jang, *ACS Nano*, 2013, **7**, 10563.

239 M. Li, X. Zhou, W. Ding, S. Guo and N. Wu, *Biosens. Bioelectron.*, 2013, **41**, 889.

240 Y. Wen, F. Xing, S. He, S. Song, L. Wang, Y. Long, D. Li and C. Fan, *Chem. Commun. (Cambridge, U. K.)*, 2010, **46**, 2596.

241 S. Guo, D. Wen, Y. Zhai, S. Dong and E. Wang, *ACS Nano*, 2010, **4**, 3959.

242 J. Luo, S. Jiang, H. Zhang, J. Jiang and X. Liu, *Anal. Chim. Acta*, 2012, **709**, 47.

243 D. Cohen-Tanugi and J. C. Grossman, *Nano Lett.*, 2012, **12**, 3602.

244 M. E. Suk and N. R. Aluru, *J. Phys. Chem. Lett.*, 2010, **1**, 1590.

245 S. P. Surwade, S. N. Smirnov, I. V. Vlassiouk, R. R. Unocic, G. M. Veith, S. Dai and S. M. Mahurin, *Nat. Nanotechnol.*, 2015, **10**, 459.

246 A. Nicolaï, B. G. Sumpter and V. Meunier, *Phys. Chem. Chem. Phys.*, 2014, **16**, 8646.

247 R. R. Nair, H. A. Wu, P. N. Jayaram, I. V. Grigorieva and A. K. Geim, *Science*, 2012, **335**, 442.

248 D. Pakulski, W. Czepa, S. D. Buffa, A. Ciesielski and P. Samorì, *Adv. Funct. Mater.*, 2019, **30**, 1902394.

249 F. Perreault, A. Fonseca de Faria and M. Elimelech, *Chem. Soc. Rev.*, 2015, **44**, 5861.

250 M. Hu and B. Mi, *Environ. Sci. Technol.*, 2013, **47**, 3715.

251 J.-Q. Hu, Z. Liu, Z.-H. Chen, Q.-W. Cai, X.-Y. Li, R. Xie, X.-J. Ju, W. Wang and L.-Y. Chu, *Ind. Eng. Chem. Res.*, 2020, **59**, 12441.

252 S. J. Gao, H. Qin, P. Liu and J. Jin, *J. Mater. Chem. A*, 2015, **3**, 6649.

253 Y. Han, Y. Jiang and C. Gao, *ACS Appl. Mater. Interfaces*, 2015, **7**, 8147.

254 A. Hassanpour, S. Nahar, X. Tong, G. Zhang, M. A. Gauthier and S. Sun, *Desalination*, 2020, **475**, 114174.

255 K. Zhang, V. Dwivedi, C. Chi and J. Wu, *J. Hazard. Mater.*, 2010, **182**, 162.

256 X. Luo, C. Wang, S. Luo, R. Dong, X. Tu and G. Zeng, *Chem. Eng. J. (Lausanne)*, 2012, **187**, 45.

257 X. Guo, B. Du, Q. Wei, J. Yang, L. Hu, L. Yan and W. Xu, *J. Hazard. Mater.*, 2014, **278**, 211.

258 H. Jabeen, V. Chandra, S. Jung, J. W. Lee, K. S. Kim and S. B. Kim, *Nanoscale*, 2011, **3**, 3583.

259 V. Chandra and K. S. Kim, *Chem. Commun. (Cambridge, U. K.)*, 2011, **47**, 3942.

260 A. Docoslis, S. Li, X. Lu, Y. Xue, J. Lei, T. Zheng and C. Wang, *PLoS One*, 2012, **7**, e43328.

261 L. Fan, C. Luo, M. Sun, H. Qiu and X. Li, *Colloids Surf., B*, 2013, **103**, 601.

262 N. Zhang, H. Qiu, Y. Si, W. Wang and J. Gao, *Carbon*, 2011, **49**, 827.

263 A. Shahzad, W. Miran, K. Rasool, M. Nawaz, J. Jang, S.-R. Lim and D. S. Lee, *RSC Adv.*, 2017, **7**, 9764.

264 L. Fan, C. Luo, X. Li, F. Lu, H. Qiu and M. Sun, *J. Hazard. Mater.*, 2012, **215-216**, 272.

265 X. Dong, J. Chen, Y. Ma, J. Wang, M. B. Chan-Park, X. Liu, L. Wang, W. Huang and P. Chen, *Chem. Commun. (Cambridge, U. K.)*, 2012, **48**, 10660.

266 T.-D. Nguyen-Phan, V. H. Pham, E. J. Kim, E.-S. Oh, S. H. Hur, J. S. Chung, B. Lee and E. W. Shin, *Appl. Surf. Sci.*, 2012, **258**, 4551.

267 B. Li, H. Cao and G. Yin, *J. Mater. Chem.*, 2011, **21**, 13765.

268 B. Xia, Y. Yan, X. Wang and X. W. Lou, *Mater. Horiz.*, 2014, **1**, 379.

269 X. Li and L. Zhi, *Chem. Soc. Rev.*, 2018, **47**, 3189.

270 Z. Yang, H. Nie, X. a. Chen, X. Chen and S. Huang, *J. Power Sources*, 2013, **236**, 238.

271 G. Williams, B. Seger and P. V. Kamat, *ACS Nano*, 2008, **2**, 1487.

272 X.-Y. Zhang, H.-P. Li, X.-L. Cui and Y. Lin, *J. Mater. Chem.*, 2010, **20**, 2801.

273 Q. Xiang, J. Yu and M. Jaroniec, *Nanoscale*, 2011, **3**, 3670.

274 H. Zhang, X. Lv, Y. Li, Y. Wang and J. Li, *ACS Nano*, 2009, **4**, 380.

275 J. S. Lee, K. H. You and C. B. Park, *Adv. Mater.*, 2012, **24**, 1084.

276 C. Chen, W. Cai, M. Long, B. Zhou, Y. Wu, D. Wu and Y. Feng, *ACS Nano*, 2010, **4**, 6425.

277 J. Liu, H. Bai, Y. Wang, Z. Liu, X. Zhang and D. D. Sun, *Adv. Funct. Mater.*, 2010, **20**, 4175.

278 E. Yoo, T. Okata, T. Akita, M. Kohyama, J. Nakamura and I. Honma, *Nano Lett.*, 2009, **9**, 2255.

279 Y.-P. Xiao, S. Wan, X. Zhang, J.-S. Hu, Z.-D. Wei and L.-J. Wan, *Chem. Commun. (Cambridge, U. K.)*, 2012, **48**, 10331.

280 J. N. Tiwari, K. C. Kemp, K. Nath, R. N. Tiwari, H.-G. Nam and K. S. Kim, *ACS Nano*, 2013, **7**, 9223.

281 J. N. Tiwari, K. Nath, S. Kumar, R. N. Tiwari, K. C. Kemp, N. H. Le, D. H. Youn, J. S. Lee and K. S. Kim, *Nat. Comm.*, 2013, **4**, 2221.

282 Y. Liang, Y. Li, H. Wang, J. Zhou, J. Wang, T. Regier and H. Dai, *Nat. Mater.*, 2011, **10**, 780.

283 Y. Li, H. Wang, L. Xie, Y. Liang, G. Hong and H. Dai, *J. Am. Chem. Soc.*, 2011, **133**, 7296.

284 X. Zheng, J. Xu, K. Yan, H. Wang, Z. Wang and S. Yang, *Chem. Mater.*, 2014, **26**, 2344.

285 R. K. Biroju, D. Das, R. Sharma, S. Pal, L. P. L. Mawlong, K. Bhorkar, P. K. Giri, A. K. Singh and T. N. Narayanan, *ACS Energy Lett.*, 2017, **2**, 1355.

286 A. Ruiz, M. A. Lucherelli, D. Murera, D. Lamon, C. Ménard-Moyon and A. Bianco, *Carbon*, 2020, **170**, 347.

287 A. Bianco, *Angew. Chem., Int. Ed.*, 2013, **52**, 4986.

288 X. Sun, Z. Liu, K. Welsher, J. T. Robinson, A. Goodwin, S. Zaric and H. Dai, *Nano Res.*, 2008, **1**, 203.

289 Z. Liu, J. T. Robinson, X. Sun and H. Dai, *J. Am. Chem. Soc.*, 2008, **130**, 10876.

290 C. Wang, J. Li, C. Amatore, Y. Chen, H. Jiang and X.-M. Wang, *Angew. Chem., Int. Ed.*, 2011, **50**, 11644.

291 M. de Sousa, L. A. Visani de Luna, L. C. Fonseca, S. Giorgio and O. L. Alves, *ACS Appl. Nano Mater.*, 2018, **1**, 922.

292 G. Reina, J. M. González-Domínguez, A. Criado, E. Vázquez, A. Bianco and M. Prato, *Chem. Soc. Rev.*, 2017, **46**, 4400.

293 K. Yang, S. Zhang, G. Zhang, X. Sun, S.-T. Lee and Z. Liu, *Nano Lett.*, 2010, **10**, 3318.

294 X. Shi, H. Gong, Y. Li, C. Wang, L. Cheng and Z. Liu, *Biomaterials*, 2013, **34**, 4786.

295 P. Rong, K. Yang, A. Srivastan, D. O. Kiesewetter, X. Yue, F. Wang, L. Nie, A. Bhirde, Z. Wang, Z. Liu, G. Niu, W. Wang and X. Chen, *Theranostics*, 2014, **4**, 229.

296 L. Feng, S. Zhang and Z. Liu, *Nanoscale*, 2011, **3**, 1252.

297 M. A. Lucherelli, Y. Yu, G. Reina, G. Abellán, E. Miyako and A. Bianco, *Angew. Chem.*, 2020, **132**, 14138.

298 Y. Liang, W.-H. Lai, Z. Miao and S.-L. Chou, *Small*, 2018, **14**, 1702514.

299 E. Yoo, J. Kim, E. Hosono, H.-s. Zhou, T. Kudo and I. Honma, *Nano Lett.*, 2008, **8**, 2277.

300 S.-M. Paek, E. Yoo and I. Honma, *Nano Lett.*, 2009, **9**, 72.

301 X. Zhou, L.-J. Wan and Y.-G. Guo, *Adv. Mater.*, 2013, **25**, 2152.

302 D. Wang, D. Choi, J. Li, Z. Yang, Z. Nie, R. Kou, D. Hu, C. Wang, L. V. Saraf, J. Zhang, I. A. Aksay and J. Liu, *ACS Nano*, 2009, **3**, 907.

303 H. Wang, L.-F. Cui, Y. Yang, H. Sanchez Casalongue, J. T. Robinson, Y. Liang, Y. Cui and H. Dai, *J. Am. Chem. Soc.*, 2010, **132**, 13978.

304 J. Luo, X. Zhao, J. Wu, H. D. Jang, H. H. Kung and J. Huang, *J. Phys. Chem. Lett.*, 2012, **3**, 1824.

305 D. Y. W. Yu, P. V. Prikhodchenko, C. W. Mason, S. K. Batabyal, J. Gun, S. Sladkevich, A. G. Medvedev and O. Lev, *Nat. Comm.*, 2013, **4**, 2922.

306 M. Liu, P. Zhang, Z. Qu, Y. Yan, C. Lai, T. Liu and S. Zhang, *Nat. Comm.*, 2019, **10**, 3917.

307 J. Yan, Z. Fan, T. Wei, W. Qian, M. Zhang and F. Wei, *Carbon*, 2010, **48**, 3825.

308 L. Peng, X. Peng, B. Liu, C. Wu, Y. Xie and G. Yu, *Nano Lett.*, 2013, **13**, 2151.

309 B. Xie, Y. Chen, M. Yu, T. Sun, L. Lu, T. Xie, Y. Zhang and Y. Wu, *Carbon*, 2016, **99**, 35.

310 H. Zhang, X. Yu, D. Guo, B. Qu, M. Zhang, Q. Li and T. Wang, *ACS Appl. Mater. Interfaces*, 2013, **5**, 7335.

311 Q. Wu, Y. Xu, Z. Yao, A. Liu and G. Shi, *ACS Nano*, 2010, **4**, 1963.

312 J. An, J. Liu, Y. Zhou, H. Zhao, Y. Ma, M. Li, M. Yu and S. Li, *J. Phys. Chem. C*, 2012, **116**, 19699.

313 S. Witomska, Z. Liu, W. Czepa, A. Aliprandi, D. Pakulski, P. Pawluć, A. Ciesielski and P. Samorì, *J. Am. Chem. Soc.*, 2018, **141**, 482.

314 M. Morales-Masis, S. De Wolf, R. Woods-Robinson, J. W. Ager and C. Ballif, *Adv. Electron. Mater.*, 2017, **3**, 1600529.

315 M. Pandey, Z. Wang, G. Kapil, A. K. Baranwal, D. Hirotani, K. Hamada and S. Hayase, *Adv. Eng. Mater.*, 2019, **21**, 1900288.

316 N. N. Rosli, M. A. Ibrahim, N. Ahmad Ludin, M. A. Mat Teridi and K. Sopian, *Renewable Sustainable Energy Rev.*, 2019, **99**, 83.

317 K. Rana, J. Singh and J.-H. Ahn, *J. Mater. Chem. C*, 2014, **2**, 2646.

318 Y. Ma and L. Zhi, *Small Methods*, 2019, **3**, 1800199.

319 H. Bi, F. Huang, J. Liang, X. Xie and M. Jiang, *Adv. Mater.*, 2011, **23**, 3202.

320 S. Bae, H. Kim, Y. Lee, X. Xu, J.-S. Park, Y. Zheng, J. Balakrishnan, T. Lei, H. Ri Kim, Y. I. Song, Y.-J. Kim, K. S. Kim, B. Özyilmaz, J.-H. Ahn, B. H. Hong and S. Iijima, *Nat. Nanotechnol.*, 2010, **5**, 574.

321 X. Lin, J. Jia, N. Yousefi, X. Shen and J.-K. Kim, *J. Mater. Chem. C*, 2013, **1**, 6869.

322 X. Miao, S. Tongay, M. K. Petterson, K. Berke, A. G. Rinzler, B. R. Appleton and A. F. Hebard, *Nano Lett.*, 2012, **12**, 2745.

323 C.-L. Hsu, C.-T. Lin, J.-H. Huang, C.-W. Chu, K.-H. Wei and L.-J. Li, *ACS Nano*, 2012, **6**, 5031.

324 Z. Liu, J. Li, Z.-H. Sun, G. Tai, S.-P. Lau and F. Yan, *ACS Nano*, 2011, **6**, 810.

325 B. H. Lee, J.-H. Lee, Y. H. Kahng, N. Kim, Y. J. Kim, J. Lee, T. Lee and K. Lee, *Adv. Funct. Mater.*, 2014, **24**, 1847.

326 G. Zhu, L. Pan, T. Lu, T. Xu and Z. Sun, *J. Mater. Chem.*, 2011, **21**, 14869.

327 H. Dong, Z. Wu, Y. Jiang, W. Liu, X. Li, B. Jiao, W. Abbas and X. Hou, *ACS Appl. Mater. Interfaces*, 2016, **8**, 31212.

328 N. Li, S. Oida, G. S. Tulevski, S.-J. Han, J. B. Hannon, D. K. Sadana and T.-C. Chen, *Nat. Comm.*, 2013, **4**, 3294.

329 J. Meyer, P. R. Kidambi, B. C. Bayer, C. Weijtens, A. Kuhn, A. Centeno, A. Pesquera, A. Zurutuza, J. Robertson and S. Hofmann, *Sci. Rep.*, 2014, **4**, 5380.

330 H. Chang, G. Wang, A. Yang, X. Tao, X. Liu, Y. Shen and Z. Zheng, *Adv. Funct. Mater.*, 2010, **20**, 2893.

331 I. N. Kholmanov, C. W. Magnuson, R. Piner, J. Y. Kim, A. E. Aliev, C. Tan, T. Y. Kim, A. A. Zakhidov, G. Sberveglieri, R. H. Baughman and R. S. Ruoff, *Adv. Mater.*, 2015, **27**, 3053.

332 F. Xia, T. Mueller, Y.-m. Lin, A. Valdes-Garcia and P. Avouris, *Nat. Nanotechnol.*, 2009, **4**, 839.

333 F. H. L. Koppens, T. Mueller, P. Avouris, A. C. Ferrari, M. S. Vitiello and M. Polini, *Nat. Nanotechnol.*, 2014, **9**, 780.

334 W. J. Yu, Y. Liu, H. Zhou, A. Yin, Z. Li, Y. Huang and X. Duan, *Nat. Nanotechnol.*, 2013, **8**, 952.

335 Z. Ni, L. Ma, S. Du, Y. Xu, M. Yuan, H. Fang, Z. Wang, M. Xu, D. Li, J. Yang, W. Hu, X. Pi and D. Yang, *ACS Nano*, 2017, **11**, 9854.

336 S. J. Kim, W. Song, S. Kim, M.-A. Kang, S. Myung, S. Sook Lee, J. Lim and K.-S. An, *Nanotechnology*, 2016, **27**, 075709.

337 K. K. Manga, J. Wang, M. Lin, J. Zhang, M. Nesladek, V. Nalla, W. Ji and K. P. Loh, *Adv. Mater.*, 2012, **24**, 1697.

338 J. Du and H.-M. Cheng, *Macromol. Chem. Phys.*, 2012, **213**, 1060.

339 G. Shi, S. Araby, C. T. Gibson, Q. Meng, S. Zhu and J. Ma, *Adv. Funct. Mater.*, 2018, **28**, 1706705.

340 V. Palermo, I. A. Kinloch, S. Ligi and N. M. Pugno, *Adv. Mater.*, 2016, **28**, 6232.

341 I. A. Kinloch, J. Suhr, J. Lou, R. J. Young and P. M. Ajayan, *Science*, 2018, **362**, 547.

342 C. C. Chusuei and D. W. Goodman, in *Encyclopedia of Physical Science and Technology*, 2002, vol. 17.

343 J. M. Hollander and W. L. Jolly, *Acc. Chem. Res.*, 1970, **3**, 193.

344 V. Balzani, P. Ceroni and A. Juris, *Photochemistry and photophysics: concepts, research, applications*, John Wiley & Sons, 2014.

345 G. G. Hammes, *Spectroscopy for the biological sciences*, John Wiley & Sons, 2005.

346 D. C. Harris and M. D. Bertolucci, *Symmetry and spectroscopy : an introduction to vibrational and electronic spectroscopy*, Dover Publications, New York, 1989.

347 G. D. Christian, *Analytical chemistry*, Wiley, Hoboken, NJ, 6th edn., 2004.

348 D. A. Skoog, F. J. Holler and S. R. Crouch, *Principles of instrumental analysis*, Thomson Brooks/Cole, Belmont, CA, 6th edn., 2007.

349 B. E. Warren, *X-ray diffraction*, Dover, New York, Facsim. ed. edn., 1990.

350 J. H. Robertson, *Acta Crystallogr., Sect. A*, 1979, **35**, 350.

351 S. E. Dann, *Reactions and characterization of solids*, Wiley-Interscience, New York, 2002.

352 N. Saadatkhah, A. Carillo Garcia, S. Ackermann, P. Leclerc, M. Latifi, S. Samih, G. S. Patience and J. Chaouki, *Can. J. Chem. Eng.*, 2019, **98**, 34.

353 A. W. Coats and J. P. Redfern, *Analyst*, 1963, **88**, 906.

354 T. Sunaoshi, K. Kaji, Y. Orai, C. T. Schamp and E. Voelkl, *Microsc. Microanal.*, 2016, **22**, 604.

355 W. Zhou, R. Apkarian, Z. L. Wang and D. Joy, 2006, DOI: 10.1007/978-0-387-39620-0_1, 1.

356 B. Cheney, ed. M. E. d. S. J. S. University, Materials Engineering department San Jose State University 2007.

357 in *MyScope training for advanced research*, ed. M. Australia, MyScope, 2014.

358 H.-J. Butt, B. Cappella and M. Kappl, *Surf. Sci. Rep.*, 2005, **59**, 1.

359 S. Bradbury, *An introduction to the optical microscope*, Oxford University Press ; Royal Microscopical Society, Oxford ; New York, Rev. edn., 1988.

360 M. W. Davidson and M. Abramowitz, *Encyclopedia of imaging science and technology*, 2002.

361 P. D. Rack and J. Fitz-Geral, *Optical microscopy*, 1987.

362 M. Song, D. S. You, K. Lim, S. Park, S. Jung, C. S. Kim, D.-H. Kim, D.-G. Kim, J.-K. Kim, J. Park, Y.-C. Kang, J. Heo, S.-H. Jin, J. H. Park and J.-W. Kang, *Adv. Funct. Mater.*, 2013, **23**, 4177.

363 S. Zhao, F. Han, J. Li, X. Meng, W. Huang, D. Cao, G. Zhang, R. Sun and C.-P. Wong, *Small*, 2018, **14**, 1800047.

364 V. B. Nam and D. Lee, *Nanomaterials*, 2016, **6**.

365 D. V. Ravi Kumar, I. Kim, Z. Zhong, K. Kim, D. Lee and J. Moon, *Phys. Chem. Chem. Phys.*, 2014, **16**, 22107.

366 Y. Chang, M. L. Lye and H. C. Zeng, *Langmuir*, 2005, **21**, 3746.

367 A. R. Rathmell, S. M. Bergin, Y.-L. Hua, Z.-Y. Li and B. J. Wiley, *Adv. Mater.*, 2010, **22**, 3558.

368 Y. Shi, H. Li, L. Chen and X. Huang, *Sci. Technol. Adv. Mater.*, 2005, **6**, 761.

369 E. Ye, S.-Y. Zhang, S. Liu and M.-Y. Han, *Chem. - Eur. J.*, 2011, **17**, 3074.

370 D. Zhang, R. Wang, M. Wen, D. Weng, X. Cui, J. Sun, H. Li and Y. Lu, *J. Am. Chem. Soc.*, 2012, **134**, 14283.

371 H. Guo, N. Lin, Y. Chen, Z. Wang, Q. Xie, T. Zheng, N. Gao, S. Li, J. Kang, D. Cai and D.-L. Peng, *Sci. Rep.*, 2013, **3**.

372 Z. Yin, C. Lee, S. Cho, J. Yoo, Y. Piao and Y. S. Kim, *Small*, 2014, **10**, 5047.

373 F. Cui, Y. Yu, L. Dou, J. Sun, Q. Yang, C. Schildknecht, K. Schierle-Arndt and P. Yang, *Nano Lett.*, 2015, **15**, 7610.

374 M. Mohl, P. Pusztai, A. Kukovecz, Z. Konya, J. Kukkola, K. Kordas, R. Vajtai and P. M. Ajayan, *Langmuir*, 2010, **26**, 16496.

375 M. Jin, G. He, H. Zhang, J. Zeng, Z. Xie and Y. Xia, *Angew. Chem., Int. Ed.*, 2011, **50**, 10560.

376 Y. Sakai, Y. Sadaoka and M. Matsuguchi, *Sens. Actuator B-Chem.*, 1996, **35**, 85.

377 D. Zhang, J. Tong, B. Xia and Q. Xue, *Sens. Actuator B-Chem.*, 2014, **203**, 263.

378 U. Kang and K. D. Wise, *IEEE Trans. Electron Devices*, 2000, **47**, 702.

379 Z. Chen and C. Lu, *Sens. Lett.*, 2005, **3**, 274.

380 Q. Kuang, C. Lao, Z. L. Wang, Z. Xie and L. Zheng, *J. Am. Chem. Soc.*, 2007, **129**, 6070.

381 H.-W. Chen, R.-J. Wu, K.-H. Chan, Y.-L. Sun and P.-G. Su, *Sens. Actuator B-Chem.*, 2005, **104**, 80.

382 S. Borini, R. White, D. Wei, M. Astley, S. Haque, E. Spigone, N. Harris, J. Kivioja and T. Ryhänen, *ACS Nano*, 2013, **7**, 11166.

383 I. Jung, D. Dikin, S. Park, W. Cai, S. L. Mielke and R. S. Ruoff, *J. Phys. Chem. C*, 2008, **112**, 20264.

384 Y. Yao, X. Chen, J. Zhu, B. Zeng, Z. Wu and X. Li, *Nanoscale Res. Lett.*, 2012, **7**, 363.

385 Y. Tai, T. K. Bera, G. Lubineau and Z. Yang, *J. Mater. Chem. C*, 2017, **5**, 3848.

386 W. Yuan and G. Shi, *J. Mater. Chem. A*, 2013, **1**, 10078.

387 K. Rathi and K. Pal, *ACS Omega*, 2017, **2**, 842.

388 G. Naik and S. Krishnaswamy, *Graphene*, 2016, **5**, 1.

389 S. Papamatthaiou, D. P. Argyropoulos, F. Farmakis, A. Masurkar, K. Alexandrou, I. Kymissis and N. Georgoulas, *Procedia Eng.*, 2016, **168**, 301.

390 S. H. Hwang, D. Kang, R. S. Ruoff, H. S. Shin and Y. B. Park, *ACS Nano*, 2014, **8**, 6739.

391 H. C. Bi, K. B. Yin, X. Xie, J. Ji, S. Wan, L. T. Sun, M. Terrones and M. S. Dresselhaus, *Sci. Rep.*, 2013, **3**, 2714.

392 M. Tang, C. Zhang, J. Y. Zhang, Q. L. Zhao, Z. L. Hou and K. T. Zhan, *Phys. Status Solidi A*, 2020, **217**.

393 S. G. Kim, S. S. Lee, E. Lee, J. Yoon and H. S. Lee, *RSC Adv.*, 2015, **5**, 102567.

394 D. T. Phan and G. S. Chung, *Sens. Actuator B-Chem.*, 2015, **220**, 1050.

395 S.-W. Lee, B. I. Choi, J. C. Kim, S.-B. Woo, Y.-G. Kim, S. Kwon, J. Yoo and Y.-S. Seo, *Sens. Actuator B-Chem.*, 2016, **237**, 575.

396 K. D. Park, R. Liu and H. Kohn, *Chem. Biol.*, 2009, **16**, 763.

397 H. Kim, Y. J. Kang, E. S. Jeong, S. Kang and K. T. Kim, *ACS Macro Lett.*, 2012, **1**, 1194.

398 L. Greenspan, *J. Res. Natl. Bur. Stand. Sect. A Phys. Chem.*, 1977, **81 A**, 89.

399 J. P. M. Jämbeck and A. P. Lyubartsev, *J. Phys. Chem. B*, 2014, **118**, 3793.

400 Z. E. Hughes, S. M. Tomásio and T. R. Walsh, *Nanoscale*, 2014, **6**, 5438.

401 V. A. Ngo, I. Kim, T. W. Allen and S. Y. Noskov, *J. Chem. Theory Comput.*, 2016, **12**, 1000.

402 D. R. Dreyer, H.-P. Jia and C. W. Bielawski, *Angew. Chem., Int. Ed.*, 2010, **49**, 6813.

403 X. Zhang, A. Ciesielski, F. Richard, P. Chen, E. A. Prasetyanto, L. De Cola and P. Samorì, *Small*, 2016, **12**, 1044.

404 Y. Lin, J. Jin and M. Song, *J. Mater. Chem.*, 2011, **21**, 3455.

405 T. Kuila, S. Bose, A. K. Mishra, P. Khanra, N. H. Kim and J. H. Lee, *Prog. Mater. Sci.*, 2012, **57**, 1061.

406 D. R. Dreyer, A. D. Todd and C. W. Bielawski, *Chem. Soc. Rev.*, 2014, **43**, 5288.

407 G. Wang, X. Shen, B. Wang, J. Yao and J. Park, *Carbon*, 2009, **47**, 1359.

408 Y. Zhao, H. Ding and Q. Zhong, *Appl. Surf. Sci.*, 2012, **258**, 4301.

409 W. Li, X.-Z. Tang, H.-B. Zhang, Z.-G. Jiang, Z.-Z. Yu, X.-S. Du and Y.-W. Mai, *Carbon*, 2011, **49**, 4724.

410 O. M. Slobodian, P. M. Lytvyn, A. S. Nikolenko, V. M. Naseka, O. Y. Khyzhun, A. V. Vasin, S. V. Sevostianov and A. N. Nazarov, *Nanoscale Res. Lett.*, 2018, **13**, 1.

411 E. Tegou, G. Pseiropoulos, M. K. Filippidou and S. Chatzandroulis, *Microelectron. Eng.*, 2016, **159**, 146.

412 S. C. Moldoveanu, in *Pyrolysis of Organic Molecules (Second Edition)*, ed. S. C. Moldoveanu, Elsevier, 2019, DOI: https://doi.org/10.1016/B978-0-444-64000-0.00008-1, pp. 327.

413 M. Patel, W. Feng, K. Savaram, M. R. Khoshi, R. Huang, J. Sun, E. Rabie, C. Flach, R. Mendelsohn, E. Garfunkel and H. He, *Small*, 2015, **11**, 3358.

414 Y. Wang, X. Liao, Y. Luo, Q. Yang and G. Li, *J. Mater. Sci. Technol.*, 2015, **31**, 463.

415 M. Acik, G. Lee, C. Mattevi, A. Pirkle, R. M. Wallace, M. Chhowalla, K. Cho and Y. Chabal, *J. Phys. Chem. C*, 2011, **115**, 19761.

416 Y. Chen, X. Zhang, D. Zhang, P. Yu and Y. Ma, *Carbon*, 2011, **49**, 573.

417 T. Wu, X. Wang, H. Qiu, J. Gao, W. Wang and Y. Liu, *J. Mater. Chem.*, 2012, **22**, 4772.

418 M.-C. Hsiao, C.-C. M. Ma, J.-C. Chiang, K.-K. Ho, T.-Y. Chou, X. Xie, C.-H. Tsai, L.-H. Chang and C.-K. Hsieh, *Nanoscale*, 2013, **5**, 5863.

419 A. Bagri, C. Mattevi, M. Acik, Y. J. Chabal, M. Chhowalla and V. B. Shenoy, *Nat. Chem.*, 2010, **2**, 581.

420 S. Pei and H.-M. Cheng, *Carbon*, 2012, **50**, 3210.

421 A. C. Ferrari and J. Robertson, *Physical Review B*, 2000, **61**, 14095.

422 A. C. Ferrari, *Solid State Commun.*, 2007, **143**, 47.

423 S. Cerveny, F. Barroso-Bujans, A. Alegria and J. Colmenero, *J. Phys. Chem. C*, 2010, **114**, 2604.

424 B. Muchharla, T. N. Narayanan, K. Balakrishnan, P. M. Ajayan and S. Talapatra, *2d Mater*, 2014, **1**.

425 J. Yla-Mella and E. Pongracz, *Resources-Basel*, 2016, **5**.

426 M. Fangsheng, Y. Tiechui, C. Aimin and L. Ruidi, *J. Eur. Ceram. Soc.*, 2019, **39**, 4806.

427 W. Cao, J. Li, H. Chen and J. Xue, *J. Photonics Energy*, 2014, **4**, 040990.

428 A. R. Rathmell and B. J. Wiley, *Adv. Mater.*, 2011, **23**, 4798.

429 S. Li, Y. Chen, L. Huang and D. Pan, *Inorg. Chem.*, 2014, **53**, 4440.

430 S. Ding, J. Jiu, Y. Gao, Y. Tian, T. Araki, T. Sugahara, S. Nagao, M. Nogi, H. Koga, K. Suganuma and H. Uchida, *ACS Applied Materials & Interfaces*, 2016, **8**, 6190.

431 A. R. Rathmell, M. Nguyen, M. Chi and B. J. Wiley, *Nano Lett.*, 2012, **12**, 3193.

432 Z. Chen, S. Ye, I. E. Stewart and B. J. Wiley, *ACS Nano*, 2014, **8**, 9673.

433 P.-C. Hsu, H. Wu, T. J. Carney, M. T. McDowell, Y. Yang, E. C. Garnett, M. Li, L. Hu and Y. Cui, *ACS Nano*, 2012, **6**, 5150.

434 L. Shi, R. Wang, H. Zhai, Y. Liu, L. Gao and J. Sun, *Phys. Chem. Chem. Phys.*, 2015, **17**, 4231.

435 S. Chen, L. Brown, M. Levendorf, W. Cai, S.-Y. Ju, J. Edgeworth, X. Li, C. W. Magnuson, A. Velamakanni, R. D. Piner, J. Kang, J. Park and R. S. Ruoff, *ACS Nano*, 2011, **5**, 1321.

436 Y. Ahn, Y. Jeong, D. Lee and Y. Lee, *ACS Nano*, 2015, **9**, 3125.

437 F. Qian, P. C. Lan, T. Olson, C. Zhu, E. B. Duoss, C. M. Spadaccini and T. Y. J. Han, *Chem. Commun. (Cambridge, U. K.)*, 2016, **52**, 11627.

438 S. R. Ye, I. E. Stewart, Z. F. Chen, B. Li, A. R. Rathmell and B. J. Wiley, *Acc. Chem. Res.*, 2016, **49**, 442.

439 K. C. Pradel, K. Sohn and J. Huang, *Angew. Chem., Int. Ed.*, 2011, **50**, 3412.

440 O. Akbulut, C. R. Mace, R. V. Martinez, A. A. Kumar, Z. Nie, M. R. Patton and G. M. Whitesides, *Nano Lett.*, 2012, **12**, 4060.

441 B. Li, S. Ye, I. E. Stewart, S. Alvarez and B. J. Wiley, *Nano Lett.*, 2015, **15**, 6722.

442 M. Bobinger, J. Mock, P. La Torraca, M. Becherer, P. Lugli and L. Larcher, *Adv Mater Interfaces*, 2017, **4**, 1700568.

443 R. Deshmukh, M. Calvo, M. Schreck, E. Tervoort, A. S. Sologubenko and M. Niederberger, *ACS Appl. Mater. Interfaces*, 2018, **10**, 20748.

444 R. M. Mutiso, M. C. Sherrott, A. R. Rathmell, B. J. Wiley and K. I. Winey, *ACS Nano*, 2013, **7**, 7654.

445 A. S. Hashimi, M. A. N. M. Nohan, S. X. Chin, P. S. Khiew, S. Zakaria and C. H. Chia, *Nanomaterials*, 2020, **10**, 1153.

446 X. Zhou, X. Huang, X. Qi, S. Wu, C. Xue, F. Y. C. Boey, Q. Yan, P. Chen and H. Zhang, *J. Phys. Chem. C*, 2009, **113**, 10842.

447 P. Monk, R. Mortimer and D. Rosseinsky, *Electrochromism and Electrochromic Devices*, Cambridge University Press, 2007.

448 L. Gomes, A. Marques, A. Branco, J. Araújo, M. Simões, S. Cardoso, F. Silva, I. Henriques, C. A. T. Laia and C. Costa, *Displays*, 2013, **34**, 326.

449 L. Gomes, A. Branco, T. Moreira, F. Feliciano, C. Pinheiro and C. Costa, *Sol. Energy Mater. Sol. Cells*, 2016, **144**, 631.

450 C. Costa, C. Pinheiro, I. Henriques and C. A. T. Laia, *ACS Applied Materials & Interfaces*, 2012, **4**, 1330.

451 C. Costa, C. Pinheiro, I. Henriques and C. A. T. Laia, *ACS Applied Materials & Interfaces*, 2012, **4**, 5266.

452 S. M. Fonseca, T. Moreira, A. J. Parola, C. Pinheiro and C. A. T. Laia, *Sol. Energy Mater. Sol. Cells*, 2017, **159**, 94.

453 C. G. Wu, M. I. Lu, S. J. Chang and C. S. Wei, *Adv. Funct. Mater.*, 2007, **17**, 1063.

454 W. Wei, C. Xu, J. Ren, B. Xu and X. Qu, *Chem. Commun.*, 2012, **48**, 1284.

455 M. Koppitz, E. Wegner, T. Rödlmeier and A. Colsmann, *Energy Technol.*, 2018, **6**, 1275.

456 Z. Zhu, T. Mankowski, K. Balakrishnan, A. S. Shikoh, F. Touati, M. A. Benammar, M. Mansuripur and C. M. Falco, *ACS Appl. Mater. Interfaces*, 2015, **7**, 16223.

457 Y. Xu, X. Wei, C. Wang, J. Cao, Y. Chen, Z. Ma, Y. You, J. Wan, X. Fang and X. Chen, *Sci. Rep.*, 2017, **7**.

458 W. He, G. Li, S. Zhang, Y. Wei, J. Wang, Q. Li and X. Zhang, *ACS Nano*, 2015, **9**, 4244.

459 J. L. Miao, H. H. Liu, W. Li and X. X. Zhang, *Langmuir*, 2016, **32**, 5365.

460 W. Xu, Y. Zhang, Z. Guo, X. Chen, J. Liu, X. Huang and S.-H. Yu, *Small*, 2012, **8**, 53.

461 H. Lee, S. Hong, J. Lee, Y. D. Suh, J. Kwon, H. Moon, H. Kim, J. Yeo and S. H. Ko, *ACS Appl. Mater. Interfaces*, 2016, **8**, 15449.

462 D. Q. Zeng, Y. Z. Chen, A. L. Lu, M. Li, H. Z. Guo, J. B. Wang and D. L. Peng, *Chem. Commun. (Cambridge, U. K.)*, 2013, **49**, 11545.

463 I. E. Stewart, S. Ye, Z. Chen, P. F. Flowers and B. J. Wiley, *Chem. Mater.*, 2015, **27**, 7788.

464 J. Song, J. Li, J. Xu and H. Zeng, *Nano Lett.*, 2014, **14**, 6298.

465 J. Y. Chen, J. Chen, Y. Li, W. X. Zhou, X. M. Feng, Q. L. Huang, J. G. Zheng, R. Q. Liu, Y. W. Ma and W. Huang, *Nanoscale*, 2015, **7**, 16874.

466 H. Guo, Y. Chen, H. Ping, J. Jin and D.-L. Peng, *Nanoscale*, 2013, **5**, 2394.

467 M. B. P. Mihajlovic and M. M. Antonijevic, *Int. J. Electrochem. Sci.*, 2015, **10**, 1027.

468 A. Zurutuza and C. Marinelli, *Nat. Nanotechnol.*, 2014, **9**, 730.

469 B. E. Deal and J. M. Early, *J. Electrochem. Soc.*, 1979, **126**, 20C.

Acknowledgements

This project has been carried out at the *Institut de Science et d'Ingénierie Supramoléculaires*, University of Strasbourg, in the Nanochemistry Laboratory under the supervision of Professor Paolo Samorì. First of all, I would like to express my deepest gratitude to him for having accepted me as a PhD student in his research group. I am profoundly honoured to have been supervised by a great scientist like him and to have been part of its top-notch research group. I would also like to thank him for his guidance, encouragement and positivism transmitted during the development of this thesis project and, at the same time, for the confidence and freedom that he gave me, allowing me to develop my own ideas and build my independence. I am also grateful to him for introducing me in the DecoChrom project, thanks to which I have travelled around Europe and met and created connections with fantastic people.

I would like to thank the members of this PhD jury: Dr Massimiliano Cavallini, Prof. Slawomir Boncel, and Dr Adrian-Mihail Stadler for having accepted to be referees and for the valuable time dedicated to this thesis.

A special thanks goes to Artur Ciesielski and Alessandro Aliprandi, for their precious scientific help and the time they dedicated to following my thesis project. Without their suggestions, many of the results here presented would not have been possible.

Very special thanks must go to the all the present and past colleagues of the Nanochemistry Group, who accompanied me during these special years for all their kind help and availability. Thanks for inspiring me, supporting me, and sharing with me great time both in and outside the Lab. In particular, I would like to thank Sara B., Marco C., Matilde, Agostino, Dani, Chang-Bo, Nicholas, Luca, Pietro, Stefano (Ippo), Ye, Haijun, Sara G., Stefano DB, Rafael, Veronica, Stefano C., Simone, Marc-Antoine, Tim, Yuda, Zhaoyang, Can, Roald, Yfan, Fernando, Valentina, Stefania for the help in the lab, and for all the great moments we shared in the Christmas dinners, annual BBQ, in the after-work aperitives and in the many dinners we had. Also, thanks to Corinne, Nicolas and Fanny for their help during these years.

A warm thanks to the other friends in Strasbourg who have made me happy and made me spend a good time during these years, Matteo B., Matteo Andrea, Edoardo, Livia, Alice, Agnese, Gianni, Lorenzo, Lukas, Alessandro, Elenia, Elisabetta, Antonella, Flavio.

I am deeply thankful to my family, and my Father especially, who has always encouraged me and supported me. I would not have come this far without him.

I dedicate this thesis to the memory of my Mother, I am sure she would be proud of me.

And last, but not least, the warmest and most heartfelt gratitude goes to Cristina, for the years we shared together, for the love, the happiness and the positivity she transmits me and for keeping on accompanying me in life. Our love has won over distance and separation.

1 November 2020

Cosimo

Publications

1. Alessandro Aliprandi, Tiago Moreira, **Cosimo Anichini**, Marc-Antoine Stoeckel, Matilde Eredia, Ugo Sassi, Matteo Bruna, Carlos Pinheiro, César A. T. Laia, Sara Bonacchi and Paolo Samorì. Hybrid Copper-Nanowire-Reduced-Graphene-Oxide Coatings: A "Green Solution" Toward Highly Transparent, Highly Conductive, and Flexible Electrodes for (Opto)Electronics, *Adv. Mater.*, **2017**, 29, 1703225. DOI: 10.1002/adma.201703225

2. **Cosimo Anichini**, Włodzimierz Czepa, Dawid Pakulski, Alessandro Aliprandi, Artur Ciesielski and Paolo Samorì. Chemical sensing with 2D materials, *Chem. Soc. Rev.*, **2018**, 47, 4860. DOI: 10.1039/C8CS00417J

3. Alessandro Aliprandi, Matilde Eredia, **Cosimo Anichini**, Walid Baaziz, Ovidiu Ersen, Artur Ciesielski and Paolo Samorì. Persian waxing of graphite: towards green large-scale production of graphene, *Chem. Commun.*, **2019**, 55, 5331. DOI: 10.1039/C9CC01822K

4. **Cosimo Anichini**, Alessandro Aliprandi, Sai Manoj Gali, Fabiola Liscio, Vittorio Morandi, Andrea Minoia, David Beljonne, Artur Ciesielski and Paolo Samorì. Ultrafast and Highly Sensitive Chemically Functionalized Graphene Oxide-Based Humidity Sensors: Harnessing Device Performances via the Supramolecular Approach. *ACS Appl. Mater. Interfaces.*,**2020**, 12 *(39)*, 44017. DOI: 10.1021/acsami.0c11236

Conference Presentations

- **Poster** *: Hybrid structures for low resistance and high transmittance electrodes,*

  Cosimo Anichini, Alessandro Aliprandi, Tiago Moreira, Marc-Antoine Stoeckel, Matilde Eredia, Ugo Sassi, Matteo Bruna, Carlos Pinheiro, César A. T. Laia, Sara Bonacchi, Paolo Samorì*

  28th International Conference on Photochemistry, Strasbourg, 18/07/2017

- **Poster** : *Hybrid copper nanowires-reduced graphene oxide films as flexible, transparent and highly conductive electrodes for (opto)electronics*

  Cosimo Anichini, Alessandro Aliprandi, Tiago Moreira, Marc-Antoine Stoeckel, Matilde Eredia, Ugo Sassi, Matteo Bruna, Carlos Pinheiro, César A. T. Laia, Sara Bonacchi, Paolo Samorì*

  Chem2DMat, Strasbourg, 25/08/2017

- **Oral communication** *: Chemical approach towards enhancing the sensitivity of graphene oxide based humidity sensors*

  Cosimo Anichini, Alessandro Aliprandi, Artur Ciesielski, Paolo Samorì*

  E-MRS Spring Meeting 2019, Nice (Fr), 29/05/2019

Cosimo ANICHINI

Matériaux fonctionnels hybrides à base de graphène

Résumé

L'objectif de cette thèse a été l'utilisation d'interactions non covalentes et covalentes afin de développer des structures hybrides à base d'oxyde de graphène réduit (rGO) associé à des molécules et des nanofils de cuivre (Cu NWs) pour des applications en tant que systèmes conducteurs, en optoélectronique et en détection.

D'abord, nous avons exploité la fonctionnalisation covalente de rGO avec des molécules fonctionnelles simples pour former un matériel hybride avec des performances de détection d'humidité remarquables. Cet hybride, qui combine la conductivité et la stabilité du rGO hydrophobe avec la nature hydrophile des molécules de triéthylène glycol, possède une stabilité élevée, une bonne conductivité et une haute sensibilité à l'humidité et sélectivité.

Puis, nous avons exploité l'assemblage non covalent de rGO avec des Cu NWs pour obtenir des électrodes hybrides flexibles et transparentes pour des dispositifs optoélectroniques avec une robustesse accrue. Dans ce cas, la conductivité, la transparence et la flexibilité élevées des films de Cu NWs sont combinées avec la transparence, la conductivité, la flexibilité, l'inertie et les propriétés imperméables des films rGO.

Keywords :
structures hybrides, graphène, oxyde de graphène réduit, nanofils de cuivre, détection, optoélectronique

Résumé en anglais

The aim of this thesis has been the use of non-covalent and covalent interactions to develop hybrid structures based on reduced graphene oxide (rGO) combined with molecules and 1D metallic nanostructures for applications as conductive systems, in opto-electronics and sensing.

First, we have exploited the covalent functionalization of rGO with simple functional molecules to form a rGO-molecules hybrid with remarkable humidity sensing performances. This hybrid combines the conductivity and stability of the hydrophobic rGO with the hydrophilic nature of triethylene glycol molecules to obtain a hydrophilic rGO-molecules hybrid with high stability, good conductivity, and high selective sensitivity to water.

Then, we have exploited the non-covalent assembly of rGO with copper nanowires to obtain hybrid flexible and transparent electrodes for optoelectronic devices. In this case, the high conductivity, transparency and flexibility of films of copper nanowires are combined with the transparency, conductivity, flexibility, inertness and impermeability of rGO films to obtain a hybrid transparent, conductive and flexible film with enhanced robustness.

Keywords :
Graphene, graphene oxide, hybrids, hybrid structures, sensing, optoelectronics, copper nanowires, graphene hybrids